Investigation of Molecular Assisted Recombination Detachment Physics in Fusion Relevant Hydrogen Plasmas

Joseph Branson

Doctor of Philosophy

University of York

Physics

September 2019

Abstract

The Molecular Assisted Recombination (MAR) regime is investigated in hydrogen plasmas in both a linear divertor simulator device, the York Linear Plasma Device, and a Gaseous Electronics Conference standardised reference cell. The aim of this work has been to characterise both the negative ion population within the YLPD and the significance of the surface material choice in divertors by using a well known plasma source in the form of the GEC. Hollow radial profiles with varying profile shapes and absolute maxima have been found for negative ion densities on the YLPD with good spatial resolution. The fraction of H^- has been found to typically lay within 10% of the electron density for most pressures which is in agreement with previous work. Rotational gas temperatures have been found to be around 400-700 K on the YLPD in an MAR state while vibrational temperatures were estimated at 2000-3500 K, also in agreement with literature. The results on the GEC cell for surface effect on negative ion production for stainless steel, tungsten and molybdenum have shown significant differences, the causes of which are not yet fully understood. There was enhancement of negative ion production for both steel and tungsten when compared to molybdenum at 25 Pascals pressure. The trends of negative ion density with applied radio frequency power 9 mm above the samples were similar between materials however the curves appear to be shifted along the power axis based on the specific material as well as scaled in their respective maxima. It is hoped that these measurements will assist in the improvement of MAR understanding and modelling for future research with applications in tokamak divertor design, linear device study and simulation as well as potential broader applications in negative ion devices. The overarching aim is to improve the understanding of MAR negative ion production for divertor optimization.

Contents

List of Tables

List of Figures

Acknowledgments

I would like to thank the following for their contributions to this work, through supervision, experimental assistance and advice, data analysis and complimentary measurements: Dr. Erik Wagenaars, Prof. Timo Gans, Prof. Kieran Gibson, Dr. Kari Niemi, Richard Armitage, Dr. Stefan Briefi, Professor Ursel Fantz, James Ellis, Dr. Hannah Willett, Dr. Cormac Corr, Dr. Rory Scannell, Dr. Thomas O'Gorman, the staff and students at CCFE, and my friends and family for their support.

Declaration

This thesis has not previously been accepted for any degree and is not being concurrently submitted in candidature for any degree other than Doctor of Philosophy of the University of York. This thesis is the result of my own investigations, except where otherwise stated. All other sources are acknowledged by explicit references.

Other things to declare:

Signed: Joe Brannon

Date: 26.09.2019

Chapter 1

Introduction

1.1 Nuclear fusion

1.1.1 Introduction

Humanity's energy needs are increasing to match population needs and our continuing desire for consumer good and electrical devices. It may also become necessary for new problems such as sanitation of waste or purification of salt water into drinking water requiring copious amounts of energy constantly. The continual reliance on fossil fuels is not sustainable from both greenhouse gas release and supply perspectives. Alternative energy sources are used to varying degrees to provide baseline power such as wind, hydroelectric, solar and nuclear fission. There are practical issues with each of these, requiring specific geographical or weather conditions, being at present rather inefficient, or providing a radiation hazard due to the waste output in the case of fission. As such, to fulfill the base energy loads for the foreseeable future requires new large scale commercial power solutions which are relatively abundant, powerful and clean with respect to exhaust gas and long lasting radioactive byproducts. It is believed that nuclear fusion could provide a significant portion of the answer to these demands in the coming decades and continue to provide a solution long-term [17, 18]. While there are different research paths to fusion energy such as inertial confinement fusion, the more promising route appears to be that of magnetic confinement fusion which forms the basis of this work. Despite the challenging nature of the physics of both paths, not to mention the economical and political ramifications of investment, development of fusion relevant technologies is progressing and providing insights into the wider field of

plasma physics.

1.1.2 Fusion Definition

Nuclear fusion is the broad terminology used to describe the process by which multiple atomic nuclei combine to form a smaller number of larger nuclei while converting some mass into energy. Earth's star is sustained by fusion reactions which combine lighter nuclei into heavier ones until these processes are no longer energetically favourable whereupon the star begins to die. Within the sun, the most notable process fuses hydrogen into helium via a relatively inefficient mechanism that involves several stages known as the proton-proton chain [19]. It is then fairly obvious that the process of fusing hydrogen liberates energy and, given the abundance of hydrogen in the universe, it would be prudent to investigate it as a large-scale fuel source. As such, a current subject of much international research is the potential for fusion to be effectively harnessed for the generation of electricity.

1.1.3 Fusion Process

There are several candidate processes for terrestrial commercial fusion involving Hydrogen, its isotopes and those of Helium. There are three primary candidates for fusion that match these reactants. These are: D-D fusion where two Deuterons (D^+) fuse to form a Triton (T^+) and a proton (H^+), Deuterium-Tritium fusion where a Deuteron reacts with a Triton releasing Helium-4 (an alpha particle and an energetic Neutron, and Deuterium-Helium-3 fusion between a Deuteron and an isotopic Helium nucleus producing a proton and an alpha particle. These reactions are only possible with highly energetic incident particles due to their electrostatic potential. This necessitates the reactants at high temperatures on the order of 10^8 K (10 keV) or above. Under these conditions the heat completely ionizes the reactants and the ions and electrons form a system of interacting free particles called a plasma.

The fusion reaction chosen as most appropriate for early stage testing and likely power generation is that between Deuterium and Tritium for a number of reasons. The reaction in detail is given by [4]:

$$ {}^{2}_{1}\mathrm{D}^{+} + {}^{3}_{1}\mathrm{T}^{+} \rightarrow {}^{4}_{2}\mathrm{He}^{2+}\ (3.5\ \mathrm{MeV}) + {}^{1}_{0}\mathrm{n}\ (14.1\ \mathrm{MeV}) \tag{1.1} $$

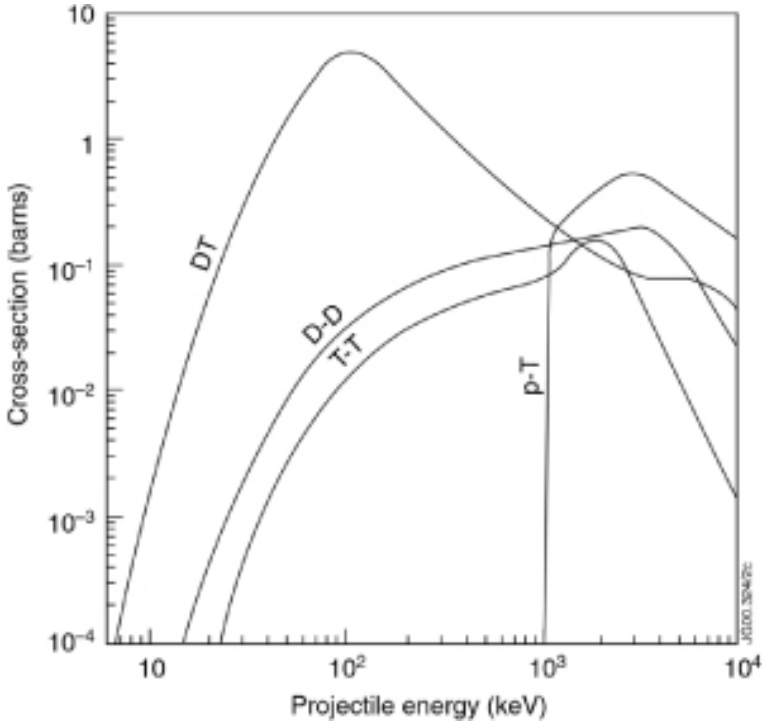

Figure 1.1: Fusion reaction cross section obtained from [1]. This shows the relative ease of access of the various candidate fusion reactions and thus the reasoning behind the use of deuterium and tritium as the fuel mixture.

The reason for this choice of reaction is the high reaction cross section relative to other fuels at significantly lower incident energy as shown in figure 1.1. The energies required are around 10 KeV or 10^8 K and optimal around 100 keV which while still an objectively high temperature range, contrasts with other processes which peak at several MeV. This is not to say that other fuels could not be used at a later time. So-called advanced fuels could eventually provide additional energy with certain advantages, should the cross section requirements be superseded.

Deuterium is abundant as a stable isotope of hydrogen (accounting for approximately 0.0156% by number of all hydrogen in the oceans), tritium is not stable with a half life of around twelve years and needs to be produced in reliable quantities. This may be producible in-situ to the reactor in order to work around the lack of significant amounts of naturally occurring tritium. One of the attractive features of the D-T reaction is the energetic neutron which carries the majority of the energy from the reaction ($\approx 80\%$). This is also a source of major problems due to the damage these energetic neutrons cause to surrounding materials. This energetic neutron can be used to produce tritium through reactions with lithium:

$$^{6}_{3}\mathrm{Li} + \mathrm{n} \rightarrow {}^{3}_{1}\mathrm{T} + {}^{4}_{2}\mathrm{He} \quad {}^{7}_{3}\mathrm{Li} + \mathrm{n} \rightarrow {}^{3}_{1}\mathrm{T} + {}^{4}_{2}\mathrm{He} + \mathrm{n} \tag{1.2}$$

Some of the energy carried by the neutron is also ideally transferred as heat to an intermediate coolant which can be used to drive a conventional steam turbine. There are designs which utilize the lithium itself in liquid state, along with lead which acts as a neutron multiplier, to perform both tasks simultaneously [20]. The alpha particles are ideally used to assist in driving the fusion reactions by way of transferring momentum to the primary reactants through collisions known unsurprisingly as alpha heating.

The necessity in having such high temperatures precludes the sole use of solid walls as a confinement system as they would suffer significant damage and the ablated material would quench the plasma. This is particularly problematic if the ablated material contains high-Z elements as these particles absorb significant thermal energy and re-radiate it as largely useless photons. Instead the electrically charged nature of the plasma is used to confine it via externally applied magnetic fields. Numerous designs have been attempted over the decades including but not limited to: linear machines such as magnetic mirrors [21] and pinch devices [22] , and toroidal machines such as tokamaks [4] and stellarators [23]. All of these are designed to keep the majority of the energetic ionized particle flux away from solid material surfaces.

1.1.4 Plasma basics

This plasma state common to most conventional fusion and fusion science devices is core to this thesis and thus requires a brief introduction and definition of its own before proceeding. The plasma state is recognised as distinct from a gaseous state and is defined by a few criteria. The first criterion is that the integral charge density of the ions must be wholly or mostly balanced by the integral charge density of electrons such that the plasma exists in a quasi-neutral state including within smaller regions. In the plasma state each ion is shielded from its neighbours by a local cloud of electrons attracted by electrostatic forces called a Debye sphere. Over length scales much larger than the diameter of these spheres, known as the Debye length, the total populations of positive and negative charges equate. The second criterion follows that the Debye length is small compared to the overall scale or size of the plasma. The third criterion is that the frequency of electron oscillations in the plasma is

high with respect to interactions with neutrals such that electrostatic interactions dominate over gas kinetics.This essentially means that the gas collision physics do not dominate to the point where the plasma is snuffed out and simply behaves like a warm or hot gas. A longer general overview of the plasma state can be found in many if not all relevant textbooks e.g. [24].

Plasma is found in many widespread applications such as nano-fabrication, lighting and deposition of exotic coatings on complex geometries as well as in nature such as lightning, stars and the inter-stellar medium. Fusion power devices, regardless of specific methodology, render the necessary fuel into a plasma state in order to allow reactions to occur hence the importance of understanding how this state behaves. The material in this thesis focuses on the partially recombined plasma found in one region of one class of fusion device in the hopes of enhancing understanding the specifics of this plasma environment.

1.1.5 Tokamaks

1.1.5.1 Magnetic confinement devices and Tokamak origins

Currently the most popular and thus-far successful device in magnetic confinement fusion is the tokamak. This device consists of a toroidal vacuum vessel within which a toroidal magnetic field (B_ϕ) is generated. This is done by a series of electromagnetic coils at regular intervals around the circumference of the vacuum vessel known as toroidal field coils (henceforth TF coils). The electrons and ions then travel in opposing circular orbits around the field lines. The radius of each particle's orbit is based on its mass and is called the Larmor radius (r_L). This trajectory generally keeps charged species away from material surfaces hence the term magnetic confinement. A central winding transformer coil is commonly found working in conjunction with the TF coils to produce a toroidal current in the plasma (I_p). This induces a poloidal component to the field (B_θ) and a corresponding helicity to the field lines. A diagram comparing the toroidal geometry to a linear geometry is show below in figure 1.2.

This arrangement balances magnetic forces confining the plasma and the pressure forces within the plasma pushing particles radially outwards. Striking a balance between these forces forms the basis of magnetic plasma confinement.

There are various drift mechanisms in the plasma, a notable example being those arising from the gradient of the toroidal field [4], there may be net vertical motion to the particles

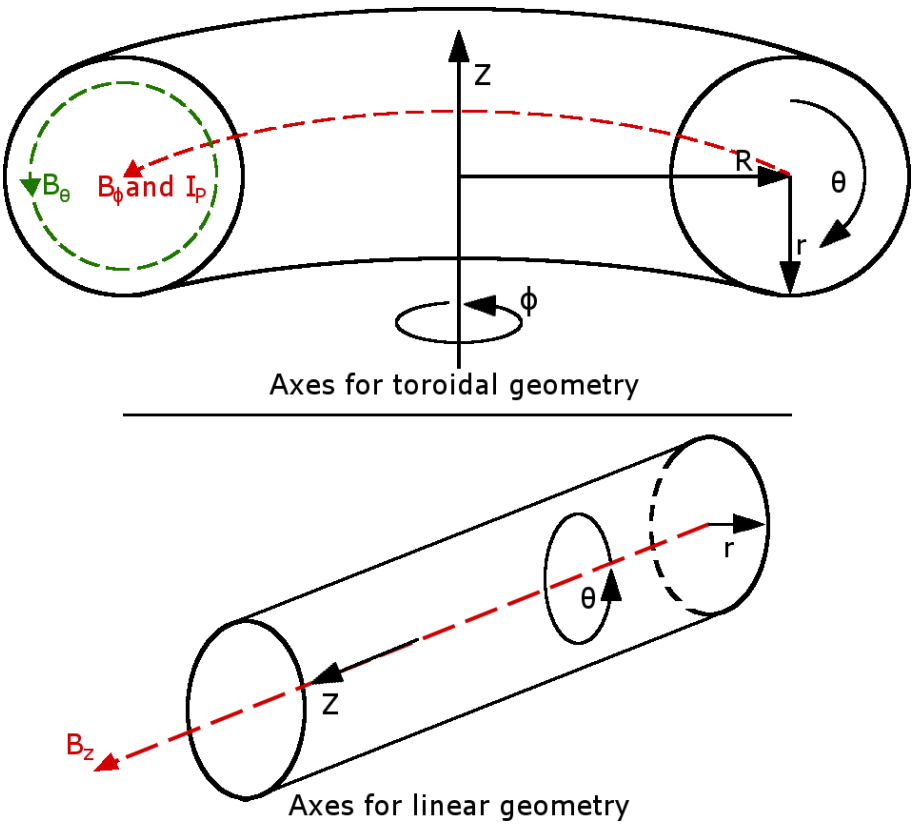

Figure 1.2: This diagram illustrates the basic differences in the geometry associated with a toroidal device and a linear device. It can be seen that the magnetic field runs along the Z axis in the linear case whereas in the toroidal geometry, the field components are in the ϕ and θ directions. The Z axis in the toroidal case represents the height of a point above or below a given plane, sometimes the mid-plane of the device.

which can cause the plasma to contact the vessel walls leading to damage and plasma failure. The plasma current averages some relevant drifts to zero, improving the confinement while additional poloidal field coils assist in positioning and shaping the plasma. This is the basic minimal layout of a tokamak and is shown in figure 1.3.

The first tokamak was constructed in the former USSR [25] as a solution to the common problem with linear plasma devices whereby, regardless of the field strength at the ends, particle losses were found to be inevitable and unsustainable. The tokamak solved this problem by simply not providing any ends from which the particles could escape. Linear devices did not become obsolete however and have retained their use as vehicles for various fusion-relevant plasma studies, including the York Linear Plasma Device (YLPD - formerly UMIST linear device) which is the primary device of interest to this thesis.

Tokamaks have grown steadily in size to be able to achieve higher plasma densities (n_p),

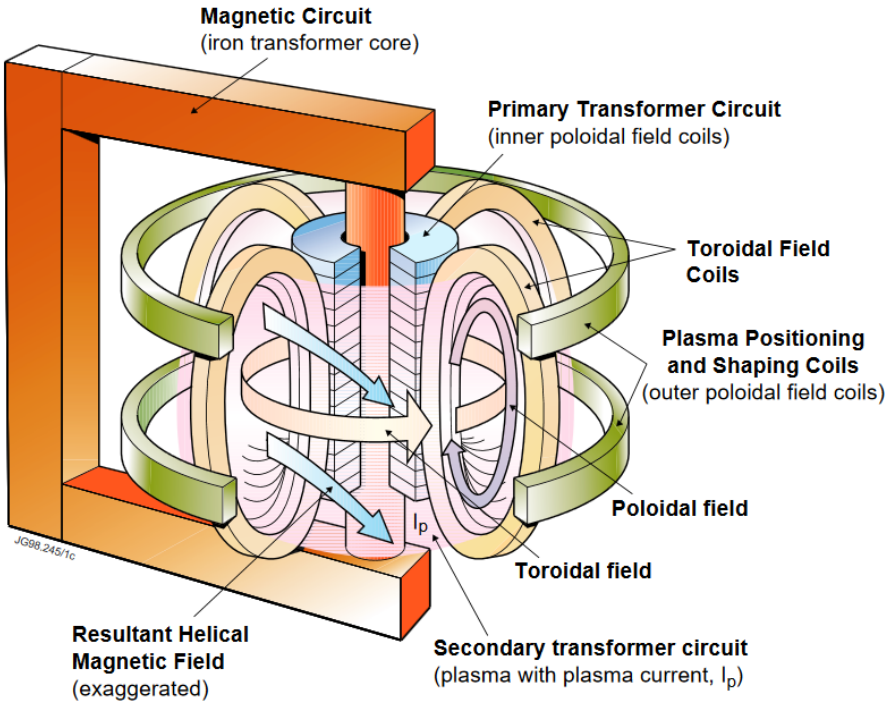

Figure 1.3: Basic Tokamak layout, magnetic confinement systems. (Structure not shown) [2]

temperatures (T_p) and confinement times (τ_E). These factors are combined by way of the fusion triple product: $n_p T_p \tau_E$ which gives a general measure of the proximity to sustainable reactor plasma conditions. If the condition is met that $n_p T_p \tau_E > 5{\times}10^{21}$ m^{-3} s keV ignition may be achieved whereby the plasma self-sustains and may be the basis of a functional power plant. These devices are approaching the point where they will be able to attain or exceed the triple product threshold allowing engineers to construct a viable reactor. The triple product record for what a current large scale tokamak is able to achieve is $1.5{\times}10^{21}$ m^{-3} s keV by JT-60 U [26] while the primary next generation device, ITER, is targeted to be able to achieve $6.138{\times}10^{21}$ m^{-3} s keV [27]. ITER will be the largest tokamak in the world once it is operational and is tasked with achieving a ratio of fusion power measured being ten times the power used to heat the plasma. This primary goal is supplemented by developing the engineering understanding for practical tritium breeding and power extraction for power plant scenarios.

1.1.5.2 Exhaust plasma challenges and the scrape-off layer

One of the main problems facing tokamaks preventing access to a sustaining reaction is the presence of impurities. It is necessary to exhaust Helium ash and high-Z particles from a fusion plasma because of the significant impact these species have on the stored energy and fusion process. High-Z impurities are most likely to ingress from the walls where they are evaporated before recycling into the core. The energy transferred to these impurities is rapidly radiated away via bremsstrahlung emission, which scales with the value of Z^2, cooling the plasma over a short period of time and potentially destroying the plasma entirely. Impurities can also dilute the primary fusion process given sufficient number densities by preventing the desired collisions between D and T. As such it is vital to remove impurities from the core and thermalised alpha particles once their energy has been transferred to fuel species to sustain the reaction.

When viewed as a poloidal cross section, the magnetic field consists of a series of nested flux surfaces along which the helical field lines of the convolved B_θ and B_ϕ run (figure 1.4). There is a separation between this core region where the field lines lie on closed flux surfaces and an outer region where the field lines intersect a material surface on the inside of the vacuum vessel. These outer flux surfaces too, are closed but are functionally open within the vacuum vessel, hence this boundary is known as the last closed flux surface (LCFS). Particles outside the LCFS generally travel rapidly parallel to the field lines until they either impact a surface, return to their original position or recycle into the core with a characteristic transition path length of $L = \pi R q$. The quantity q is a numerical expression for the ratio of the number of complete torroidal to poloidal transits known as the safety factor, so called because at values ≤ 2 the plasma is MHD unstable. Conversely, the plasma inside the LCFS preferentially moves relatively slowly radially across the poloidal cross section.

Design choices have been employed to separate or at least restrict the contact point/s between the plasma and the inside vessel wall. This was motivated by the issue of surface damage and also to minimize the recycling of impurities back into the core. The first design, still used in some devices today was the limiter, a solid toroidally positioned or sometimes fully symmetric structure protruding inward from the wall. This structure would "scrape-off" the outermost portion of plasma in the open flux region resulting in the term "scrape-off layer" (SOL) which has been used as a moniker for this portion of outer plasma since. The second and more recent design is the divertor: a distinct configuration accessed by

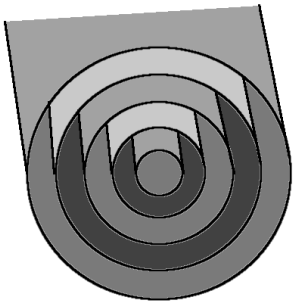

Figure 1.4: Basic schematic of nested flux surfaces based on image from [3].

altered magnetic geometry shown in figure 1.5. In this configuration the plasma in the SOL is directed away from the main body of plasma onto separate plates further away to be terminated. These systems were both implemented also as a means to remove impurities from the bulk via the SOL. In both cases the SOL is similar in scale and pumping has been employed to attempt to remove carried impurities before re-circulation into the bulk.

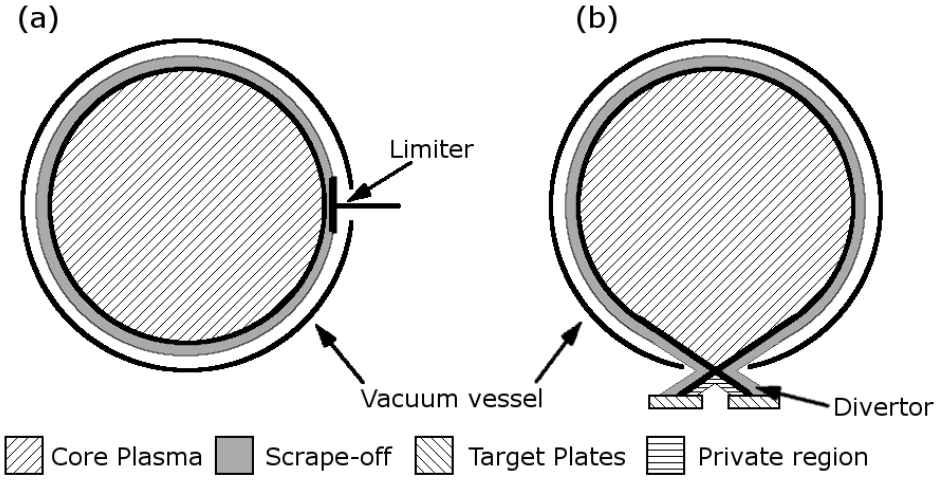

Figure 1.5: (a): Basic schematic of limiter configuration and (b): basic layout of divertor configuration - [3, 4].

Experiments on TFTR [28], TEXTOR and DIII-D [29] and JT60 [30] have been performed which investigated impurity transport for differing plasma conditions using edge puffing and neutral beams targeted at the core. These experiments, together, show that helium ash which makes it to the LCFS may be pumped away through interaction with a limiter and pumping system or a divertor pumping system. It has been shown in those

devices capable of H-mode such as DIII-D [29] and JT60-U [31], the removal may be more difficult in reactor-relevant H-mode compared to the lower performance L-mode. The removal of impurities allows the core plasma to retain performance for longer periods which is essential to commercial reactor operation and next generation experiments.

1.1.5.3 Tokamak divertor

Limiters were used early in tokamak development as a simple and effective means to prevent damage to the majority of the inner vessel wall. The weaknesses of this design were the relative inflexibility of the small strike point which concentrated the particle flux causing significant limiter surface ablation, and the proximity of freshly ablated material to the core plasma. High Z impurities from the surface stood a significant chance of recycling into the core and causing substantial radiative losses. This was found to be a critical factor moving forwards with tokamak development for high power operation. Enter the divertor concept which largely solved this problem by introducing a change in the geometry of the confining field to a cut down figure 8 which results in one or more magnetic nulls at the "x-point" of the figure 8. In this case, the LCFS takes on a new name: the separatrix and separates the outer portion of the field into new regions. These are the outer and inner scrape-off layers where parallel impurity transport is high, and the private flux regions where some plasma arises and cannot easily escape.

The overall field in tokamaks equipped with a divertor is usually more elliptical or triangular in nature where the field lines of the inner and outer SOL regions may be directed away from the core in a number of directions called divertor legs. The plasma may then be targeted onto divertor plates located such that ablated impurities are redirected back down towards the plates or become trapped in the private-flux region. The divertor has been a successful addition to tokamak designs, showing that the impurity fraction can be reduced appreciably compared to similar experiments with limiters [32, 33]. The divertor also allows adequate pumping of helium ash and can be used to optimize volumetric dissipation of power via radiation and recombination. Due to the distant nature of the divertor plates, neutral gas may be injected nearby in order to set up a steep temperature gradient close to the surface, parallel to the poloidal component of the magnetic field ($B_{Poloidal}$). This is achieved without fear of said gas migrating in significant density into the core. The relatively cool plasma near the plate surface reduces ablation and heat damage, allowing longer running

times due to the reduction in impurities and less frequent repairs.

The performance of the divertor concept has allowed scaling to larger devices with higher power and better confinement.Tokamak divertors are thus found on most large, modern fusion devices such as JET [34], ASDEX-Upgrade [35] and JT-60 U (now moving to JT-60 SA [36]). The design of ITER incorporates a single null type lower divertor where the exhaust power and particle flux will be handled in what is known as a detached plasma configuration (see section 2.1). The merits of double vs single null divertors may be summarized as spreading power over larger area, improving confinement and improving fuelling efficiency at the expense of ease of ELM suppression, device complexity and stability of operating scenario [37].

Divertors may be a necessity for future tokamak devices and are even effective at heat flux reduction however they are still not effective enough without assistance. The scrape-off layer plasma is constrained to the magnetic field lines which terminate at the divertor plate surface over a relatively small area. This means that in order to more effectively utilise the divertor for high power future tokamaks, the high temperature particle load must be more effectively spread over the available area. One of the easiest methods to achieve this would be the removal or reduction of the magnetic field in the divertor region. Seeing as this is not practical, it is instead prudent to change the nature of the plasma which leads on to the proposed solution known as detachment.

1.1.5.4 Detachment

Detachment with regards to tokamak science refers to the phenomenon whereby the visible plasma boundary moves upstream away from the divertor surface. This manifests in a significant proportion of the plasma species being neutralised resulting in their detachment from the influence of the magnetic field lines. This neutralization radiates some of the energy of the charged species away into 4π steradians which simultaneously reduces their kinetic temperature and spreads the radiated heat over a significantly larger area of the plasma facing components, predominantly within the divertor region. The walls can tolerate this heating in comparison to the concentrated particle flux on smaller areas. The other desirable result of the detachment process is that both the remaining charged particle flux is reduced and the still relatively high temperature neutrals may also offload their energy to wall regions far from the flux lines.

There are two main regimes generally independently acknowledged [38] for detachment: the Electron Ion Recombination (EIR) dominated regime and the Molecular Activated Recombination (MAR) dominated regime. The work in this thesis predominantly focuses on the MAR regime as the interactions within the partially ionised plasma involving molecular species are generally less well understood than the interactions of EIR plasmas. This molecular regime is comprised of a wider variety of particle species which is a large part of why this regime is more challenging to examine.

1.1.5.5 Significance of detachment in fusion research

Detachment is a critical operating parameter for future tokamak devices, particularly ITER. Without a reliable detached state in the ITER divertor, the device will be practically inoperable as damage will occur too rapidly to allow the necessary pulse duration. Despite the critical nature of divertor detachment and the research undertaken thus far, the full scope of the physics is not yet fully understood. In particular, due to the complex interactions with molecules the MAR state has not been fully mapped out. The relative contribution of different reaction pathways under the parameter space available in a tokamak divertor is not known. The distribution and abundance/dominance of different plasma species is not fully understood and the relative importance of the wall surfaces in the divertor and their contribution to the recombination processes is not fully understood. This thesis looks to provide new measurements under divertor relevant hydrogen plasma conditions and their relationships with the available surface materials in somewhat similar conditions. In doing this new insights into the MAR detachment state will be gained and new data will be acquired for use in bench-marking simulations of divertor-like experiments.

1.2 Thesis outline

This thesis looks to examine the MAR detached plasma state on the York Linear Plasma Device (YLPD) as well as the relationship with other partially ionised molecular plasmas found in a Gaseous Electronics Conference (GEC) type device. This was predominantly done by examining the negative ion populations in both devices along with the electron densities and temperatures, and the rotational and vibrational gas temperatures. Negative ions are crucial to the MAR recombination reaction chains but are somewhat difficult to

measure in an environment which has such a significant electron population. This study includes the effects of nearby surface materials to the recombination processes in similar plasmas. The materials examined were Tungsten, steel and Molybdenum which are used in various parts of tokamak construction particularly Tungsten and steel. The implication is that simply building the divertor out of Tungsten for its heat resistance may not be the optimal choice for plasma recombination and temperature reduction. The background and theory chapter covers the MAR plasma definition and some of the body of work concerning MAR in existing tokamaks before looking at examples of work on relevant surface material effects. Beyond this, the two primary experimental devices are explained and the various diagnostic techniques used are covered in detail.

The results for the experiments on the GEC are presented first followed by the YLPD as a divertor simulator of sorts. Finally a short chapter is presented on a collaborative project undertaken with the Culham Centre for Fusion Energy (CCFE) in Oxfordshire in the UK. This project was undertaken due to the relevance of Thomson scattering diagnostics for obtaining more precise measurements of electron temperature and density which are critical to the understanding of the MAR active plasma. The project involved an analysis of the background light collected by the Joint European Torus (JET) High Resolution Thomson Scattering (HRTS) diagnostic. This was necessary because of concerns regarding sensor overload due to bremsstrahlung radiation and line emission when faced with the scale of the ITER experiment. Due to the projected increase in line radiation associated with predominantly hydrogen and helium, and to a lesser extent wall materials such as beryllium, the signal to noise ratio of the Thomson scattering diagnostic may be deteriorated. Similar to the system commissioned on JET, a series of optical filters are to be placed in front of the individual spectral channels to form a filter profile in order to minimise such interference from line radiation. As such, a filter profile was decided upon following this study to be implemented in the ITER Thomson scattering diagnostic minimising the impact of stray background light.

Chapter 2

Background and theory

2.1 Detachment overview

Detachment is the state whereby a magnetically confined plasma is removed or "detached" from the magnetic field by neutralization of ionic species. Shortly after the publication of the first design documents for ITER, it was clear that the divertor heat loading needed to be limited to 10 megawatts per square metre due to the thermal limitations of available wall materials. This would only be achieved by dissipating 80-90% of the exhaust power before the plasma was intercepted by any divertor components [39].

Detachment is typically achieved through increasing the rate of recombination of charged plasma species, whether passively by allowing recombination along the field lines or actively through constant flow or intermittent puffing of additional neutral gas into the region where recombination enhancement is desired. This added gas interacts with the plasma through collisions creating new ionic and neutral species, distributing the energy of the plasma over a greater number of particles and increasing the power loss through emission of electromagnetic radiation. Alternatively, the neutrals absorb energy from the ions, meaning that while the total stored energy in the region remains unchanged, it is no longer as constrained to the charged species and thus the magnetic field. This prevents localized heating by allowing the collisional heating to spread across a larger surface area within the divertor and encourages radiative energy loss along lines of sight to large sections of the inner wall of the tokamak. The gas used need not be the same as the species found in the upstream plasma as long as it is not detrimentally reactive with the upstream plasma species (such as oxygen in a predominantly hydrogen plasma). The gas should also be comprised of low Z elements so

that particles transported into the core do not absorb and re-radiate the heat stored in the core plasma as high energy (x-ray) photons. Sufficient radiative loss, while beneficial in the divertor, drains enough energy from the core plasma to snuff the reaction.

Specifically, the characteristics of detachment are described by Stangeby [40], The ITER Group [41], Mathews [42] and others. The three primary features can be surmised as:

- **Ion current condition:** The ion current to the target is diminished by recombination events
- **Plasma pressure condition:** The plasma pressure reduces at the target plate due to momentum losses.
- **Energy flux condition:** The power reaching the target plate reduces due to volume recombination.

If the plasma pressure condition and the energy flux condition above are both satisfied, the plasma may be referred to as fully detached. This is in contrast to the partially detached case where only one of these is true. While it is generally acceptable for either the energy flux or particle flux to be reduced, each has its own issues in terms of damage such that a reduction in both is ideal. In the case of high particle flux, ion bombardment may remove material whereas high energy flux results in more standard melting problems.

Detachment has been observed and studied in a number of experiments around the world which are summarized in this section. The detached state has been further subdivided into two sub-regimes following investigation into its properties and behaviour by the research community. These two regimes are distinguished by the primary active channels which dominate the overall recombination. The two regimes of interest are the Electron-Ion Recombination regime (EIR) and the Molecular Activated (Assisted) Recombination (MAR) regime.

2.2 Electron Ion Recombination (EIR) detachment

EIR detachment is any detached plasma state where the predominant mechanism for recombination is the direct recombination of relatively slow electrons and ions. This can occur via simple radiative recombination (RR), three-body-recombination (TBR) [43] or dielectronic recombination (DR). As a result of the direct radiative recombination (RR), the light radiated from the plasma tends to be constrained to x-rays as the unbound electrons are

captured by the ions. Dielectronic recombination (DR) is sometimes considered separately as the electron and ion recombine to a metastable state and undergo atomic transitions as the electrons de-excite within the atoms afterwards. In the case of three-body recombination (TBR) the third body leaves the recombination event with the surplus energy. Electron-ion recombination is most efficient at high density and low electron temperature ≤ 1 eV [44] and the predominant process is that of three-body recombination. These processes are united in that they all involve at least one electron and one hydrogenic nucleus (H^+, D^+ etc.). The three processes are associated with the following expressions:

$$e^- + H^+ \rightarrow H + h\nu \qquad (RR) \tag{2.1}$$

$$e^- + H^+ \rightarrow H^{**} \rightarrow H + h\nu \qquad (DR) \tag{2.2}$$

$$e^- + H^+ + \vartheta \rightarrow H^* + \vartheta' \qquad (TBR) \tag{2.3}$$

Radiative recombination, eq. 2.1, is the process by which a roaming electron is captured by an ion, subsequently relaxing directly into a bound state by emitting electromagnetic radiation of frequency ν. This contrasts with dielectronic recombination, eq. 2.2, where the electron is captured with excess energy leaving the newly formed Hydrogen atom temporarily in an excited state. From this the electron releases its excess energy by transitioning to a lower state, emitting another characteristic photon of frequency ν. Finally, the three body process, eq. 2.3, occurs with notable frequency for high n_e. This process involves a third "chaperone" species (ϑ) which can be any particle within the plasma with differing outcomes depending on the specific particle involved in the interaction. If the third body is an electron, it may carry excess energy and/or momentum back into the plasma, however if the third body is a neutral atomic or molecular species, that energy is removed from the recombining plasma system. This process is generally dark as the majority of interactions will emit no electromagnetic energy, however this is possible in the event of an excited state recombined Hydrogen atom which then relaxes in a similar fashion to DR. In the YLPD the extra particle in three body recombination is usually an electron.

2.3 MAR detachment

MAR detachment is any detached plasma state where the predominant mechanism/s for recombination involve/s molecules directly as part of the recombination reaction chain/s. This regime is more complex due to the active participation of molecular species. The energy distribution functions of the molecules are important to the dynamics of the system because the reaction processes are often dependant on the initial state of the molecules that participate in the relevant reactions. The MAR processes are more dominant at lower densities and slightly higher electron temperatures (0.8 eV $\rightarrow$ 2 eV) [45] due to the requirement of populating vibrational states within the molecules. A more complete explanation of the state of MAR detachment physics, as well as previous developments in MAR research are given in the following section.

2.3.1 Initial suggestion of MAR

The MAR process was initially theorized to exist for some plasma conditions by [46, 47]. They used a collisional radiative model to examine a recombining plasma with molecular species and found that recombination was enhanced by vibrationally excited molecules mediating the overall recombination process. The conditions theorized to be optimal for this recombination enhancement were electron temperatures between one and three electron volts and electron densities approximately ten times the density of molecules. This modelling also highlighted the presence of negative ions and their importance in the electron channel of the MAR state.

2.3.2 MAR processes

There are two reaction chains associated with the MAR detachment state. These two chains are distinguished by which of the two primary charged species interacts with the excited hydrogen molecule. The hydrogen molecules have kinetic, rotational and vibrational energy distribution functions describing their initial energy state. The processes below are not particularly sensitive to the rotational energy distribution and the molecules are moving slowly with respect to the electrons and ions. As a result, the reaction collision energy is usually taken to be the energy of the fast charged particle thus, the kinetic energy of the molecules is not significant. $H_2{}^*$ (and later $H_2(V)$) therefore signifies the vibrationally excited molecule. These MAR processes are summarised below in expressions (2.4, 2.5, 2.6,

2.7):

$$H_2^* + e^- \rightarrow H^- + H \qquad (DA) \tag{2.4}$$

$$H^- + A^+ \rightarrow H + A \qquad (CER) \tag{2.5}$$

$$H_2^* + A^+ \rightarrow (AH)^+ + H \qquad (CN+) \tag{2.6}$$

$$(AH)^+ + e^- \rightarrow A + H \qquad (DiR) \tag{2.7}$$

The line indicates the split between the two reaction chains. In the first case, a vibrationally excited molecule, usually excited by impact excitation from an energetic particle, collides with an electron which dissociates the excited molecule. If the energy of the electron is high enough to dissociate the molecule yet not too high, the electron may attach to one of the hydrogen atoms creating a hydride ion. This hydride ion reacts readily with a positive ion, usually a proton/deuteron in the case of a fusion relevant divertor plasma, forming two neutral atoms, one in the ground state and another in an electronically excited state. Because these atoms are not strongly bound to the magnetic field, they may diffuse away from the interaction site. During this time they will take part in further collisions with other particles or plasma facing components. As a result, the average particle energy will decrease and density of neutrals will increase allowing preservation of plasma facing surfaces. The reduced influence of the magnetic field also facilitates the collisional migration of some neutralized particles into pumping components over time. By verifying the presence of negative hydrogen ions in the plasma using diagnostics like laser photodetachment 2.7.2, this can be taken as evidence of where the initial MAR process is occurring.

Similarly the molecule may encounter a positive ion resulting in an ion conversion event where the positive ion substitutes with one of the hydrogen atoms forming a molecular ion and a free hydrogen atom. This molecular ion may then react with an electron to form two neutral atoms, completing the chain. If the environment contains $H_3{}^+$ in any reasonable number density, these may also neutralise negative ions leading to the formation

of a neutral molecule and two atoms, two molecules, or four atoms given enough collision energy. In principle, a hydride ion may also react with the molecular ion to form three neutrals depending on the abundance of each. In the case of the YLPD and most fusion experiments using hydrogen isotopes, the positive ion is a proton or deuteron etc. making the reaction chain that shown below.

$$H_2^* + H^+ \rightarrow H_2^+ + H \qquad (CN+_H) \tag{2.8}$$

$$H_2^+ + e^- \rightarrow H + H(2H) \qquad (DiR_H) \tag{2.9}$$

In some cases, other non-hazardous gasses are puffed into a relatively high temperature plasma to encourage predominantly radiation such as argon and nitrogen [48]. In these cases, positive ions of these gasses may take the role of the extra particle for ion conversion but they are low in energy in the first place and so detract from the aim of the MAR processes.

2.4 Conditions and rate constant

The rate constants for the combined EIR processes as functions of electron temperature are displayed in figure 2.1 for a range of plasma densities. It is clear from this figure that EIR significantly dominates at $T_e < 1$ eV and improves consistently with increasing orders of magnitude of n_e. The rate constant increases beyond the low temperature bound implying that this process only improves as the electron temperature is reduced. This makes sense as the process relies on capture of an electron by an ion directly as mediated predominantly by an additional electron. The available interaction time is longer for electrons with low kinetic energy due to their lower speed, hence the higher rate constant for an electron population with a lower temperature. The MAR process is more complex and its rate constant reflects this in the shape of the trend. The rate constant for MAR increases rapidly with temperature up to around 2 eV before remaining more stable for increasing temperature into the 5-10 eV range. At the temperature threshold of the onset of MAR detachment, the MAR rate constant dominates by several orders of magnitude and remains dominant as the EIR rate constant collapses towards zero with increasing temperature.

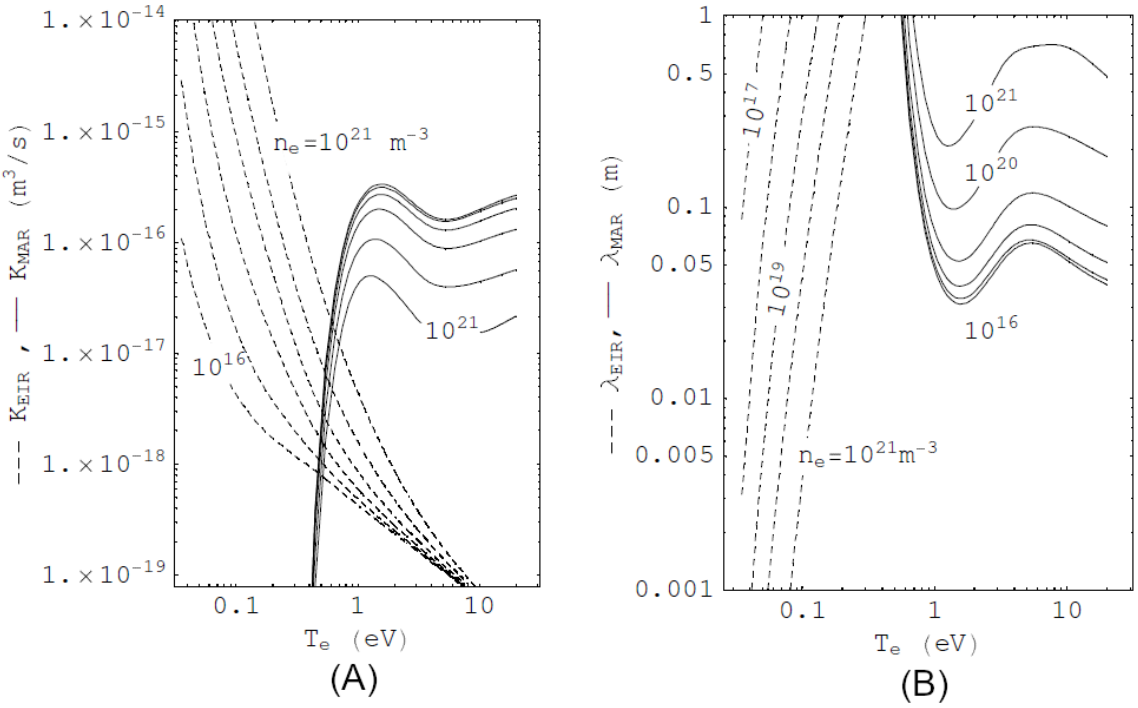

Figure 2.1: Calculations of: (A) the rate coefficient and (B) the mean free path for the total EIR process and MAR process as functions of electron temperature T_e and density n_e for an ion temperature 440 K and gas pressure of 1 Pa. Figure reproduced from [3] originally calculated by U. Fantz for the YLPD.

In the YLPD, as discussed in [3], the dimensions of the target chamber allow MAR processes to exist in some capacity for a wide parameter range due to the mean free path scaling. This is visible for conditions where a detached plasma is formed by way of a pink glowing MAR zone. Under conditions resulting in the predominantly blue radiating plasma of EIR, the MAR recombining plasma may be found upstream, closer to the plasma source. This proximity also implies a hybrid mode somewhere between the two which has not been extensively examined.

The following section covers some work on detachment in tokamaks and more prominently, studies on existing linear devices around the globe.

2.5 Existing work on detachment in tokamaks and tokamak relevant experiments

2.5.1 Detachment research in tokamaks

Some work has been performed on tokamak devices both experimental and simulated in order to examine the role of MAR detachment. Some studies on tokamaks or tokamak relevant plasmas seem to indicate that the role of MAR is small in divertor recombination physics. A recent model of the ITER divertor by Pitts et.al. [49] estimates typical outer target plate operating conditions (without detachment) as follows: peak heat flux - q_{pk} around 10-15 MWm^{-2}, electron temperature - T_e between 30-40 eV and electron density - n_e between $0.5 - 1.0 \times 10^{21}$ m^{-3}. The same study estimates values for the same quantities under partially detached conditions to be: q_{pk} around 4 MWm^{-2}, T_e in the range of 1 eV and n_e between $1.0 - 2.0 \times 10^{21}$ m^{-3}.

Another model produced results indicating that the contribution of MAR processes to the overall recombination rate would be negligible when compared with the three body processes found in the EIR regime. This study was presented by Kukushkin et. al. [50] and cited in [51]. It is worth noting however, that if steps could be taken to increase the prevalence of MAR to where it improved survivability significantly, an MAR detachment dominated operating regime may be preferable for continuous operation.

Experimental observations on the ASDEX-U tokamak showed that the fraction of molecules in the V >0 vibrational levels was only a few percent (experiment development [52], application to ASDEX-U [53]). Further experiments on ASDEX-U [54] also concluded that the MAR processes were not prevalent due to the significantly higher rates of dissociation. Simulations using the B2-EIRENE [55] code re-examined the role of neutrals and molecular species in the recombining divertor in order to explore the potentially high recombination rates of MAR and radiative recombination over thee-body recombination. Simulations were also performed using B2-EIRENE to compliment the measurements on ASDEX-U in [54] which showed good agreement with the measurements. Experiments on Alcator C-Mod [56] however showed MAR rates comparable to and under some conditions 50% greater than the EIR or three-body recombination rate which is significant. Of note, these experiments and simulations were all performed without additional puffing of gas into the divertor chamber.

Given that specifically MAR detachment is not widely used in tokamaks at this time,

it could represent a large improvement in recombination as required to move forward. In contrast to a large proportion of tokamak studies, work has been performed on smaller devices which seek to study divertor relevant physics in a more easily accessible form. These devices are collectively known as divertor simulators.

2.5.2 Divertor simulators

Experimental divertor simulators exist in many forms, but are usually linear in nature such as TPD-sheet, PISCES-A and the York Linear Plasma Device (YLPD) with some toroidal machines such as NAGDIS-T. Ohno 2017 [57] provides an overview of the research done on linear divertor simulators from which many of the details and references in this section are sourced. The reasons for divertor simulator experiments such as linear devices are twofold: The devices simulate a scrape-off layer plasma with an open field and they are simpler and more cost-effective to produce and operate. They are also advantageous due to their ability to operate in steady state and their simpler geometry allowing for easier comparisons with simulations. Another useful characteristic is the relative ease of access to various positions along the direction parallel to the magnetic field allowing for diagnostics and the introduction of gas at various locations. There are however, significant differences between these machines and real and proposed tokamak divertors such as the magnetic connection length and curved field which influence the transport properties of the plasma [58].

This section covers the body of work previously performed on detachment physics in divertor simulator devices akin in many ways to the YLPD with emphasis placed on MAR studies and those relating to MAR plasmas. Toroidal devices are not considered here but literature can be found in the paper mentioned previously by Ohno [57].

2.5.2.1 QED

QED (the Quiet Energetic Device) was a pioneering machine in the demonstration of detachment as a realistic divertor operating concept [5]. The device is shown schematically in figure: 2.2. The experiments on this device showed a dramatic reduction in collected energy flux along the axial (Z) direction as a function of the gas pressure. The energy stored in the plasma was largely absorbed into the neutral population and spread over the inside of the device by radiation and slow particle impact. Studies on this device also began to examine the interactions between neutrals and plasma species, attempting to compare rate

coefficients of some of the potential processes [59]. The work on this device instigated much of the following work on linear plasma divertor simulators.

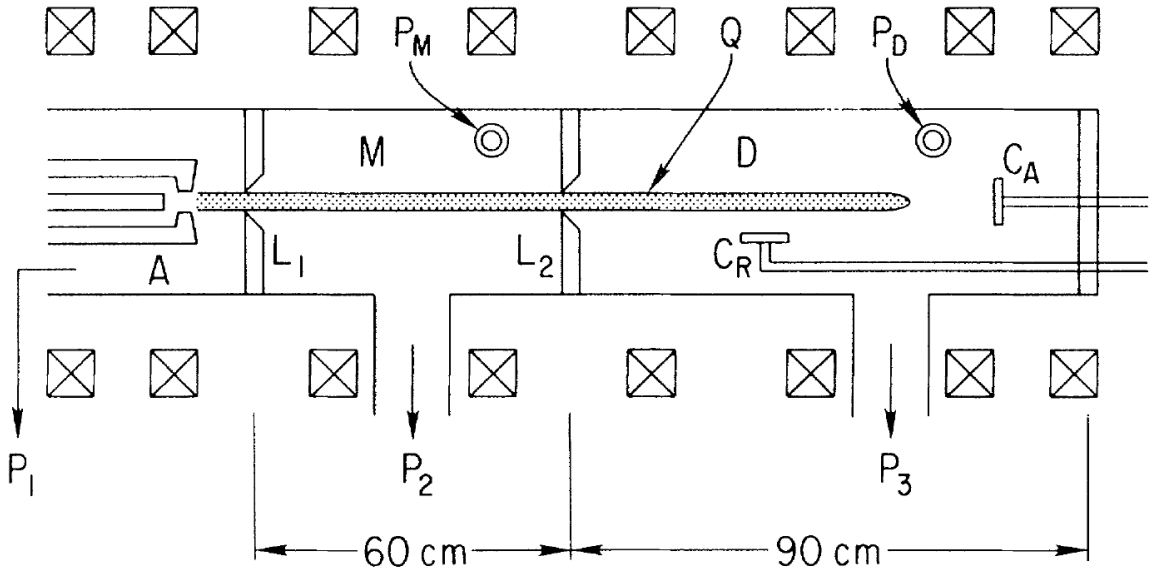

Figure 2.2: Schematic diagram of the QED linear plasma device. Key: (A) arc-jet type plasma source; (Q) plasma column; ($L_{1,2}$) limiters; ($C_{A,K}$) calorimeters; (M) main plasma chamber; (D) divertor chamber; ($P_{M,D}$) pressure gauges; ($P_{1,2,3}$) vacuum pumps. Reproduced from [5]

2.5.2.2 NAGDIS-II

NAGDIS-II is a divertor plasma simulator at Nagoya university and may be credited with the first definitive observation of MAR in a linear divertor simulator [60]. In the study pertaining to this observation, hydrogen gas was puffed into a TP-D type DC helium discharge in order to create a detached plasma at the target end of the device (schematic in figure 2.3). At hydrogen partial pressures above 0.18 Pa, MAR was the dominant process affecting plasma recombination evidenced by the sharp transition in spectral output away from Balmer line emission. This coincided with a complete to near complete cessation of EIR processes in the plasma region studied. Measurements were also performed to quantify the electron temperature and density trends as functions of the hydrogen partial pressure [61]. These showed a brief rise in electron density with pressure followed by a continual reduction with additional pressure increases. The electron temperature fell over the entire pressure range. There have been no negative ion measurements made on the NAGDIS-II device to this date.

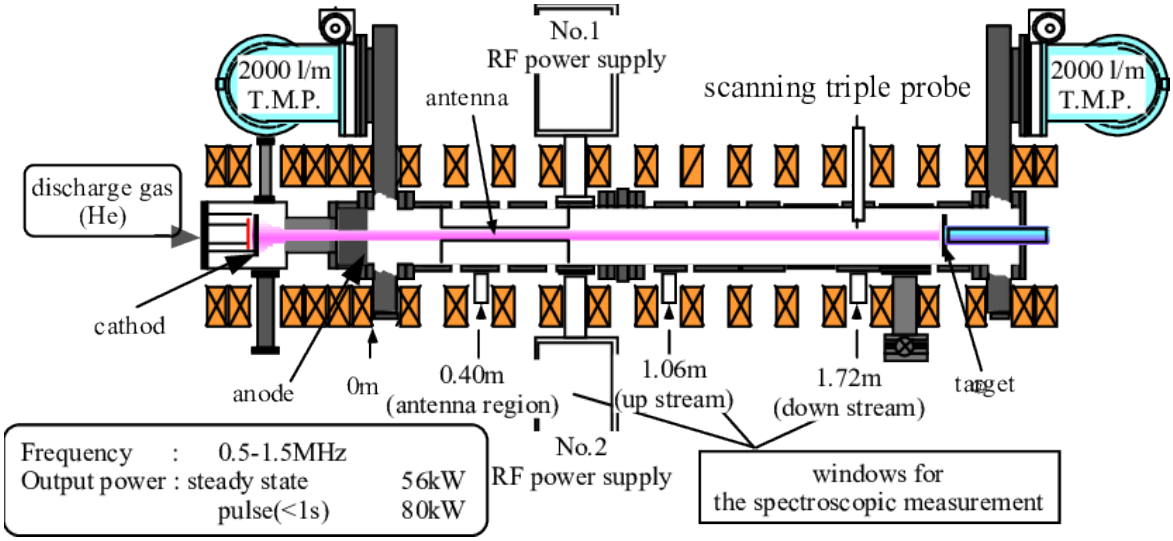

Figure 2.3: Schematic view of NAGDIS-II [6], a device with notable similarities to the YLPD used to study divertor plasma physics

2.5.2.3 PISCES-A

PISCES-A, the Plasma Surface Interaction Experimental Facility, is a linear plasma device, built around or before the 1980s at UCLA [62] for the purpose of examining the interactions between plasma and material surfaces under continuous or near continuous flux of particles and energy expected in advanced fusion devices and research machines. A schematic of the device is shown in figure 2.4 circa 1995. The device is still used to study the effects of plasma on materials such as plasma-facing mirrors [63] and tritium retention [64].

Work on PISCES has shown that a gaseous divertor concept could reduce the high energy particle flux to a target plate downstream along a magnetic field [7]. This experiment showed the effectiveness of MAR detachment in a pure hydrogen discharge using gas feeding in proximity to the target plate. The plasma density reduced significantly towards the target with strong gas puffing and the electron temperature was reduced to 2.55 eV compared to the case with no additional gas (20 eV). The plasma density exhibited a sharp peak associated with the ionization front where the neutral population met the high energy plasma and began to dissociate. This front separated the main plasma from the target by significantly decreasing the effect of the field near the target which is exactly a detached plasma by definition.

A more recent study observed molecular assisted recombination physics on a helium

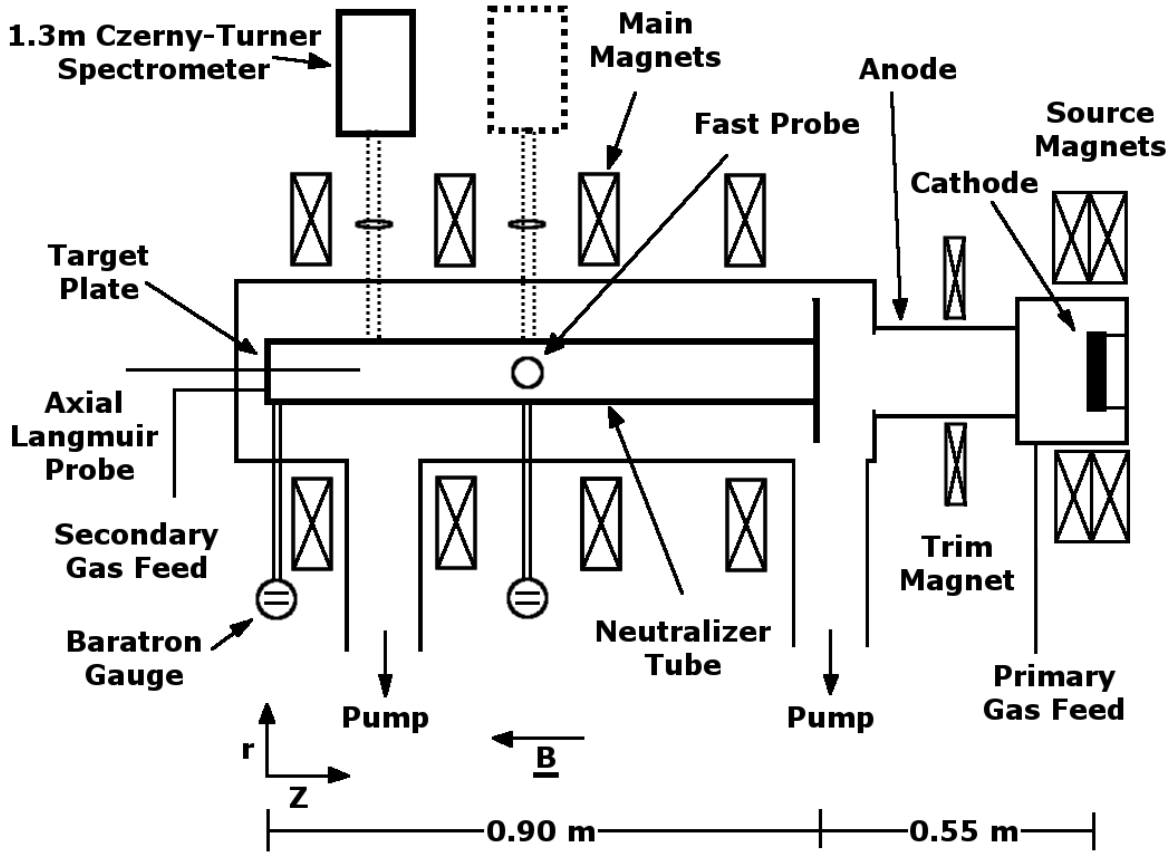

Figure 2.4: PISCES-A Schematic reproduced from [7]. The device has been used to study plasma-surface interaction physics as well as detachment and detached plasma regimes. Radial transport and significant flux reduction have both been observed in the associated literature.

plasma with added hydrogen [65]. The hydrogen molecules mediated the recombination of the helium evidenced by reduced particle flux to the chamber wall for non-zero hydrogen admixtures and a reduction in downstream flow velocity at a few percent partial pressure of hydrogen. The loss term for the He^+ ions was reduced by an order of magnitude more for the hydrogen injected MAR scheme than the corresponding EIR scheme. As a side note, this experiment also found that radial transport was a key factor in the detachment process, a phenomenon which has been supported by more work on the same device [66, 67] and work on other devices (see other subsections).

Pisces-A identified the vibrational gas temperature as being the most important neutral channel for moving energy out of the plasma compared to the rotational and kinetic gas temperatures. There is also evidence to support H_3^+ being an important species at pressures around 0.2-0.3 Pa at field strength of 0.12 T [57]. This is relevant because the dominant

ion on the standardised device used outside fusion research on low temperature plasmas for research and industry, the Gaseous Electronics Conference research cell (see section 3.1.1), is H_3^+ by a significant margin [68–71] potentially allowing some parallels between the GEC and some linear machines. The GEC device was also used in part for the experimental work presented in this thesis. The presence of this ion within the YLPD at significant number densities has not been confirmed and the source type does not lend itself to formation of this ion upstream.

2.5.2.4 MAGPIE

MAGPIE, the MAGnetized Plasma Interaction Experiment is one of the more modern linear plasma experiments. It was constructed in order to examine the interactions, known or hitherto unknown, that may occur between fusion relevant plasmas and plasma facing surfaces [8]. A schematic of MAGPIE shown in figure 2.5 displays the main design features which allows the device to operate in a fairly flexible manner. MAGPIE is a helicon source experiment meaning that the plasma is generated using a helical radio frequency power coupling coil wrapped around a portion of the source chamber. The magnets surrounding the target chamber may be controlled independently of those around the source chamber allowing for flexible magnetic field geometry along the central axis particularly near the target itself.

MAGPIE has been used to investigate radial transport physics [72] in tandem with the B2.5-EIRENE plasma fluid modelling code. There have also been experiments examining the negative ion densities in the target chamber as functions of axial field strength at two gas pressures (around 0.7 Pa and 1.3 Pa) [73] finding negative ion densities approximately 10% of the electron densities at a given set of control parameters. They also found that there was a peak in electron density, known as the low-field peak associated with helicon devices [74, 75]. The negative ion density followed this trend approximately though with a less defined peak. More negative ions were observed at the higher pressure throughout the entire range of applied axial field strengths while the negative ion fraction agreed with this save for the zero field data point. Experiments performed by H. Willett [76] studied the axial distribution of negative ions over the course of a 40 ms plasma pulse. This showed that the negative ion density was most prominent in the first 5 ms of the pulse, behaviour which may have been related to the neutral particle dynamics but was not fully understood. Negative ions were detected spatially at the location in the target chamber where the electron temperature

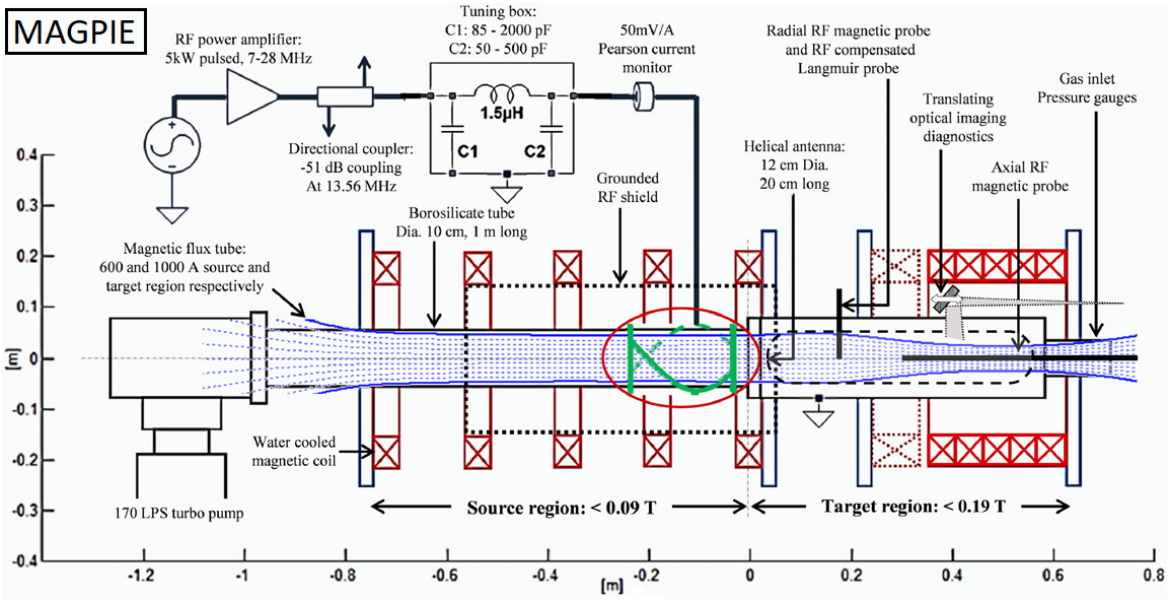

Figure 2.5: Schematic view of MAGPIE reproduced from [8]; the device has been used in fusion relevant plasma-surface studies including some experiments on the MAR plasma state. There have been a number of negative ion experiments on this device using the laser photodetachment technique.

dipped below 2.5 eV and the molecular and atomic densities were relatively high, agreeing with modelling performed by J. Santoso displayed in the same work.

2.5.2.5 TPDSHEET-IV

TPDSHEET-IV is a linear plasma divertor simulator which creates and confines a planar plasma sheet in order to simulate plasma flux similar to what might be observed in a divertor. A schematic of the device is shown in figure 2.6 while further illustration of the geometry of the plasma may be found in [9]. This device has been used to study heat and particle flux reduction by various means. Recently, this device has been used to study reduction of heat flux through only alteration of the magnetic geometry [77]. Evidence has been collected showing radial transport of blobs of plasma as well as undulating motion in the direction of the primary flow [78].

There has also been extensive work on MAR plasma on this device. Radial [9, 79] measurements of the negative ion density have been made which showed a hollow profile when compared to the central ion density peak. This was attributed to radial diffusion of vibrationally excited hydrogen molecules which have obtained energy through electron impact in the beam center. The excited molecules would then encounter low-temperature/energy elec-

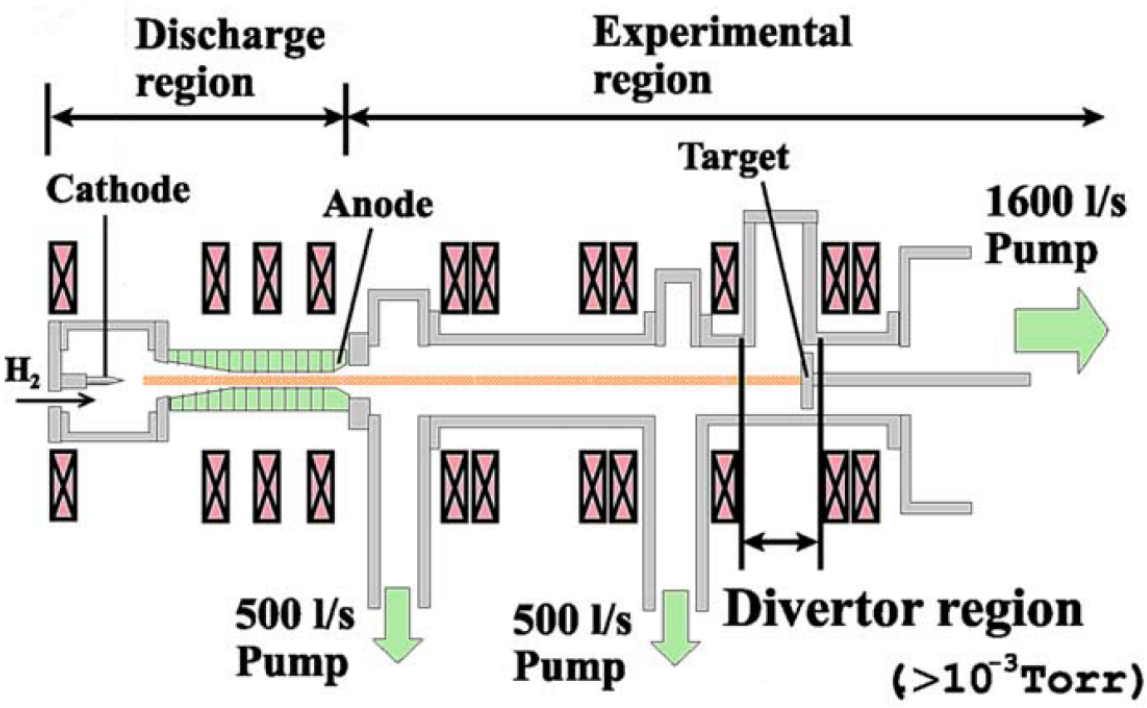

Figure 2.6: The TPDSHEET-IV device, schematic reproduced from [9]. TPDSHEET has similar characteristics to the YLPD and has been used to measure some radial distributions of negative ions in order to study MAR.

trons outside and undergo dissociative attachment creating H^-. This supports the work on PISCES in terms of the transport of energy by vibrationally excited molecules being critical.

TPDSHEET has notable similarities to the YLPD (ULS) including the maximum electron temperature, maximum solenoid field strength and beam width scale. The maximum electron density in TPDSHEET-IV is around an order of magnitude higher than that found in the YLPD and the geometry of the plasma is slightly different, being a flat namesake sheet as opposed to a cylindrical column. Despite the minor differences, the plasmas, particularly those studied in [9] with regards to negative ions, are comparable to the YLPD plasmas studied in this thesis.

2.5.2.6 MAGNUM-PSI

MAGNUM-PSI is the largest linear divertor simulator covered in this work with central electron densities of order 10^{21} m^{-3} [57, 80, 81] and temperatures up to 10 eV [10]. This device, shown schematically in figure 2.7, allows studies of high particle fluxes not possible in other devices. Detachment experiments have been performed on MAGNUM by seeding

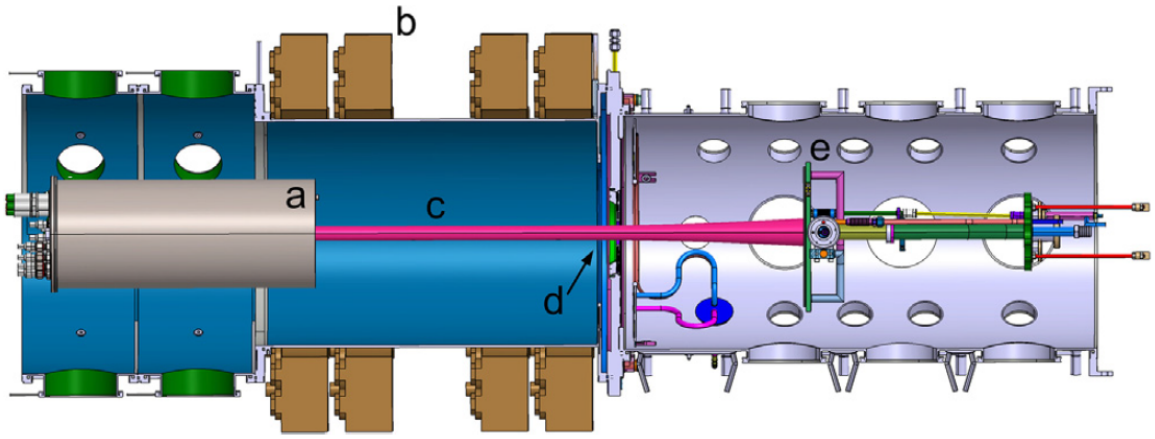

Figure 2.7: MAGNUM PSI linear device, obtained from [10]. a: Plasma source - Cascaded arc type, b: Bitter type field coils to constrain source plasma, c: magnetized beam, d: skimmer (similar to an aperture), e: target and coolant systems.

neutral hydrogen gas into the target region such as those in [82] and simulations of the molecular population and excitation levels using B2-EIRENE [83, 84].

2.5.2.7 York Linear Plasma Device - formerly ULS

The YLPD is a linear divertor simulator located at the University of York Plasma Institute a schematic of which may be found in section 3.2. There have been several studies into detachment on this device with a significant body of measurements. B. Mihaljcic performed an extensive parameterisation of the transition between EIR and MAR in the YLPD over the course of his PhD [3] backed up by gas target research performed by previous students [85, 86]. The prior works by Kay and Sewell established that there were two separate detachment regimes on the device as evidenced by the reduction of T_e and n_e within 15-30 cm of the end flange. Mihaljcic used Langmuir probes and spectroscopy techniques to establish relations between the upstream parameters and the corresponding detachment regime. An example plot (2.8) shows that MAR dominated at lower densities and temperatures a few eV above 1 eV. Similar plots and an approximated expression for the threshold may also be found in the related paper by Gibson et.al. [87]. This paper also provided evidence which pointed to the MAR process dominating over cross-field transport in terms of reducing the target plate flux. This was true at least in the YLPD in contrast to devices like PISCES.

Spectroscopic measurements have also been performed in [3] which showed the differences between EIR and MAR in terms of light emission. In the EIR detached case, the high n

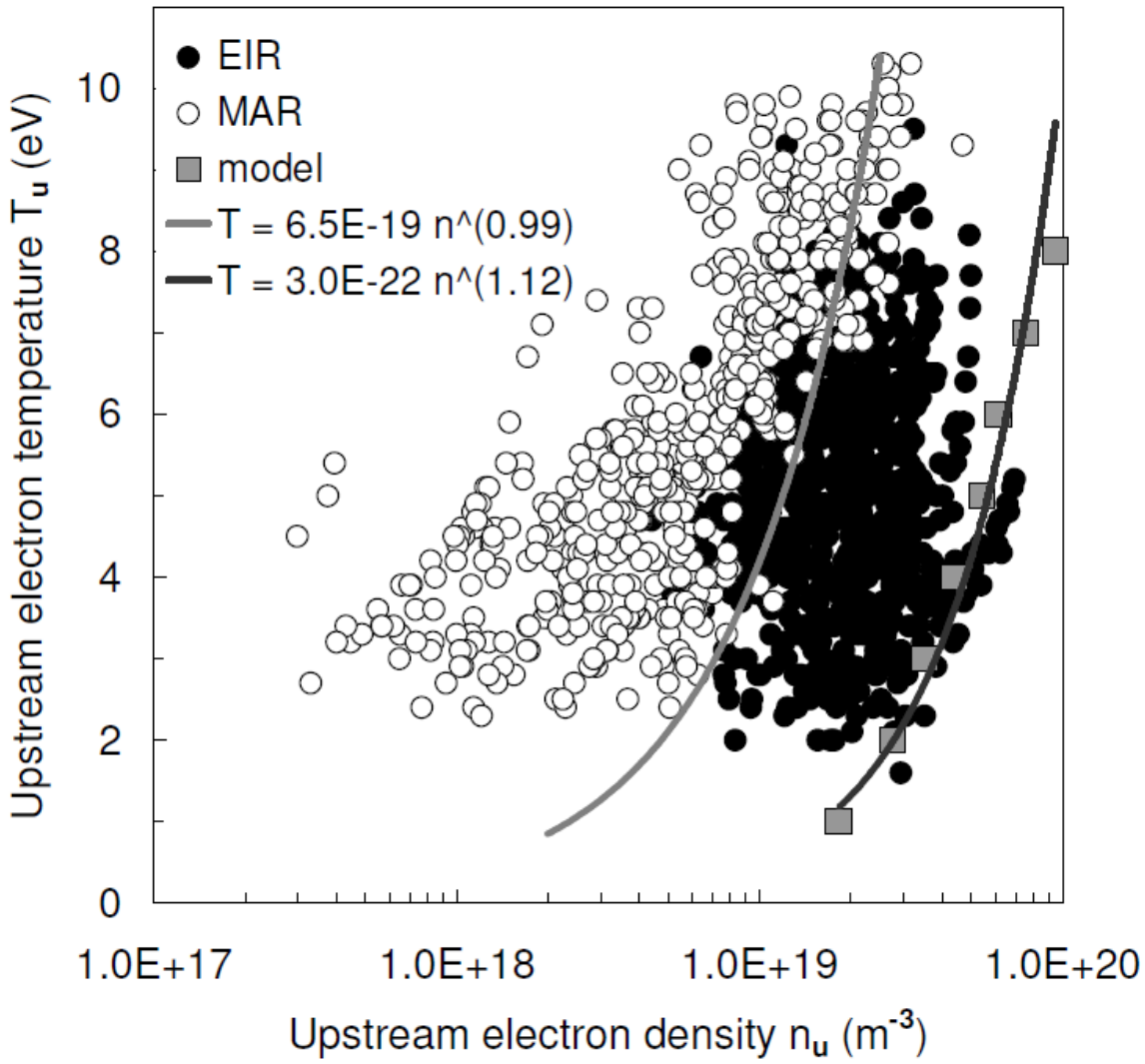

Figure 2.8: Threshold study figure obtained from [3]. This showed that there was a threshold density and corresponding threshold temperature associated with the transition from EIR to MAR at a given pressure.

value Balmer lines were enhanced and the molecular Fulcher band was functionally absent. In the MAR regime, the molecular band was significant and provided a general estimate of the rotational temperature of around 450 K and an estimate of the vibrational temperature around 2000-2500 K. The spectral emission of the hydrogen alpha line was recorded for different pressures and axial positions in order to locate the recombination front associated with EIR detachment. In many cases, this represents a transition zone between upstream MAR processes and the EIR region.

The viability of the YLPD as a divertor simulator is generally good however due to the nature of the device, the ion speed exceeds the local sound speed by approximately a factor of three which is not typical of a tokamak divertor. Despite this fact, the physics of plasma interaction with neutrals is still valuable to the characterization of detachment and many parameters are still divertor relevant. The source has been reconfigured somewhat since the majority of previous work meaning that some plasma parameters may be slightly different for a given set of input parameters. Further details as to the construction, diagnostic access and plasma characteristics of the YLPD are to be found in section 3.2.

2.5.2.8 Summary of work on linear devices

From this body of work, a good picture of MAR plasma is already available due to the variety of devices which compensate for each others' shortcomings. It is possible to conclude that the existence of an MAR detached hydrogen plasma on linear divertor simulators is well known and the heat flux reduction on the devices is fairly consistent. The approximate range of electron temperatures and the low density criterion (approximately 10^{19} m^{-3}) have been established as well as the critical nature of the vibrational energy distribution function. There is reasonably good agreement between experiments and models where they have both been performed on the same devices although there are still discrepancies in the populations of some species. In some devices, the presence of H_3^+ has been found to be relevant, its presence in appreciable numbers dependant on the nature of the gas system and the source type.

Despite good progress, there is still need for more experimental data regarding different spatial distributions of particles in these devices in order to benchmark existing models and assist in their development. There has been little to no research as of yet regarding the production of MAR-relevant negative ions from surfaces within the divertor as a comparable

parameter worthy of optimization. While volume recombination is the overall goal, volumetric production of negative ions should not be the only consideration given that surface production can be a dominant factor in some cases [88]. Negative ions have been measured in two devices, MAGPIE and TPDSHEET-IV. The radial distribution has only been measured on TPDSHEET-IV which is one of the devices most relevant to the YLPD in terms of comparisons. The work done in this thesis will contribute high resolution radially resolved measurements of negative ion density with simultaneous electron temperature and density measurements for several plasma conditions (pressure, core temperature, solenoid field). This will help to establish and solidify device independent trends regarding negative ions in similar hydrogen plasmas.

2.5.3 Relation to hydrogen plasmas in the GEC

It is worth noting, as will be mentioned in the section covering previous work on linear devices, that in some devices H_3^+ forms a significant proportion of the positive ion fraction such as PISCES-A. This is also a feature of other experimental devices including the RF driven Gaseous Electronics Conference (GEC) reference cell. The GEC can be a useful tool for studying plasma surface interaction effects on MAR relevant plasma processes such as negative ion production. This could then be used to influence divertor material choices, plate positioning and plate geometry. The GEC is a highly studied and cross-referenced device as shown in the following sub-sections which is helpful for finding reliable parallels between the GEC research community and the divertor research community. The experiments performed for this thesis on the GEC cell were performed to investigate the potential importance of plasma facing surfaces to aiding the recombination processes as opposed to simply resisting high heat flux. The following sections highlight previous work on MAR relevant hydrogen plasmas in the GEC and similar RF sources common to low-temperature plasma research. This includes research on negative ion production with emphasis on any research on surface contributions.

2.6 Existing work on RF plasmas with emphasis on the GEC reference cell

The benefit of devices like the GEC is the ability to study plasma physics under a particularly reproducible set of conditions. This includes the size and spacing of the electrodes, the internal volume, chamber material (stainless steel) and inner wall surface area, pumping system, gas delivery system and diagnostic access.

2.6.1 Negative ion experiments overview

Experiments on RF plasma devices concerning the formation of negative ions, including often negative hydrogen ions, have been performed in several fields such as the propulsion of small spacecraft [89, 90], negative ion sources for accelerator experiments [91, 92], micro-electronics [93, 94] and nuclear fusion. Fusion relevant experiments have predominantly been directed towards developing negative hydrogen ion sources for neutral beam injection (NBI) heating systems [95, 96]. There have been relevant publications on the study of relevant plasmas through he use of global models also which predict negative ion densities in radio frequency ICPs [68, 97] (though not necessarily on or limited to the GEC geometry). These show that the negative ion density tends to be a few % of the electron density, scaling with power. Gans et.al. [98] show some evidence of the dominance of this ion by measuring it as the positive ion component of a hydrogen ICP for medical sterilization.

2.6.2 Negative ion production for particle accelerators

Some particle accelerators use negative ion sources to generate H^- which are then converted into protons via charge exchange which are then injected into the main portion of the accelerator [99]. Significant work has been done on devices such as the J-PARC [92] and Linac4 [91] accelerators negative ion sources. The work on J-PARC used a caesium free Lanthanum-Hexaboraide filament in an internally nickel plated oxygen free copper chamber to achieve high output of negative ions. The surface geometry and composition of the filament are critical parameters in this paper; there was also consideration given to the negative ion production at the tapered aperture surface because these ions could be deflected into the beam region and accelerated outwards, improving the yield. On Linac4, a ceasiated source produces negative ions in a lined volume which are then extracted. The H^- are produced by

interaction between the hydrogen plasma and the ceasium covered molybdenum chamber. The vast majority of negative ion sources in accelerator physics rely on surface interactions to create large negative hydrogen flux. This makes this body of work an ideal place to find novel research on optimisation of the surfaces responsible.

2.6.3 Negative ion production in the microelectronics industry

There are many points of relevance to negative ions in the microelectronics industry. Marinov et.al. [93] investigated the extraction of negative ions from an electronegative ICP as a means of creating a high energy neutral beam for fine scale lithography techniques. The source in this instance was intended as a volume source, however it was theorized that some of the discrepancies in the output were caused by surface effects. A design shift to utilise surface production may be able to provide more stable or higher intensity sources in similar devices. Thomas et.al [94] show the results of using one of these negative ion based neutral beam etching systems and provide more references to its development.

Chlorine negative ions are measured by Ahn, Nakamura and Sugai [100] in order to quantify the cooling effect of the electron population in their etching ICP through dissociative attachment. There are parallels therefore to the dissociative attachment process in MAR hydrogen plasmas found in fusion. In addition they use the photodetachment technique instead of quadrupole mass spectrometry or time of flight diagnostics.

2.6.4 Surface production in fusion devices

Negative ion production relating to fusion research has almost exclusively related to the creation of more efficient NBI heating systems. Neutral beams are effective at transferring significant energy to plasma species through collisions using highly accelerated ions which are neutralized shortly prior to entering the core plasma. The interest in negative ion sources is high because there is a dramatic limitation on the energy of neutrals produced by positive-ion neutral beam injection (P-NBI) systems. This limit arises due to the difficulty in neutralizing the positive ions (protons or deuterons) when they approach energies towards and above this limit of around 100 keV [101]. Negative ion NBI (N-NBI) systems by contrast are able to retain up to 60% neutralization efficiency for incident ion energies ten times what is possible for P-NBI.

Of particular interest from the research from the NBI community is the importance of

the surface of the source in the negative ion production physics. Most existing high-yield negative ion sources use caesium as the negative ion production surface material [102, 103]. The application of caesium to metals for improving negative ion yields is attributed to reducing the energy barrier faced by an electron which would attempt to leave the surface and attach to an atom. Electron affinity in atoms like hydrogen is of the order 1 eV and the work function of most metals sits in the 4-5 eV range. It was theorized that the application of a fine layer of alkali metal could reduce the work function of the surface to a minimum value which itself lies below the work function of the bulk alkali metal [104]. This behaviour was observed by scientists such as Langmuir and Kingdon [105] among others cited in Lang.

There is considerable research, however, being invested in investigating caesium-free negative ion sources due to the metal's properties which make the engineering more challenging, more expensive, and more prone to maintenance and reliability issues [106]. These caesium-free sources aim to use optimized RF driven hydrogen plasmas to create negative ion fluxes comparable to those achieved by caesium sources. One example of a caesium free source is that mentioned previously in the particle accelerator J-PARC [92]. As part of the effort to remove the dependency on caesium, different materials are being examined such as tungsten and other stable, abundant metals.

2.6.5 Effect of material type on surface negative ion production - general research

There have been numerous studies on the effect of material surface compositions pertaining to negative ions. This has been done using ion and/or electron beams generated by various means [107–109], directed onto surfaces. There have also been some studies regarding plasma in close proximity to the surface sample [110–115].

Ahmad et.al. studied the interaction between a low-pressure 13.56 MHz hydrogen plasma and carbon allotrope surfaces such as diamond like carbon (DLC) and highly oriented polycrystalline graphite (HOPG). They found that there were differences in negative ion formation between different carbon surfaces, HOPG was best at room temperature while a boron doped diamond surface was more effective at higher temperatures around 700 K. While there were variations between specific sample types, there were similarities in the trends observed with increasing energy for some samples. There were also similar variations with surface temperature between samples which indicated that the mechanism was not changing funda-

mentally with temperature. Kumar et.al. also studied the effects of different carbon surfaces showing that the temperature dependence of HOPG was a result of high temperatures baking off adsorbed hydrogen which would otherwise provide an effective channel for negative ion production (sputtering [116, 117]). Instead, the H^- production became reliant, at high surface temperature, on backscattering processes [117] whereby an ion impacts the surface, captures two electrons then leaves as H^-. This research provides two mechanisms for negative ion production from surfaces sputtering and backscattering. Sputtering relies heavily on the adsorption of hydrogen to the surface which varies with temperature and surface type. Despite the fact that carbon divertors are no longer being investigated due to tritium retention issues, this is still useful information when trying to examine surface production as a whole.

Fukumasa and Saeki [110] performed work investigating the differences in H^- production for varying inner wall material between aluminium, copper and stainless steel. Their work showed that, in their multicusp-source experiment, the aluminium surface was most effective for negative ion production but that the values and the differences between surfaces varied with fill pressure. This was built on their earlier simulation work [118] done predicting the surface to be an important, and in the cases studied dominant, factor. Within this work, references were made to other research done on surface material effects. Work done by Graham [119] showed that the negative ion production was enhanced for stainless steel walls over Pyrex walls. By comparison, work done by Bacal [120, 121] showed that the use of stainless steel reduced the negative ion fraction significantly compared to Pyrex. Pèalat et.al. [122] performed measurements which showed that there was an enhancement in the negative ion density when the plasma was exposed to a stainless steel surface when compared to a copper coating.

Bacal et.al. also summarized some of this research in 2004 [113] including that of Inoue et.al. [112] and Leung et.al. [111] (for efficiency rolled together here). Leung et.al. investigated wall lining materials in a similar fashion to Fukumasa while Inoue et.al. found that tantalum filaments, when used to evaporate material onto the chamber walls, yielded H^- enhancement of 50% in place of tungsten filament. They suggested that this difference was due to the increased coefficient γ associated with hydrogen atom recombination on the surface arising due to a reduction in the bulk atomic density which hinders the creation of H^- in the volume. Hall et.al. studied the contribution of surface material variation to the recombinative desorption of vibrationally excited hydrogen molecules [123]. This describes

the process of a free plasma atom recombining with an adsorbed atom on the surface which then may leave in an excited state. These vibrationally excited molecules of course being of critical importance to volume production of negative ions through the dissociative attachment process. Modelling by Bacal and colleagues however showed that the contribution to vibrational states (4-5+) relevant for dissociative attachment was not significant via this process compared to radiative de-excitation from collisional excitation. Their study in [113] investigated a fresh coating of tantalum as a wall material which showed enhanced negative ion production and an increase in higher temperature negative ions in the plasma.

2.6.6 Effect of material type on surface negative ion production - GEC cell studies

Negative ions were studied in a GEC type device by Hebner et.al. [124] using four different surface types exposed to a chlorine containing plasma (the ion of interest being Cl^-). The surfaces examined were aluminium, alumina (aluminium oxide), a photoresistive material and a 50% by area aluminium/photoresist target. Alumina was used because it is a commonly found material in plasma devices and the photoresists were investigated because of other potential negative ion producing species unique to the plasma when operated with the photoresist. Measurements were made using laser photodetachment however negative ion data was not obtainable for the patterned wafer because the averaging time required for the photodetachment signal was significantly longer than the time required to cause notable etching of the deposited aluminium layer. The measurements showed a general increase in both electron and negative ion densities with applied power for all surfaces as well as an enhancement of negative ions with the photoresist over both the alumina and aluminium. This was attributed to changes in both the surface creation and gas phase chemistry resulting from the presence of the photoresist that were dramatically different, evidenced by the changes in electron density, to the aluminium and alumina. Of note: if the negative ion density in those experiments had increased on a one-to-one basis with the electron density, it could be reasoned that dissociative attachment was dominant however this was not the case, prompting theories regarding enhanced recombination of atoms into excited molecules.

A. Greb et.al. [125] studied the effects of surfaces on the general behaviour of oxygen plasmas relevant to industrial processes including the creation and destruction of O^-. This study was motivated by the trend in simulations to neglect the effects of the surfaces of

interest on the plasma being used to affect them due to lack of available data. For etching, deposition and surface modification processes, the interaction between the plasma and surface is crucial and existing models chose to assume that the surface did not notably affect the plasma above. This was shown to potentially be a significant departure from reality where the surface may dramatically alter the physics of the processing plasma and thus set up something of a feedback loop.

Greb et.al. found increases in the density of O^- correlating with increases in the probability of destruction of singlet delta oxygen (SDO) at the surfaces. SDO is important in this case because of its role as a dominant loss channel for O^- ions in plasmas of this type. This is supported by work done by Katsch et.al. [126] who studied the axial distribution, and variation with respect to applied RF power, of negative oxygen ions in an asymmetric geometry GEC type device without varying the surface. Katsch et.al. highlighted work by Goehlich et.al. [127] who found that the atomic densities were relatively low and not part of the dominant destruction pathway for O^-. Returning to Greb et.al. the increase in the loss of SDO increased the electronegativity of the plasma which caused additional acceleration when the sheath collapsed as part of the RF power cycle. This enhanced the excitation of species in proximity to the surface, some of which could then diffuse into the bulk. The loss coefficient of SDO at the surface is a material specific parameter which varies with temperature; in his thesis, Greb also mentions the relevance of the secondary electron emission coefficient as a surface parameter [128]. In his case, the SDO effects were dominant, however fast electrons liberated from the surface by atom impact are worth considering in all similar plasma-surface interfaces including those with hydrogen.

The relevance of the aforementioned work on oxygen to the current study is that the surface can affect the plasma in numerous ways which can have an impact on the negative ion dynamics. For example in a fusion relevant plasma with a divertor type material such as tungsten, not only may the surface enhance production of negative ions, but it may enhance or diminish the creation of species which readily destroy the negative ions before they have a chance to undergo MAR reactions in the desired regions.

2.6.7 Summary of work on negative ion production in the wider plasma research community

From the body of work which currently exists, it is clear that the system of a hydrogen plasma interacting with a surface is complex. The full picture of surface effects on negative ions and the interaction with relevant species is not known. The precise material properties contributing to the creation of negative ions is not known, nor is the full scope of reactions which can either create negative ions or enhance species within the plasma which cause volume production of negative ions. Any insights into this will assist in the improvement of models and narrow down the parameters responsible for negative ion formation under varying surface type. Despite the current lack of a full understanding of the surface production mechanisms of negative ions, it is abundantly clear that the surface is a vital player. As a result, it is worth studying, even with emphasis on the effect it has on volume recombination, as the body of work on this is small.

2.7 Theory of plasma diagnostics and techniques used

2.7.1 Electrical probes - Langmuir Probes

One of the most commonly used diagnostics in plasma physics is the electrostatic probe system originally developed by Irving Langmuir. These probes are more commonly referred to as Langmuir probes. Langmuir probes measure the variation in the current through a metallic structure inserted into the body of a plasma in response to an externally controlled voltage. The I-V characteristics recorded can be analysed to give plasma parameters such as electron temperature and electron density. This is possible due to the interactions between plasmas and material surfaces under the broader topic of sheath physics. A brief explanation of sheath physics and Langmuir probe physics and design follows as these topics are crucial to the measurements and photodetachment experiments performed.

2.7.1.1 Basics of probe sheath physics

A floating surface or probe in a plasma will rapidly become negatively charged after the two come into contact. This happens because the higher mobility of the much lower mass electrons allows them to impact and charge the surface more quickly than the positive ions. As the surface builds negative charge, a potential barrier between the probe and the plasma

forms and increases reducing the incoming electron flux to all but those with the most energy. This repels the majority of electrons away from the surface creating a net positive charge region between the surface and the bulk plasma called the Debye sheath. A dynamic equilibrium is reached when the sheath potential is several times greater than the electron temperature of the plasma. The sheath is often some number of Debye lengths thick and its potential is defined as the potential difference between the sheath edge and the surface.

2.7.1.2 The Debye length

The Debye length, λ_D, is the characteristic length scale of the Debye spheres found in the plasma. These are clouds of electron density which form around the positive ions in a spherical distribution with radius λ_D. The magnitude of this originates from applying Maxwell's equation to the resulting electric field and charge separation.

$$\nabla \cdot \mathbf{E} = \frac{\rho}{\epsilon_0} \tag{2.10}$$

where ρ is the overall charge density given by $e(n_e - Zn_i)$, e is the fundamental charge constant, Z is the ion proton number and ϵ_0 is the free space permittivity constant. If we substitute the relation between the electric field and the potential $E = -\Delta\phi$ we obtain Poisson's equation:

$$\nabla^2\phi = -\frac{e}{\epsilon_0}(Zn_i - n_e) \tag{2.11}$$

n_e and n_i are the electron and ion densities and we can see that when they are equal such as in the plasma bulk, there is no charge separation and no electric field. If it is assumed that the electron energy distribution function (EEDF) is a Maxwell-Boltzmann distribution for electron temperature T_e and bias voltage between the probe and sheath edge we may write (for negative potential):

$$n_e = n_{e0} \exp\left(\frac{e\phi}{k_b T_e}\right) \tag{2.12}$$

If we assume that the ion density in the sheath is equal to the electron density at the sheath edge, $(n_i = n_{e0})$ we can substitute this and 2.12 into Poisson's equation in one dimension (x) giving:

$$\frac{d^2\phi}{dx^2} = -\frac{en_{e0}}{\epsilon_0}\left[1 - \exp\frac{e\phi}{k_bT_e}\right] \tag{2.13}$$

If the bracket is expanded as a Taylor series and terms of order 2+ are removed we obtain:

$$\frac{d^2\phi}{dx^2} = -\frac{en_{e0}}{\epsilon_0}\frac{e\phi}{k_bT_e} \tag{2.14}$$

This differential equation is assumed to have a solution which takes the form:

$$\phi(x) = \phi_0 \exp\left(\frac{-x}{L}\right) \tag{2.15}$$

with x as the positional coordinate and L as a constant, characteristic length associated with the system. This allows comparison between 2.15 and 2.14, differentiating twice to obtain:

$$\frac{d^2\phi}{dx^2} = \frac{\phi_0}{L^2}\exp\left(\frac{-x}{L}\right) \tag{2.16}$$

Substituting equations 2.16 and 2.15 into equation 2.14 shows that the collection of parameters in 2.17 has dimensions equivalent to a length and thus we obtain the Debye length:

$$\lambda_D = \sqrt{\frac{\epsilon_0 k_b T_e}{e^2 n_0}} \tag{2.17}$$

Typical values of λ_D for the GEC plasmas studied in this thesis are on the order of ten microns, while for the linear device they range from hundreds of nanometres to ten microns or so.

2.7.1.3 Principle of probe operation

Here we examine the basic process of acquiring an electrical characteristic and analysing the data. When a large negative bias voltage is applied, the electrons are repelled creating a similar positively charged sheath region. Due to the low mobility of the ions, the positive current drawn is limited regardless of the probe voltage beyond a specific negative value. This is known as the ion saturation current and is solely dependant on the ion charge, ion density and the sound speed in the plasma given by the Bohm criterion 2.18. v_{0i} is the magnitude of the ion velocity, v_B is the Bohm velocity, [T_e is the electron temperature and m_i is the ion rest mass]. The Bohm velocity is thus simply the local ion sound speed c_s and will henceforth be written as such. If the ions do not satisfy this criterion, they do not

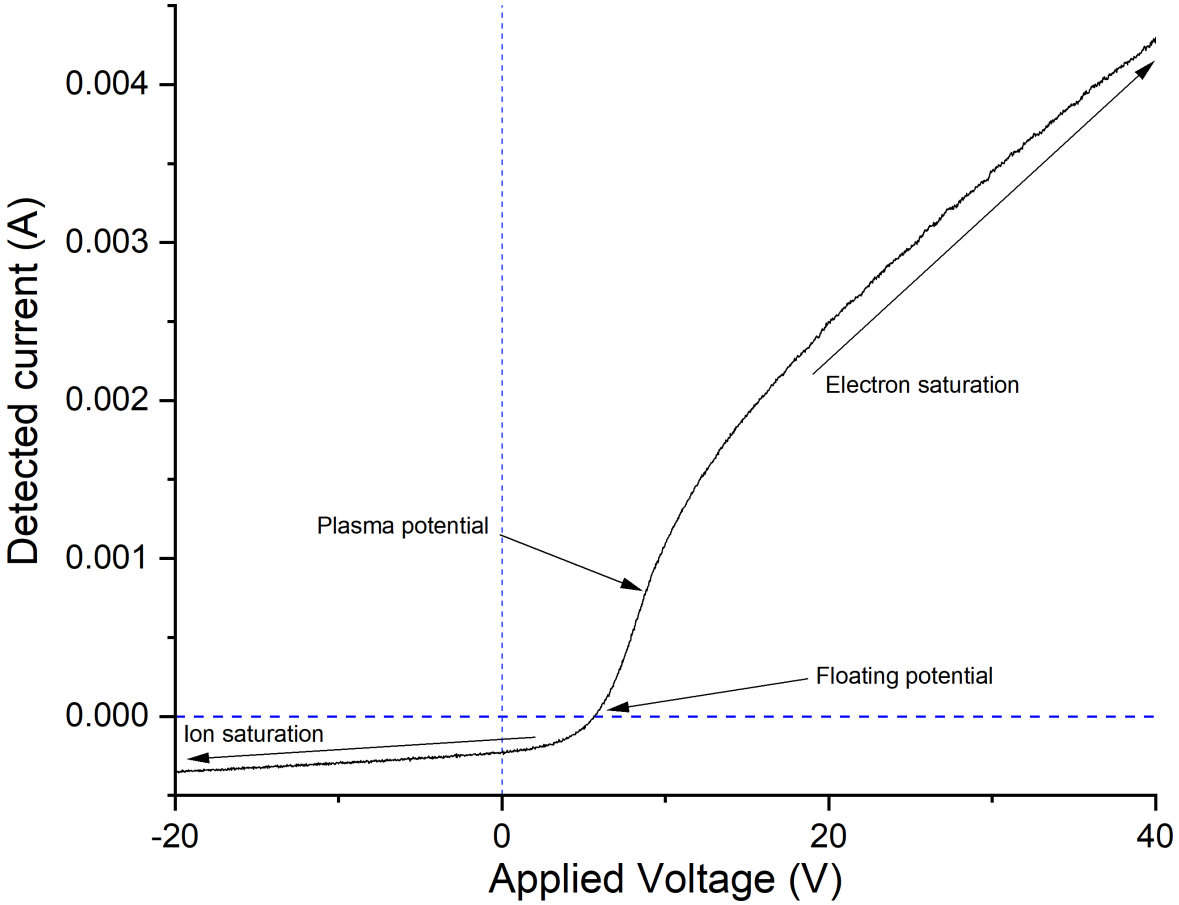

Figure 2.9: Example IV curve taken on the outer portion of the YLPD plasma where magnetization effects were less significant.

have sufficient mobility to build up the positive space-charge to shield the plasma and the negative wall from each other.

$$v_{0i}^2 \geq v_B^2 = \frac{kT_e}{m_i} \tag{2.18}$$

An example characteristic is shown in figure 2.9. Beginning from a strong negative bias, the probe voltage may be swept towards zero to observe changes in the current drawn. As the voltage ramp occurs, the population of electrons with sufficient energy to reach the surface increases. The electron velocity distribution is modelled as Maxwellian as before 2.12 hence electrons with velocities in the upper portion of the distribution may pass.

This process is exponential for a range of potentials as the electron current increases to the probe. The continuing ion flux onto the surface means that the total measured current is the sum of the ion and electron currents. The convention is to define positive current as

that which moves into the plasma from the probe. When the measured net probe current is zero, the probe is said to have reached the "floating potential" V_{float}. At this point the contributions of the electron and ion currents are equivalent. Beyond this bias, ions continue to be collected, however due to the difference in mobility, the relative contributions are no longer equal. This continues until the probe reaches the plasma potential V_p. At this bias, a portion of the ions are repelled from the probe based on their kinetic energy. Those with the lowest energy are repelled at values close to and in excess of V_p.

When the applied bias sufficiently exceeds the plasma potential is passed, the ions are repelled from the probe surface completely and only the electrons form a current to the surface. Eventually, the repulsion of the ions allows the electrons to begin shielding the probe from the bulk plasma, causing the rate of increase in electron flux to diminish shown by the gradient of the slope. This is known as the electron saturation region wherein the current will eventually reach a fixed saturated value given sufficiently high positive bias.

The portion of the IV characteristic between the plasma potential and the electron saturation region is known as the transition region. The measurements from this region may be used to estimate the electron temperature. Extracting an electron temperature from the saturation region is possible in principle although this is not usually undertaken as the random thermal flux of the electrons prevents saturation from being easily reached.

2.7.1.4 Langmuir probe models and mathematical formalism

Here, we shall examine more closely the mathematical formalism that governs the acquisition of useful information from Langmuir probe measurements. For a DC Langmuir probe, it is important that the end of the wire, the probe tip is a simple geometry such as a plate, sphere or cylindrical shape to a good approximation. This simplifies the mathematics of calculating the exposed surface area of the probe which is directly proportional to the current collected. It also fits more in line with probe theory outlined in this section which is generally based on ideal geometries such as infinite planes or perfect infinite cylinders. The mathematics of Langmuir probes has been of considerable study since their conception. There are multiple probe theories which range in complexity and applicability under different plasma conditions. A useful summary of the three models presented here can be found in [129].

2.7.1.5 Allen-Boyd-Reynolds theory

The most simplistic theory is that of Allen-Boyd-Reynolds (ABR) which describes collection of ions with such low energy that their velocity transverse to the probe is functionally zero. In this limit, the ions begin at an infinite radial position where the potential they feel is zero and all are drawn radially into the probe.

To determine the ion current, the starting point is Poisson's equation in cylindrical polar coordinates.

$$\frac{1}{r}\frac{\delta}{\delta r}\left(r\frac{\delta V}{\delta r}\right) = \frac{e}{\epsilon_0}(n_e - n_i) \tag{2.19}$$

By assuming a Maxwellian energy distribution for the electrons and defining I_L as the ion flux per unit length collected by the probe it is possible to obtain an expression for the flux per unit length at any radial coordinate. This is due to the continuity of current through the system. The expression for the flux is:

$$\Gamma = n_i v_i = \frac{I_L}{2\pi r} \qquad \text{with} \qquad v_i = \left(\frac{-2eV}{M}\right)^{-\frac{1}{2}} \tag{2.20}$$

so then n_i becomes:

$$n_i = \frac{\Gamma}{v_i} = \frac{I_L}{2\pi r}\left(\frac{-2eV}{M}\right)^{-\frac{1}{2}} \tag{2.21}$$

by substituting equation 2.21 into equation 2.19 and defining the following:

$$\eta \equiv \frac{-eV}{k_B T_e} \qquad \text{and} \qquad C_s \equiv \left(\frac{k_B T_e}{M}\right)^{\frac{1}{2}} \tag{2.22}$$

we obtain:

$$\frac{-\epsilon_0 k_B T_e}{n_0 e^2}\frac{1}{r}\frac{\delta}{\delta r}\left(r\frac{\delta \eta}{\delta r}\right) = \frac{I_L}{2\pi r}\frac{(2\eta)^{-\frac{1}{2}}}{n_0 C_s} - e^{-\eta} \tag{2.23}$$

by noticing that the left of equation 2.23 includes the square of the Debye length, the radial coordinate may be normalised to the Debye length by $\xi = r/\lambda_D$. This, along with some rearranging yields:

$$\frac{eI_L}{2\pi k_B T_e}\left(\frac{M}{2\epsilon_0 n_0}\right)^{\frac{1}{2}} \eta^{-\frac{1}{2}} - \xi e^{-\eta} \tag{2.24}$$

If the normalised probe current is then defined as:

$$J = \frac{eI_L}{2\pi k_B T_e}\left(\frac{M}{2\epsilon_0 n_0}\right)^{\frac{1}{2}} \tag{2.25}$$

the final expression for the ABR theory for a cylindrical probe is:

$$\frac{\delta}{\delta\xi}\left(\xi\frac{\delta\eta}{\delta\xi}\right) = J\eta^{-\frac{1}{2}} - \xi e^{-\eta} \tag{2.26}$$

This is then integrated between $\xi = \infty$ down to arbitrarily small ξ (usually the probe radius) for assumed values of J and solved computationally to find the ion density. More details on this stage are found in [129] and are not explained here because the ABR theory was not used extensively for analysis in this work.

This theory holds fairly well for larger spherical and cylindrical probes where it is possible to neglect orbital motion of charged particles around the probe. The ABR theory is useful in some cases but is arguably oversimplified for other scenarios [130]. This leads to the use of the Orbital Motion Limited (OML) theory created by Mott-Smith and Langmuir [131]. This theory considered particle orbits inside a space-charge sheath surrounding a cylindrical or spherical probe. Outside the sheath, the plasma is assumed to be neutral with perfect charge balance and it is assumed that there is no boundary between the sheath and the bulk such as a pre-sheath region. The I-V characteristics are assumed to be affected by orbital motion limiting the flow of current to the probe tip. This model is often not viable because it assumes that a finite number of particles of all energies graze the surface of the probe. In truth, it is more realistic to consider an absorption radius outside the probe which acts as a functional probe radius. Particles that cross this radius will certainly be collected.

2.7.1.6 Orbital Motion Limited (OML) theory

A brief outline of Orbital Motion Limited theory is given in this section. This outline was sourced from a review by J. E. Allen [132]

We consider a cylindrical probe operating under electron saturation, that is attracting electrons with probe voltage V_p positive with respect to the surrounding or adjacent plasma. If the length of the probe L_p is significantly larger than the radius of the probe r_p, the electrons move in a centralized field of force centered on the probe tip. The sheath boundary is not solidly defined in OML theory but rather exists as a result of the impact parameter

[129]. Conservation of energy for the electrons gives:

$$\frac{1}{2}m_e v^2 = \frac{1}{2}m_e v_p^2 - eV_p \tag{2.27}$$

where v_p is the velocity of the electron at the probe surface, V_p is the potential at the probe surface, v is the electron velocity at the sheath boundary (outside the influence of V_p), and e and m_e are as expected the fundamental charge and electron rest mass. For an electron at grazing incidence, if we consider conservation of angular momentum we can write:

$$m_e v h_p = m_e r_p v_p \tag{2.28}$$

where h_p is a parameter which we define as the impact parameter describing the effective radius of the probe. If we rephrase the electron energy at the sheath boundary from equation 2.27 as being equal to eV_0 as if accelerated by an arbitrary external potential V_0, we can combine equation 2.27 with equation 2.28 to obtain an expression for the impact parameter: equation 2.29.

$$h_p = r_p \left(1 + \frac{V_p}{V_0}\right)^{\frac{1}{2}} \tag{2.29}$$

The total current to the probe tip I represents the flux of the total population of electrons n_0 with any given velocity distribution which are collected by the probe tip. The contribution to the probe current dI due to a sample, dn, of the electrons with a narrow portion of the velocity distribution is given by:

$$dI = 2\pi r_p L_p e \left(1 + \frac{V_p}{V_0}\right)^{\frac{1}{2}} \frac{v}{\pi} dn \tag{2.30}$$

where $(v/\pi)dn$ is the particle flux per unit area when considering electrons that move in planes perpendicular to the axis of the probe tip. For this model, velocity components parallel to the probe axis are not considered important. For a Maxwellian electron velocity distribution reduced in this manner we obtain the 2-D variant:

$$dn = n_0 \left(\frac{m}{2\pi kT}\right) \exp\left\{-\frac{mv^2}{2kT}\right\} 2\pi v dv \tag{2.31}$$

which can be substituted into 2.30 along with some simplifications:

$$x^2 = \frac{mv^2}{2kT} \quad \text{and} \quad a^2 = \frac{eV_p}{kT} \tag{2.32}$$

to give:

$$dI = 4n_0 r_p L_p e \left(\frac{2kT}{m}\right)^{\frac{1}{2}} x \exp\{-x^2\}(x^2 + a^2)^{\frac{1}{2}} dx \tag{2.33}$$

This expression may be integrated to obtain the total current to the probe giving the rather unwieldy equation:

$$I = 2\pi n_0 r_p L_p e \left(\frac{kT}{2\pi m}\right)^{\frac{1}{2}} \left(\frac{2a}{\sqrt{\pi}} + e^{a^2} \operatorname{erfc} a\right) \tag{2.34}$$

In the limit that a^2 is significantly greater than 2, the complimentary error function portion of 2.34 can be substituted thus:

$$\left(\frac{2a}{\sqrt{\pi}} + e^{a^2} \operatorname{erfc} a\right) = \frac{2(1 + a^2)^{\frac{1}{2}}}{\sqrt{\pi}} \tag{2.35}$$

In this limit we obtain the electron current to be:

$$I = 2\pi n_0 r_p L_p e \left(\frac{kT}{2\pi m}\right)^{\frac{1}{2}} \frac{2}{\sqrt{\pi}} \left(1 + \frac{eV_p}{kT}\right)^{\frac{1}{2}} \tag{2.36}$$

and the corresponding expression for the ion current is:

$$I_i = 2\pi n_0 r_p L_p e \left(\frac{kT_i}{2\pi M}\right)^{\frac{1}{2}} \frac{2}{\sqrt{\pi}} \left(1 + \frac{eV_p}{kT_i}\right)^{\frac{1}{2}} \tag{2.37}$$

The validity condition of this equation is that a^2 is much greater than two as stated before which translates to the sheath thickness being significantly large compared to the radius of the probe r_p (≈ 0.1 mm in the case of these experiments). A practical limitation of the use of this theory in this work is discussed later in section [ref] and applies in principle to the other theories in this section. The OML theory was extended significantly by Bernstein, and Rabinowitz [133] to use Poisson's equation in cylindrical polar coordinates (see equation 2.19 in section 2.7.1.5) and the Boltzmann equation:

$$\frac{df}{dt} = \mathbf{v} \cdot \Delta f - \frac{Ze}{m} \Delta\phi \cdot \Delta_v f = 0 \tag{2.38}$$

This was further extended by Laframboise [134] to include the Maxwellian distribution of

attracted particles.

2.7.1.7 Bernstein-Rabinowitz-Laframboise (BRL) Theory

This theory accounts for the formation of sheaths and orbital motion while Laframboise added a Maxwellian distribution for the ion temperatures. This is much more complex than ABR wherein all ions are collected by the probe due to having $T_i = 0$ (see section 2.7.1.5). In ABR the flux at distance r depends only on the conditions at ∞ and not on the radius of the probe tip. In BRL theory, the probe radius is more important and must be specified before hand.

BRL theory separately accounts for ions with inbound velocity and those with outbound velocity. Ions which are collected by the probe surface will only contribute once as they only have an inbound velocity. Ions that orbit the probe (in an infinite plasma) or are deflected by it (in a confined plasma), will contribute twice to the ion density at a given radius r. As in other probe theories, the Poisson equation must be solved however, the ion density must be known in order to do this which somewhat defeats the point of using the probe diagnostic. Bernstein solved this problem by expressing the ion distribution in terms of energy, E, and angular momentum, J, instead of radial and transverse velocity, V_r and $V_\perp$. Ions with a given J see an effective potential barrier between themselves and the probe. They must have sufficient energy to overcome this barrier for collection. For a given J there must exist an absorption radius larger than the probe radius within which any ions will be collected.

For a cylindrical probe tip, the BRL theory requires the solution of the modified Poisson equation:

$$\frac{1}{\xi}\frac{d}{d\xi}\left(\xi\frac{d\eta}{d\xi}\right) = 1 - \frac{1}{\pi}\sin^{-1}\left(\frac{\iota/\xi^2}{1+\eta/\beta}\right), \quad \xi > \xi_0 \tag{2.39}$$

and

$$\frac{1}{\xi}\frac{d}{d\xi}\left(\xi\frac{d\eta}{d\xi}\right) = \frac{1}{\pi}\sin^{-1}\left(\frac{\iota/\xi^2}{1+\eta/\beta}\right), \quad \xi < \xi_0 \tag{2.40}$$

where $\beta = E_i/(k_b T_e)$, ι is a dimensionless quantity denoting probe current per unit length, ξ_0 is the absorption radius, and ξ and η (the normalised radial coordinate) are defined as earlier in section 2.7.1.5. In the experiments performed, because of the dimensions of the probe being slim and long, OML theory was likely valid for the experiments performed in

this thesis. As an additional check, manual analyses were performed using spreadsheets from Hiden analytical. These checks showed that for the YLPD, the BRL theory results were in all cases close to/near identical to those given by OML theory. For cases where the probe shape is more significant (i.e. unusual geometry not restricted to cylindrical, spherical or planar bodies) BRL theory may be more appropriate. It is worth mentioning in brief however OML was used in all cases moving forwards involving Langmuir probe usage.

2.7.1.8 Langmuir Probes on the YLPD

As described in the introduction to fusion, the tokamak device confines the plasma by using strong magnetic fields. These fields alter the trajectories of the particles in the plasma through the Lorentz force:

$$\mathbf{F} = q\mathbf{V} \times \mathbf{B} \tag{2.41}$$

Particles freely stream along the field lines of $\mathbf{B}$ executing Larmor orbits in the plane perpendicular to $\mathbf{B}$. The radius of these orbits is given by:

$$r_L = \frac{\mathbf{v_t} m}{eB} \tag{2.42}$$

where v_t is the velocity transverse to the magnetic field $\mathbf{B}$, m is the particle mass. If the Larmor radius is small compared to the dimensions of the plasma it is said to be magnetized. More specifically, because different plasma species can have different Larmor radii, some species can be magnetized while others are not. Generally, the plasma is considered magnetized if all/both species are magnetized. The YLPD contains a magnetically confined plasma that is magnetized by design and contains a non-zero population of supersonic particles. There is a coil in the source of the YLPD tasked with magnetizing the plasma with a field of 0.17 Tesla. Under these conditions with electron temperature ranging from $0.1 \rightarrow 10$ eV, the electron Larmor radius is of the order 10^{-5} m which satisfies the criterion given the length of the plasma is $\approx$ 1m and the diameter of the beam is $\approx$ 20mm. If the ions are in thermal equilibrium with the electrons, at 10eV, the ion Larmor radius is $\approx$ 1-3 mm which is on the order of the column width. It is much more likely, however that while the ion velocity along the field line is high, the random ion velocity and thus the transverse is low. Under these conditions the ions will also be magnetized resulting in an overall magnetized plasma.

For a probe which satisfies the geometric constraints fairly well such as a thin, cylindrical wire, spherical or semi spherical protrusion we may evaluate the flux of electrons to the surface. The electron flux to the probe surface is governed by the average electron speed and the electron density at the probe, as described by equation 2.43:

$$\Gamma_e = \frac{1}{4} n_{ep} \bar{c}_e \tag{2.43}$$

where $\bar{c}_e$ is the mean electron speed, n_{ep} is the density of electrons at the probe surface and Γ_e is the electron flux.

If the electron velocity distribution is generally Maxwellian, the flux may be expressed in terms of the plasma density at the boundary of the sheath n_{es} instead of that at the probe surface n_{ep}. It also relates the flux to the bias voltage on the probe V and the electron temperature T_e.

$$\Gamma_e = \frac{1}{4} n_{es} \bar{c}_e \exp\left\{ \frac{eV}{kT_e} \right\} \tag{2.44}$$

Ion flux is conserved through the sheath [135] and thus the flux onto the probe is equal to the flux into the sheath at the edge. We imposed that the Bohm criterion 2.18 must be satisfied where the ions enter the sheath at least at the local sound speed c_s. This means we can write, for the ion flux:

$$\Gamma_i = n_{es} c_s \tag{2.45}$$

Because the ions enter the sheath at c_s, the density at the sheath edge n_{es} can be expressed as half the bulk ion density n_i which is by extension half the bulk plasma density n_0. In the electron saturation regime above the plasma potential V_P this theory breaks down as the magnitude of the positive bias prevents a sheath from forming and thus no sheath physics exist.

At the floating potential, because the total current on the probe is zero, we may equate the electron and ion fluxes from equations 2.43 and 2.45, giving a more concrete expression for Γ_i and relates the ion sound speed and the mean electron speed: c_s and $\bar{c}_e$. The equation relating the two speeds is:

$$c_s = \frac{1}{4}\bar{c}_e \exp\left\{\frac{eV_{float}}{kT_e}\right\} \tag{2.46}$$

While the new equation for Γ_i is calculated to be:

$$\Gamma_i = \frac{1}{4}n_{es}\bar{c}_e \exp\left\{\frac{eV_{float}}{kT_e}\right\} \tag{2.47}$$

If we express the total current to the probe as equation 2.48, the two ion flux expressions can be united giving an expression for the current which links the electron temperature, mean electron speed and sheath edge ion density shown by equation 2.49.

$$I_P = A_P e(\Gamma_e - \Gamma_i) \tag{2.48}$$

$$I = \frac{1}{4}A_P e n_{es}\bar{c}_e \left[\exp\left\{\frac{eV}{kT_e}\right\} - \exp\left\{\frac{eV_f}{kT_e}\right\}\right] \tag{2.49}$$

It is possible to simplify this expression by invoking the sheath edge density relation and pulling the first exponent out giving:

$$I = -\frac{1}{2}A_P e n_0 c_s \left[1 - \exp\left\{\frac{(eV - V_{float})}{kT_e}\right\}\right] \tag{2.50}$$

The constants become the ion saturation current as a final simplification to give:

$$I = -I_{sat}\left[1 - \exp\left\{\frac{e(V - V_{float})}{kT_e}\right\}\right] \tag{2.51}$$

This would be the ion current assuming an ion collection region that is simply cylindrical around the probe tip, such as in a plasma with no net flow. The YLPD axial magnetic field confines particles which are streaming along the magnetic axis with a drift velocity greater than the thermal velocity, $V_{drift} > V_{Thermal}$. As such there exists a series of flux tubes extending upstream towards the plasma source within which particles are destined to be absorbed by the probe. This results in a much larger effective ion collection area. This was not accounted for in this study which is a weakness of the methodology, however the offset this represents should be a multiplicative factor and should not change the shape of the trends observed. Due to the restriction of cross field transport, particles outside these flux tubes are unlikely to be collected by the probe tip.

2.7.2 Laser photodetachment theory

2.7.2.1 Overview of technique

It is possible to obtain more information about the contents of the plasma by perturbing the plasma in the vicinity of the probe and observing the response. Laser photodetachment is one such diagnostic technique which is used to detect negative ions. This technique was used in this work to measure negative ions on the GEC cell above changing surface materials under varying neutral pressure and applied RF power. It was also used to measure negative ions in the YLPD for the first time as a function of radial position for a few varying plasma conditions. This subsection explains the physics principles behind the diagnostic.

The laser photodetachment diagnostic operates using a Langmuir probe to measure the electron density in a specific region and inferring the local negative ion density from the electron density measurements. These negative ions (while whole) do not constitute a significant current to the probe tip when compared to the electron current. In order to measure the negative ions in the vicinity, instead the electrons are removed from the negative ions within a certain radius of the probe tip. This removal process is achieved using a collimated, pulsed laser beam aligned to engulf the probe tip whose photons carry sufficient energy to liberate the extra electron readily without causing further photo-ionization. These electrons, now easily accelerated by a stable positive voltage applied to the probe, are collected by the probe tip each time the laser pulse passes through the probe region.

Typically, the Langmuir probe tip is thin and long, normally bent to a right angle to allow the laser to surround a significant portion of tip-wire. This increases the surface area available for collection and therefore the signal to noise ratio. The laser needs to have a diameter large enough to encompass the probe tip by at least a millimetre to photodetach enough negative ions to create a significant change in the local electron density while also allowing this increase to be in range of the tip for collection. The voltage applied to the tip V_{App} to collect the electrons is slightly higher than the plasma potential V_P so as to be in the electron saturation region of the corresponding IV characteristic. This ensures that all electrons detached from negative ions in the region are collected quickly to form the signal pulse. This short pulse of electrons is recorded by a suitable recording device such as a DAC or oscilloscope as a short voltage pulse across a measuring resistor. This voltage can be converted into a corresponding current pulse amplitude ΔI and then compared to the

current measured without the laser pulse at V_{App} to give a ratio of negative ions to electrons. The mathematics and details of this follow.

2.7.2.2 Photodetachment diagnostic theory mathematics and finer details

In a singly ionised plasma (i.e. a fully ionized hydrogen plasma), the quasineutrality condition is stated as 2.52 where the number density of positive ions equals the number density of electrons for length scales much larger than the Debye length.

$$n_e \simeq n_i \tag{2.52}$$

Where, as expected, n_e and n_i are the electron and ion densities respectively. When taking into account negative ions, assuming they form an appreciable portion of the total density of negative species, the positive ion density obviously becomes equal to the sum over all negatively charged species - the sum of the electron and negative ion densities. This is given in equation 2.53 where A^- represents a generic atomic or, in some cases, molecular negative ion.

$$n_e + n_{A^-} \simeq n_i \tag{2.53}$$

The density of negative ions may be found from the negative ion fraction which is the quantity obtained by the diagnostic. Equation 2.54 shows the various terms associated with the negative ion fraction, where the fraction is equal to by definition the number density of negative ions divided by the electron density which is also equal to the change in local electron density divided by the electron density which, in turn, is measured as the current pulse divided by the probe current at V_{App}.

$$A^-_{fraction} = \frac{n_{A^-}}{n_e} = \frac{\Delta n_e}{n_e} = \frac{\Delta I}{I_{V_{App}}} \tag{2.54}$$

By substituting equation 2.53 into equation 2.54 which gives the negative ion density in terms of measurable quantities. The only sources of error are the measurement errors associated with the current pulse magnitude which is small due to large numbers of pulse averages, and the error in the ion density obtained from the IV curve which is relatively small compared to that associated with measuring the electron density directly from the IV curve.

$$n_{A^-} = n_i \times \left(1 + \frac{\Delta I}{I_{V_P}}\right) = n_i \times (1 + A^-_{fraction}) \tag{2.55}$$

This theory holds provided that the energy of each laser photon does not meaningfully exceed the binding energy of the additional electron to the H^- ion. More modern understanding of the photodetachment technique has investigated the validity of this under common experimental conditions. A discussion of this is found in the next section.

2.7.2.3 Validity of Langmuir probe assisted laser photodetachment in this work

It must be stressed that the theory presented here for negative ion density determination by Langmuir probe assisted laser photodetachment was chosen for simplicity. This short section describes some recent work (performed in the last 5-6 years) which highlights some shortcomings of this approach and presents an improves theory and analysis method which is valid for certain conditions. There has been extensive work performed by Sirse, Oudini, Taccogna, Ellingboe, Bendib and others involving simulation and comparison to experiment looking to explore the validity of traditional photodetachment methods [136–139] even going so far as to suggest a variant diagnostic which operates with a negatively biased probe [140].

The crux of the critical reviews centers upon the assumptions made in the original, simpler theory. These assumptions are as follows:

- The density and temperature of the electrons comprising the background within the electropositive channel created by the laser pulse are not meaningfully perturbed and can be assumed to be constant throughout the pulse.
- The entire photodetachment process happens on a much shorter timescale than the transit time of the detached electrons through the channel.
- The electrons photo-detached from the negative ions relax near instantaneously to a Maxwellian distribution matching that of the background electrons thus meaning there is no meaningful difference in their energy distribution functions shortly after the pulse ($\sim$ 10 ns).
- The increase in the current to the probe is exclusively a result of the complete collection of the photo-detached electrons.

In reality, when the laser passes through the plasma, the processes which evolve within the electropositive channel are complex and need to be accounted for. In the recent literature, numerical studies were carried out using a particle-in-cell Monte-Carlo collision model for a hydrogen plasma [136]. This model revealed that a double-layer was formed at the border formed between the electropositive channel and the bulk plasma. This double layer consists of a perturbation in the plasma potential and electron density which evolves over time both into the illuminated channel and also outwards from the channel border. This double-layer has an effect on the dynamics of the electrons, background and photo-detached within the channel as well as slightly outside the channel which affects the current to the Langmuir probe. Within the laser spot region, the plasma potential increases quickly following the pulse while the plasma potential outside stays relatively constant.

In agreement with the original theory, all of the negative ions in the channel are destroyed by photodetachment, splitting into electron-atom pairs. The electrons released this way can egress the spot region on ballistic trajectories, however the in-flux of negative charges attempting to balance this cannot match the loss-rate. The plasma potential then evolves over time in order to trap some of the photo-detached electrons, maintaining quasineutrality. The time scales of the formation of the double layer are of the order of a few nanoseconds. In this limit the ions are approximately stationary. The double layer relaxes over a period of time between 500 ns to 2 μs via a pair of waves one of which propagates within the channel and the other outside the channel. These waves can interact with the electrons and ions inside the channel via Landau damping and Fermi acceleration depending on the wave amplitude.

As such the electrostatic potential barrier/double layer formed at the edge of the electropositive channel affects the electron temperature and density within the channel. If the background density changes, the calculations based on this value will be somewhat erroneous. In the case of the subsequent determination of n_{H^-} is an overestimate due to the change in the electron density close to the probe being a result of both negative ion dissociation and an increase in the background electron density.

Another effect of the laser pulse is the rapid ($\sim$ 3 ns) introduction of a monoenergetic population of photo-detached electrons based on the laser energy isotropically within the channel. The thermalization of these photo-electrons occurs primarily through collisionless processes like Landau damping and Fermi acceleration brought on by the existence and

relaxation of the double layer. This thermalization period can last on the order of 250 ns which contradicts the assumption that the photo-detached electrons relax to a Maxwellian energy distribution near instantly. This coupled with the effect on T_e through interaction with the electrostatic double layer renders the background EEDF non-Maxwellian at least for some portion of the measurement and laser pulse cycle.

These effects are detailed more completely in the cited work and can lead to miss-measurements of n_{H^-} by up to an order of magnitude. A new analysis method was proposed in [138] which should be valid for electronegative plasmas with moderate electronegativity (ratio of negative ions to electrons), and relatively low collisionality (mean free path of electrons much less than the radius of the laser beam - typical of plasmas at neutral pressures below 40 Pa). Under these conditions the accuracy of the analysis for negative ion densities is closer to 10-20%. This would likely be applicable to the experiments performed on the GEC and, time allowing this experiment would be repeated with this new methodology. In the case of the measurements performed on the linear device, the validity of this model is not well known. While the electronegativity condition is likely fulfilled, the mean free path condition is more difficult to quantify. The presence of the magnetic field changes the electron dynamics and the electron temperature and density are high. This coupled with the inhomogeneous spatial distribution of n_e and T_e due to the source parameters and confining magnetic field complicate the problem. In both cases, the simpler original method was applied which, while suffering from errors resulting from the oversimplified assumptions, still provides useful measurements for the observation of trends in the negative ion density.

2.7.3 Optical emission spectroscopy diagnostic theory

Spectroscopic techniques may be employed as a non-invasive diagnostic methods to, in principle, infer many plasma parameters [141, 142].

2.7.3.1 Hydrogen Fulcher-α band spectroscopy

The Fulcher bands of hydrogen are a series of emission lines associated with rotational-vibrational (rovibrational) energy transitions occurring in hydrogen plasmas containing hydrogen molecules. These transitions occur within the framework of the rovibronic structure of molecules such as that shown for the hydrogen molecule in figure 2.10. This diagram shows the first two electronic states of the hydrogen molecule as the curved potential wells

marked by $X^1\Sigma_g^+$ (the ground state) and $B'\Sigma_u^+$ (the first excited state). The vibrational levels are marked and labeled to the left of these curves and the clustered rotational levels to the right. In particular the α band is the series of transitions from the $d^3\Pi_u$ state to the $a^3\Sigma_g$ state which may be used primarily to determine the rotational gas temperature. The vibrational gas temperature may also in principle be estimated from these, however more spectral lines are desirable to reduce the errors associated with this.

The transitions specific to the diagonal branch of the Fulcher alpha band are shown in figure 2.11. The molecules are assumed to start in the ground electronic state with some rovibrational energy distribution function. In the case of sufficient energy, the distribution function across the available rotational and vibrational states is a Boltzmann distribution. For the rotational energy levels, these are close together and so it is relatively easy to form a local equilibrium resulting in a Boltzmann distribution among the lower states while the upper states may be overpopulated, this is common in low pressure discharges [143]. The vibrational levels, however have energy transitions larger by an order of magnitude and so require much higher temperatures to reach equilibrium across the states. This means that the lower vibrational levels in many low to medium temperature plasmas are not in vibrational equilibrium. Instead a partial equilibrium is assumed where the closer-spaced higher vibrational levels are in equilibrium with each other.

The rovibrational distribution in the ground state is preserved when the molecule is electronically excited by electron impact to a $d^3\Pi_u^{\pm}$ state. This state is short-lived which means that redistribution of energy between the levels is not significant before a spontaneous de-excitation event results in the emission of a photon corresponding to one of these rovibrational states. There is insufficient time for the restructuring to occur through impact of another particle. The emission lines typically used for determining temperatures are the Q-branch transitions on the right-hand side of the diagram 2.11 where the vibrational and rotational quantum numbers are unchanged after the de-excitation process.

2.7.3.2 Calculating rotational gas temperatures from Fulcher spectra

This subsection covers the mathematical formalism of the molecular energy distribution function in the ground electronic state and how it is possible to extract temperature information from measurable quantities. The summary comprises work found in [144–149].

For a given rovibronic spontaneous decay transition, the intensity of the line $I^{n'v'N'}_{n''v''N''}$

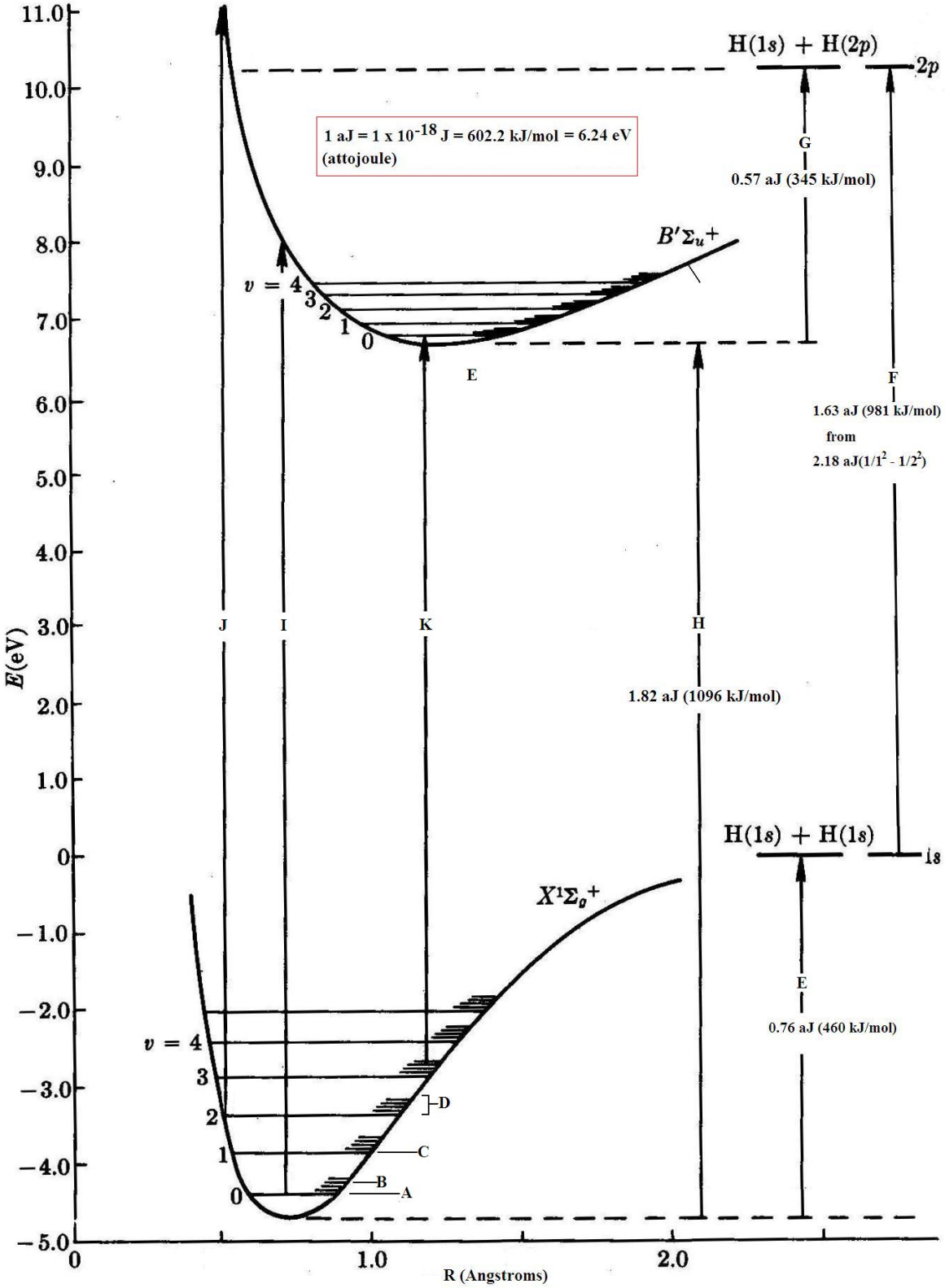

Figure 2.10: The molecular energy structure of the ground electronic state and first excited electronic state of H_2, obtained from the website of St. Olaf College (chemistry department) [11]. This shows the rotational and vibrational structure of H_2

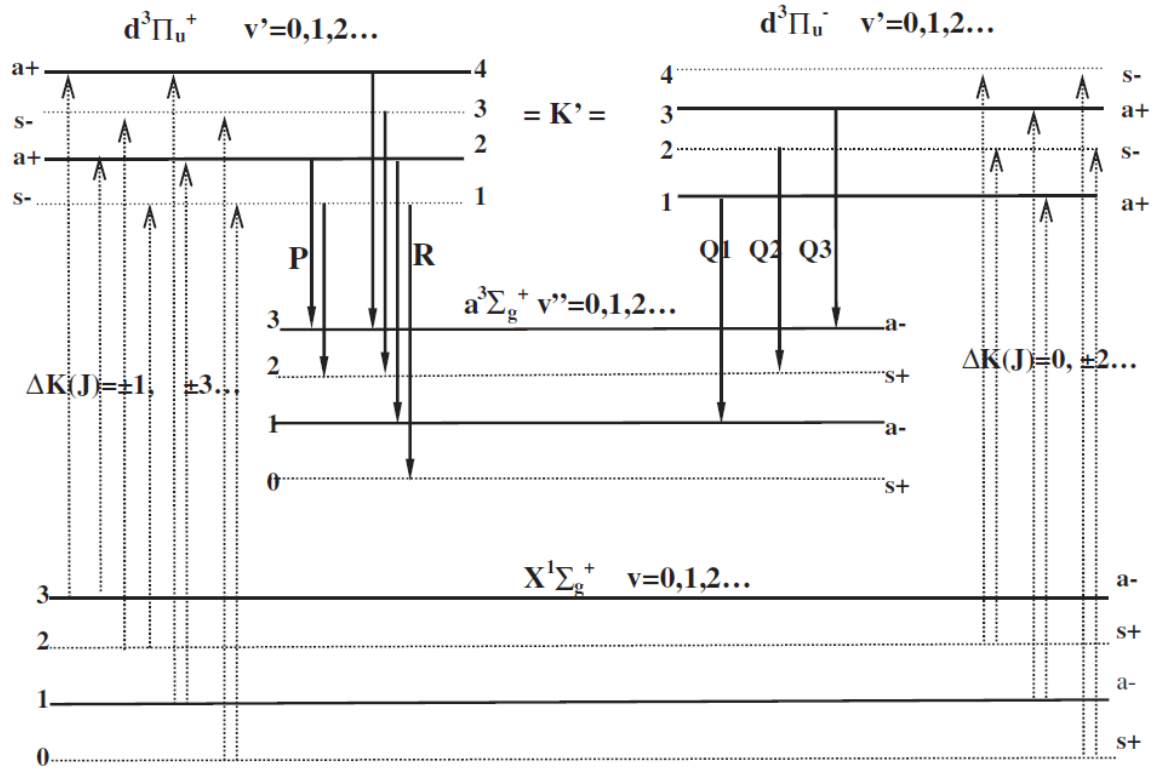

Figure 2.11: The transitions associated with the Fulcher-α transitions. The molecule is initially in the ground state with an initial rovibrational energy. The molecule is promoted to a higher electronic state typically by electron impact excitation preserving its initial rovibrational state. The molecule then undergoes a spontaneous radiative decay, releasing a photon. The ratio of transition photons can then be used to estimate the rotational and vibrational temperatures. Obtained from [12]

associated with said transition is given by equation 2.56:

$$I^{n'v'N'}_{n''v''N''} = h\nu^{n'v'N'}_{n''v''N''} N_{n'v'N'} A^{n'v'N'}_{n''v''N''} \tag{2.56}$$

where h is Planck's constant, $\nu^{n'v'N'}_{n''v''N''}$ is the wavenumber of the emitted photons, $n_{n'v'N'}$ is the population density of the initial rovibronic level and $A^{n'v'N'}_{n''v''N''}$ is the transition probability between the upper and lower rovibronic states [145]. The transition probability can be expressed using equation 2.57 [149].

$$A^{n'v'N'}_{n''v''N''} = \frac{64\pi^4}{(4\pi\epsilon_0)3hC^3}\nu^3 \frac{\sum_{M'M''} |\langle\phi'|T^1_q(\mu_e)|\phi''\rangle|^2}{2N'+1} \tag{2.57}$$

where ϵ_0 is the permittivity of free space, C is the speed of light in vacuum, ν represents the transition photon wavenumber (simplified for ease of writing), M is the magnetic field

directional component of J which in turn is the total electronic angular momentum quantum number. The transition dipole moment is given by $\mu_{\mathbf{e}}$, the subscript q indicates that the frame of reference is fixed on the molecule and is equal to zero along the inter-nuclear axis. The square of the dipole transition moment can be decomposed using the Born-Oppenheimer approximation which yields:

$$|\left\langle \phi' \right| T_q^1(\mu_{\mathbf{e}}) \left| \phi'' \right\rangle|^2 = \langle R_e \rangle^2 q_{v'v''} S_{N'N''} S_{M',M''} \tag{2.58}$$

where $\langle R_e \rangle^2$ is specifically the electronic dipolar transition moment, $q_{v'v''}$ is the Franck-Condon (FC) factor for vibrational transitions, ϕ is the wavefunction, and $S_{N'N''}S_{M'M''}$ is the Hönl-London (HL) factor.

The Hönl-London factor follows a series of normalization conditions which are listed below. These are useful for tailoring the mathematics to the transitions under investigation.

$$\sum_{M'M''} S_{M'M''} = 1 \tag{2.59}$$

and for the P,Q and R branches respectively:

$$\sum_{N''J''} S_{N''-1,N''} = [2 - \delta_0, \Lambda' + \Lambda'](2S' + 1)\frac{N'}{2} \qquad (P) \tag{2.60}$$

$$\sum_{N''J''} S_{N'',N''} = [2 - \delta_0, \Lambda' + \Lambda'](2S' + 1)\left(N' + \frac{1}{2}\right) \qquad (Q) \tag{2.61}$$

$$\sum_{N''J''} S_{N''+1,N''} = [2 - \delta_0, \Lambda' + \Lambda'](2S' + 1)\left(\frac{N' + 1}{2}\right) \qquad (R) \tag{2.62}$$

where S is the total spin quantum number and Λ is the projection of the total orbital angular momentum quantum number L along the inter-nuclear axis. In the work done in this thesis, only Q-branch transitions are used because the P and R branch transitions exhibit unusual behaviour regarding the HL factors. The δ_0 term in square brackets depends on the Λ values [148] according to:

$$\delta_0 = 1 \;\; if \;\; \Lambda = 0 \tag{2.63}$$

$$\delta_0 = 0 \;\; if \;\; \Lambda > 0 \tag{2.64}$$

In this case Λ >0 so the square brackets term reduces to 2. The total spin for a hydrogen molecule in the ground state is zero as there is one spin up and one spin down electron forming the bond. This reduces equation 2.61 to 2.65:

$$\sum_{N''J''} S_{N'',N''} = \left(N' + \frac{1}{2}\right) \tag{2.65}$$

Substituting equations 2.59, and 2.58 into equation 2.56 and cancelling relevant terms, the intensity of a transition becomes:

$$I^{n'v'N'}_{n''v''N''} = \frac{16\pi^3}{3\epsilon_0 C^3}\nu^4 n_{n'v'N'} \frac{\langle R_e\rangle^2 q_{v'v''} S_{N'N''}}{2N'+1} \tag{2.66}$$

This can be further reduced by combining constants and terms which are functionally invariant within one vibrational band. For example, the FC factor $q_{v'v''}$ is a vibrational quantity and is constant when examining the relative intensities of rotational emission lines. Similarly, $\langle R_e\rangle^2$ is purely a vibronic term and is constant for a given Q-branch. When these simplifications are applied, the intensity is:

$$I^{n'v'N'}_{n''v''N''} = Y\nu^4 n_{n'v'N'} \frac{S_{N'N''}}{2N'+1} \tag{2.67}$$

At this point, it is necessary to invoke an assumption about the distribution of rotational energy levels. If the population is in thermodynamic equilibrium, which is likely for the closely spaced rotational states, it may be described by a Boltzmann distribution of the form 2.68:

$$State\ pop. = Total\ pop. \;\times\; Degeneracy \times \exp\left[\frac{State\ Energy}{Pop.\ temperature}\right] \tag{2.68}$$

then the population of the rovibronic state of interest may be written as:

$$N_{n'v'N'} = N_0\, g_{n'v'N'} \times \frac{\exp\left(\frac{-E_{n'v'N'}}{k_B T_{Rot}}\right)}{Q} \tag{2.69}$$

where N_0 is the total population density of molecules, $g_{n'v'N'}$ is the statistical weight or degeneracy of the state, $E_{n'v'N'}$ is the state energy, Q is the partition sum and k_B and T_{Rot}

are respectively Boltzmann's constant and the rotational temperature. The partition sum represents the sum over all of the available states so is a constant for a given (rotational) temperature and density of molecules. It is given by:

$$Q = \sum_i g_i \exp\left(\frac{-E_i}{k_B T}\right) \tag{2.70}$$

where i is the state, g_i is the degeneracy of state i and E_i is its energy. The degeneracy $g_{n'v'N'}$ from equation 2.69 can be split into its component parts: vibrational, rotational and nuclear spin degeneracies such that:

$$g_{n'v'N'} = g_v g_N g_{as} \tag{2.71}$$

where in the case of diatomic molecules like hydrogen, g_v is equal to one as there is only one possible axis of vibration and g_N is equal to $2N + 1$.

Performing the final substitutions of equations 2.71, 2.65 and 2.69 into equation 2.67 and simplifying once more yields the final expression for the intensity of a transition within one vibronic level as a function of rotational temperature, equation 2.72:

$$I^{n'v'N'}_{n''v''N''} = Y\nu^4 g_{as}(2N' + 1) \times \exp\left(\frac{-E_{n'v'N'}}{k_B T_{Rot}}\right) \tag{2.72}$$

In literature, sometimes the intensity is proportional to the third power of the wavenumber instead. This is simply a choice of units between intensity in terms of power vs photons. It is possible to obtain vibrational temperatures also from this data provided sufficient number of emission lines. The determination of the vibrational temperature is, however more complex. Several of the terms in the analysis taken as constants have to be enumerated and either the overall plasma temperature must be sufficiently high so as to render a Boltzmann distribution among the vibrational levels valid, or the vibrational distribution function is measured or fit to the emission instead of a simple temperature value. It is usually not valid to assume a Boltzmann distribution among vibrational states as the energy gaps between neighbouring levels are an order of magnitude larger than those for rotational levels.

2.8 Summary of chapter

This chapter has covered some previous relevant work on negative ions and MAR plasmas particularly linear devices and RF plasmas, either in a GEC type geometry or containing hydrogen. The theory is also presented governing the major diagnostic techniques used in the experiments performed for this thesis. The specifics of these techniques applied to the experiments performed are detailed in the following chapter on methodological information. This is followed by the results of those experiments and then a short chapter on a collaboration project and the overall conclusions.

Chapter 3

Experimental methodologies

3.1 Experimental technique for measuring negative ions on the GEC

3.1.1 Overview of GEC Reference cell

3.1.1.1 GEC cell - Purpose

The Gaseous Electronics Conference reference cell (henceforth GEC cell) is a plasma source proposed in 1988 in order to better facilitate the study of plasmas with respect to the manufacture of microelectronics. The motivation was to allow many independent research groups to study any appropriate plasma with reduced variation between individual experiments resulting from drastically different geometries or material choices. The basics of the original specification are still largely obeyed although some modifications have been made (see [150, 151]) in many cases to facilitate studies which would otherwise be impossible on the standard configuration. The York Plasma Institute owns two such cells which have been slightly modified for their intended purposes (one for pulsed laser deposition experiments and one for more pure plasma based experiments). Even with modification the physics largely commutes between cells, preserving the original motivation behind the design.

3.1.1.2 Basic original design spec

The basics of the original design [152] revolve around two electrodes in a vacuum chamber separated by a prescribed distance. The source is contained within readily available stainless steel Ultra-High-Vacuum (UHV) parts which may be expanded upon to accommodate

diagnostics and pumping constrains. In the standard design, the two 10.2 cm (4 ") electrodes are separated by 2.54 cm (1 ") and are each surrounded by a series of insulating plates and gaskets followed by grounded shielding walls. The electrodes are so designed to allow for independent grounding or application of power to one or both electrodes. The grounded walls dramatically reduce the sputtering of the insulator into the chamber and help restrict the formation of the plasma to the region between the electrode plates. Radio frequency power is applied to the desired electrode/s at 13.4 MHz, higher harmonics or sometimes combinations thereof. This creates a capacitive discharge between the electrodes with plasma qualities influenced by the power applied known as a capacitively coupled plasma (CCP). The electrodes are both configured to allow water-cooling for cases where the power dissipated by the plasma is sufficiently high such that the electrodes or other surfaces may become hot enough to cause permanent damage. A schematic (not to scale) is shown in figure 3.1.

The inclusion of large access ports at several mutually perpendicular positions (see figure 3.4) provides particularly effective access for optical diagnostics while the smaller interstitial ports allow for mounting any CF40 compatible devices or adapters. The larger ports allow lines of sight to the region covered by the electrode surfaces as well as some way beyond if the region be of interest. The vacuum is provided by a roughing pump connected to the lower portion of the chamber via four pipe connectors distributed equally around the circumference of the chamber. If necessary, a turbomolecular pump depending on the desired discharge conditions. Gas is admitted to the chamber through a mass flow controller by a showerhead pattern in the upper electrode or sometimes by gas inlet attached to one of the smaller ports on the mid-plane, bypassing the mass flow controller. An inductor coil was implemented in the design at a later stage such as in [153] which may be powered independently to couple power into the plasma inductively instead forming an inductively coupled plasma (ICP). The specifics of CCPs and ICPs is discussed later in section 3.1.1.4. The overall design is largely the same as those used at the York Plasma Institute, with any notable deviations described in the following subsection. For a more detailed description, the references already mentioned and the original designs [154] provide a more complete overview.

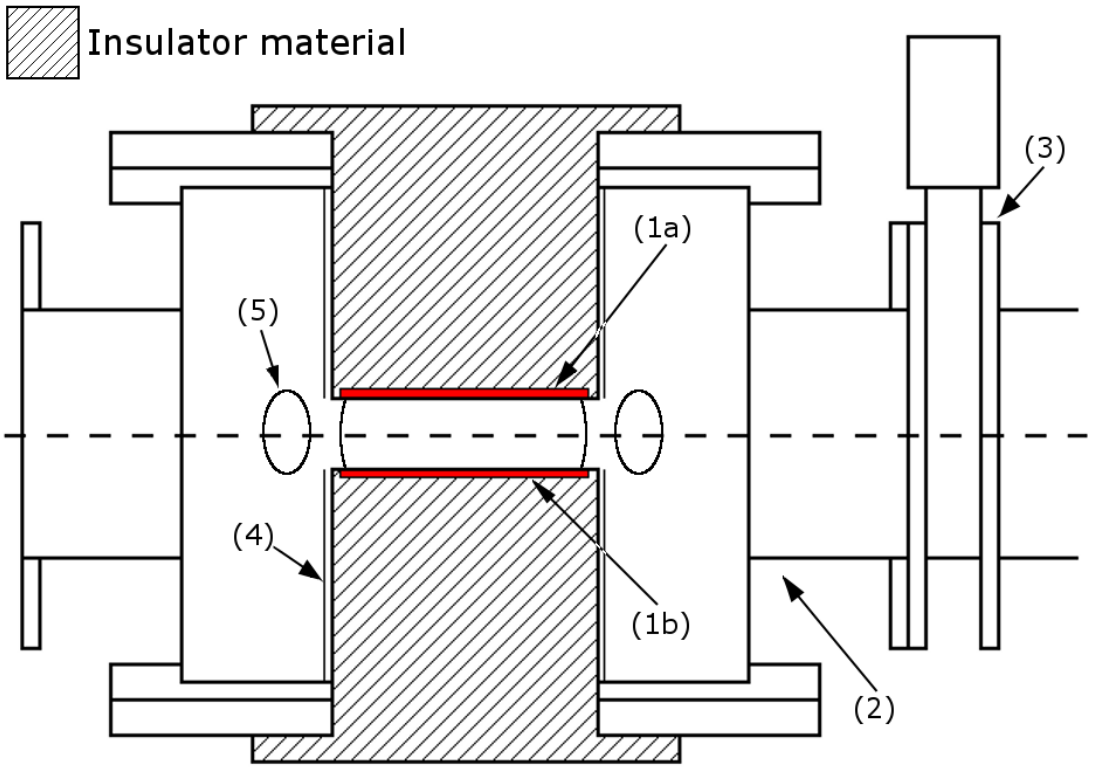

Figure 3.1: Layout of standardized GEC Cell according to original design documents. The York design is slightly modified and is explained presently, however the majority of the construction parameters are the same and thus comparable to the standard design

3.1.1.3 York design spec

The GEC cell used in this work is a slight modification of the standard design. The electrode spacing (H) is also larger at (42 mm) and was not changed throughout all work in this thesis. The electrodes are stainless steel instead of aluminium and the insulating material has been replaced with a ceramic substitute for increased durability under higher thermal stresses. Further details on the modifications made to this device can be found in [98, 155] and associated literature. Power was supplied by an Advanced Energy Cesar 1310 RF generator connected through an automatic matching network (Advanced energy RF Navio) directly into the upper 5-turn copper coil. The York GEC is shown in figure 3.2 with its alternate electrode spacing.

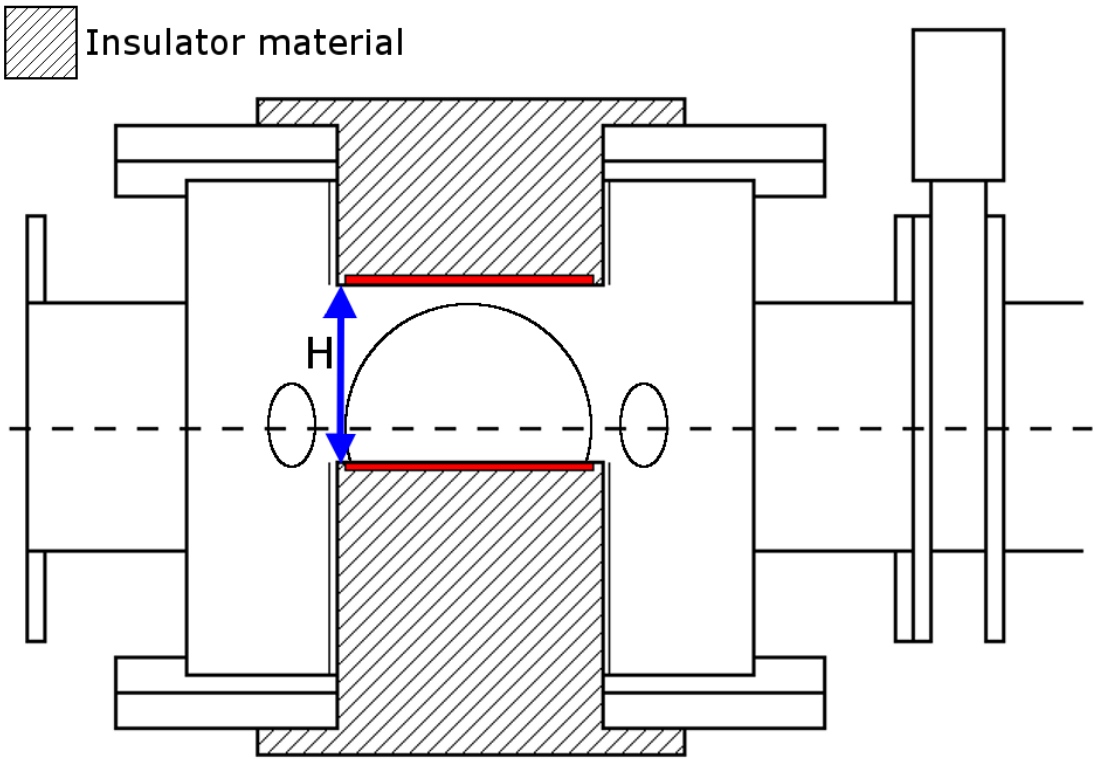

Figure 3.2: Layout of the York GEC Cell used in the photodetachment - negative ion density and fraction experiments for different surface materials. The diagnostic access is good, making experiments like these simple

3.1.1.4 GEC operating modes CCP and ICP

The GEC cell may be operated in two primary configurations, capacitively coupled and inductively coupled. The capacitively coupled plasma is generated between parallel plates while the ICP is generated by a planar coil within the upper electrode housing. In both cases the plasma is created by applying radio frequency power to the respective electrode to create an oscillating electric or magnetic field [156]. The details of the processes by which these plasmas are generated in each case are briefly explained in following subsections and more details can be found in the mentioned literature.

3.1.1.5 CCP – Generation overview

The CCP configuration consists of an RF powered plate electrode and a separate grounded electrode of similar or identical area similar to a parallel plate capacitor. The RF applied to the powered electrode generates an alternating electric field between the plates. The electric field causes the electrons of the gas atoms/molecules to accelerate which can dissociate them from their host particles. Once free they may cause further ionization events through collisions leading to a population of secondary electrons. If the applied field is strong enough this effect can lead to an electron avalanche resulting in a sufficient density of free electrons so as to render the gas electrically conductive constituting a plasma state. In addition to bulk heating, electrons are accelerated, in some cases more efficiently, by the alternating sheath at the powered electrode [107].

3.1.1.6 CCP – Typical conditions / parameter ranges

Capacitive plasmas have been characterized by simulations [157] and measurements [158]. The conditions within a GEC CCP are typically electron temperatures of the order $T_e \leq 5$ eV, while the densities tend to cap around $n_e = 10^{17}$per cubic metre [156]. Gas pressures are typically below 20 Pa [156] which is integral to the function of the vast majority of industrial processing plasmas.

3.1.1.7 ICP – Generation overview

The ICP configuration uses the planar inductor coil as the powered electrode with the same grounded planar surface electrode as the CCP case. When RF power is applied to the coil, a temporally variant magnetic field is generated around the coil which permeates into the gap between the electrodes. This also generates a time varying induced electric field by Faraday's law which accelerates the electrons in the gas in a similar fashion to the CCP case, forming the plasma. The use of an inductor coil to drive a electric field and plasma current is highly efficient compared to achieving a similar state with a CCP. As more complete description of the generation and modes present in an ICP, including the tendency for the coil to couple a small fraction of the applied power capacitively, is found in brief in [159] and in detail in [156].

3.1.1.8 ICP – Typical conditions / parameter ranges

Inductively coupled plasmas are also used widely in the plasma processing industry and as a source of light. Gas pressures occupy a similar parameter space to the CCP case however it may be difficult with some gasses to ignite a plasma at pressures around 15 Pa and below at relatively low RF power ($\approx$ 200 W). Other ICP devices may be designed to operate at lower pressures such as [159] depending on the nature of the plasma processing to be done. The electron temperatures are largely of a similar order of magnitude, though for similar operating conditions, the core electron temperature may be lower for the ICP case, rising towards the edge while the CCP case displays the inverse (higher central, trailing near the edge) [160]. The electron densities achievable through the ICP configuration are, however often around an order of magnitude higher for similar operating pressure and power [160] or potentially higher [159]. This was beneficial to this study by allowing a greater number of lower energy electrons to be present in the plasma bulk for dissociative attachment, corresponding to relative ease of measurement of negative ion signals using the photodetachment diagnostic described in 3.1.2. Further to this point, there is a larger body of work on negative ions in the GEC using an ICP which informed the decision to operate in a hydrogen ICP for these experiments.

Models for inductively coupled hydrogen plasmas relevant to this study give some indication as to the potential distribution of species found in plasmas of this nature. For example, these models show that the dominant ion is overwhelmingly the trihydrogen cation (H_3^+) [68, 97] for the range of applied power available in this case ($\leq$ 1000 W applied). They also show the distribution among the vibrational states in the case of the work done by Samuel and Corr [68] as a function of applied RF power. The dominance of the H_3^+ ion is evident from an experimental standpoint from the use of it as the positive ion component under investigation in [69–71, 161] using a retarding field analyser.

3.1.2 Laser photodetachment experiments on the GEC reference cell

3.1.2.1 Overview

The laser photodetachment experiments performed on the GEC cell are described here. In particular the details of the construction and operation of the experiment are discussed as well as the means of analysis. The associated theoretical background may be found in section

2.7.2. Specifics of individual pieces of equipment and their settings are explained and justified if necessary. The aim of the experiments was to examine the potential effects of different surface materials on the negative ion populations in a hydrogen plasma in proximity to the surface. The plasma in question bears some similarities to a plasma that might be found in a tokamak divertor albeit with much higher concentration of H_3^+ and potentially some other differences. It was of interest to explore how the behaviour of the plasma changed for each surface type with increasing power coupled into the plasma and varying gas pressure.

The experiment at its core consisted of a dog-legged Langmuir probe inserted into the plasma with the dog-leg portion of the probe coincident with the axis of a pulsed laser. The probe was biased a few volts above the plasma potential and connected to the 1 MΩ output of a Teledyne Lecroy Wavesurfer 3054 oscilloscope which was synchronized with the output sync TTL pulse of the laser q-switch. As described in the theory section 2.7.2 the laser pulse temporarily increases the local electron density by stripping electrons from negative ions. This creates a short, small current spike through the probe which is measured through a resistor by the oscilloscope as a voltage pulse. The basic layout of the whole diagnostic in component form is displayed in figure 3.3 as a rudimentary block diagram. The connections A and B were connected independently for either: A, the recording of I-V characteristics to the computer or B, The acquisition of photodetachment pulse data.

3.1.2.2 Electrode plate - variable surface material

In order to investigate the effect of differing surface materials on the negative ion population in the plasma, sputtering target plates were acquired from Testbourne LTD. of uniform thickness (3.1 mm) to be placed centrally onto the grounded lower electrode of the GEC. These plates were 104 mm in diameter so as to completely cover the lower electrode without touching the surrounding shielding walls. This plate size also ensured that the material of study was functionally the dominant surface in interactions with the plasma in the probed region as little to none of the steel electrode was left exposed. The uniformity in thickness ensured that the relative position of the probe above the surface was the same between samples, improving the comparisons between sample material.

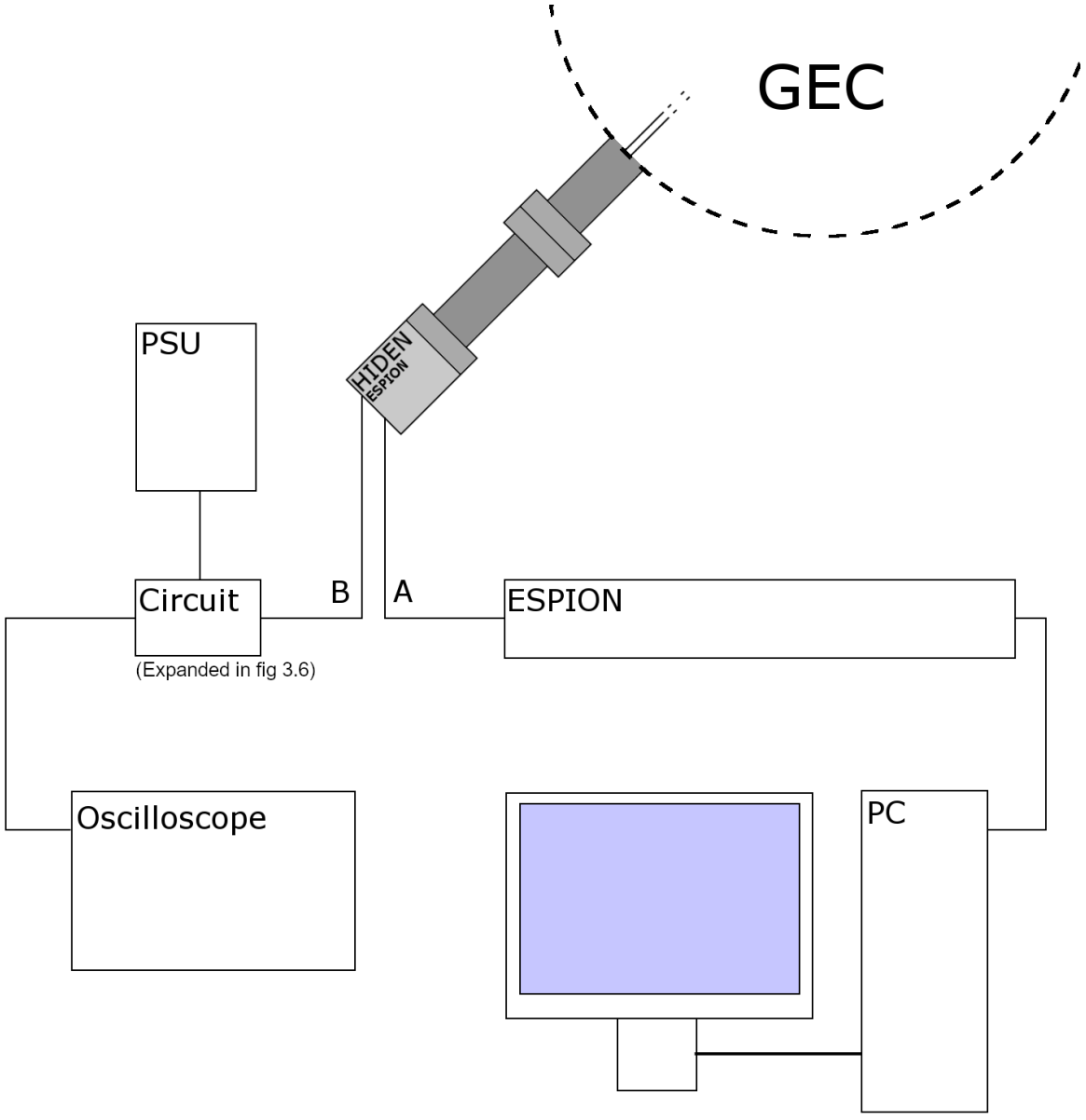

Figure 3.3: Block diagram showing the two parts of the photodetachment experiment performed on the GEC cell

3.1.2.3 Plasma control

Hydrogen gas of 99.9995% purity was admitted through the mass flow controller and the pressure controlled via a motorized butterfly valve on the outgoing pipe to the pumping system. The plasma was run in a pulsed ICP mode due to undesirable heating effects at high power observed in constant wave (CW) operation which prevented reliable measurement. The plasma was pulsed at 10 Hz with a duty cycle of 10%. This significantly lowered the surface temperature and allowed the sample plates to remain at consistent temperatures during their respective plasma measurements and repeated runs. This duty cycle also made the surface temperatures consistent between samples. For reference, under CW after 40 minutes (time for one measurement series) the plate, when measured after re-admission of air using an IR thermometer, reached upwards of 60 °C. By contrast with pulsed operation this was restricted to around 25 °C after approximately the same time period. The plate temperatures typically began between 20 °C and 22 °C depending on the initial conditions of the room during the day. Temperature consistency was vital because of the temperature dependence of plasma-surface interactions [162].

3.1.2.4 Laser system, alignment and timing

The laser used in the experiments was a *Continuum minilite-2* q-switched Nd-YAG laser system. The wavelength used was the frequency-doubled 532 nm mode. This was because the gain in photodetachment cross section between this and the 1064 nm mode is relatively marginal ($\approx 10\%$) [163] and the alignment was significantly simpler with visible light. The pulse is short (≈ 5 ns) and stable with low jitter which results in highly consistent pulses in both time and energy (≈ 20 mJ). This led to current pulses which could be averaged on the scope to produce a signal with high signal to noise ratio. The laser beam was directed through the GEC's diagonal ports so as to share its centre axis with the dog-legged portion of the probe tip. The FWHM of the beam's Gaussian profile was approximately 3mm which was sufficient to completely encompass the probe tip. This arrangement is shown in figure 3.4.

3.1.2.5 Probe and electronics

The Langmuir probe used was a Hiden Analytical ESPion® probe and controller system shown in figure 3.5. In detail, the Langmuir probe tip (1) was 9 mm long (the dog-legged

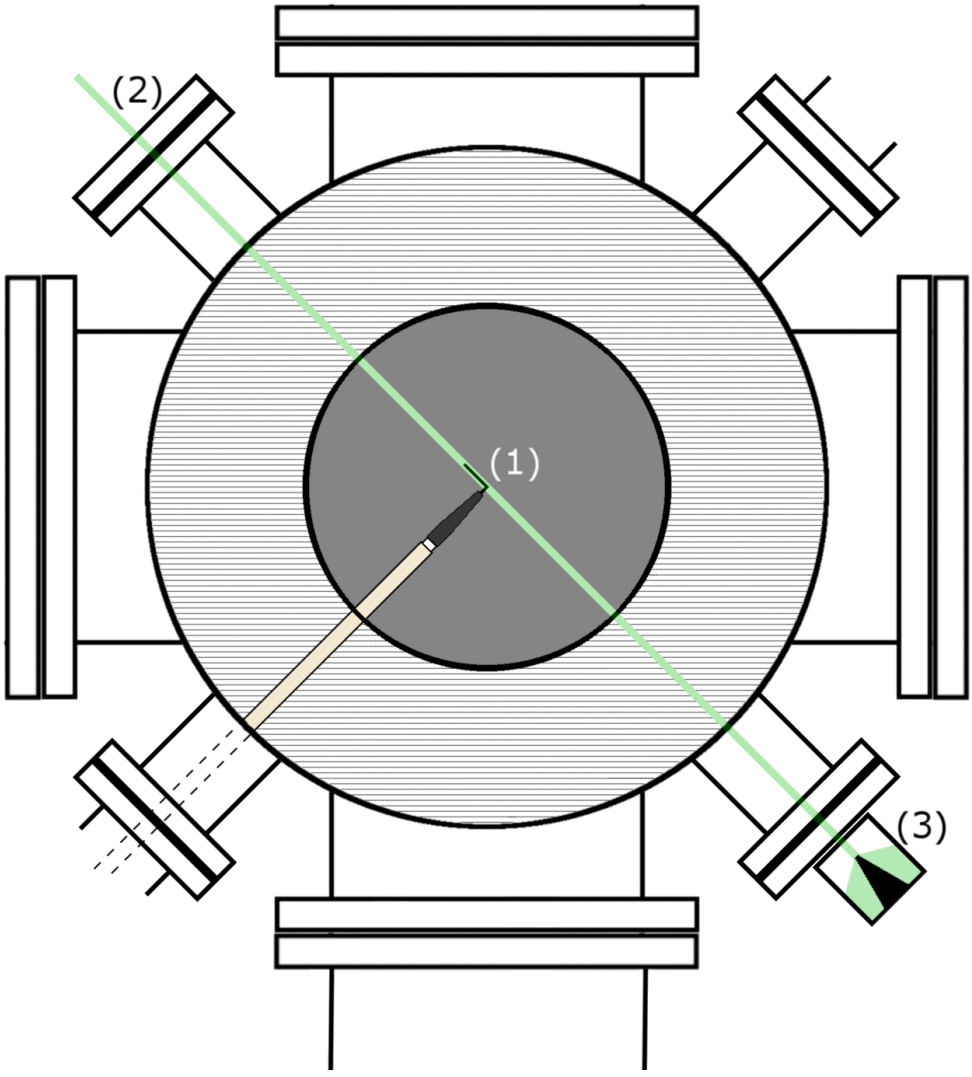

Figure 3.4: Diagram showing the path of the laser through the GEC via (1) the probe tip, (2) the entrance laser window and (3) the beam dump suspended over the exit window.

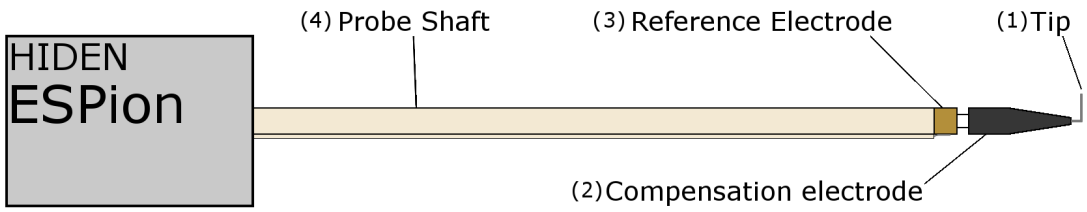

Figure 3.5: ESPion® Advanced Langmuir probe by Hiden analytical. The tip is typically straight but needed to be bent for this application.

portion), 0.15mm in diameter and comprised of solid tungsten. Tungsten is a common material choice for Langmuir probes due to its high melting point and decent thermal conductivity combined with its rigidity. The probe tip was connected via ferrule into the body of the probe which consisted of an insulating alumina shaft (4) which routed the signal through a number of filtering components into the rear housing of the device. The components within the shaft and the compensation electrode (4) provide radio frequency compensation to filter out at least 13.56 MHz and the first few harmonics to provide a more accurate and representative measurement. The reference electrode (3) was a brass cylindrical sheath connected into the rear housing which can be used to acquire a secondary I-V curve; however this feature was not used in these experiments.

The probe was connected to a dedicated ESPion® controller for the acquisition of IV-characteristics using the appropriate ESPsoft® software package and a windows computer.

For the photodetachment pulse measurements, the probe was instead connected to the oscilloscope via path (B) in figure 3.3. The intermediate circuitry was necessary for three reasons. The primary reason was the three-way connection between the HP 6115A 0-50 V DC power supply, the Langmuir probe and the scope. Secondly, the 1 MΩ input was set to DC coupling and so required a DC blocking capacitor to prevent the DC bias voltage from moving the oscilloscope trace off-screen (out of range). This blocking capacitor was placed in the circuit. Thirdly, the circuit also allowed for some noise filtering on the PSU input. This circuit was based on the diagram found in the paper by J. Santoso et. al. [73] and the version used in this study is displayed in figure 3.6.

The 51 Ω resistor was the load resistor for the circuit through which the majority of the current from the photodetachment pulse flowed. This is due to the much larger MΩ scope termination impedance acting in a fashion identical to a voltmeter. Close to 100%

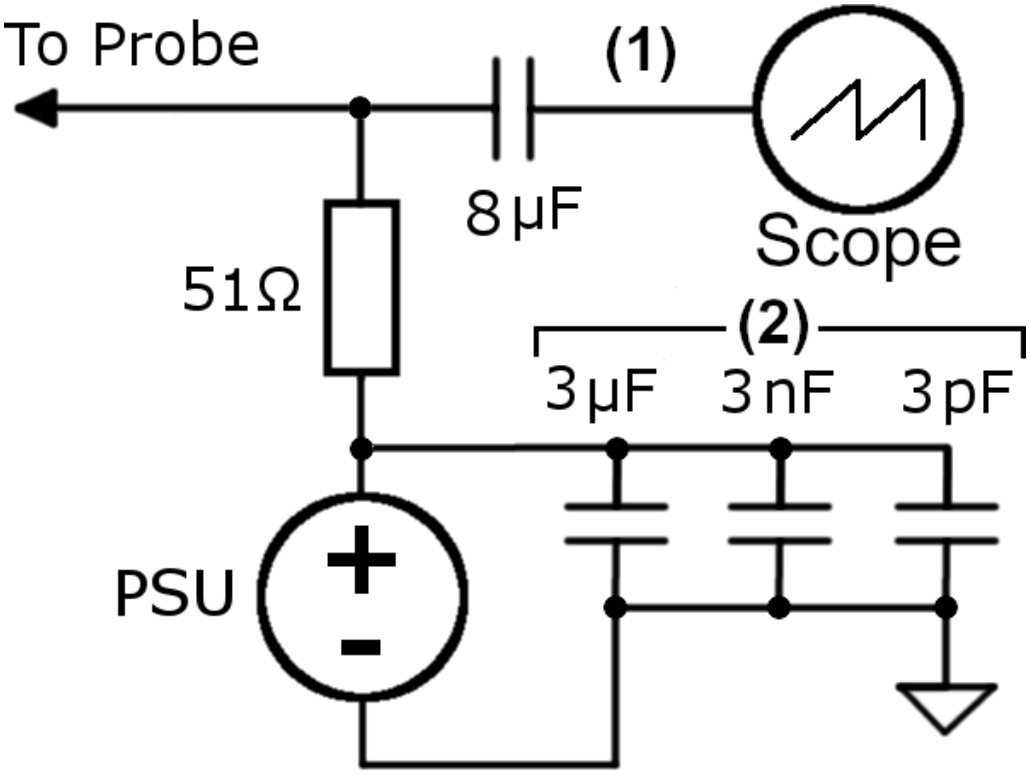

Figure 3.6: Laser photodetachment circuit - The ratio of the scope impedance to the measurement impedance means that realistically 100% of the signal is captured by the scope. The cable length (1) was kept to a length of 0.5 m (capacitance ≈ 25 pF) and the capacitor triplet (2) was installed in order to reduce noise feeding back from the connection to ground.

of the current flows to ground through the load resistor while the voltage drop is mostly routed through to the oscilloscope. This meant that there was no need to double the pulse magnitude for analysis as it was already practically correct. The 8 μF capacitor formed the DC block by acting as an RC high-pass analogue filter with a cut-off frequency around 400 Hz. As can be seen in figure 3.7 (http://sim.okawa-denshi.jp/en/CRtool.php) the amplitude of the signals passing through the filter are not meaningfully attenuated above 1 KHz if at all. The set of three capacitors to ground provided filtering for whatever noise frequencies which may come from the power supply and interfere with the measurement. The power supply itself had a max output of 50 V which is ideal for measurements whereby the bias required to supersede plasma potential may be high.

3.1.2.6 Measurement procedure

The data for these photodetachment experiments were obtained using the equipment described above according to the following procedure. A Hydrogen RF discharge plasma was

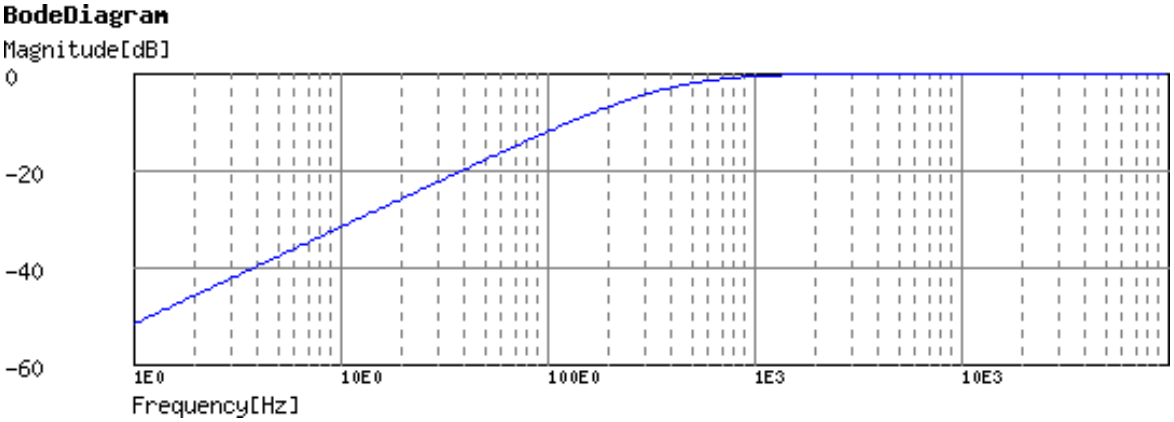

Figure 3.7: High-pass filter circuit theoretical response curve for photodetachment measurements. The signal blocks DC voltage effectively while preserving high frequency features of the signal.

created over the plate of the desired material at a stable pressure (minimum 17 Pa or 100 mTorr). Once the plasma was pulsing correctly, the Hiden ESPsoft software was used to acquire an I-V curve for the pulse at 6ms after the pulse onset using the ESPion hardware. At this point in time the electron saturation region of the I-V curves was less noisy and in principle the electron density should have long since stabilized (shortly after pulse onset [100, 164]). The I-V curve was then used to obtain the value for the plasma potential and thus decide the voltage at which the probe would be biased during the laser pulses. An example of an IV curve taken on the GEC over multiple pulses of the same type is shown below in figure 3.8.

In these experiments, the probe was generally biased at 7 V above the plasma potential (to the nearest volt). Given that the plasma potential was typically around 8 V, this meant a bias voltage (V_{bias}) of 15 V most of the time. With these values of V_{bias}, the measurements took place well within the electron saturation region while the bias was not so high that secondary electron emission effects would have become significant. The I-V curve was then used to record the values of the current to the probe tip at V_{bias} for each set of input parameters. After sampling the I-V characteristics, the probe was disconnected from the ESPion controller unit and was instead connected to the photodetachment circuit pathway (Path B in figure 3.3). The laser was running for the entire duration to allow a consistent output and the acquisition timing staggered such that the I-V data was taken before the laser pulse could affect the conditions local to the probe tip.

For the photodetachment pulse measurements, the minilite laser was timed to fire 6 ms

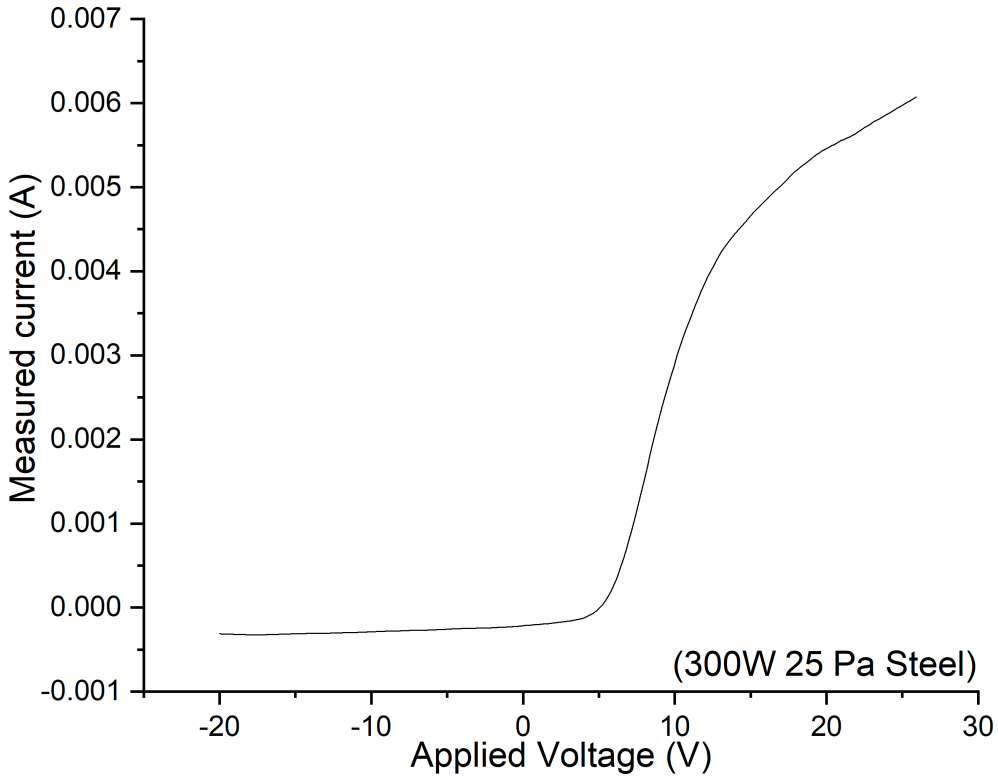

Figure 3.8: Example IV curve from GEC photodetachment experiments.

after ignition as with the I-V curve measurements due the the plasma being in a quasi-steady state. The oscilloscope was triggered by the external sync output connection on the q-switch of the laser consisting of a TTL pulse synchronized with the firing of the q-switch. The signal jitter of 0.5 ns was small enough to ensure reliable triggering. This ensured that the current pulse was always captured on the scope in its entirety. Another option would have been to connect a photodiode and set a trigger threshold however this was not deemed necessary after testing. The scope was set to 128 rolling averages (128 scans with continuously updated average) to reduce noise to an appropriate level. This pulse trace was then saved and processed to obtain the negative ion fraction and absolute negative ion density for each instance of applied power, metal type and pressure examined. An example of a pulse recorded on the GEC setup is shown in figure 3.9.

The probe was cleaned every few scans by heating the probe tip to glow point. This was done by setting a short voltage range in the ESP software between 55 V and 60 V where the collected current was always high and relatively stable. This caused electron current heating of the tip sufficient to burn off the majority of accumulated impurities. These cleaning scans were run until the I-V curve in that small voltage range no longer changed noticeably

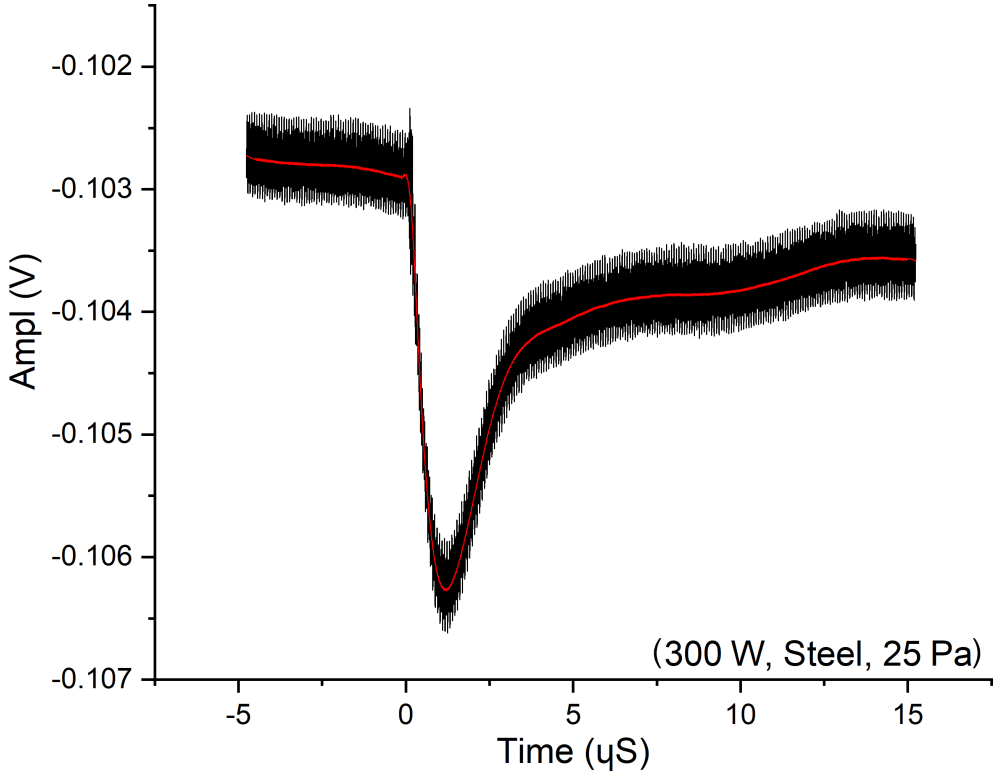

Figure 3.9: Example of Photodetachment pulse on the GEC system for a Hydrogen plasma. The averaged signal is shown as well as the smoothed average.

between scans (typically 2-10 scans depending on contamination level). Cleaning was done in a 500 W CW plasma to speed up the cleaning process using reasonably high electron density and performed for as little time as possible to achieve a clean surface. This was to prevent the tip from losing significant mass and thus surface area which could potentially jeopardize measurement consistency by adding an otherwise avoidable systematic error.

The data analysis was performed in accordance with the underlying theory outlined in section 2.7.2. First, the pulse data were smoothed in python by Savitzky-Golay routine and the minimum in the smoothed curve found by array parsing. This local data minimum was then used as the central point for a second order polynomial fit for 100 data points either side. This was to fit for a more reliable minimum in case some noise remained after the smoothing. The script then asked the user to manually pick a point just before the pulse to use as the pre-pulse voltage value. This was done because the error associated with choosing this point intelligently in this manner was negligible and sped up the analysis. The difference between these two values (ΔV) was then divided through by the load resistance of 51 Ω to get the magnitude of the current pulse (ΔI). This value could then be divided

through by the current value at V_{bias} to get (ΔI/I) which is equal by the diagnostic theory to the negative ion fraction. The errors associated with this value were the 1% error on the current measurement from the Langmuir probe, and the error in the value of the pulse minimum from the polynomial fit. These were convolved for the error in the negative ion fraction.

To obtain the absolute densities of negative ions the electron density was necessary. The Hiden ESPsoft package provides an automatic or semi-automatic analysis tool which analyses the I-V characteristics using orbital motion limited probe theory as discussed in detail in section 2.7.1.6. The use of BRL theory (section 2.7.1.7) was not necessary for consideration here due to the lack of strong magnetic fields. While the electron density was returned by the analysis routine, it was typically less reliable than the ion density which is not as susceptible to secondary emission effects. The positive ion density is obviously related to the negative ion density by:

$$n_e + n_{H-} = n_i \tag{3.1}$$

and the negative ion density could be related to the electron density by the measured fraction values. Thus the absolute value of negative ions was obtained by:

$$n_{H-} = \frac{n_{H-}}{n_e} \times \frac{n_i}{1 + \frac{n_{H-}}{n_e}} \tag{3.2}$$

Worthy of note is the fact that the IV curve analysis had to be conducted with an ion mass of 3 because, as described earlier in section 3.1.1, the dominant ion in GEC hydrogen ICPs such as this is the tri-hydrogen cation; H_3^+. In this regard n_i is the sum of the various positive ion types although this had no effect on the mathematics used in the analysis.

3.1.2.7 Varied parameters

In order to investigate the surface effects in conjunction with the plasma, three parameters were varied independently. Three tokamak divertor relevant materials were chosen for investigation: 304 stainless steel, tungsten and molybdenum. The electrode plates of these materials were each placed onto the lower electrode in turn whereby photodetachment measurements were made for varying RF powers for a selection of gas pressures. The plasma was kept below the H-mode transition for two reasons: the first being that the probe tip

did not survive enough H-mode pulses and secondly because the transition from E-H mode was not consistent between pulses. This would have meant that some pulse measurements would have been made in E-mode and some in H-mode, giving misleading data. By using the photodiode triggering technique it may be possible to record and store measurements from E-mode and H-mode plasmas separately overcoming the reliability issue and obtaining data for both cases at the same time. That is beyond the scope of this work though. The negative ion fractions, electron densities and temperatures, and the absolute negative ion densities were then graphed appropriately to allow for meaningful comparison of any trends with applied power between surface types, and gas pressures.

Some measurements were performed by a colleague (James Ellis) using different diagnostic techniques (PROES and TALIF) which assisted in determining some of the effects and conclusions of this portion of the work on the GEC. This is covered in more detail in the relevant results chapter 4 and the combined work is published in [165]. Any contributions by this and other individuals are clearly marked and credited.

3.2 Experimental techniques performed on the YLPD

This chapter details the design of the linear plasma device as well as the various available diagnostic tools that have been used on this device and their application.

3.2.1 Overview of the YLPD linear divertor simulator

3.2.1.1 Diagnostic port overview

Originally created to study plasma-surface interactions, the York Linear Plasma Device (YLPD - formerly UMIST Linear Device) is a device for the study of fusion relevant Hydrogen plasmas. The device creates and contains a steady state Hydrogen plasma in a column along its axis with the ability to alter the temperature and density. The characterization of the linear device was performed somewhat recently by Branislav Mijalchic [3] which can serve as a rough guide for controlling the plasma, however modifications have been made to the source and power system since then. The plasma formed is a reasonable analogue for the study of tokamak relevant plasma surface interactions as well as scrape-of layer and divertor plasmas. In a tokamak, the plasma is not generally supersonic but due to the nature of the source in the YLPD, the ion species formed can exceed the local sound speed along the

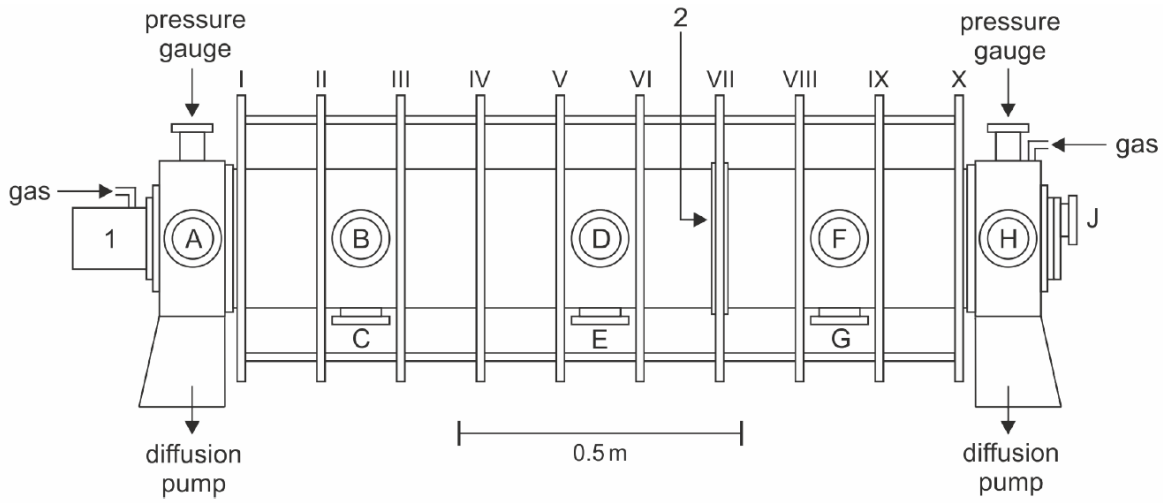

Figure 3.10: The linear device as it appears from the side with [1] the source, [2] the longitudinal position of the aperture, [I-X] are the axial field coils and [A-J] are the available diagnostic ports including opposite ports [A-H] on the far side. Port [C] is occupied by the pumping outlet used to rough the chamber to 10^{-5} Bar

axis [166]. The machine may be operated with or without additional neutral gas flow so as to study the interaction between the plasma and neutral species. These interactions are of importance to detachment scenarios moving forward with tokamak divertor research and development and are the primary subject of study in this work.

Figure 3.10 [76] shows a side view of the linear device wherein can be seen the primary features. The source is a Demirkhanov duoplasmotron source which generates the magnetized hydrogen plasma. This plasma is then accelerated into the vacuum vessel where it is contained by a series of ten water-cooled axial field coils in two sets of five. At ≈ 58 cm from the inside of the target plate, in the plane of coil 7, the plasma passes through a tapered aperture which separates the chamber into what is known as the target chamber. This creates two distinct regions whose plasma conditions may be significantly different, mimicking an upstream plasma in a similar fashion to the scrape-off layer and protecting the source. The plasma impacts on the floating steel target flange which typically houses a small, offset window for viewing into the diagnostic chamber. The vacuum vessel is 1.5 m long and 24 cm in diameter, made from stainless steel with occasional access ports at the positions marked in the figure.

The field coils are each comprised of 18 turns of hollow copper tubing through which cooling water is fed at 3 bar. These coils carry currents ranging up to 650 A that produce axial field strengths up to a theoretical limit of $\approx$ 110 mT but in practice 90 mT (900

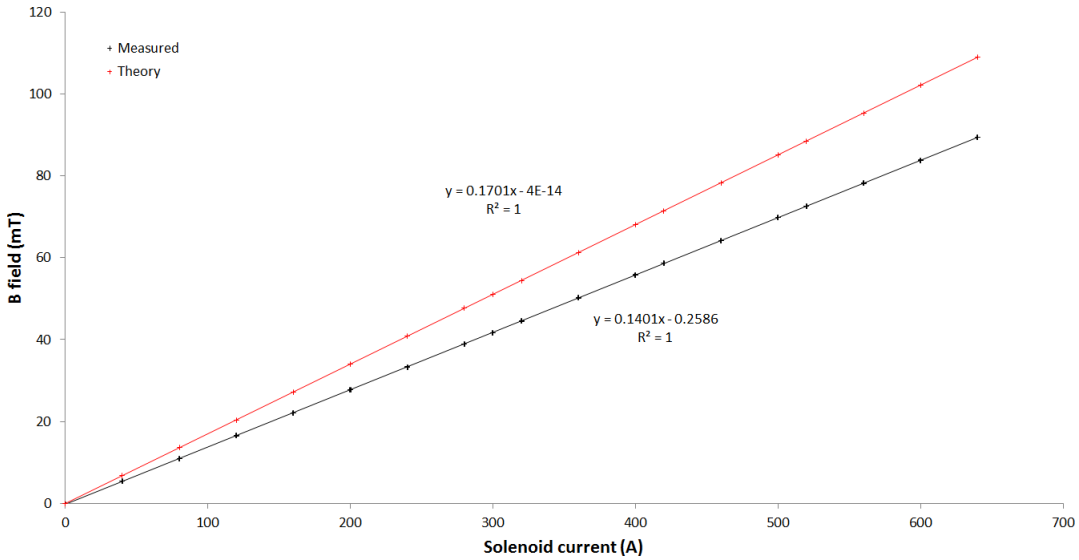

Figure 3.11: The Theoretical and Measured values of the axial field as a function of the coil current. Measurements taken 20 cm inside the target chamber (between coils IX and X).

Gs) shown in figure 3.11. This theoretical limit assumes that the coils act as one 180 turn uniform solenoid with no spacing over the 133 cm distance between the first and last coil. The distribution of the coils in discrete segments spaced 145mm apart and their age likely leads to the discrepancy in the field strength. There is an error field which is created due to the bus bars connecting each set of 5 coils in series however this is largely removed by a return buss that runs in the reverse direction.

There are two pressure gauges, one at either end as shown in the diagram. The gauge at the source end is an Edwards WRG-S ion gauge with a TIC instrument controller 3 - D39700000 which is suitable for measuring the base pressure without plasma or feed gas. The gauge at the target end is an Edwards APG-L-NW16 Pirani gauge connected to an active gauge controller - D386540000. This gauge is used during operation because the target chamber section pressure is not necessarily equal to the pressure in the rest of the vacuum vessel when the plasma is running with higher gas influx to the target chamber through the secondary input valve.

Rough pumping of the complete chamber is provided by two rotary pumps which reach a backing pressure of 2 Pa after which a pair of 300 ls^{-1} diffusion pumps bring the base pressure down to 200 μPa (minimum). Without the plasma ignited, the initial pressure before breakdown is between 8 - 12 mPa. The upper limit on the target chamber pressure is the operational limit of the diffusion pumps before oil back-streaming which is around 10

Pa.

3.2.1.2 Plasma source

Figure 3.12 shows a schematic of the plasma source found on the YLPD and further detail on its operation may be found in [14] and [3]. A brief overview of construction and function is given here for context and a basic understanding of the origins of the upstream parameters.

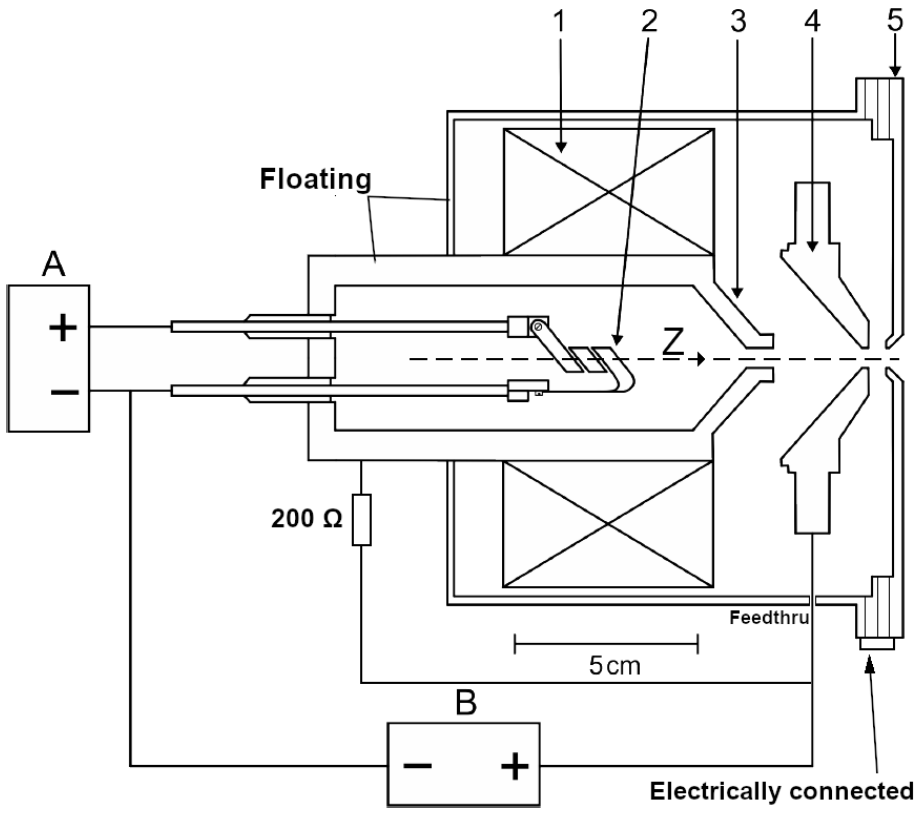

Figure 3.12: A slightly simplified diagram of the plasma source installed on the LPD with: (1) the solenoid coil; (2) the filament; (3) the intermediate electrode (floating); (4) the anode; (5) the reflector electrode and outer housing (floating). (A) and (B) are the power supplies for heating the cathode and the DC bias between the anode and cathode respectively. The solenoid coil of (1) is technically outside the housing (5) in the current configuration. A more complex diagram can be found in [3]

The YLPD plasma source operates fairly simply by the heating of a metal cathode to sufficiently high temperatures which causes thermionic emission of electrons which then ionize a hydrogen gas supply inside a powered coil to form a magnetized plasma. In detail, the source contains a filament consisting of a nickel mesh curled into a helix coated with a powder mixture of nickel powder enriched with 10% Barium carbonate and 10% strontium carbonate. This powder is slowly baked onto the filament before being conditioned by using

it to ignite the Hydrogen plasma. The powder mixture provides a highly electron-emissive surface where the heavy elements in particular increase the number density of electrons burned off due to their high emissivity.

Under normal operation, the filament is heated by a $\approx$ 28 A current causing electron emission. The electrons then impact hydrogen molecules dissociating them into atoms which are then ionized forming a plasma. A potential of 100$\rightarrow$200 V is applied to the anode which accelerates the plasma down the vacuum chamber. The source contains an intermediate electrode (3) with a 5.5 mm aperture. During use, a potential hill (see figure 3.13 for a sketch) forms between the anode and the intermediate electrode that reflects low energy ions formed on the cathode side of the hill back towards the cathode. This bombardment causes additional heating and thus further emission from the surface, increasing the efficiency of the source. The floating reflector electrode reaches a similar potential to the intermediate electrode which traps a population of electrons with then oscillate, improving the gas ionization efficiency on the anode side of the potential hill. Ions formed on this side of the potential hill are accelerated through by the anode, out of the source into the main chamber.Electrons ejected from the anode region can drag ions with them in order to maintain quasineutrality along with the ions ejected by the accelerating anode voltage.

Around the intermediate electrode and anode is a magnetizing coil consisting of 25 turns of copper wire over approximately 8 cm holding a 300 A fixed current, which pre-magnetizes the plasma before it is injected into the main chamber. This improves the heavy ion fraction and the total number density of ions emitted by the source as well as keeping the plasma away from the walls reducing wall recombination events.

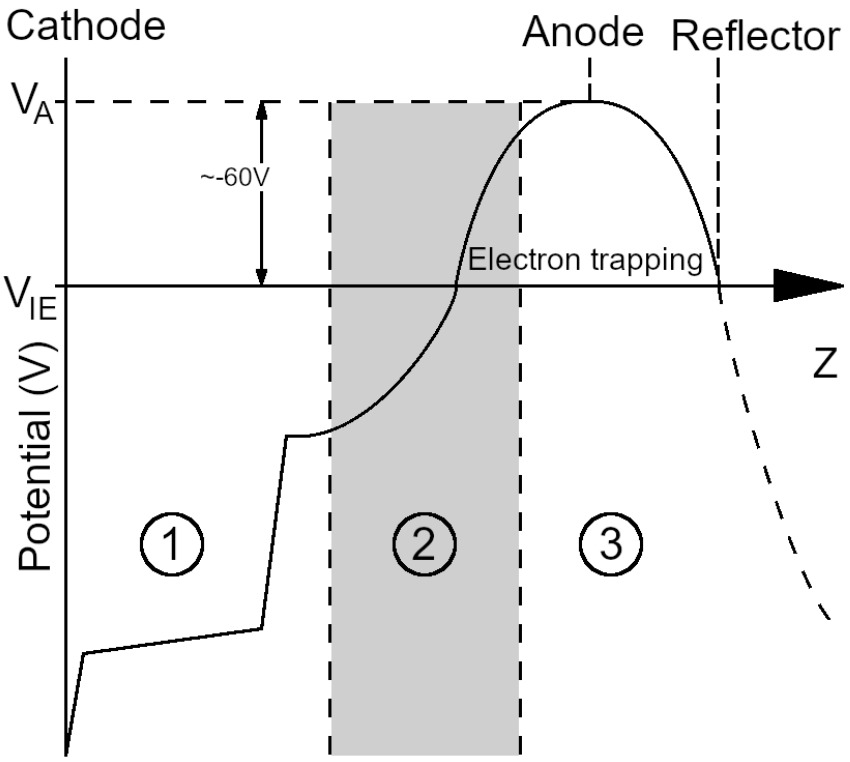

Figure 3.13: Sketch of the axial potential profile in the LPD duoplasmotron source. This sketch is based partly on the potential plots and sketches found in work by Lejeune [13] and Bradley, Forder and Russbridge [14].The three regions are (1): the cathode region, (2): the intermediate region and (3): the anode region. A detailed description of the potential profile in region (1) is found in Lejeune. In brief, these are potential jumps associated with the cathode sheath and a sheath resulting from the constriction of the electron beam by the magnetizing field

3.2.1.3 Source plasma characteristics

Assuming the plasma is completely or near-completely ionized, the electron collision frequency ν_e is given by 3.3:

$$\nu_e = 2.91 \times 10^{-6} n_e \ln(\Lambda) T_e^{-3/2} \ \text{s}^{-1} \ (\text{Hz}) \tag{3.3}$$

where n_e is the electron density, $\ln(\Lambda)$ is the Coulomb logarithm (taken to be 10 [167]), and T_e is the electron temperature. In addition, the electron gyro-frequency or cyclotron frequency is given by:

$$\omega_{ce} = \frac{1}{2\pi} \times \frac{e|\mathbf{B}|}{m_e} = 2.79 \times 10^{10} \ |\mathbf{B}| \ \text{Hz} \tag{3.4}$$

where **B** is the magnetic field, e is the fundamental charge, m_e is the electron rest mass and c is the speed of light in vacuum.

As can be seen in work done by Mihaljcic [3], the upstream electron temperature ranges from 2-10 eV and the corresponding electron densities from 10^{18} to 10^{19} m^{-3}. Assuming these are representative of the values inside the source, the electron collision frequency ranges from 9 or 10 MHz at lower temperatures and densities up to around 40 MHz at the upper limits. The electron cyclotron frequency is around 2.5 GHz (for 90 mT) and independent of temperature and density. In this case is is clear that the magnetization condition: $\omega_{ce}/\nu_e > 1$ holds.

3.2.1.4 Target chamber

The target chamber in the YLPD occupies the last third of the volume of the vacuum chamber. The two are separated by an aperture which allows the target chamber pressure to be controlled somewhat independently of the upstream chamber. The aperture is around 40 mm in diameter compared to the majority of the plasma beam which is around 20 mm in diameter. This aperture therefore has little effect on the plasma beam profile and the differential pressure between the gas target chamber and the upstream chamber [76]. The target chamber diagnostic ports allow measurements to be made perpendicular to the beam using ports F,H, their counterparts, and port G. A stainless steel flange electrically insulated from the chamber forms the target or plasma stop. Port J provides optical access close to the beam axis and a small crunch seal port on the main chamber target end face allows some access further out.

3.2.1.5 Plasma characteristics

A detailed overview of the plasma characteristics may be found in [3]. Despite some alterations to the source, measurements made in this thesis show that the range of electron temperatures and densities are similar so those recorded previously. Regardless a brief overview of the parameter ranges is given here for convenience. In the upstream portion of the chamber, the electron density varies from 10^{17} up to 10^{19} particles per cubic meter depending largely on the solenoid field, and more weakly on the arc current and intermediate floating electrode voltage. The electron temperature varies between a few eV up to 10-15 eV mostly affected by the intermediate floating electrode voltage, itself a function of the source gas flow

rate. Where the temperature ranges from similar values down to significantly lower values, and the density is lower across a chord perpendicular to the magnetic axis, the electron collision frequency is around 5KHz while the electron cyclotron frequency stays at 1.5 GHz. For the ions, the collision rate is only of the order 100 Hz while the cyclotron frequency is around 830 KHz. Owing to these calculations, the charged species within the plasma may still be expected to be magnetized in the target chamber.

The control parameters in these experiments were chosen based on a MAR case established in Mihaljcic's work reasonably distant from the MAR-EIR boundary to account for changes in the source. The intermediate electrode voltage was kept within the range -64.8 V to -65.2 V to limit the effects of the intermediate electrode voltage on the upstream particle temperature unless variation was desired. Similarly, the magnetic field was restricted fairly closely to 55.8 mT and the arc current to 12 A where the density began to plateau in the previous measurements [3]. Gas flow rates using the source end needle vale range from around 20-40 cubic centimetres per minute as the plasma arc is enabled at 20 sccm and increased as necessary depending on desired plasma characteristics and detachment status. This calibration has not been repeated since D. Forder in 1991 but should suffice for any relevant comparisons as the pressure is more important to the experiments.

3.2.2 Measurements of Ion flux to the end/target plate

In order to characterize the degree of detachment, the ion flux onto the target plate was required. The transition to the detached state is characterized by a peak in the ion flux after a temporary increase which indicates the onset of the dominance of recombination effects (see figure 3.14). While the ion flux has been measured once before on this device, the measurement was repeated for an enhanced pressure range and several solenoid fields in order to more completely examine the flux as a function of pressure.

Because the target plate flange of the YLPD is isolated from the rest of the chamber, it was possible to construct a simple circuit to measure only the integrated ion flux onto the flange. This turned the flange essentially into an oversized planar Langmuir probe. A sufficiently high negative bias ($\approx$ -30 V) applied to the flange allowed measurement of the integral ion current over its surface. The ion current was collected and fed through a circuit shown in figure 3.15. The voltage across the 0.1 Ω resistor was measured using the 1 MΩ termination on a Teledyne Lecroy wavejet 354 A. The ion flux in 3.15 was obtained by

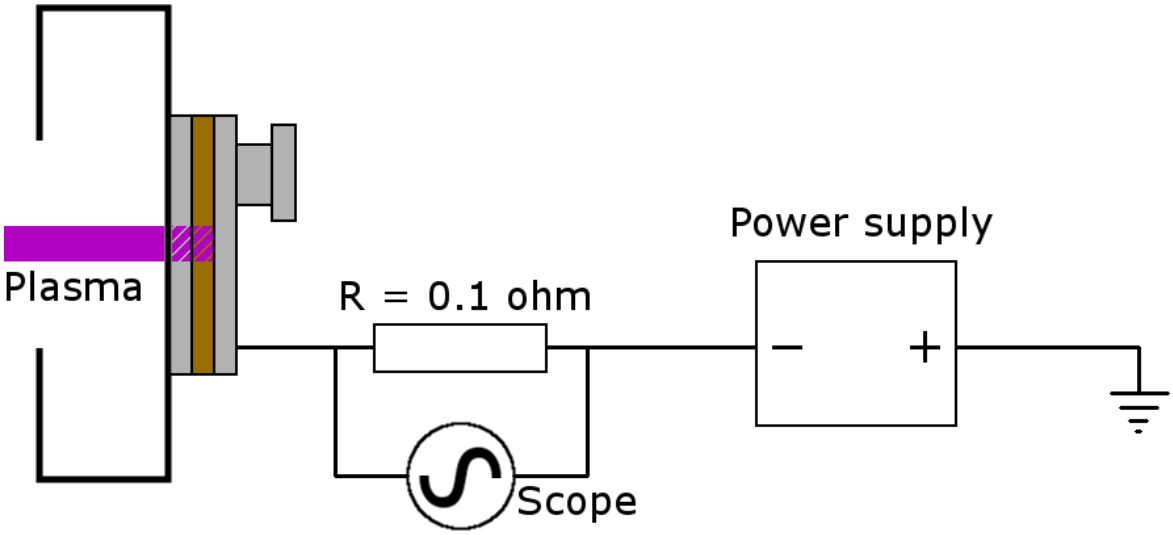

Figure 3.14: Ion flux measurement circuit. The plasma impacts the plate which can be used as a current probe in a similar fashion to a planar Langmuir probe.

averaging the value over a couple of hundred milliseconds of data on the scope to smooth the noise rising from the rapid fluctuations within the plasma.

The current passing through the plate and thus the resistor was calculated by Ohms law and divided by the fundamental electronic charge to obtain the number flux of ions to the plate. Expressed mathematically this is:

$$\Gamma_{ion} = \frac{V_R}{eR} \tag{3.5}$$

These measurements allowed for a basic qualification regarding the degree of detachment while also informing the parameter ranges for following experiments. The result of these measurements is shown in figure 3.15.

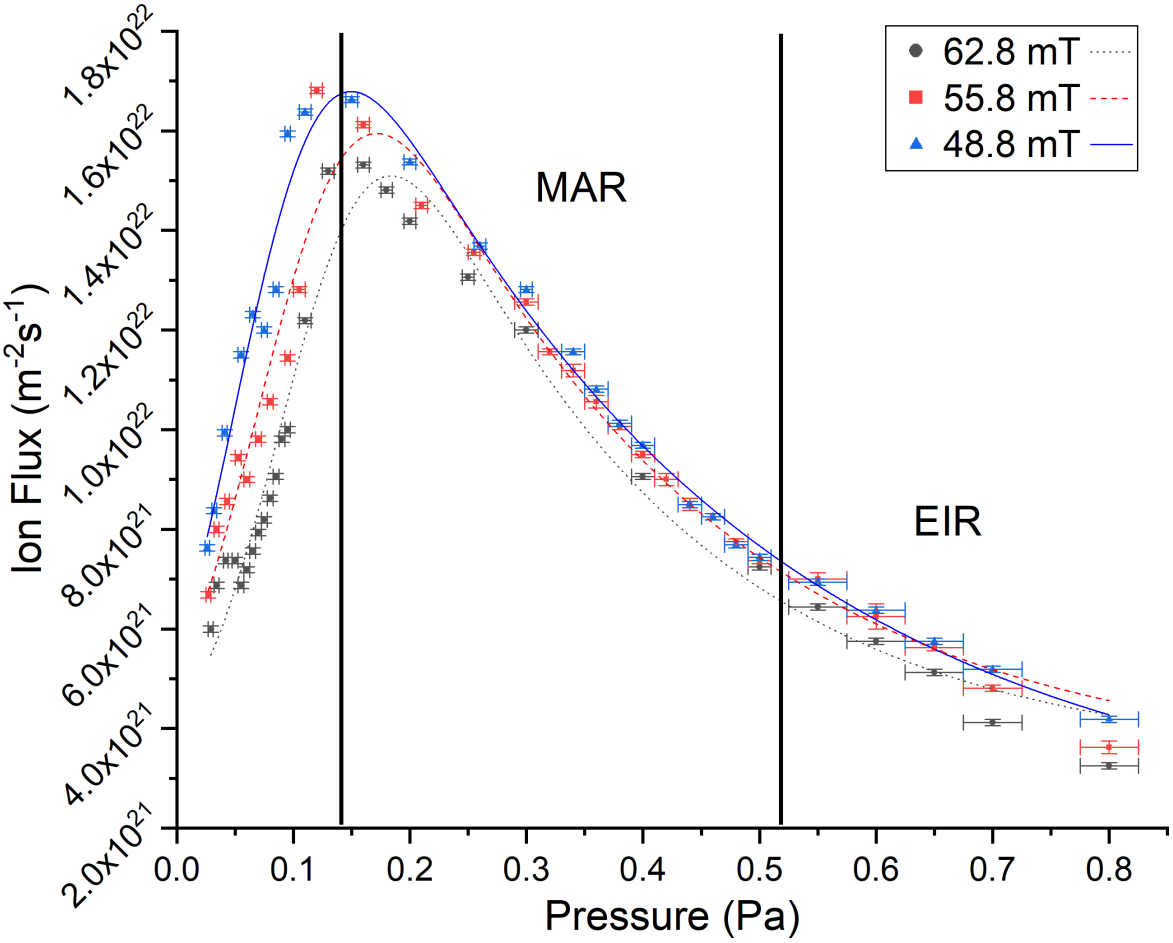

Figure 3.15: The ion flux to the target plate (Ion current available in appendix). This shows the degree of detachment as a function of gas pressure by showing the reduction in ion flux as neutral gas is admitted to the target chamber.

3.2.3 Fulcher band optical emission spectroscopy

In order to obtain some idea of the molecular properties within the plasma in the YLPD target chamber, spectroscopy of the hydrogen Fulcher band was employed. The Fulcher alpha band contains a large number of molecular ro-vibrational emission lines which can be used to infer rotational and/or vibrational temperatures. Due to the importance of the vibrational energy distribution function on the negative ion production process, the vibrational temperature was deemed worthy of measurement. The rotational temperature was also calculated from the same spectral data and provides additional information on the YLPD and comparison with similar experiments.

An example of a Fulcher band spectrum (calibrated for relative sensitivity and normalized) is shown in figure 3.16, the wavelengths of interest are given in table 3.1. It is possible,

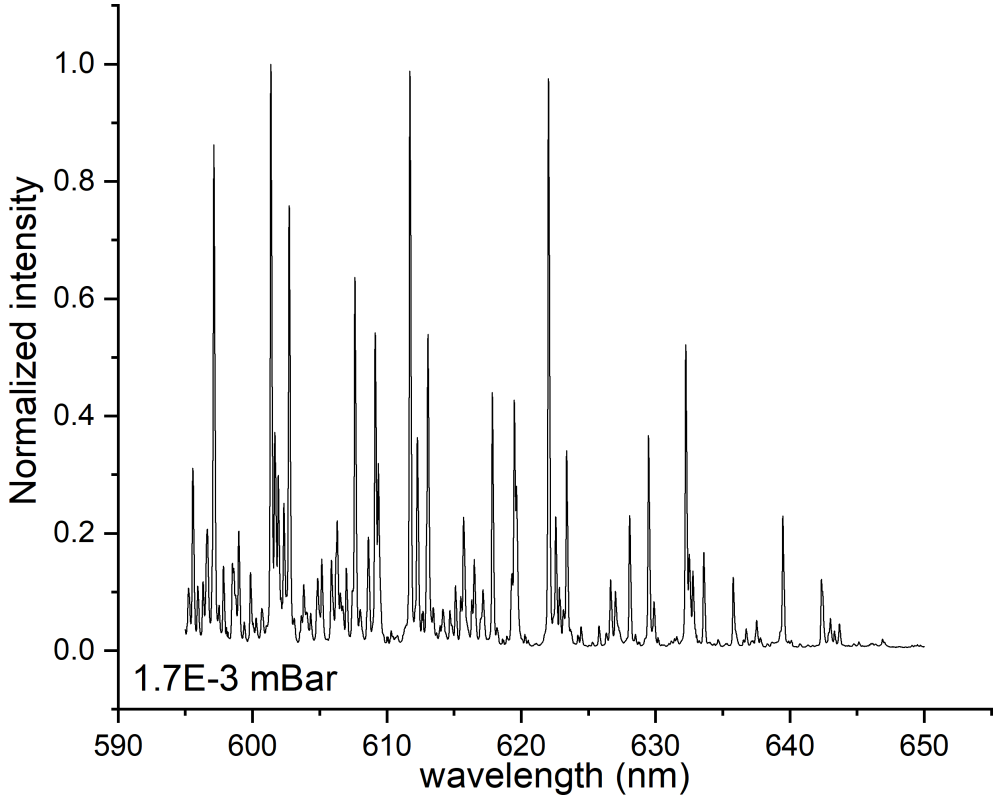

Figure 3.16: An example of a normalized emission profile in the Fulcher alpha band wavelength range taken on the YLPD. This spectral range contains information about the rotational and vibrational conditions of the gas. The rotational temperature can sometimes be used as a proxy for the kinetic/translational gas temperature.

and even likely given lower values of electron temperature, that only the higher vibrational energy levels would be in local thermodynamic equilibrium (LTE). This means that only the higher levels may be fit with a Boltzmann analysis. Comparatively, because the rotational levels are only a small distance apart in the energy domain, they are more likely to be in equilibrium with each other, meaning a Boltzmann analysis to determine the rotational gas temperature was easier to apply. The example spectrum shows that the population of the first three levels were likely not in equilibrium as their intensities are similar by inspection.

The spectra were obtained using a Princeton Instruments Isoplane SCT320 Czerny-Turner spectrometer connected to a ProEM 512 EMCCD camera. The light was collected by a 25.4 mm diameter, 50 mm focal length collimating lens focused onto a 1mm single fiber such as in figure 3.17. The lens improves collection efficiency of the apparatus, reducing the exposure time required, increasing the signal to dark current ratio. The grating/spectrograph used had with 1200 lines per mm, blazed at 500 nm. This is the middle option of the three

available in the SCT320 in terms of resolution; It was chosen due to the aberrations present in the installed 2400 lines per mm grating which made its spectra more difficult to interpret.

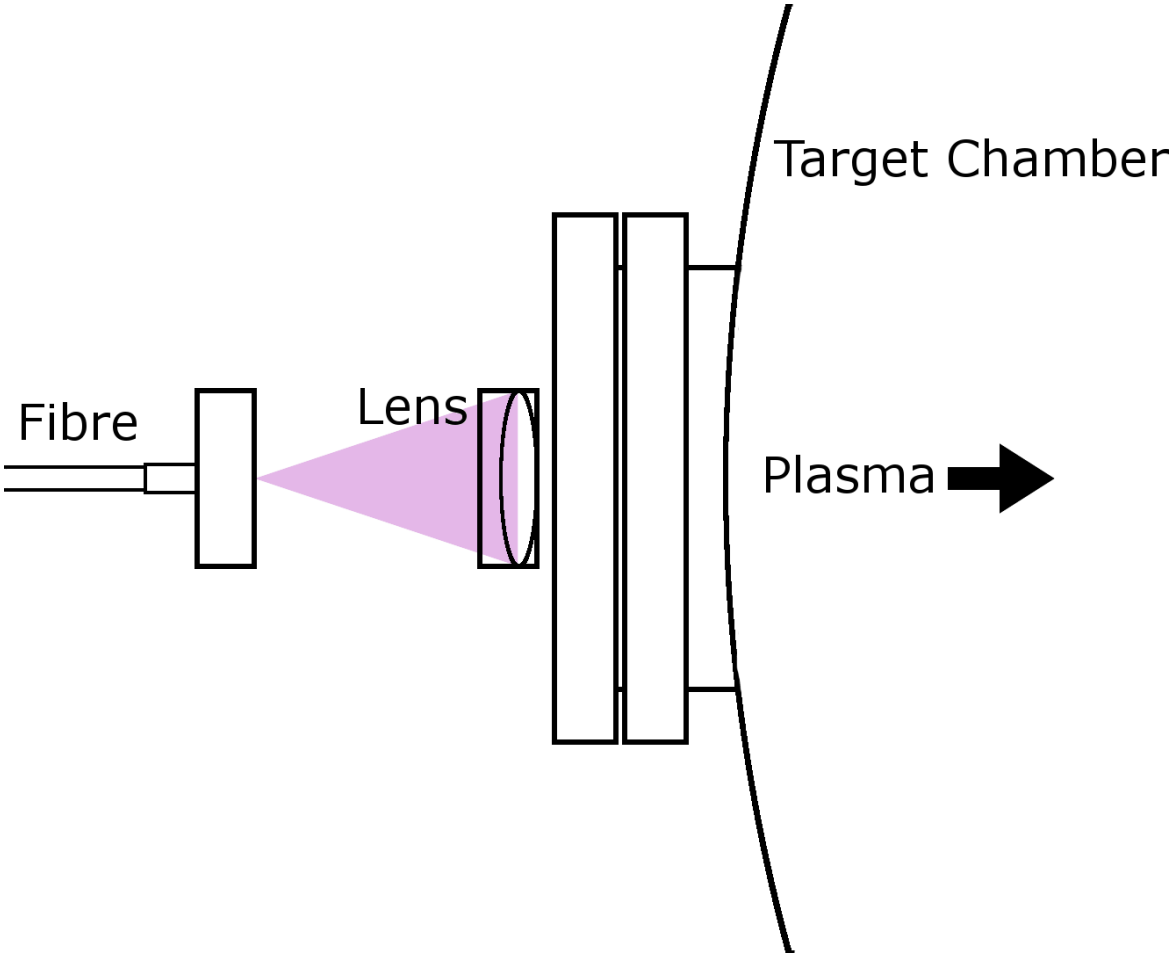

Figure 3.17: OES collection optic and fiber position. This simple setup was used to collect OES data where the lens served to improve signal to noise ratio.

Some additional spectra were taken at a later date at higher resolution to undergo a more advanced analysis for vibrational temperature measurements to go with the negative ion profiles measured. These measurements were taken using the same lens, coupled into a fiber bundle leading into an older Princeton Instruments 320 Pi Czerny-Turner spectrometer fitted with a PiMAX ICCD intensified camera. Spectra were taken this way at several pressures between 0.03 Pa and 0.5 Pa and the estimated temperatures can be seen in section 5.2.2.2. This was done because the increased resolution was necessary for the analysis. Ideally, higher resolution and longer total exposure would have provided more optimal spectra for analysis, however the means with which to do this were not present currently at the YPI.

3.2.4 Fulcher band rotational temperature analysis

The Fulcher band spectra taken initially were analyzed for rotational temperature according to the procedure explained here. The fiber-spectrometer-EMCCD calibration was already performed to correct for the relative intensity as a function of wavelength. The calibration was performed with an ocean optics calibration source connected directly to the spectrometer in question. The lamp had a known spectral power output close to that of a blackbody so the relative emission as a function of wavelength was well defined. By comparing the spectrometer measured value of the lamp to the known output, a wavelength calibration could be performed for relative intensity.All analysis was performed on relative-intensity corrected data, not absolutely calibrated data (exact photon output not accounted for due to difficulty of implementation).

The 0-0 and 2-2 bands were chosen for analysis due to the relatively small number of interfering peaks near those of interest. This also allowed a cross-comparison of rotational temperatures as functions of pressure according to two bands. The wavelengths of the Fulcher Q-band peaks used are shown in table 3.1.

Rotational level ↓ / Band →	0-0	1-1	2-2	3-3	4-4
Q1	601.83	612.18	622.48	632.87	642.80
Q2	602.38	612.72	623.03	633.42	643.30
Q3	603.19	613.54	623.84	634.24	644.10
Q4	604.26	614.62	624.92	635.34	645.10
Q5	605.55	615.96	626.25	636.72	646.40

Table 3.1: Fulcher band transition peak wavelengths (nm) (v_f=v_i). The exact wavelengths reported may differ slightly from source to source within the literature.

The rotational peaks from the 0-0 and 2-2 bands were fit using Voigt curves to account for aberrations which may make the peaks less Gaussian in nature.These fits were then integrated to obtain the total number of relative counts for each peak. Each peak was then plotted point-wise as a function of its corresponding ground state energy in accordance with the theory from section 2.7.3.2. The error in each integral was obtained from the curves plotted using the diagonal elements of the co-variance matrix of the Voigt fit. These two curves represented the maximum and minimum extents that the fit could reasonably be expected to obey. This resulted in a set of five points with error bars which could be fit with a straight line such as the example shown in figure 3.18 for 0.12 Pa. The gradient of this line was then used to find the temperature in accordance with equation 2.72 in section 2.7.3.2.

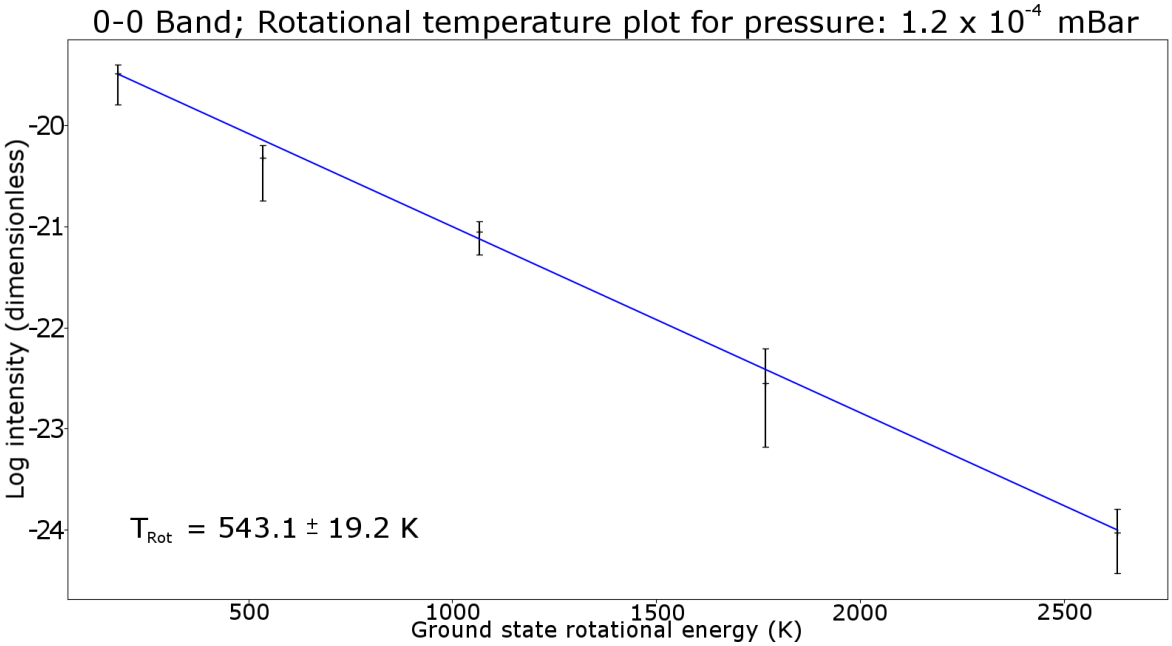

Figure 3.18: Linear fit to rotational band Q-Branch. The fit is good and in most cases fell within the error bars with perhaps one or two slightly outside on occasion.

3.2.5 Core electron density and temperature measurements

Measurements of the core electron temperatures and densities were made to show the differences between the undetached and MAR detached plasma, specifically the 0.25 Pa case visible later in section 5.3.1. These measurements were made with an existing movable Langmuir probe shown in figure 3.19. This probe was movable dues to a vacuum compatible set of bellows and a motorized threaded section. The motor moved the probe tip linearly 2 mm per full rotation allowing high spatial resolution for the measurements.

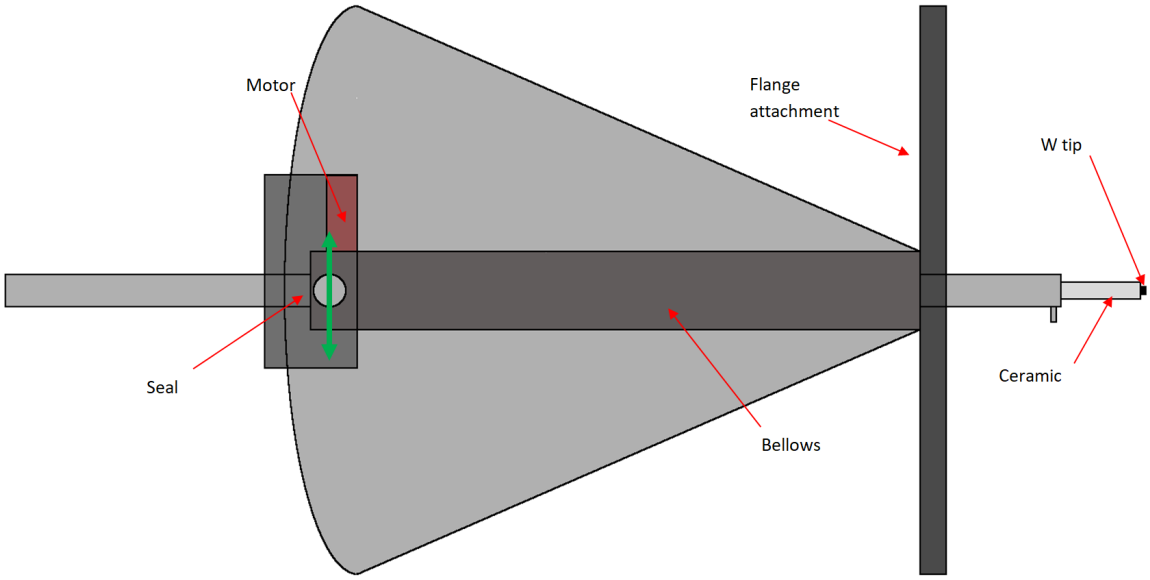

Figure 3.19: The movable probe used in the radially resolved measurements made in the hot, dense core region of the plasma column. The diameter of the tungsten tip ($\approx$ 1 mm) and small profile allowed it to operate in these regions without melting. (Larger cross sectional area allows better heat conduction away from the exposure site)

3.2.6 Linear device laser photo-detachment experiments

3.2.6.1 Overview

The experiments in this section were performed to directly investigate the role of negative ions in detached plasma conditions for a divertor relevant DC glow discharge. As discussed previously, the physics within a detached plasma at various stages is not fully understood. It has been shown however that there are multiple recombination processes which contribute to the decrease of high energy particles in the plasma via radiation and collisions. The net effect of these processes contribute to the neutralization or part neutralization of the plasma,

enabling the detached state and redistributing the deposited power of the plasma over a larger surface area. The primary mechanisms involved are thought to be molecular assisted recombination processes and direct or three-body electron ion recombination processes. The relative contributions of these processes for different plasma parameters are not well understood and a more thorough understanding would lead to optimized divertor operating regimes. The characterization of the negative ions in the target chamber may also improve modelling of recombining plasmas especially those with more filament-like geometry.

3.2.6.2 Custom probe design

A custom probe was required for the photodetachment measurements on the YLPD. This was because the existing probes had unfavourable tip geometry for experiments of this type. The requirements are typically a tip which is relatively long and runs parallel to the axis of the laser beam. This allows a large volume of negative ions to be photo-detached and their electrons be collected by the available surface area in close proximity. The custom probe was constructed by the author and consisted of a relatively simple design shown in figure 3.20. Owing to the DC nature of the plasma source in the YLPD, no radio frequency filtering circuitry was necessary. The probe itself was a continuous tungsten wire (0.1mm diameter) which runs from a dog-legged tip down to a coaxial connector outside the vacuum vessel. The bent portion of the tip which was intended for overlap with the laser beam axis was cut to 10mm long for simplicity of calculations. The wire was encased in a thin alumina capillary which extended most of the way along its length to prevent signal contamination outside the photodetachment region. The alumina protrudes from a surrounding shielding tube made from aluminium which was added after similar probes picked up significant noise in the chamber, rendering measurement nearly impossible.

The aluminium shielding significantly improved this aspect of the experiment, rendering the noise component of the signals small enough to average down below the signal magnitude. The aluminium tube was contained within a Pyrex tube which was necessary for creating a vacuum seal to the main chamber. The Pyrex also extended a short distance past the aluminium shielding to prevent direct contact with the plasma. This was to limit the current through the shielding which could create heat build-up that might compromise the sealant compounds used. The probe was sealed with TorrSeal epoxy resin at the back end to a BNC connector with the shielding tube electrically connected to the outer grounding portion of

the connector. This allowed the shielding to be grounded through its connection to any or all of the electronics in the experiment grounded through the mains connection.

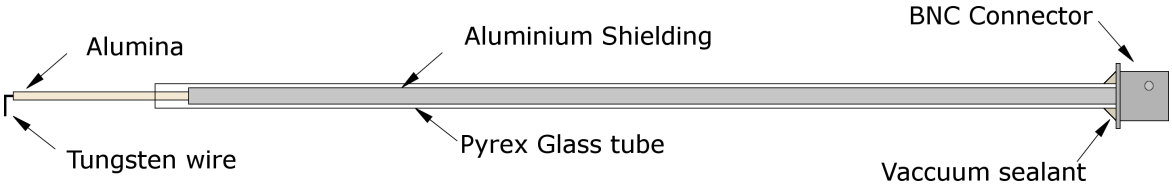

Figure 3.20: In-house manufactured custom probe for photodetachment experiments on the YLPD. The shielding provided ample noise suppression, the Pyrex provided a good vacuum seal and the alumina prevented interaction between other parts of the probe tip and the plasma while shielding from excess heat.

3.2.6.3 Probe location

The probe was housed in an assembly which was affixed to the underside of the chamber between coils 8 and 9 shown below in figure 3.21. This was unfortunately the closest available location to the target plate which had diagnostic access-ways for both the probe and the laser beam. Port H and its companion were not suitable due to the placement of flanges on the top of the machine and the diffusion pump below. The apparatus was attached to the target chamber at the next available valid location allowing for measurements involving varying neutral gas pressure. This was ≈ 250 mm from the target plate. The laser was thus directed through port F and its opposing flange.

The probe was affixed to the target chamber by a pair of Wilson (crunch) seals, one to create the vacuum seal and a second one to provide rigidity along the probe (figure: 3.22). These seals were given stability by a simple frame made of threaded steel rods to restrict the tip from moving between measurements. This probe assembly design was simple and thus had the drawback of being largely immobile while the LPD was running. This was because when loosening the crunch seal, the chamber pressure would trip the safety features on the pumping system potentially causing damage to the source.

3.2.6.4 Laser pathway relative to probe

The laser used was a continuum minilite 2 ND-YAG pulsed laser with max pulse energy of 27mJ at 532nm and a beam diameter (FWHM) of 3mm. This was the same laser used in the experiments on the GEC, chosen because the pulse energy was sufficient for saturation of

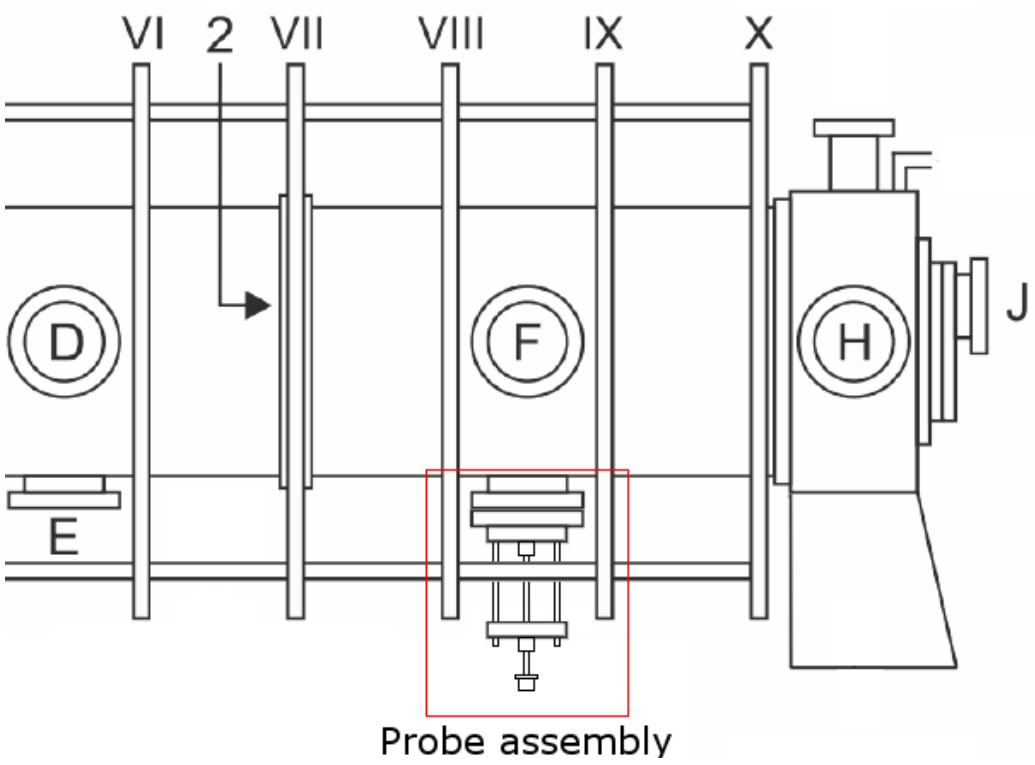

Figure 3.21: Position of PD probe assembly on the LPD zoomed to target chamber end of the device. This is the only viable location as there are no other windows closer to the target plate.

the photodetachment signal with minimal to no ablation effects when hitting the probe tip. It was also relatively simple to align to multiple paths through the diagnostic ports F and its opposite (from figure: 3.21) due to being visible at very low power. The input port opposite F was equipped with a Brewster window at 56.3° suitable for YAG laser throughput. A quarter wave plate just before the window ensured that the laser polarization was correct to pass through and could be changed without removing the window flange. A representation of the beam path relative to the probe, viewed along the YLPD magnetic axis, is shown in figure 3.23.

While in principle, moving the probe was possible between experiments along with re-aligning the laser, this would have been impractical and could have introduced unnecessary additional systematic errors to sets of measurements. It would also have increased the time required to obtain measurement sets significantly. It was, however, of interest to measure the radial density profile of negative ions to obtain a better understanding of the regions where negative ion density was highest relative to the beam. It was also important in un-

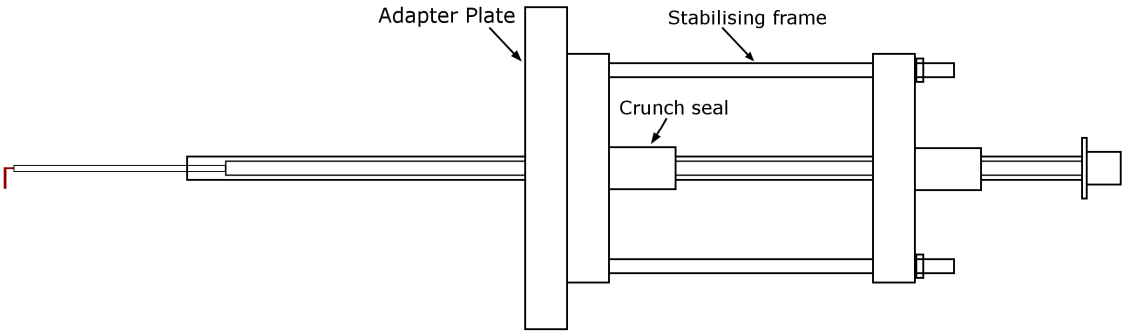

Figure 3.22: Probe mounting frame used to provide rigidity and straight alignment into the chamber. This allowed stable measurements to be made while the plasma moved around the tip.

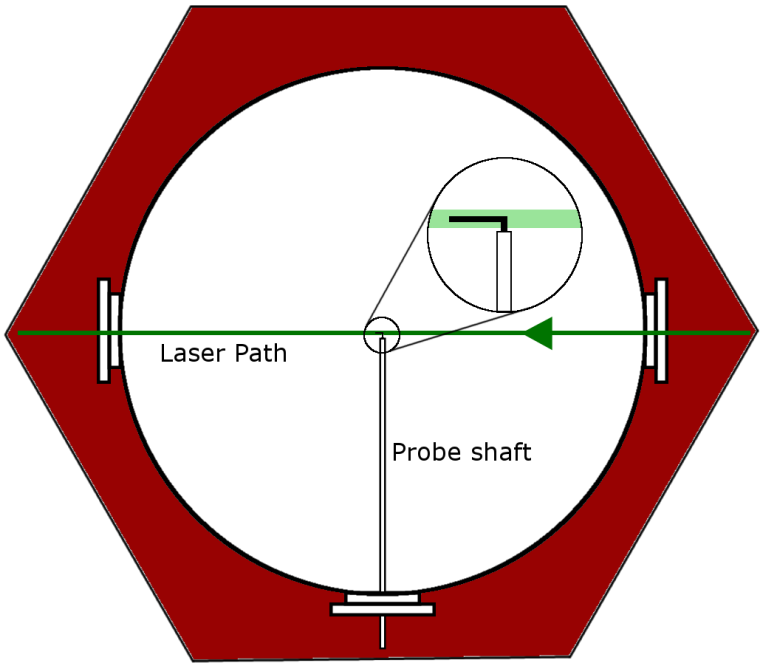

Figure 3.23: Laser path through the YLPD across the photodetachment probe tip as viewed along the magnetic axis. The tip ran perpendicular to the plasma drift velocity vector.

derstanding the effect of the changing chamber pressure and applied field because without spatial information, the data may have been misinterpreted. Thus it was necessary to find a way to make radial measurements without needing to interfere regularly with the probe position and laser alignment between readings.

3.2.6.5 Plasma bending magnet

The solution to the problem was simply to find a means to move the plasma instead. This was achieved by the introduction of a sufficiently strong, movable permanent magnet between two of the field coils upstream of the diagnostic region shown in figure: 3.24. The choice of position was determined by several factors. The magnet needed to be close enough to the target chamber to ensure the plasma had a chance to be displaced before the measurement region. There also had to be enough distance to allow the beam to level off so that it was not significantly curved close to the diagnostic region. The available locations were limited due to the construction of the LPD and the fact that many spaces between the coils were already occupied by pumping equipment. Due to the homogeneity of the field inside a solenoid, the plasma should not return appreciably to its original position on the length scale of the target chamber. The magnet was not placed closer to the source in case of interference with the source itself or in case there was enough deflection to cause plasma impact with the aperture (labelled as "2" in figure: 3.24).

This magnet could be used to create a variable vertical field component in either direction which would pull or push the electrons in the beam. The magnet was placed with its poles facing perpendicular to the magnetic axis of the main solenoid coils. This was done because the bending effect observed was more dramatic over the range of magnet positions available. This is despite the $\frac{1}{r^3}$ falloff in flux density with distance from the magnet versus the $\frac{1}{r^2}$ falloff for the case where the magnetic poles are aligned with the primary confining field. The advantage to placing the magnet horizontally would be a more gentle scaling with magnet position and greater relative beam-bending over the range of possible magnet positions however the beam was not deviated enough in the first instance to make this worth doing.

After displacing the electrons, the ions would preferentially follow the electrons due to a strong electrostatic attraction causing an overall displacement of the beam up or down. This displacement, when coupled with the ability to move the initial position of the probe to anywhere within the field of view of the diagnostic windows (F and its counterpart on the far side), allowed a wide range of radial positions to be examined with minimal reconfiguration of the experimental apparatus.

The bending effect was established through the use of a digital DSLR camera affixed to a post and aligned with the center of diagnostic port F (figure 3.10). By using an early

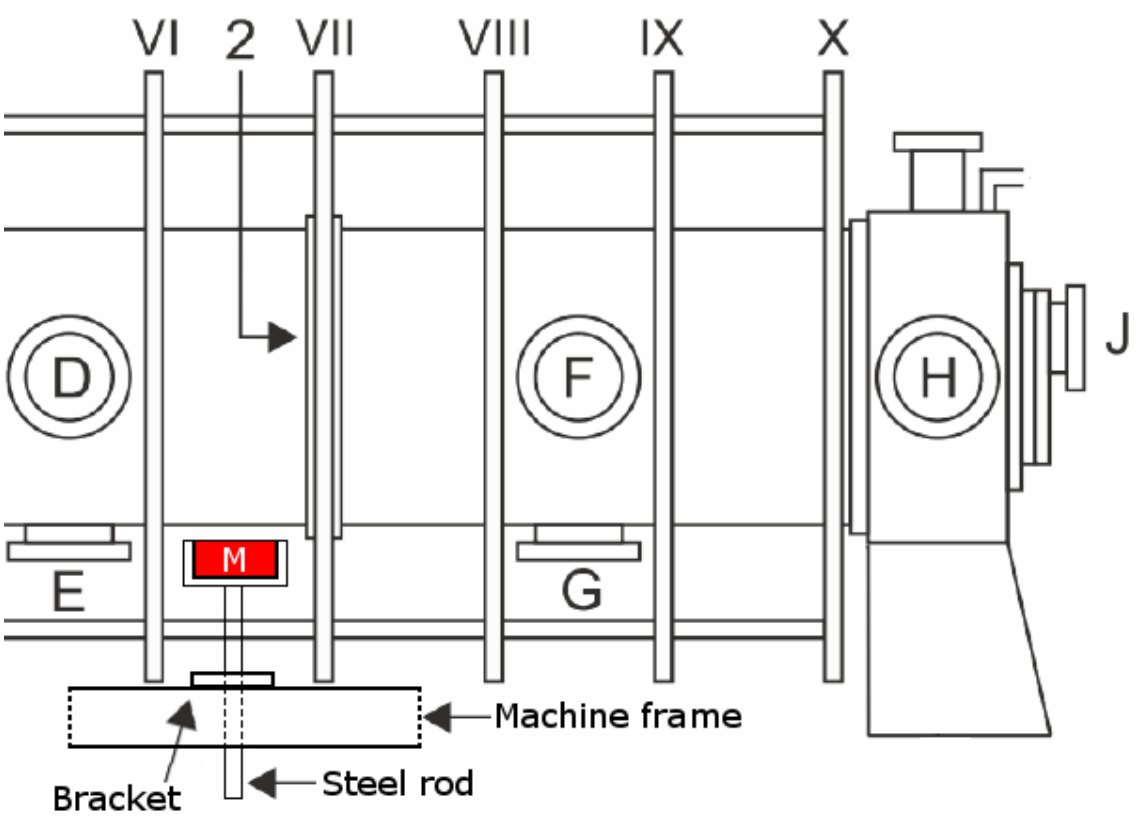

Figure 3.24: Location of bending magnet assembly underneath LPD. The probe mount assembly is not shown in this diagram so as to prevent confusion.

prototype thicker photodetachment probe as a fixed-point in the plane of the plasma column, the relative position of the beam to the probe top or the ceramic shielding could be measured. This was performed by adjusting the camera exposure so that the bulk of the plasma image was not overexposed and taking photographs with the camera in the same place for different positions of bending magnet. In cases where the probe lay inside the plasma, the tip left a wake region where the fast flowing plasma could not effectively refill as shown in figure 3.25. This region appeared as a dimmer spot in grey-value (pixel brightness) than the surrounding light emitted by the plasma as seen in figure 3.26. This light followed a Gaussian-like emission profile consistent with the scale of the beam from other measurements such as T_e and n_e. Thus a Gaussian curve was used to find the beam center while the position of the wake or ceramic was found by inspection to a good degree of accuracy.

For measurements outside the beam, the bright white ceramic could be used as a marker as its grey value also differed significantly from the surrounding pixels also labelled in figure 3.25. The distance from the beam to the ceramic could then be measured. Because the

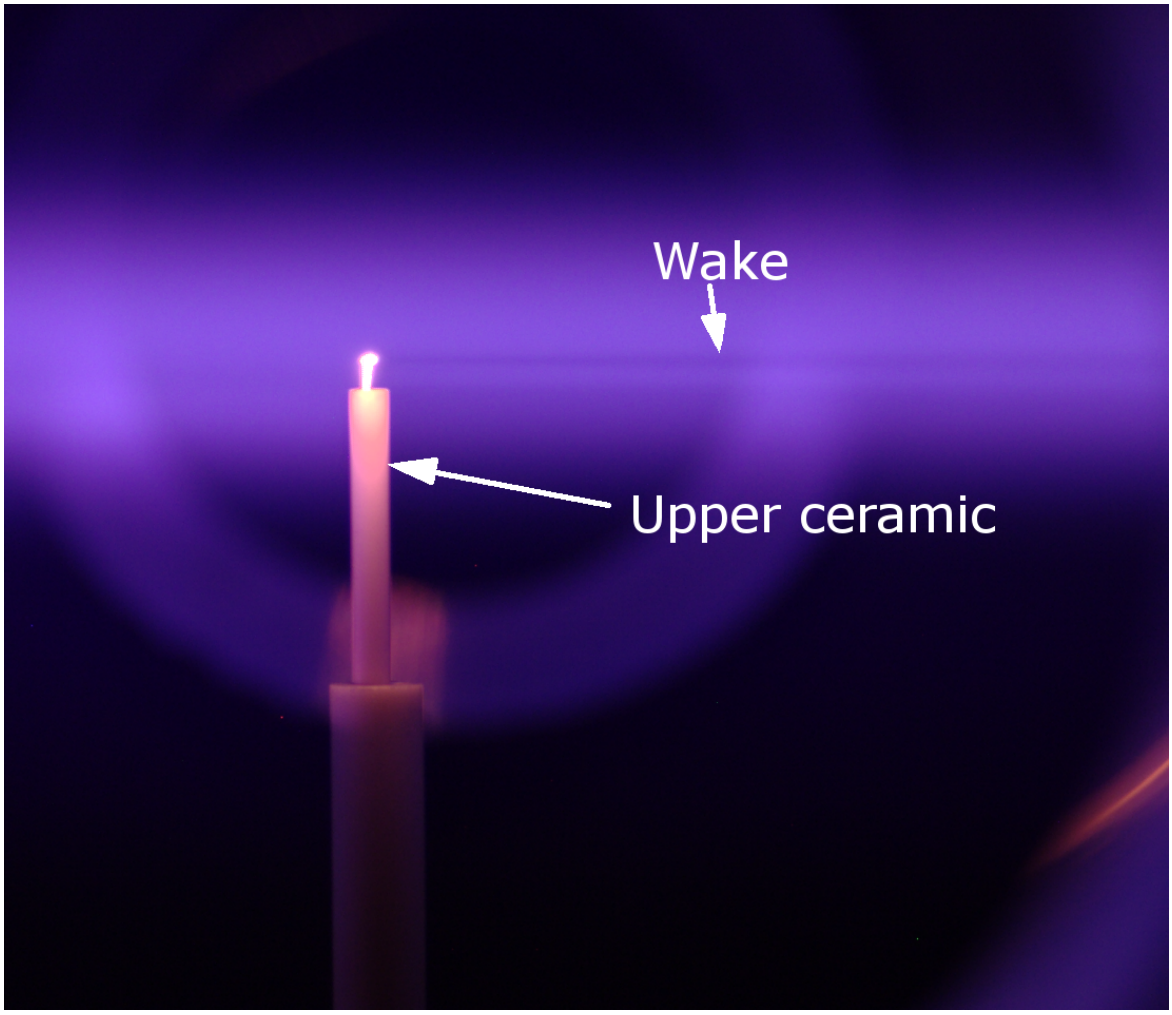

Figure 3.25: Example of image taken while calibrating the bending effect of the permanent magnet. It is possible to see the thin wake caused by the old thicker dog-legged probe which could survive the central plasma regions where T_e and n_e were large.

prototype probe had a dual-layer ceramic shield, the upper portion of this ceramic had a known length of 11.5 mm which could be used to calibrate the pixels/mm value in all of the images. The distance from the probe tip to the upper extreme of the inner ceramic shielding was also known resulting in a common reference point for all measurements. This method was chosen over attempting to later match electron temperature measurements made with the photodetachment probe to those made with the movable probe as this process would have been more subject to error and more time consuming. The exception to this was the low-field negative ion profile which was made after the setup had been disassembled so using the probe measurements was the only available recourse.

It was obvious that the solenoid field magnitude would have an effect on the degree

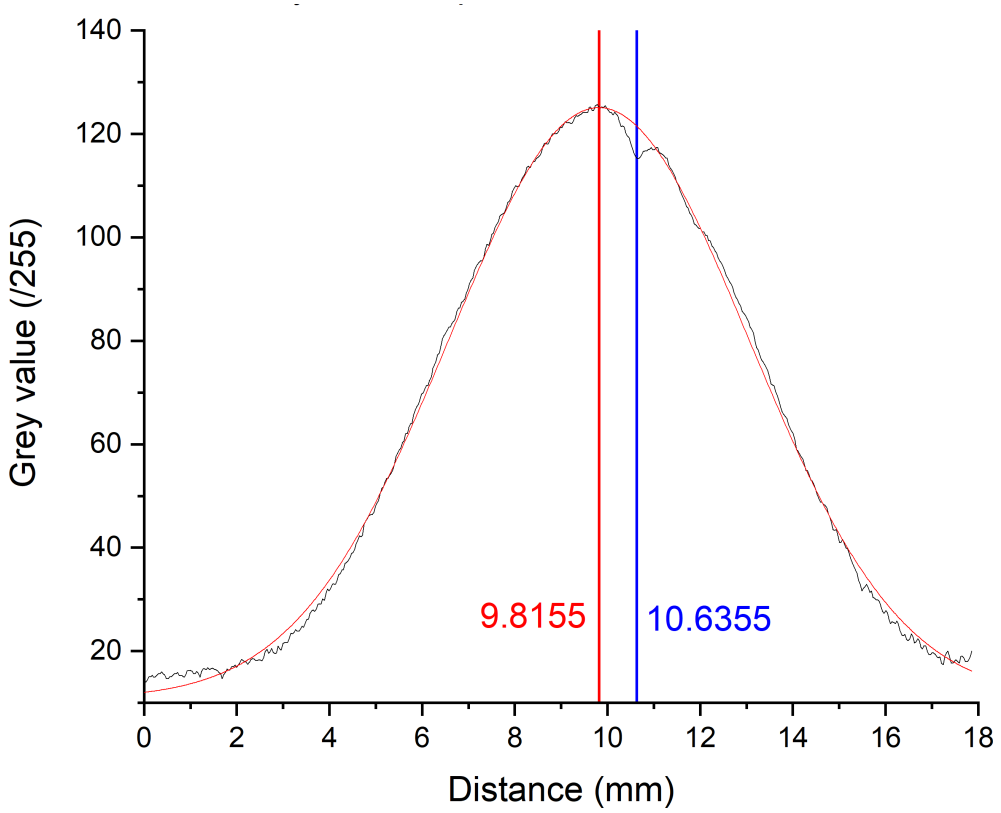

Figure 3.26: The grey value of the beam is plotted and the dip in brightness visible due to the blocking of some plasma flow due to the probe. This dip in magnitude was used to calibrate the probe-plasma position.

of displacement of the plasma and this was quantified for several values of solenoid current including the 400 A value that was used in the majority of the photodetachment experiments. Stronger fields were quantified but ultimately not studied as the primary parameters of interest to begin with were pressure and upstream temperature. One set of measurements was performed for a solenoid current of 300 A but the displacement was not quantified as thoroughly. The result is still displayed although understandably the positional error is larger. The effect of the bending magnet for a 400 A solenoid current is shown in the following figures for both the upwards (push – Figure: 3.27) and downwards (pull – Figure: 3.28) configurations.

While the pushing configuration was examined with gas feed into the target chamber, the pulling configuration was not. This was because the electron temperatures and densities close to the center of the plasma column were expected to be too high for the formation of H- ions regardless of feed gas. This was verified later whereby photodetachment measurements were attempted in and close to the center of the plasma for a few gas pressures and no

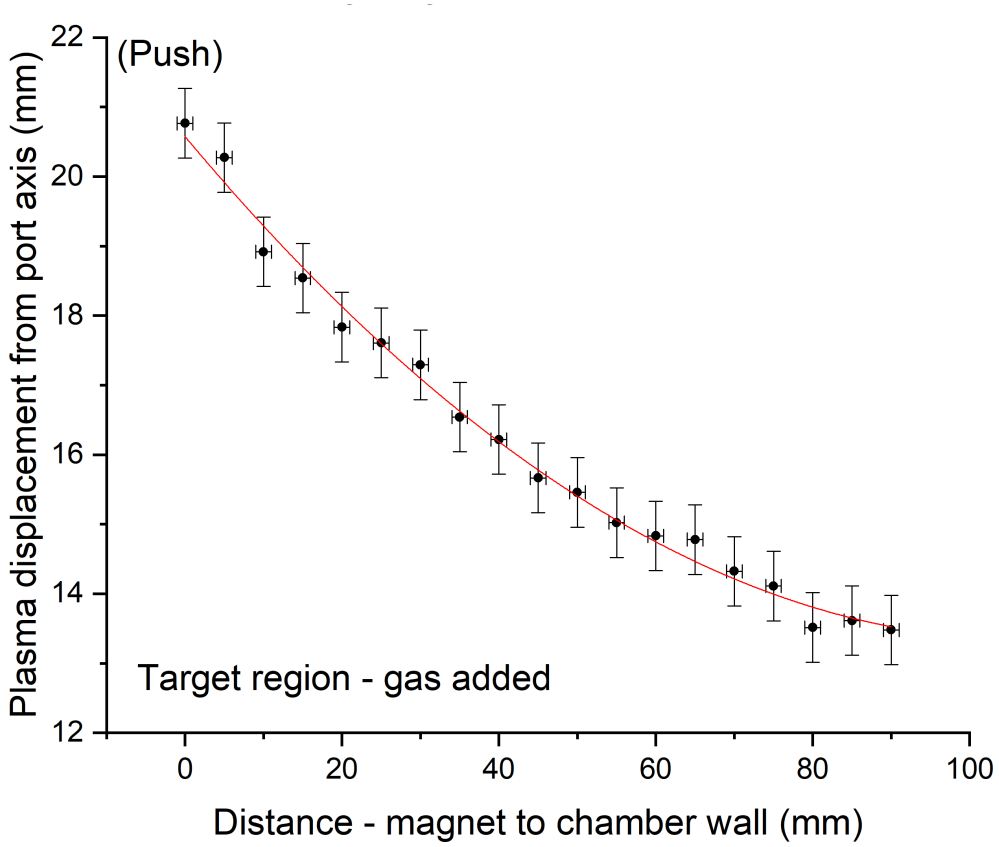

Figure 3.27: Data obtained for calibration of plasma position as function of magnet proximity to chamber in mm with the field pushing the beam upwards. The red line is indicative of the $1/r^2$ theoretical relationship expected of the field strength.

signal due to the presence of negative ions was observed regardless of pressure. It is not unreasonable that given sufficient pressure, some negative ions might be found close to the center, however this would likely be closer to the three body recombination regime whereby the MAR processes would be happening upstream if at all. These higher pressures were not studied at this time.

It was also evident from the calibration that the target chamber gas pressure had a relatively minor effect on the degree of deflection. Figure 3.29 shows the difference in deflection between two neutral gas pressures in the target chamber: one with no additional gas feed - 0.03 Pa and one with sufficient gas to constitute a strong pink glow associated with MAR plasma – around 0.3 Pa.

Separate deflection calibrations were not performed for various pressures because it was assumed that the effect for pressures close to 0.03 Pa would be similar. As a result an error bar of 0.5 mm was added to the radial position values to account for any systematic shift of

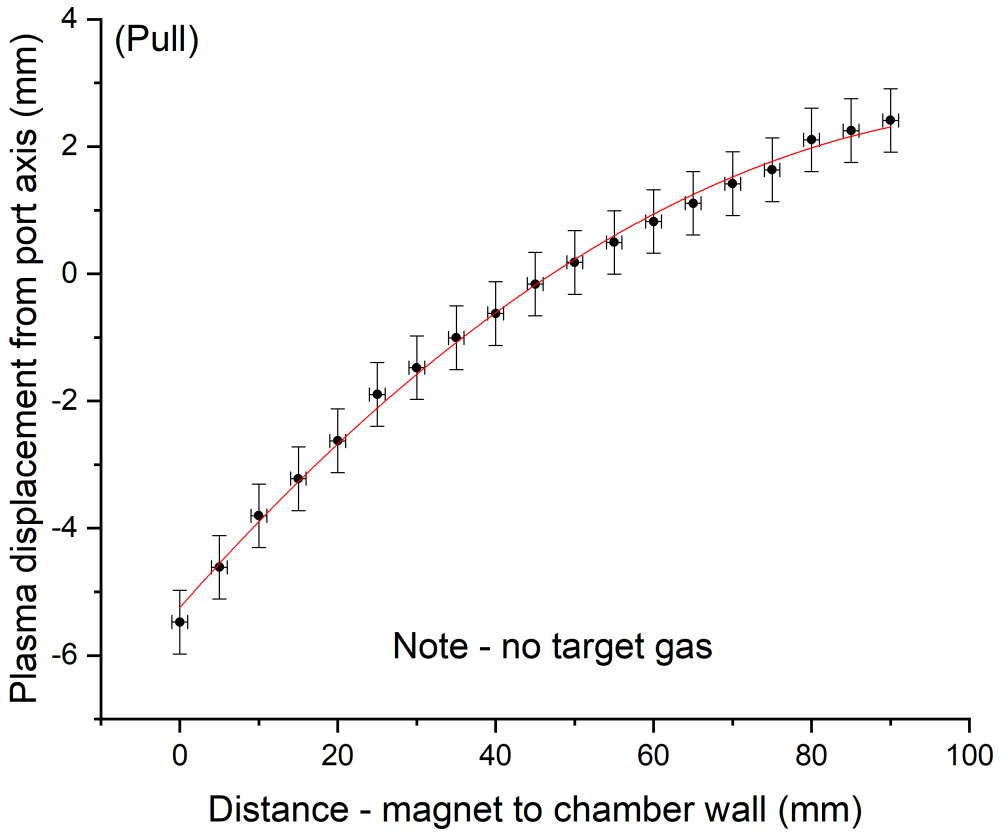

Figure 3.28: Data obtained similarly for the plasma shift with the magnet set to pull the beam downwards towards the magnet.

the deflection curve up or down due to small differences in pressure. The photodetachment measurements were, however, sensitive to this pressure variation and the radial profiles should be reasonably comparable on the calibrated scale.

After a brief initial scan of the positions available with the pushing magnet and the dogleg aligned to the center of the diagnostic ports, it was found that the negative ion signal was significant at all positions. In order to ascertain how the negative ion population varied at distances closer to the center of the plasma, the probe was moved up such that the initial position was offset by -4 mm. This meant that the range available for measurements covered a region closer to the plasma with the magnet retracted out to a larger radius where the negative ion density should be larger. This measurement region is displayed in figure 3.30.

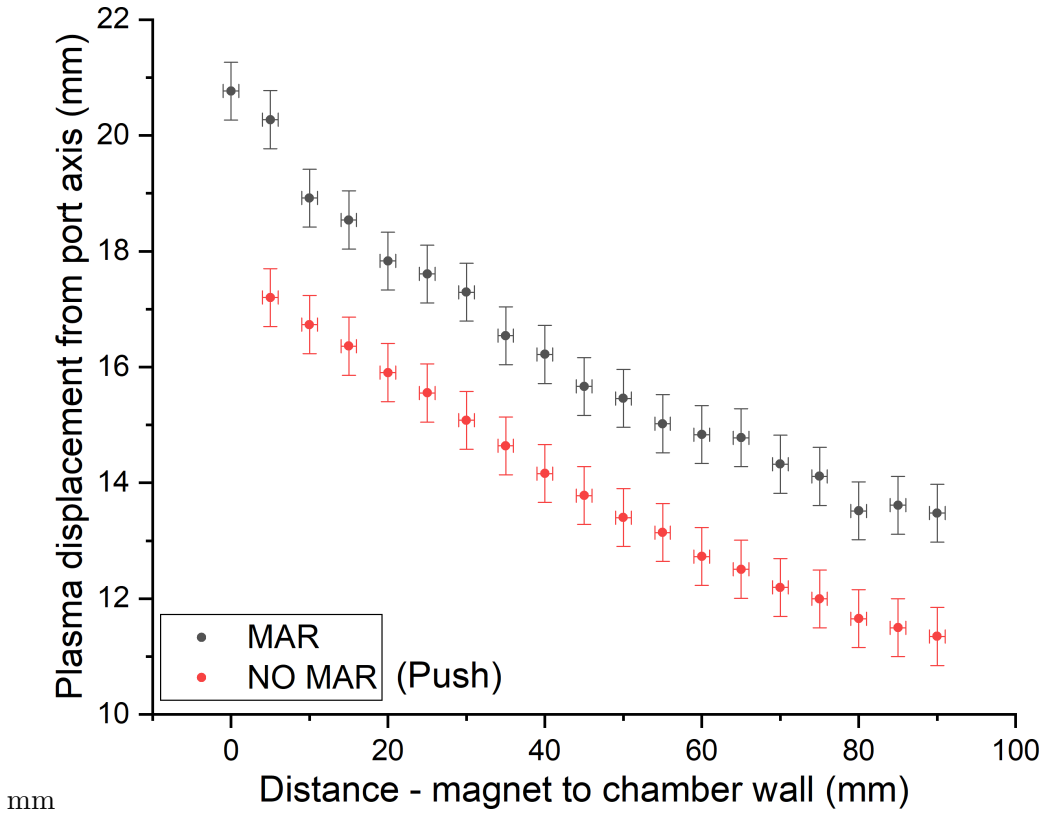

Figure 3.29: Difference between bending magnet efficacy between no additional feed gas to the target chamber and significant gas feed - enough to generate a recombining plasma with significant molecular effects.

3.2.6.6 Circuit

The circuit connecting the power supply to the custom probe and oscilloscope was the same circuit as that used in the experiments on the GEC shown in figure 3.6 from section 3.1.2.5. The oscilloscope was changed to a Teledyne LeCroy Waverunner 304 MXi-A with a higher capacity for averaging to minimise previously observed noise. This assisted the aluminium shielding in removing random noise and improved the signal to noise ratio of the photodetachment pulse measurements. By using a BNC termination on the rear of the custom probe, no adapter was needed for the connection between the probe and the rest of the circuit. Instead the adapter was used to connect the ESPion control unit to the probe for IV curve measurements. The removal of additional connections reduced noise slightly along the signal line when the probe was connected to the pulse acquisition circuit.

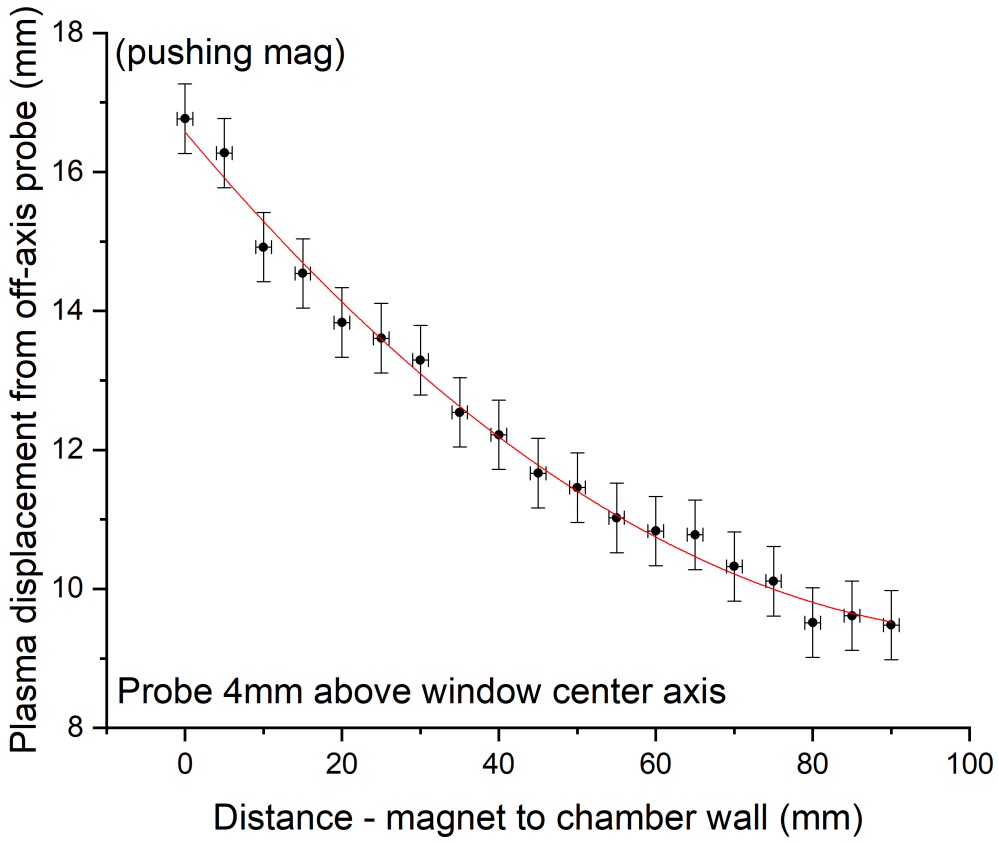

Figure 3.30: Bending magnet - plasma response with offset probe. This additional offset allowed measurements to be made which highlighted the region where the negative ion density should fall off toward the plasma.

3.2.6.7 IV curves

The IV curves for the negative ion measurements were recorded using the same probe before the pulse measurements. This was done using the ESPion probe controller by Hiden in the same way as the measurements made on the GEC with the custom probe. Far from the beam, the electron density was relatively low so the heating effect from high current through the tip could be avoided easily. The IV characteristics for the photodetachment measurements were largely unaffected by magnetization effects present in the central region. This was true regardless of pressure everywhere outside the main beam where collisions and recombination are more frequent events. This made it easier to measure the electron temperatures as the transition region was more sharply defined. Each curve was composed of an average of 300 scans which was then processed using a 25-point wide Savitsky-Golay smoothing operation. While this many points typically introduces noise into the data, the temporal resolution was so high that it was decided this effect would be minimised. A typical curve from the

photodetachment experiment is displayed in figure 2.9 in section 2.7.1.3.

3.2.6.8 Photodetachment pulse data processing methods

An example of a measured photodetachment pulse taken on the LPD is shown in figure 3.31. The initial pulse due to the laser was short, around 200 ns, followed in many cases by an oscillatory decay to pre-pulse conditions. During the pulse there was a fairly well defined noise function convolved with the signal. This was not present without a photodetachment event such as the measurements closer to the plasma or further out at lower pressures (below 0.1 Pa). These observations indicated that the noise was not simply ablation due to the laser or remote pickup from the q-switch pulse. The shielding on the probe and the distance from the laser power unit also meant that this noise was not likely to be caused by other potential nearby sources of interference. Contrary to the measurements on the GEC where it was not present, this additional signal would cause inaccuracies in the pulse measurement and so would need to be removed prior to analysis.

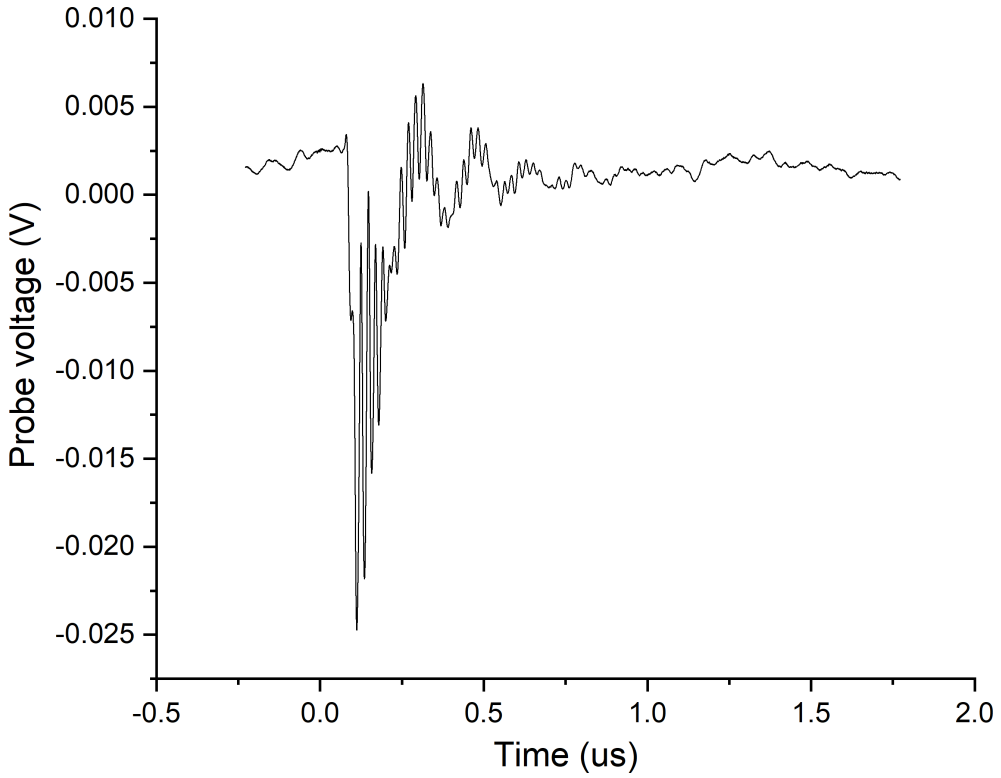

Figure 3.31: Photodetachment pulse obtained from LPD plasma. The noise frequency is visible convolved with the pulse and is not present before the pulse onset. There appears to be some ringing after the initial electron pulse.

The ringing on the pulse may be an artefact of the measurement circuit although it was not observed when used with the GEC cell. This would imply that there is either a resonance between the circuit and the LPD plasma or some other effect. It is possible that the true electron signal manifests at the midpoint of the signal envelope, though this may be at odds with the steep rising edge of the pulse onset. Alterations to the circuit and additional measurements would resolve this ringing issue and clear some additional noise from the signals.

The higher frequency noise signal was removed by applying a band block digital filter in Origin Pro 2019 to each file from ≈ 80 ns to the end of the file. The band blocked was 20 MHz - 100 MHz, chosen after performing a fast Fourier transform on a sample of the pulses and finding the frequency to be around 46MHz. The beginning of the pulse was sufficiently high frequency so as to avoid the filtering while the oscillatory decay also dodged the filter by being too slow. The filtering effect is shown in figure 3.32 as an overlay to the captured signal. Some small artefacts remained after the filtering in some cases because if the bounds were altered to try to compensate, different artefacts were introduced instead, shifting the problem instead of solving it. Either way the smoothed minimum was still good enough to be used in the analysis and was consistent across all files.

The final output of the pre-processing resembled figure 3.33 and could be taken through the rest of the analysis similar to previous experiments. Of note are a few features; the sharp peak immediately before the pulse, when present, was usually an artefact introduced by the digital filter and was ignored when selecting the pre-pulse voltage. While it appeared that the bottom of the pulse was noisy, this was not always the case and was addressed by the polynomial fit anyway. The oscillations from the pulse were higher in frequency and took much longer to decay than those on the GEC relative to the duration of the initial pulse.

3.2.6.9 Analysis and errors

The IV curves were processed by python script to find the current collected at the applied voltage in each position for each gas pressure. These values were then entered into another script that calculated the magnitude of the photodetachment pulse between a user-specified pre-pulse voltage (taken as close as possible to the drop) and the pulse minimum. The minimum was found by allowing the user to define a region within which the minimum could be found, finding the numerical minimum, then fitting a small second order polynomial to

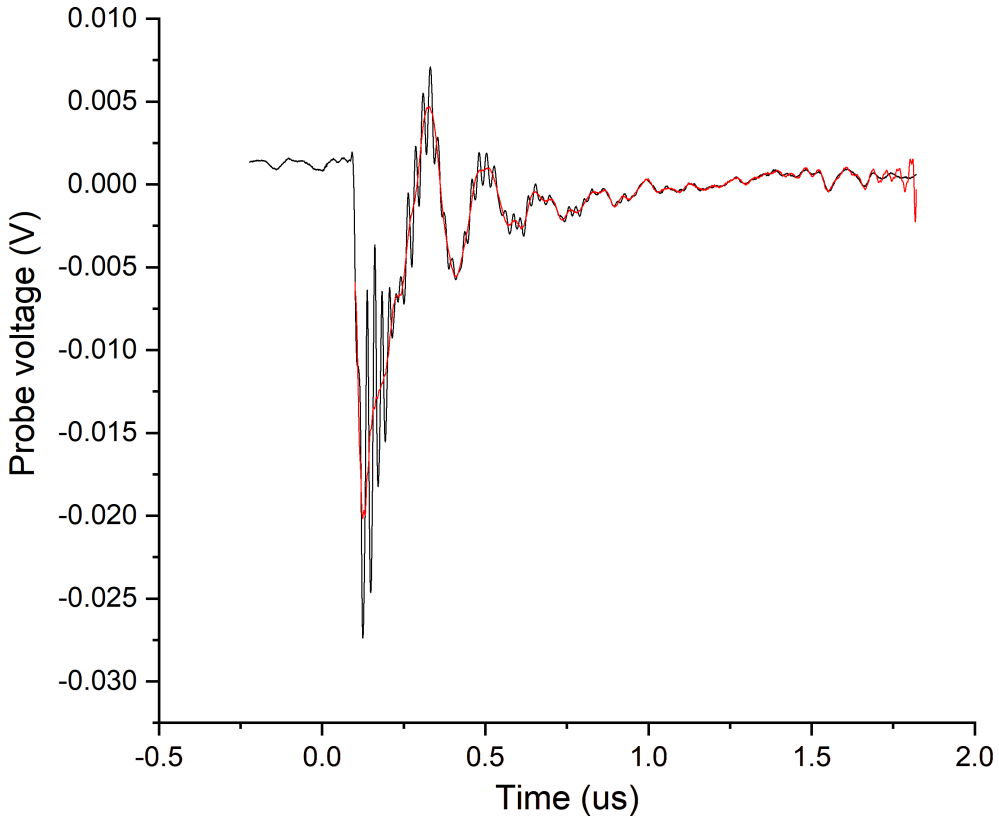

Figure 3.32: Sample of processing effect on photodetachment pulse signal. The digital Fourier blocking filter removed most of the high frequency noise.

the surrounding points. This fit accounted for any remaining noise distortion while also providing an approximate error value to the pulse minimum. The user selection of the pre-pulse voltage also did not add a significant error when compared with the fit to the pulse minimum. The error in the current value extracted from the IV curves was about 1%. This was combined with the fit error to give the error bar for the negative ion fraction.

Electron density values were obtained using the ion densities returned by the Hiden ESPsoft analysis tool. As with the previous experiments, the ion density was used because it is generally a more reliable measurement when using Langmuir probes. Combined with the quasineutrality principle and the negative ion fraction, the electron density could be deduced using the two. To estimate the error in the ion density, 12 measurements were made to represent the various inconsistencies that might arise during the course of the experiment. These were: changing the source-end gas flow to change V_{ie}, changing the target chamber pressure, and changing the magnet position before returning whichever parameter back to its original value as closely as possible. For each case, four curves were taken and analysed.

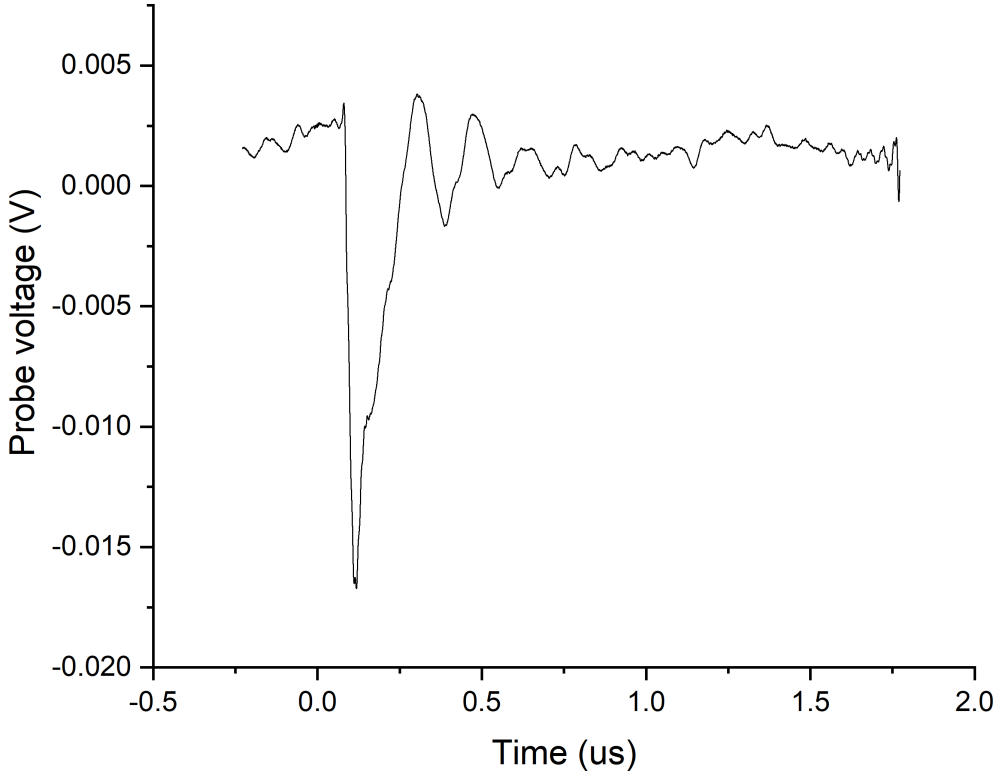

Figure 3.33: The signal after the digital filtering is shown. This was interpreted as an initial pulse followed by oscillations as the plasma returned to equilibrium.

The variation in the ion density was small resulting in an error bar of around 3%. The electron density was calculated in the same way as before, using analysis based on the mathematics found in section 2.7.1.6. The negative ion density was calculated using the simplified expression: equation 2.55 section 2.7.2. As such, for these experiments, the total error in the negative ion density was calculated to be around 3.5%.

Chapter 4

Results of surface contribution to negative ion production in the GEC reference cell

4.1 Overview of chapter

This chapter summarises the results of the experiments carried out on the modified Gaseous Electronics Conference (GEC) cell at the YPI laboratory. This device is generally well characterized making it ideal for studying plasma phenomena with little influence from the geometry and composition of the device itself (given the modifications are not too extreme). The aim of these measurements was to characterise the effect of the material composition of the top surface of the lower, grounded electrode on the negative ion dynamics of the hydrogen plasma immediately above. Measurements were made, using an RF compensated Langmuir probe, of the electron temperature and the ion density. The ion density was then used to infer the electron density via assumed satisfaction of the quasineutrality condition in the plasma bulk. The same probe was used as part of a laser photodetachment experiment to measure the negative ion fraction and thus negative ion density under the same conditions. Specifically, the T_e and n_i measurements were made immediately before each photodetachment measurement for specified gas pressure and RF input power (to the ICP coil), for a select metal plate placed over the lower electrode. Data was recorded for each metal for varying applied power, for several gas pressures.

The effect of the plasma facing surface materials is important to the density and dynamics of species in the plasma. This includes species important to the creation and destruction of H^- ions and the direct production of negative ions on the surface itself. Making an effort to quantify these processes and their respective contributions to the H^- population is important for future device development. It is hypothesized that these experiments may draw attention to the importance of surface material choice in future tokamak divertors, not solely for their thermal properties, but also for their ability to assist in the detachment process by way of enhancing MAR processes.

The plasma was operated in pulsed E-mode only due to the difficulty of consistently achieving a stable H-mode pulse and the resulting damage to the probe tip from repeated exposure to the H-mode plasma. In order to run the GEC in the H-mode, the plasma must first ignite in E-mode before transitioning to H-mode. At higher applied power the E-H transition was identified through the use of a photo-diode and an oscilloscope which showed the emission sharply transition from the lower intensity of E-mode to the brighter H-mode at varying times during the pulse. This was not consistent between individual pulses; some pulses remained in E-mode and these were not at regular intervals. Owing to the unreliable nature of pulsed H-mode plasma and the effects this could have on the measurements, in addition to the survivability of the probe tip, the decision was made to remain in E-mode for all of the measurements performed on the GEC.

4.2 Negative ion results for Tungsten electrode grounding surface

Results are first presented for the measurements of electron temperature and density above the tungsten sample followed by the negative ion fraction and calculated negative ion density. This covers the basic trends observed for one material before examining and comparing to other materials. Unless otherwise stated, trend-lines are for visual purposes and do not necessarily accurately represent physical relations.

4.2.1 Electron density and temperature variation with pressure and power (W)

The electron densities inferred from the measured ion densities as a function of gas pressure and input power are displayed in figure 4.1. For each gas pressure the electron density increased linearly with increasing applied power. This was expected because this linear trend in electron density has been observed before in numerous GEC discharges [158] including in various other gasses such as argon [154], oxygen [126], nitrogen [168], and krypton [169]. The electron density trends shown in figure 4.1 were near identical when comparing 25 Pa and 37.5 Pa. The respective slopes were calculated to be $(8.18 \pm 0.23) \times 10^{13}$ $m^{-3}W^{-1}$ and $(8.35 \pm 0.32) \times 10^{13}$ $m^{-3}W^{-1}$ which agree within error. The intercepts, $(9.37 \pm 0.65) \times 10^{15}$ and $(7.14 \pm 0.94) \times 10^{15}$, were also similar despite being just outside each other's error margins. The 17 Pa data was in relatively good agreement at low applied power (< 500 W), however above and including 500 W, the density curve appeared to show some deviation from the higher pressure data. For example, there is a ≈ 100 W difference between the point at which the 17 Pa data and the higher pressure data reaches an electron density of $\approx 5 \times 10^{16}$ m^{-3}. There may have been some gas heating effects from the inside wall or electrodes leading to early saturation of the density of electrons and ions.

There was some general increase in electron temperature with applied power as shown in figure 4.2, though not dramatically within E-mode. Generally at similar pressures, an increase in T_e may be observed with increased applied power [170, 171]. T_e sometimes does not increase dramatically with power [172] or appears relatively flat [173]. Within error margins, the electron temperature at 17 Pa agreed with a general linear increase with power. This would match existing literature, however it is possible that the beginning of the data follows a flatter profile before transitioning into a linear increase around 300 W. In this case, increasing power may have initially liberated more electrons in line with observations in figure 4.1 however successive increases in applied power struggled to liberate additional electrons leading to the deviation away from the linear trend. Instead, more power would have then been deposited into the already free electrons, increasing the overall temperature of the population at higher powers.

A simpler observation is that the electron temperature generally decreased with increasing gas pressure. Given the similarities in the ion and electron density, the higher density of other plasma species would have increased the collisionality of the plasma leading to a lower

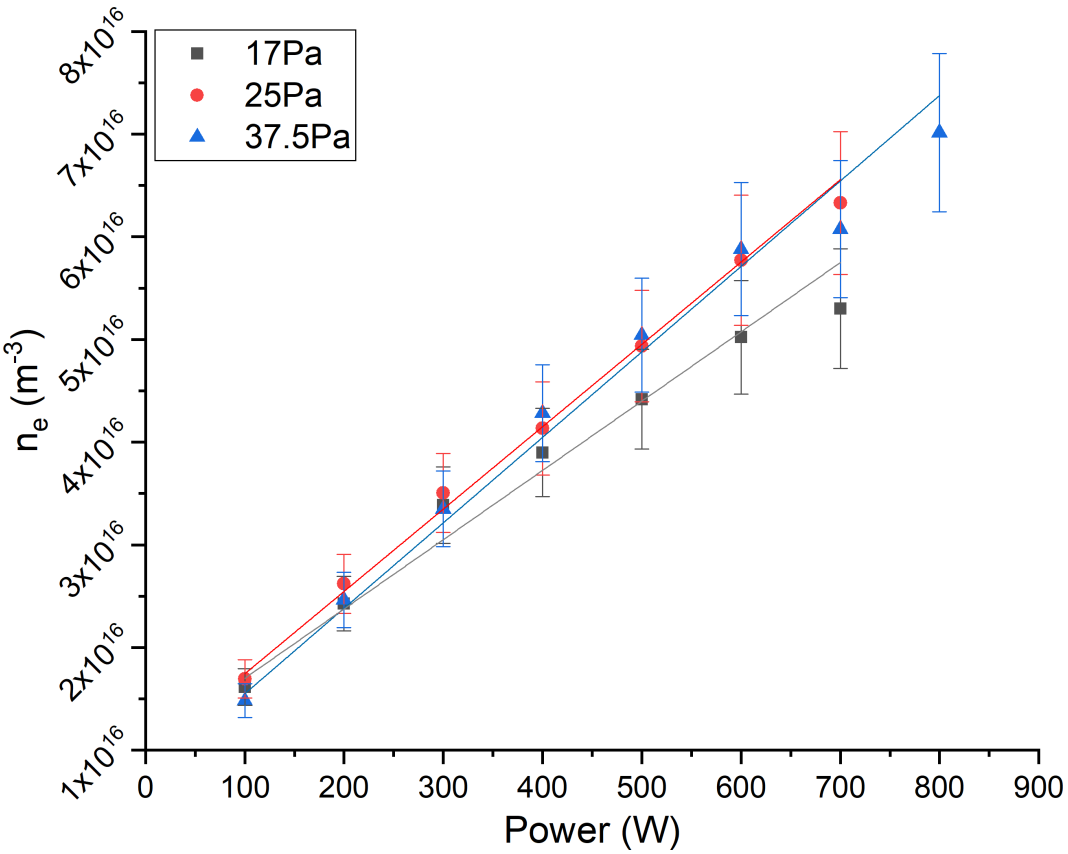

Figure 4.1: Electron density as a function of pressure and power for tungsten plate configuration. The density increased linearly with power for all pressures and was not significantly different for any of them. The fitted trends in this case can be taken to represent the linear increase in electron density with power well documented in GEC plasmas.

electron temperature. Lower electron temperatures would have significantly lowered the rates of vibrational excitation of hydrogen molecules into vibrational states conducive to the bulk formation of H^- ions. Figure 4.3 shows the normalised vibrational energy distribution function of vibrationally excited H_2 assuming a Maxwell-Boltzmann distribution of states for electron temperatures of 1.4 eV and 0.6 eV, based on the electron temperatures in figure 4.2. It can be seen that the relative populations of the levels with higher H^- formation cross sections due to the dissociative attachment (DA) process are significantly higher at 1.4 eV than at 0.6 eV. While the vibrational distribution function is likely not Maxwellian at these electron temperatures, the population of higher V states should hold for $T_e = 1.4$ eV. Because of this, it was expected that negative ion densities would be greater for the 17 Pa and 25 Pa discharges when compared to the 37.5 Pa discharge.

The discussion of the electron dynamics must include a mention of secondary electrons,

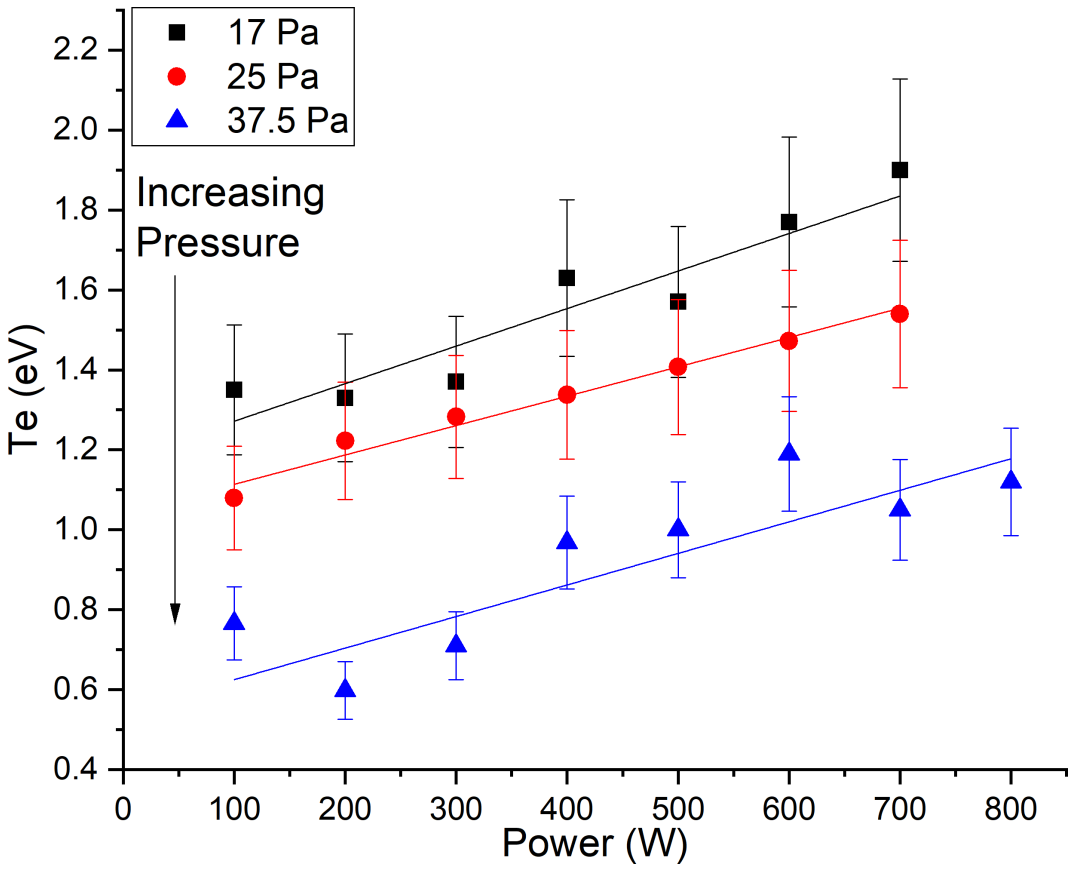

Figure 4.2: Electron temperature as a function of pressure and power for tungsten plate configuration. There was a significant drop of around 0.5 eV across the range of studied power for the higher, 37.5 Pa case. This would lead to much lower rates of vibrational excitation into higher states (V > 3). Linear fits were applied as this was thought to be the most likely underlying trend given previous experiments on similar plasmas.

so called Gamma electrons. Gamma electrons are electrons originating from surfaces in proximity to the plasma which tend to be energetic. In the capacitive E-mode of the ICP, when the applied RF power is increased, the electrode voltage is increased causing an increase in the amplitude of the time-varying electric field. This increases the acceleration of the free electrons in the bulk resulting in increased dissociation of hydrogen molecules and thus atomic species [174]. These atomic species can emerge from the dissociation in excited states or be excited by electron impact from the ground state. In particular, fast atoms or ions can migrate towards material surfaces bordering the plasma whereupon the atoms can be ionized close to the surface allowing for the ion to trigger an Auger emission [175] by capturing a surface electron. The energy of the incoming ion deforms the potential well of the surface allowing a weakly bound surface electron to jump into a low energy excited state within the

ion, neutralizing it. If the excess energy from neutralisation is higher than the workfunction of the surface material a secondary electron may be released. [176, 177].

These secondary electrons are then accelerated to high speeds and thus energies by the plasma sheath back into the bulk. Thus through the creation of more atomic species, the gamma electron population is increased. With the enhancement of these fast electrons the rate of molecular vibrational excitation is enhanced, however, the rate of destruction of negative ions is also enhanced. There is a dynamic balance between the two factors (enhanced molecular excitation versus fast electrons for dissociation of H^- at any given gas pressure. This is observed at low pressures as the negative ion density peak indicated in the 17 Pa curve/s. This is not the only contributing effect to the vibrational energy distribution within the plasma or the rate of destruction of H^- though it is an important pathway. More mechanisms are discussed in the context of the results overall may be found in section 4.5.

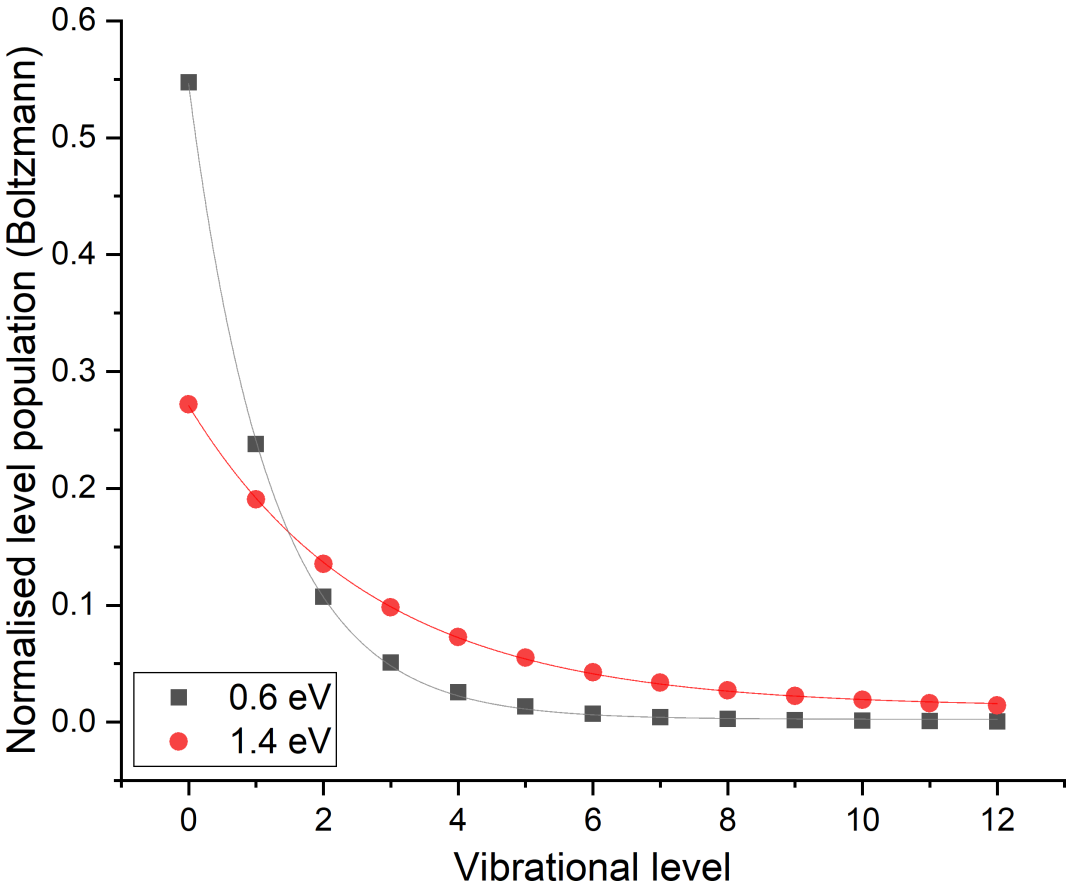

Figure 4.3: Normalized Boltzmann distribution of the vibrational level populations for 0.6 eV and 1.4 eV. The T_e values correspond to operational conditions of 200 W at 37 Pa and 17 Pa respectively. These curves show the increase in population of higher vibrational states suitable for dissociative attachment for the higher T_e.

4.2.2 Negative ion density variation with pressure and power (W)

Measurements of the negative ion density for each pressure and input power are shown in figure: 4.4. At 17 Pa, the negative ion density increased with power from 200-300 W with a maximum value likely somewhere in between 300 W and 400 W. Beyond this maximum, the negative ion density slowly decreased with increasing power up to the operational boundary which in this case was the E-mode limit of 700 W (more specifically between 700 W and 800 W). These measurements showed a transition from the dominance of H^- formation to H^- destruction.

At 25 Pa the negative ion density increased over the entire range of available input powers. The relationship was not linear and appeared to exhibit diminishing returns with increasing power heading towards H-mode. That is to say if higher powers had been available without leaving E-mode, there may have been a negative ion density maximum above the 700 W E-mode limit at this pressure. The negative ion density was significantly higher for high applied power at 25 Pa compared to 17 Pa. This implies that in some cases increased gas pressure is beneficial for negative ion production. The lack of a peak in this case meant that the power was not sufficient within the range to cause sufficient enhancement of H^- destruction so as to be the dominant process (see 17 Pa).

At 37.5 Pa, the negative ion density was significantly lower than at 25 Pa across the entire range of applied RF power. This was possibly due to the significant increase in collisionality at higher pressure lowering the density of fast electrons which in turn led to a reduction in vibrationally excited molecules and thus H^-. At this pressure, the negative ion density still increased with power though significantly slower. This increase may partly be due to the increase in the rate of secondary electron emission hence the fast electron population was increased with increasing power. This would then cause increased vibrational excitation of hydrogen molecules while collisional effects kept the electron temperature from being so high as to cause dissociation to dominate. These effects compete at high pressures resulting in the lower total densities of H^-. Both of the two higher pressure curves exemplify the competing processes by showing only the rising portion of the curves. It would appear their maxima are shifted to the right where the RF power would be high enough to generate enough gamma electrons to render H^- destruction the dominant process. For the rising portion of the curve at lower power, the negative ion density at 17 Pa was the highest among the pressures studied which pointed towards lower pressures being better for low power sources. It could

be argued that at lower gas pressure, there are fewer collisions with the surface resulting in volume effects being more dominant.

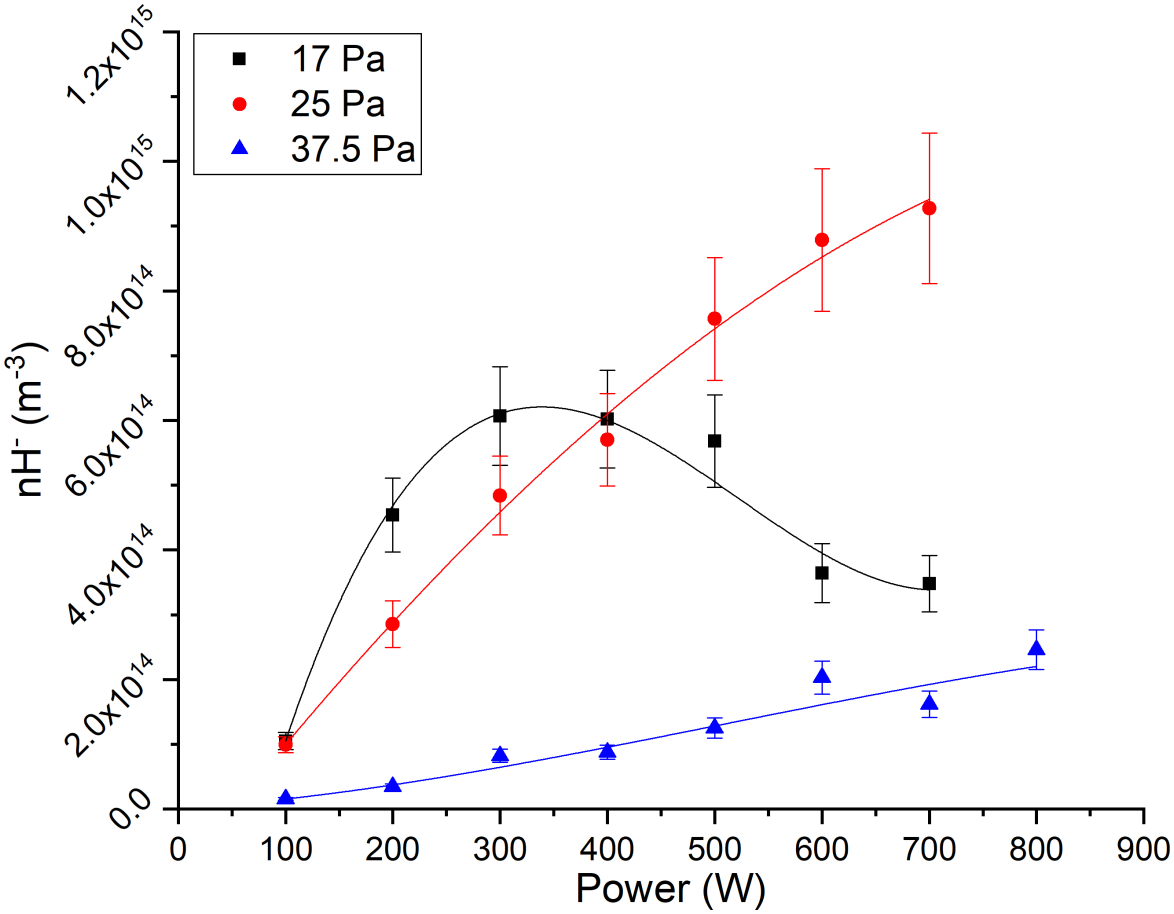

Figure 4.4: Negative ion density as a function of pressure and power for tungsten plate configuration. At 17 Pascal, the negative ion density reached a maximum at relatively low power indicating a shift from production-dominant to destruction-dominant conditions. At 25 Pa this transition had not yet been reached hence the steady increase with applied power. At 37.5 Pa, the collisionality rendered the gas relatively cool and unable to reach the necessary vibrational temperature to allow for meaningful creation of negative ions.

4.2.3 Negative ion fraction variation with pressure and power (W)

The negative ion fraction curves for the three pressures are shown in figure 4.5. The primary feature of the 17 Pa curve was the decrease in negative ion fraction with power, excluding the data point at 100 W which may be un-physical given that this measurement was performed at the lowest possible pressure for which ignition could be reliably achieved. This point is, in this case, discarded from analysis.

The negative ion fraction curves for the three pressures were similar to the absolute densities in all cases and are shown in figure 4.5. The limit wherein the destructive processes began to dominate was at relatively low power, potentially even below what was possible to measure accurately on this system. With increasing power, the curve continued in a downwards trend. Considering the increasing likelihood of dissociation through collisions with high energy electrons, it is reasonable to assume that there will be no peak at powers beyond the scope of this work. As is standard in a GEC device, the electron density increased linearly with applied power as can be seen in figure 4.1 whereas the negative ion fraction deviated below a linear trend at relatively low power. At this low pressure, the energy supplied by the increase in applied power was more effective in enhancing the creation of electrons and ions than excited hydrogen molecules. This is also due to the prevalence of low energy collisions and atomic species causing molecular de-excitation. This lack of suitable molecules would explain the negative ion production rate being too low to rival the additional electrons stripped from atoms and molecules hence the low fraction.

At 25 Pa, the negative ion fraction displayed an increase, peak, and then levelling out, potentially beginning to decrease at the edge of the available E-mode power range. This effectively illustrates the changes in the dominant plasma processes contributing to the population of negative ions. Initially, the increase in power yielded a net increase in the production rate of H^- ions due to greater population of high energy vibrational states of H_2. This was followed by a point where the increased production balanced with both the increased destruction of H^- by fast electrons and other species (notably atoms). To a lesser extent, the increase in faster electrons enhanced the dissociation of molecular hydrogen simultaneously reducing the number of molecules available for excitation and increasing the density of atomic species known to cause associative detachment, destroying H^- (see 4.5.3.3). Finally, the destruction processes began to dominate and the negative ion fraction began to decrease. If possible, the trend may have eventually resembled that of the 17 Pa case whereby the destruction

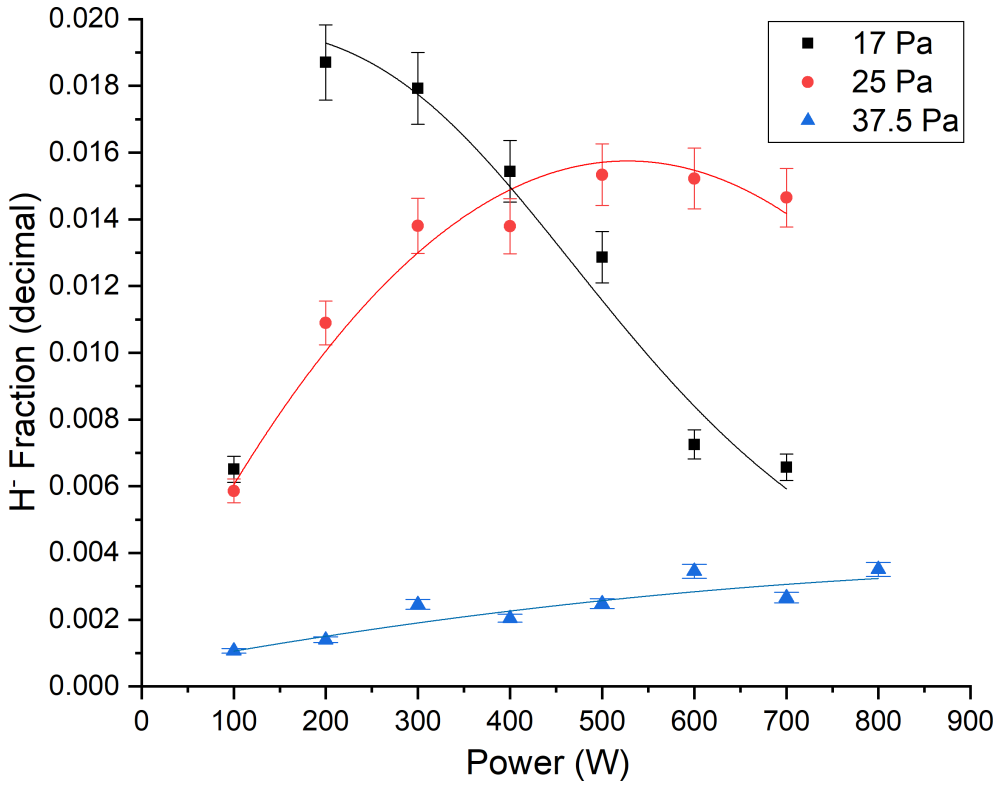

Figure 4.5: Negative ion fraction as a function of pressure and power for tungsten plate configuration. It can be seen that the low pressure, 17 Pa case quickly saturates the production channel and the destructive processes begin to overtake at low power. At 25 Pa, the H^- production rate continues to increase with applied power until it approximately stabilizes before showing signs of decreasing as the fast electron population becomes too high. At 37.5 Pa this is never reached because of the additional collisions.

processes were dominant to the point of H^- being short lived and scarce.

At 32.5 Pa, the negative ion fraction generally increased with power although the magnitude of the fraction was small throughout. This pointed to both the increase in collisionality and lower electron temperature rendering the high vibrational energy states less populated reducing the rate of dissociative attachment. This quenching of the reaction meant that any increase in either the electron temperature or density, (providing the gas temperature did not appreciably fall) would improve the creation rate of H^-. This is likely to be the reason for the slow increase in negative ion fraction and lack of peak in the 32.5 Pa result. The gentle curve plotted here serves as a guide in order to support the idea of an inaccessible peak.

It is worth noting that at all pressures studied, the negative ion fraction was only 2% or less of the electron density. This means that the negative ions were not a dominant

species in the dynamics of the plasma. The bulk plasma was still an electron-ion plasma as opposed to an ion-ion plasma. From these measurements made using the tungsten plate, the negative ion population was clearly being influenced by the overall discharge characteristics. Without additional data for other surface types the effect of the surface, if any, on negative ion populations could not be qualified. There is however, existing work which shows that surfaces can play a role in negative ion production. Work done by T. Gans et.al. [178] showed the role of the surface in the production of high energy atoms via surface ion bombardment. These atoms then would go on to lose most of their energy by vibrationally exciting hydrogen molecules in the volume. Schiesko et.al. summarise existing work and also show the strong contribution of the surface to negative ion production [117]. Additional work is described in section 4.5. Given the existence of energetic ions in plasmas, it may be reasonable to expect similar behaviour in these experiments. By examining additional surfaces, the degree to which the surface matters could be further explored.

At 17 Pa, the negative ion density peaked at 400 W which corresponded to an electron temperature of between 1.4 eV and 1.8 eV. The negative ion fraction at this pressure, however, was maximised at low power with electron temperatures from 1.2-1.5 eV. The electron temperature change was minimal between these two maxima. At 25 Pa, the negative ion density did not hit a maximum so the max value within the data corresponded to T_e of 1.3-1.6 eV. At 37.5 Pa, the electron temperature never reached this value but the negative ion density and fraction tended to increase as the temperature rose towards this value. The electron temperatures at 37.5 Pa were notably below those of the other two pressures, meaning that significant differences in vibrational excited state population were likely to be the cause of the overall significant drop in negative ion formation. In this case a drop of 1 electron volt represented a large difference in the vibrational energy distribution function visible in figure 4.3. It can be seen that a higher electron temperature corresponds a Boltzmann distribution with a much larger proportion of molecules in vibrational states above the ground state, including states with $v \geq 4$. Dissociative attachment processes are sensitive to the vibrational state of the initial molecule with increased rates at higher levels. This leads to an enhancement of H^- formation in principle, ignoring destruction effects. The 17 Pa and 25 Pa discharges at 200 W exhibit higher electron temperatures than the 37.5 Pa discharge which is consistent with this increase in H^- formation.

4.3 Negative ion results for molybdenum electrode grounding surface

The second material surface examined was high purity (99.9995%) molybdenum. The results are presented here with some comparisons calling back to the tungsten data.

4.3.1 Electron density and temperature variation with pressure and power (Mo)

In agreement with the results from the tungsten plate experiments, the ion, and thus electron densities increased linearly regardless of pressure with similar slopes, 6.31±0.17, 6.64±0.33 and 6.47±0.25 ($\times 10^{13}$ m^{-3}) in order of increasing pressure (see fig 4.6). There is no comparison point for 17 Pa because it was difficult to ignite at pressures much lower than 25 Pa. This may have been possible with additional attempts but for the purposes of this work, direct comparisons will only be made between like pressures.

The ion/electron density trends were similar between tungsten and molybdenum but there was a slight discrepancy at the upper end of the applied power scale. To quantify the discrepancy in electron density, for 37.5 Pa where the ion density reached approximately 6×10^{16} 200 W earlier in tungsten. This was despite the ion densities being similar below 300 W. The gradients of the linear fits to the tungsten n_e measurements at comparable pressures (25 Pa and 37.5 Pa) were steeper at 8.02±0.22 and 8.32±0.32 ($\times 10^{13}$ m^{-3}) respectively meaning electron production was enhanced during the tungsten runs by either the ambient conditions or the tungsten itself. Owing to the room temperature being within a degree between runs, it is more likely that the tungsten was the cause.

The temperature graph, fig. 4.7, more clearly showed the variation between the different pressures used with the molybdenum plate installed. At 25 Pa, the electron temperature increased linearly with applied power. At 32 Pa there was a general increase in electron temperature with applied power though not obviously linear. A trend-line was not added due to the slightly ambiguous nature of the increase. The 500 W data point seemed erroneously high and would otherwise have lay on a smooth curve. Alternatively, if the 500 W point was lower the data could be represented by two linear regions. The initial steeper region would end around 400 W and the second region with a shallower gradient would fit the rest of the points. This might indicate a mode change within the plasma (not E $\rightarrow$ H mode). The

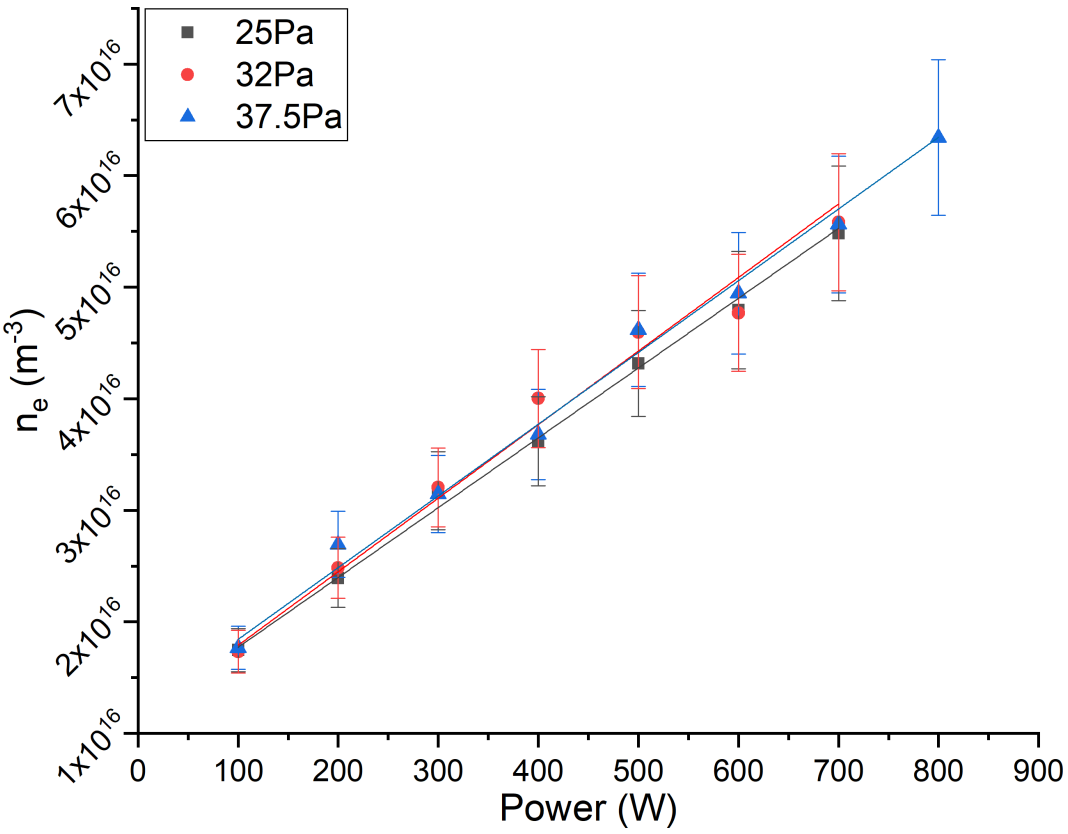

Figure 4.6: Electron density as a function of pressure and power for molybdenum plate configuration. Similarly, the densities are practically identical for all pressures and scale linearly with power. These fits are thus not simply guides for the reader.

electron temperature in this case showed a general upwards trend despite some deviations.

Many of the electron temperatures observed at 37.5 Pa lay on a straight, flat line. The 300 W and 400 W data points deviate downwards from this trend while the final point at 800 W deviates upwards. These deviations were likely systematic errors due to temporary fluctuations in the plasma or the surface condition of the probe. Additional repeat measurements in future, potentially using a second probe or additional diagnostic would determine if this was the case. For several data points at different pressures, the electron density and temperature were similar. In these instances, the differences in negative ion behaviour will be of interest because it cannot be attributed to the electron population.

At 25 Pa the electron temperature was consistently lower for the plasma above the molybdenum plate compared to the tungsten. Conversely, the electron temperature at 37.5 Pa was similar for both materials. Visual comparisons of electron temperature at 25 Pa can be found later in section 4.4.1.

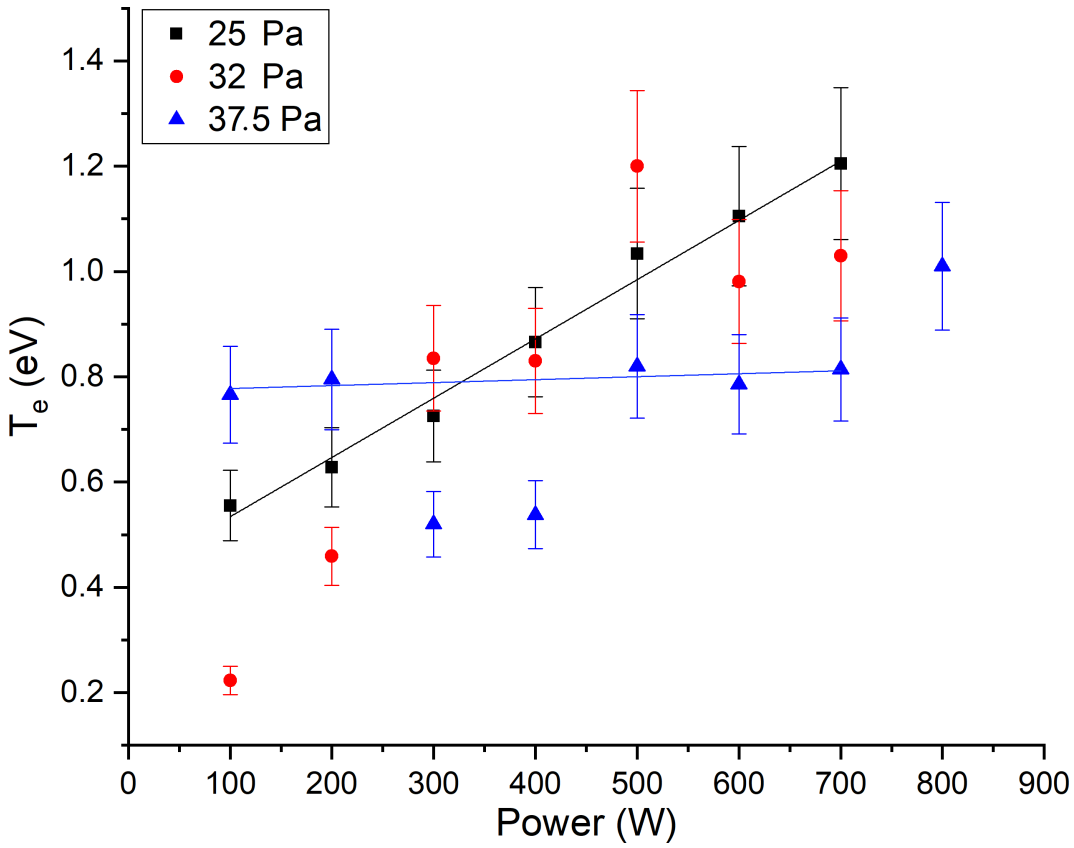

Figure 4.7: Electron temperature as a function of pressure and power (Molybdenum). The temperatures are generally similar and can be seen to be increasing with power except for the highest pressure of 37.5 Pa which was flat for most of the applied powers.

4.3.2 Negative ion density variation with pressure and power (Mo)

The negative ion measurements are shown in figure 4.8. At 25 Pa, the negative ion density was approximately constant with applied power above 100 W applied. The 100 W data point may be an outlier or may indicate a rapid increase in H^- with power to a stable value which could be identified with more granular scaling of applied RF power. Whether or not this stable region would be followed by a downward trend at power above 800 W is speculation given the available data.

The 32 Pa curve displayed similar traits to the H^- fraction from the 25 Pa tungsten data and the rising portion of the H^- density trend at 17 Pa with tungsten. This shows the same transition between the dominance of H^- formation to destruction but at higher pressure. This implies that there are similarities in the processes occurring for different surface materials but that the optimal pressure for this transition is different for each material.

At 37.5 Pa there was a slow increase in negative ion density with power across the entire

range. Given the error bars, this could have been an increase into a flat region, followed by a transition into another rising trend when approaching H-mode transition around 800 W. Alternatively, the negative ion density could be curving towards a maximum similar to the 32 Pa case but slower. If so, the power at which the curve would roll over exists beyond what was attainable in E-mode with the equipment available.

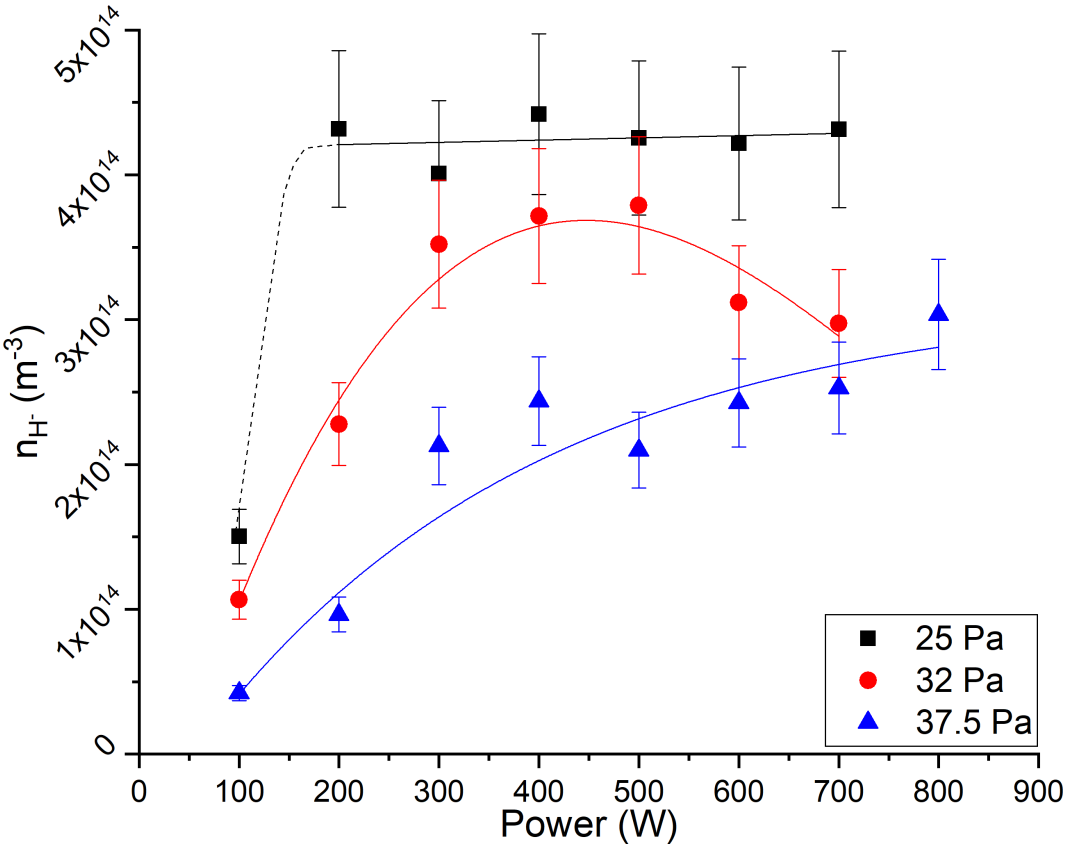

Figure 4.8: Negative ion density as a function of pressure and power for molybdenum plate configuration. The negative ion trends are similar for 32 Pa and 37.5 Pa, exhibiting some peaking nature similar to the tungsten results pictured earlier.

In contrast to the tungsten plate, for the pressures examined, there was an overall decrease in negative ions with increasing gas pressure (see figures 4.4 and 4.8). For the same neutral gas pressure and applied power e.g. 25 Pa, 700 W, the negative ion density between the two materials was significantly different. The density of H^- measured in the discharge over the tungsten plate was larger by approximately a factor of two than the equivalent density above the molybdenum plate. At higher pressure of 37.5 Pa, a comparison between the negative ion densities, shown in figure 4.9, shows that the molybdenum plate outperformed the tungsten plate significantly at 300 W and 400 W by a factor of 2→2.5 before converging somewhat

at higher power. This separation of the negative ion curves at 300 W and 400 W correlates with the lower electron temperature values at 300 W and 400 W measured for molybdenum which may have been anomalous. The trends for both metals across the range of powers available was generally increasing and the negative ion density with the molybdenum was consistently higher than that for tungsten. These observations indicate a clear effect on the negative ion density within the plasma resulting from the different metal surfaces.

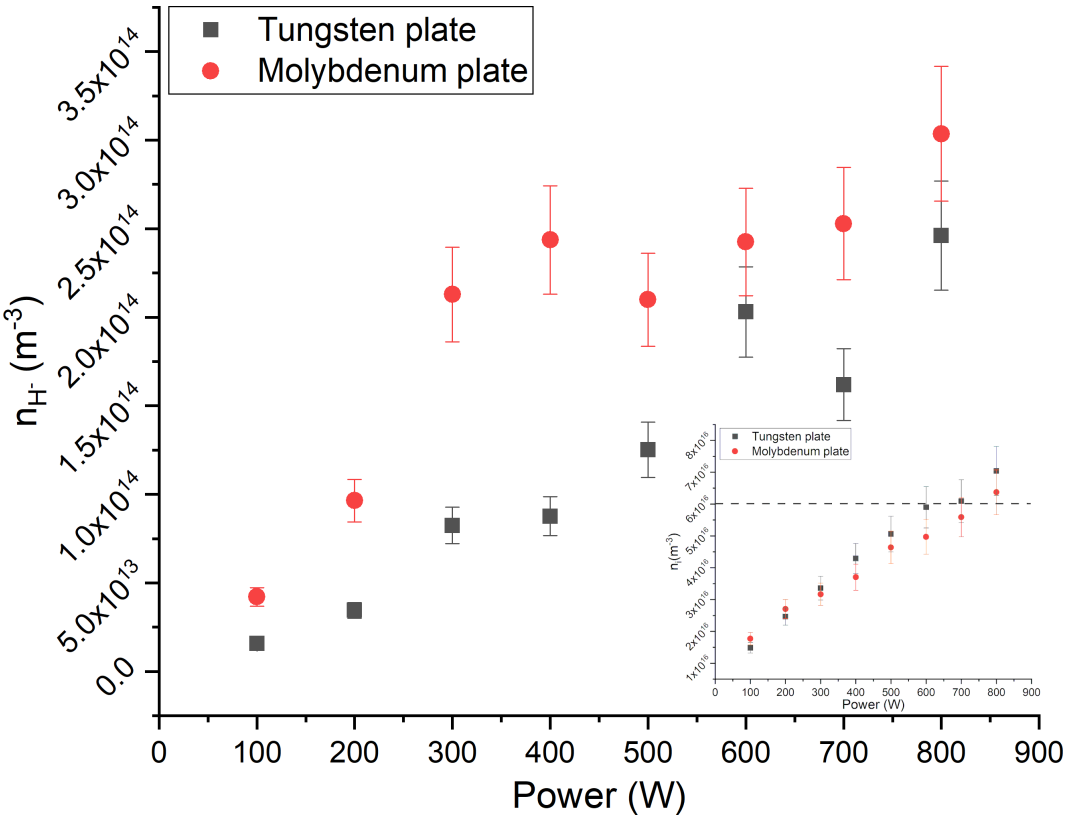

Figure 4.9: Direct comparison of the negative ion density measured for the tungsten and molybdenum target plate at 37.5 Pa. The molybdenum is above the tungsten for the entire power scan at this higher pressure. This may indicate that molybdenum outperforms tungsten at all applied powers, at high pressure. The pressure at which this behavioural transition occurs is not yet known.

Figure 4.9 highlights the increased negative ion density for the comparatively lower ion and thus electron density of the molybdenum configuration. This may support a sensitivity to the presence of a greater number of higher energy electrons causing a slight increase in destructive processes in the tungsten case at 37.5 Pa.

Two of the H^- density data sets (tungsten 17 Pa and molybdenum 32 Pa) exhibited an initial increase followed by a turning point and then decrease. It is believed that in both

cases, this was due to a shift in balance between the formation and destruction processes in the bulk as opposed to simply an eventual reduction in H^- formation rates. The data implies that for a given pressure, the negative ion density was maximised at lower applied power for the molybdenum sample. At higher pressures for both materials, a general increase in H^- with power was observed implying that the dominance of the destructive processes was never reached in those cases. The closest to this was the 25 Pa run using tungsten whose gradient began to roll off slightly though this is within the tolerances of the error bars and could instead level out. Points above the transition into H-mode were not examined in this study because the reliability of accessing H-mode and the survivability of the Langmuir probe tip were not good. In pulsed operation, the transition to H-mode was inconsistent and seemed functionally random from pulse to pulse. This means that the H-mode data would instead be an unknown mixture of E-mode and H-mode data. It was decided that the duty cycle should remain identical between measurements, keeping the thermal conditions of the walls and the plate as similar as possible. If it were possible to observe the effects of increased power without entering E-mode, it is postulated that similar peaked curves would be observed with maxima shifted both in absolute scale and along the power axis. A measurement at 32 Pa for tungsten would aid in this conclusion by potentially showing a maximum somewhere around 600-700 W with room to show the beginning of a decrease.

4.3.3 Negative ion fraction variation with pressure and power (Mo)

The negative ion fraction, shown in figure 4.10, generally decreased with increasing gas pressure, the only exception being potentially the values at high power for 37.5 Pa. In this case, the higher population of molecules was able to absorb and favourably distribute more of the energy deposited into the electron population, however the increased collisionality meant that the gains in negative ion fraction were negligible at high power.

At 25 Pa, the negative ion fraction resembled that of tungsten at 17 Pa. The fraction decreased with applied power in a slight curve with decreasing gradient. This indicated that similarly, the destructive processes were dominant with increasing power. The 200 W data point was excluded from the guideline fit in this case due to being so far above the rest of the data. Additional measurements made at intermediate power values would help to determine if this sharp peak is physical or an outlier however due to time constraints, these measurements were not made and would be done in additional work.

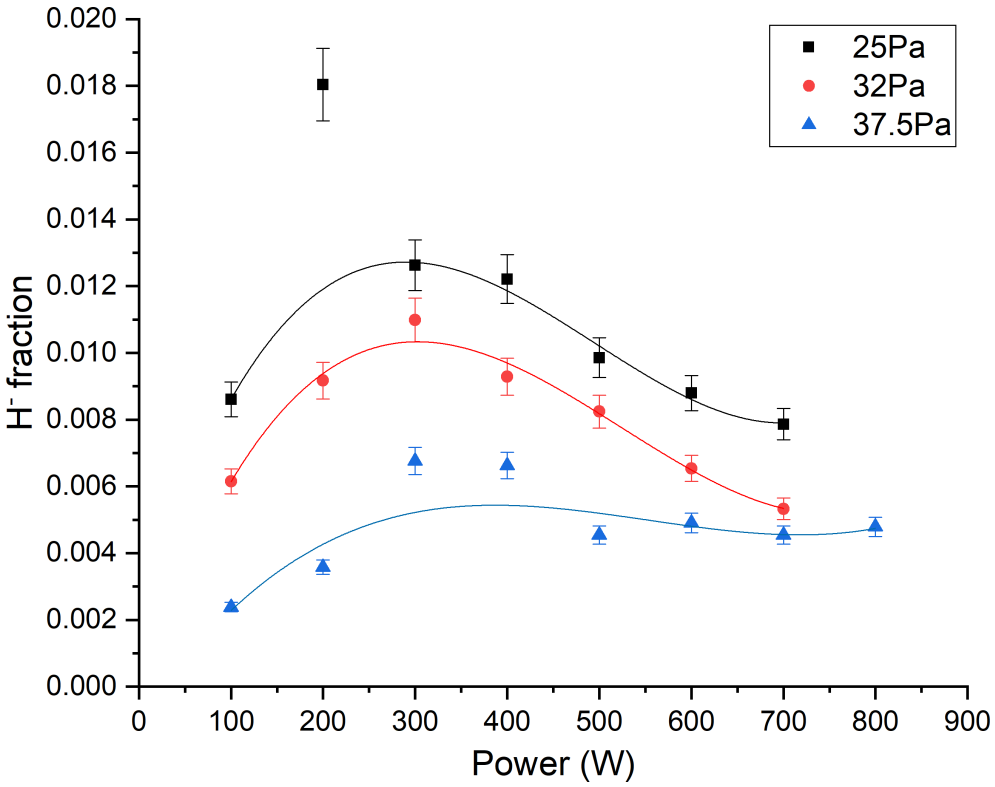

Figure 4.10: Negative ion fraction as a function of pressure and power for molybdenum plate configuration. It can be seen that, similar to tungsten, the lowest pressure (25 Pa in this case) peaked earlier than subsequent higher pressure measurements. This seems to indicate that the physics behind the negative ion dynamics are similar or perhaps the same between materials though shifted with respect to the power axis dependant on the material itself.

At 32 Pa, the negative ion fraction peaked at 300 W and then decreased with additional power. This was evident of the optimal conditions for negative ion formation followed by increased destruction; subsequent increases in applied power increased the fast electron population leading to greater destruction of negative ions. This was in contrast to the tungsten result which displayed no fraction peak within the range of powers applied. The negative ion fraction decreased with a similar relation to the 25 Pa result with the gradient indicating further decrease, potentially falling below the values in the 37.5 Pa case. By contrast the negative ion density peaked around 400-500 W which indicated that the relationship between the fraction and absolute density was not simple.

At 37.5 Pa, the negative ion fraction also peaked, this time between 300 W and 400 W. The 300 W and 400 W points may have been an overestimate. In this case the trend may have increased monotonically with power which is reasonable. If instead, these points were accurate, the trend would look somewhat similar to the 25 Pa and 32 Pa data. The fit applied

here to guide the eye represents what the author would expect with more experimental repeats.

Comparing the negative ion fraction values between tungsten and molybdenum at 25 Pa showed some similarities (see figure 4.11). For the tungsten plate the fraction rose from 0.6% to 1.6% in a smooth maximum, whereas for the molybdenum plate, while the range of absolute values was similar between 0.8% and 1.8%, the peak was much lower at $\leq$ 200 W. The 25 Pa molybdenum curve was more similar to the 17 Pa curve in the tungsten case where the values of the negative ion fraction ranged from 0.7% to 1.9%. The curve was also steeper in decline for the molybdenum plate at lower power where the tungsten only became similarly steep around 500 W. At 37.5 Pa, the molybdenum plate negative ion fraction measurements were higher by a factor of approximately two for the entire range of applied power. The exception to this was the peak between 300 W and 400 W which did not appear in the tungsten values. The enhancement factors rose to between three and four over this range. These observations support the notion that while similar processes happen with the two surfaces, they happen at lower powers for a set pressure with the molybdenum plate installed.

There was no defined maximum in the negative ion density at 25 Pa with the molybdenum plate. This is interesting because the electron temperature and density both increased linearly with respect to applied power. This implies that the various contributing factors to the formation and destruction processes were balanced for a wide range of powers. Increases in electron temperature and density, can increase the vibrational excitation rate of hydrogen molecules and increase the rate of dissociative attachment up to a point. On the other hand, the rates of dissociation of H_3^+, H_2 and H^- into atoms also increases. The additional atoms can go on to dissociate negative ions themselves leading to further reduction in negative ion density. These competing factors could have ended up in a dynamic balance along with surface interactions to explain the stable density.

The electron temperature at 700 W also approached the optimum range of 1.2-1.4 eV observed in the tungsten result with no discernible effect on the negative ion density with molybdenum. The negative ion fraction at 25 Pa in fact decreased with increased electron temperature above 0.6 eV contrary to what would be expected if the dissociative attachment process in the volume was dominant by a large margin.

The addition of molybdenum to the picture shows evidence that surfaces play a significant

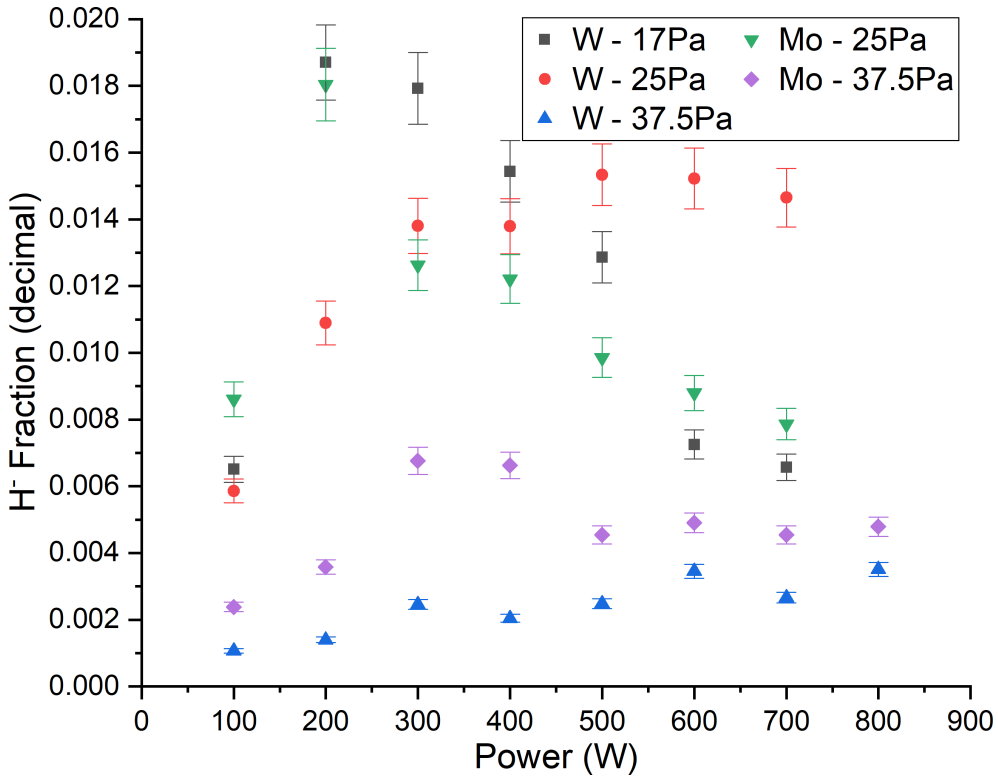

Figure 4.11: Comparison between tungsten and molybdenum in terms of negative ion fraction for varying pressure. There are similarities between the curves for 17 Pa tungsten and 25 Pa molybdenum, as well as between both metals at 37.5 Pa. The 25 Pa curves differed significantly between metal surfaces.

role in the negative ion creation chain and that the material of which the surface is comprised is also significant. While the fundamental physics observed between the plasma and the surface may be the same, the differences between molybdenum and tungsten showed that the negative ion behaviour was displaced in the energy domain with the most obvious factor being the changing surface. Where the surface provided another source of H^- to skew the equilibrium in favour of formation for a range of applied RF power, the maximum density and efficiency reached, as well as gradients involved were material dependant.

4.4 Negative ion results for varying surface material at 25 Pa

4.4.1 Electron density and temperature variation with material and power

The electron densities were similar for all three metal samples at 25 Pa; the scaling of the electron density was linear or near-linear in all three cases. The differences between the molybdenum and tungsten were more apparent in this figure (fig 4.12), showing that the

electron density with the molybdenum plate rose significantly slower than that for tungsten (taking uncertainty into account). The steel sample was almost identical to the tungsten up to 600 W after which there was a slight divergence. These last points pulled the trend line away from the tungsten trend line and there was potentially stronger agreement within the confines of the experimental uncertainty. It is worth noting that all of this may however lie within acceptable variation in the day-to-day electron density for the GEC regardless of surface.

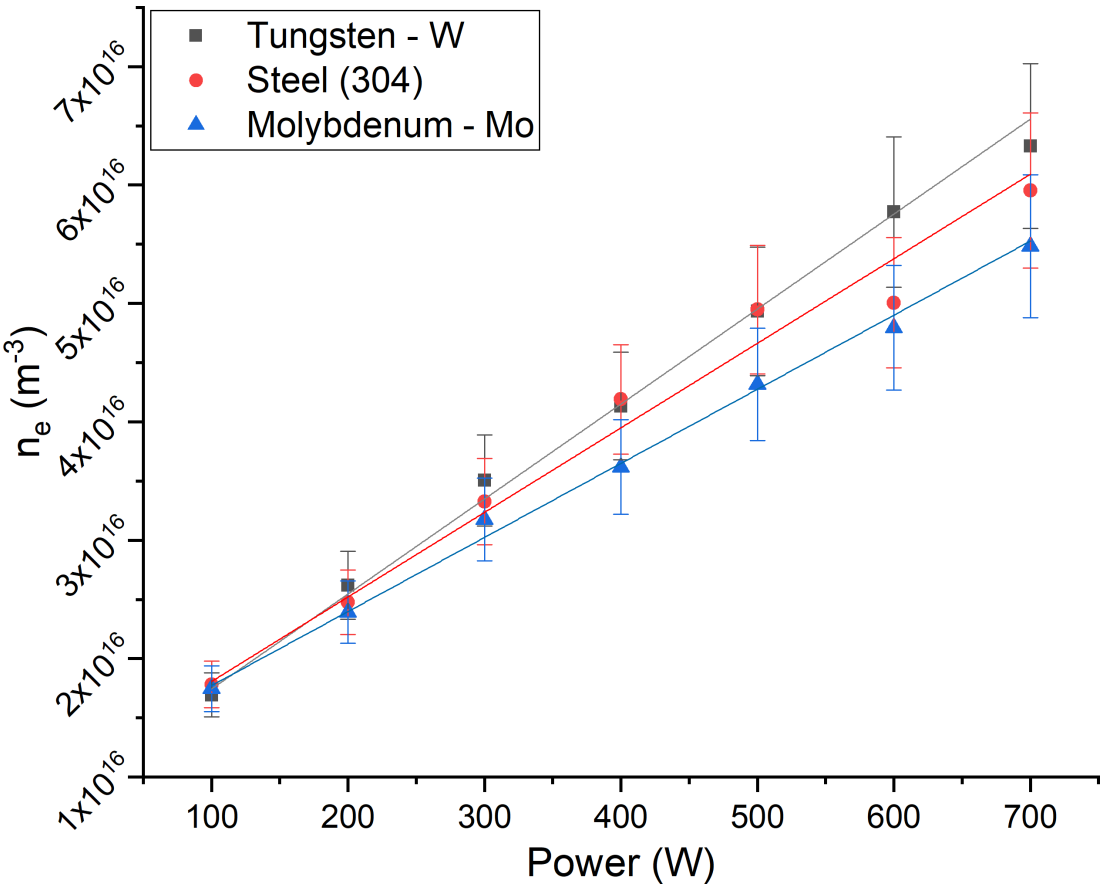

Figure 4.12: Electron densities as functions of applied RF power for various metal surfaces at 25 Pa. Within the error bars, the swap between steel and tungsten had little effect on the electron density in the plasma as a function of power. The small deviation between tungsten and steel versus molybdenum may have been day-to-day variation but could have also been due to a property of the surface causing increased secondary electron emission from steel and tungsten.

The electron temperature was significantly lower with the molybdenum plate installed for equivalent input RF power than steel and tungsten, particularly at the lower end of the range. The electron temperatures for discharges at the same pressure (25 Pa) were similar.

The temperature offset could have been a source of some aspects of the discrepancy in the negative ion data. As shown in the Boltzmann plot (4.3) earlier a difference of 1 eV is enough to cause significant enhancement or reduction of the H^- formation rate due to dissociative attachment by modifying the vibrational energy distribution of the molecules. This is true for non-Maxwellian distributions also where putting more energy into the system via hotter electron collisions tends to increase the population rate of higher vibrational levels. The temperature profiles for the steel and tungsten plates were extremely similar with 300 W being the only point which barely lies outside the error bar.

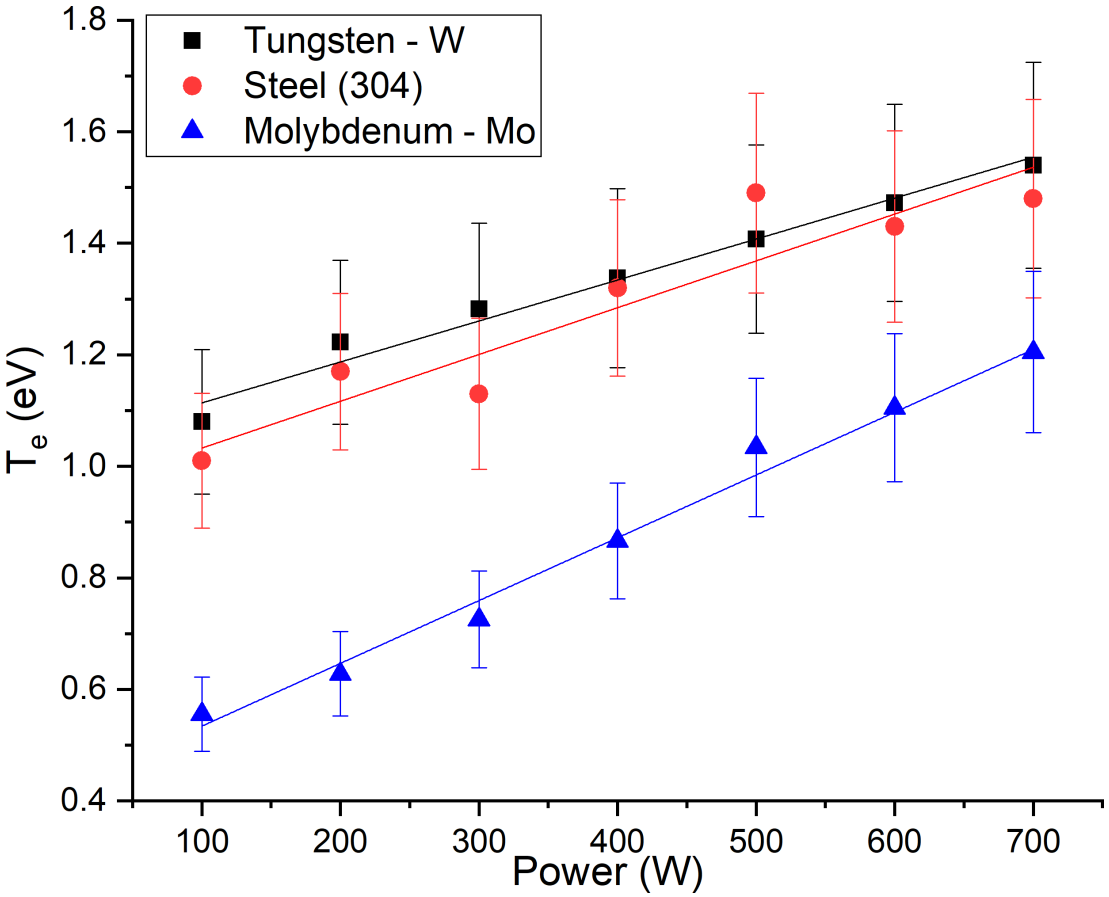

Figure 4.13: Electron temperatures as functions of applied RF power for various metal surfaces at 25 Pa. There was an appreciable drop in electron temperature with the molybdenum plate installed. This could have been part of the reason why the negative ion densities did not match those for steel and tungsten (see next section 4.4.2). A difference of approximately half an electron volt represents a significant difference in the occupation of high-V vibrational states for dissociative attachment.

4.4.2 Negative ion density variation with material and power

The results for the negative ion density variation between metals at 25 Pa are displayed in figure 4.14. The negative ion density for the tungsten plate and the steel plate significantly outperformed the molybdenum plate at 25 Pa above 300 W. This reinforced that the electrode surface material could be a significant factor in the negative ion dynamics between the surface and the plasma. Using the steel sample resulted in the highest density of negative ions at higher power with n_{H^-} increasing by a full order of magnitude over the available E-mode power range. The tungsten sample was similarly effective but showed signs of reaching a maximum towards the H-mode transition above 700 W. The molybdenum plate, discounting the point at 100 W, showed no significant change in negative ion formation over the power sweep by comparison. These results are similar to the work by Pèalat et.al. [122] which showed that a steel surface was more effective than a matching copper surface. This is particularly relevant because it was found in similar experiments to these performed with copper on the same GEC cell by J. Ellis, that copper behaved much like molybdenum in terms of negative ion production [165].

The plate surface temperature (global and localized) may have been a contributing factor to the behaviour. While the surface temperature or even temperature profile was not measured in-situ, the surface temperature was measured after each run using an infra-red thermometer with the chamber returned to ambient pressure. The temperature changed by one Celsius or less in each case from the initial plate temperature (approximately 23 Celsius ambient). It was assumed that due to the pulsing of the plasma preventing significant heat buildup in the plasma facing surfaces, along with the temperature immediately after being almost identical to the start temperature, that the temperature of the sample was stable during the experiment. Without in-situ measurement of the plate temperature or better still, the distribution measured with a thermal camera, this assumption cannot be confirmed completely and would be a subject for additional work. This factor and its place in the negative ion scheme is discussed more in section 4.5.3.1.

The scaling of the negative ion density with electron density at 25 Pa is shown in figure 4.15. These data indicate that the negative ion formation did not scale with electron density for every material. The relation between n_e and n_{H^-} is approximately linear for tungsten and steel. This supports the notion that more vibrational excitation was leading to a larger number of dissociative attachment reactions; more electrons at the right energy means a

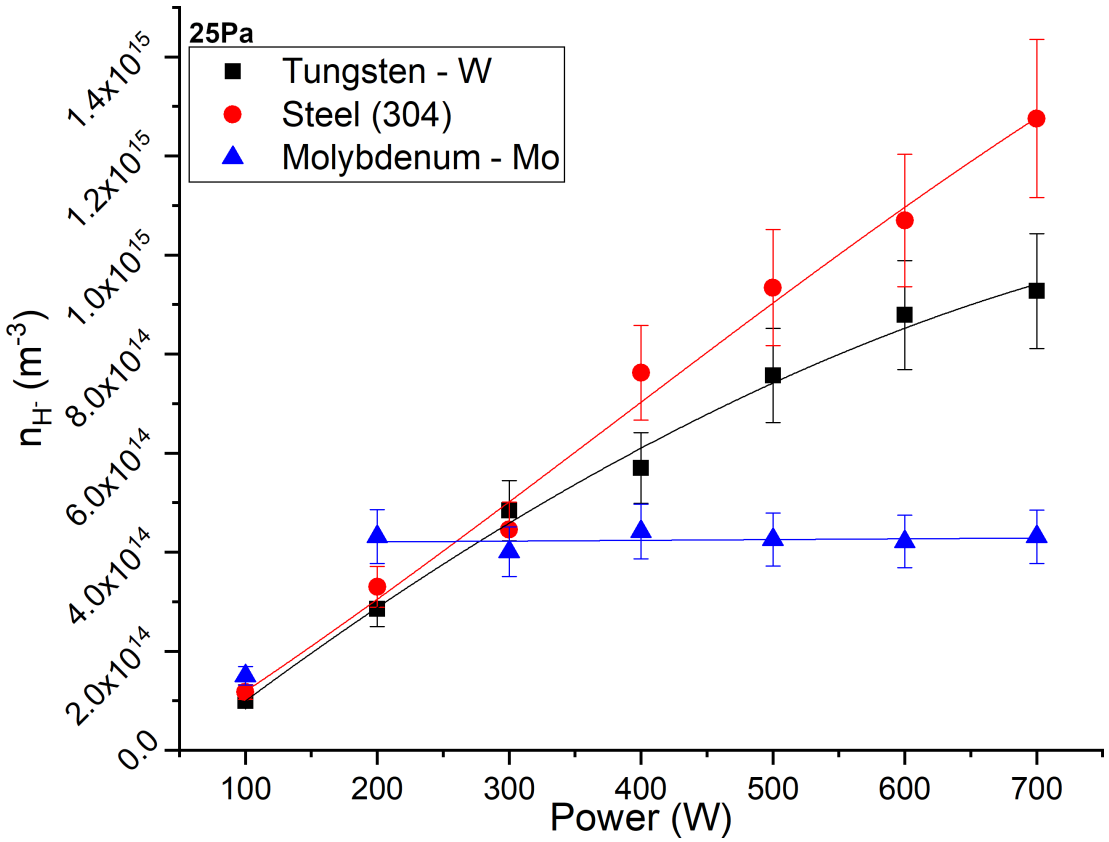

Figure 4.14: Negative ion densities as functions of applied RF power for various metal surfaces at 25 Pa. When viewed relative to each other, at 25 Pa it is clear that steel and tungsten both outperformed molybdenum and notably, in a similar fashion. With the molybdenum plate installed, the negative ion production was stable throughout the applied power range. It also appeared that steel could have exhibited a peak several hundred Watts above that for tungsten, observable due to the lack of the start of a potential turning point in the steel data.

higher probability of exciting hydrogen molecules into or above the fourth vibrational state. This does not hold for the molybdenum sample where increasing electron density did not cause any enhancement of negative ion production meaning that the picture is not as simple as the electron dynamics being the sole reason for the differences. This can be viewed in two ways: molybdenum increased the destruction rate of negative ions somehow, or tungsten and steel enhanced negative ion formation, without which their trends would have been more similar to molybdenum.

If the tungsten and steel surfaces contributed to an enhancement of vibrationally excited molecules, this too would have enhanced the DA process leading to more negative ions. As is discussed later in section 4.5.2.2, the presence of weak binding sites on a metal surface can lead to favourable conditions for the recombination of atomic hydrogen into excited molecules. Under these conditions, an increase in electron density at appropriate electron temperatures would enhance the rate of dissociative attachment considerably. This would provide an avenue for the tungsten and steel plates to outperform the molybdenum.

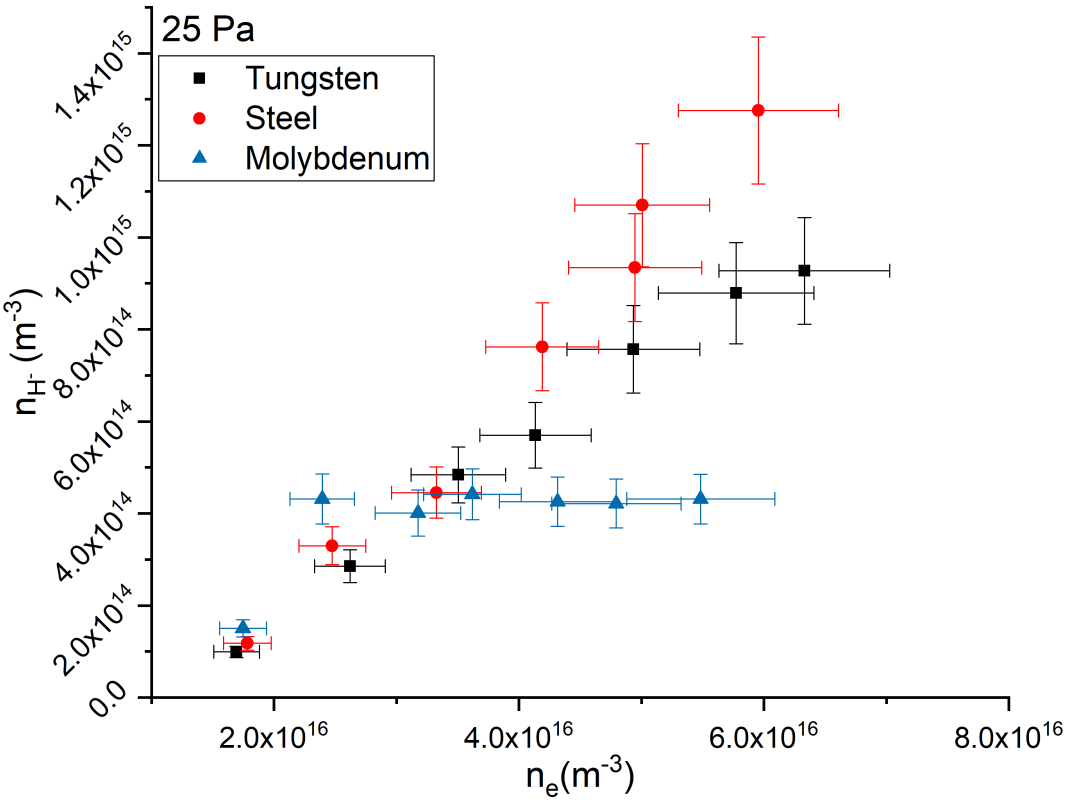

Figure 4.15: Negative ion density plotted against the corresponding electron density for all three metal plates at 25 Pa. The electron density is, as before, calculated from the measured ion density. The relationships are similar for steel and tungsten but deviate for molybdenum.

Of some note was the point at 200 W whereby the negative ion density with the molybdenum was higher than that for steel and tungsten. With additional data points in this range, it might be possible to show a small window where molybdenum constitutes a better surface for negative ion dynamics at low power.

4.4.3 Negative ion fraction variation with material and power

The negative ion fraction curves for steel and tungsten showed similar trends to the respective absolute H^- densities. Similar to the negative ion densities, at 200 W the molybdenum plate displayed a higher negative ion fraction than the other metals, deviating outside the margins of the error bars. This point appearing in both the absolute and fractional density implies that while molybdenum may not be ideal for large scale negative ion production, the surface did function better at low power which may be worth investigating further for small scale negative ion source development.

The steel and tungsten negative ion fraction measurements were similar in shape. Despite their similarity, the steel negative ion fraction in particular was up to 5% larger than that of tungsten at high power. Both of these metals exhibited a rise in negative ion fraction with power meaning that the negative ion density rose faster than the electron density in these cases. By contrast, the behaviour with molybdenum is the opposite with the fraction decreasing with power. The negative ion density did not keep pace with the linear increase in electron density. This is the result of either a reduction in formation rate, a rise in destruction rate or a combination of both effects.

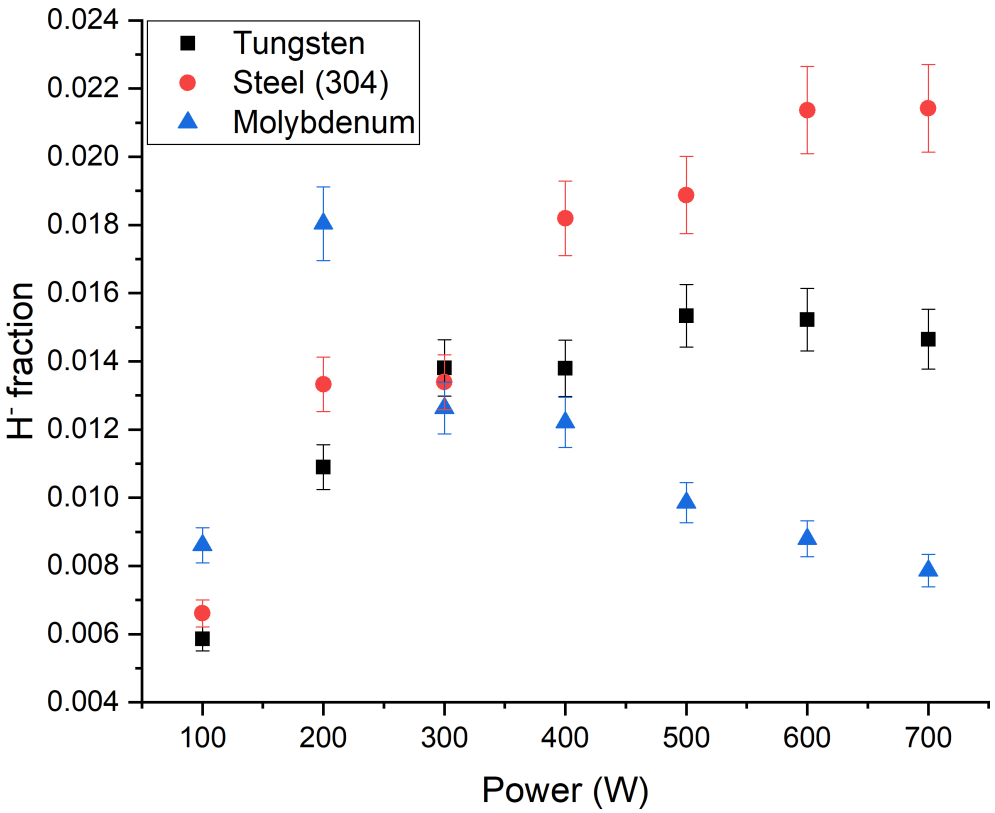

Figure 4.16: Negative ion fractions as functions of applied RF power for various metal surfaces at 25 Pa. The trends for steel and tungsten were similar in that they both showed an increase and plateau over the available range of applied power. The molybdenum was significantly different which indicated that the electron temperature effect could not be the only contributing factor. The scaling in the negative ion density did not match the somewhat consistent offset in electron temperature.

4.5 Discussion of GEC results overall

4.5.1 Similarity to other experiments and results

The order of magnitude of the negative ion fractions measured in this experiment was similar to other experiments on RF discharges. Devynck et.al. [179] measured negative ion densities at lower pressures around a few Pa and relatively low power (below 200 W applied RF at 13.54 MHz) and found values around a few percent of the electron density at the upper end of pressures investigated. In the experiments performed for this thesis, the power applied and gas pressure were higher which would explain the similar scaling of the negative ion densities from a broad standpoint. Electron temperatures in [179] were all in the sub-1 eV range, scaling with the collisionality arising from the increasing gas pressure.

Mosbach, Katsch and Döbele [180] studied post-pulse negative ion densities. The measurements made at t = 0 after the plasma was turned off are useful for comparison with measurements made on the York system. The relative densities in [180] were close to the steady state plasma by a few percent. Their reported values are close to the values reported here for all surfaces.

4.5.2 Potential sources of increased negative ions in the GEC

In order to explain the negative ion behaviour in the GEC experiments, it is necessary to account for the various properties likely to cause the discrepancy between materials. These may be separated into effects which change the production of negative ions in the bulk and effects which alter the production of negative ions at the surface.

4.5.2.1 Direct surface production of negative ions

There are a number of surface interactions to consider and potentially more which have not yet been discovered. Given the complexity of the system as a whole, narrowing the dominant physics behind the negative ion production in both the bulk and in particular at the surface is difficult. In general the surface production processes must fundamentally reduce down to a hydrogen-based species, either an atom, molecule or ionic species, adsorbing to the surface briefly before undergoing an interaction. This interaction then allows at least one negative ion to be released from the surface along with whichever other reaction products are formed with enough energy to desorb in some other direction.

What all of these interactions have in common is the requirement that at some point an electron must be removed from the surface and be captured by either the incoming particle or one of its fragments. In all cases, this requires the electron to move from a lower potential well into a higher one. This is represented by the electron affinity of atoms (hydrogen 0.754 eV) being significantly below the work function of most metal surfaces which lies around 5 eV. For slow atoms incident on a pure metal surface, the probability of electron tunnelling is low enough so as to render the occurrences of the process functionally zero. This problem may be overcome by sufficient increase in the incident energy of the atomic species, bridging the energy gap required to satisfy the work function of the metal surface.

4.5.2.2 Surface production of species which increase or decrease volume production of negative ions

There are several processes known which would indirectly contribute to the rates of negative ion formation and destruction through the creation of relevant species and/or the change in the energy distribution among those species. For the dissociative attachment (DA) process of H^- formation, the first order relevant species are vibrationally excited hydrogen molecules and electrons of appropriate energy (a few eV). Surface processes which create these species and release them into the plasma or create species which act as a detriment to the DA process are outlined here. The first three processes are collectively known as charge exchange processes.

The first process of interest is the recombination of two adsorbed surface atoms to produce molecular hydrogen. This is known as the Langmuir-Hinshelwood (LH) process and is discussed in [181]. The bond energy of the H_2 molecule is around 4.5 eV and so this process tends to be endothermic by approximately 0.3 eV. This would introduce de-excited molecules to the plasma which would both increase the number of molecules which could become vibrationally excited but also decrease the plasma temperature through collisions. This removal of energy from the plasma and creation of low energy molecules is not ideal for the DA process and thus this process is not expected to contribute significantly to negative ion formation.

Another mechanism for the creation of hydrogen molecules at the surface is the Eley-Rideal (ER) recombination process (also shown in [181]. This process involves an atom impinging from the plasma onto the surface where it reacts with a pre-adsorbed atom to form a molecule. This reaction however is exothermic due to only one of the atoms being

initially adsorbed; the reaction is exothermic by around 2 eV as detailed in [182]. This is an idealised picture because in reality there is a nonzero thermalization time between the impinging atom and the surface. The excess energy released with the molecule after the reaction is distributed among the degrees of freedom (DOF) of the molecule, including vibrational states. This means that some of these molecules are released in a vibrationally excited state contributing to the DA rate of negative ion production.

A third process was proposed by Harris and Kaseno [183] where the impinging atom is at first only weakly bound to the metal surface, allowing it to move around relatively freely. This allows energy to be transferred to other adsorbed species, resulting in the recombined molecule desorbing with more energy. This process was called "Hot Atom" (HA) recombination by Harris and Kaseno. The presence of this mechanism has been given support indirectly through studies [184, 185] in which the ER process could not account for the observations made by the authors.

These processes which lead to the formation of vibrationally excited hydrogen molecules are strongly surface dependent [123, 186] however the exact mechanisms behind the surface variation are not well understood. Some work has been done to investigate this by Markelj and Čadež [187] on copper and tungsten surfaces. They proposed that the discrepancies between the materials under study were due to the presence of weak binding sites on the surface. These weak binding sites were present on the tungsten surface, leading to a much greater population of adsorbed hydrogen atoms with various desorption energies dependent on the individual binding sites. The use of a Monte-Carlo simulation assuming predominantly hot-atom (HA) recombination identified the weak binding sites as the primary conduit for this HA recombination process, accounting for the higher energy vibrational distribution of the tungsten surface.

An effect which was suspected of contributing to both the formation and destruction of negative ions was a change in the electron dynamics due to the material surfaces. Specifically, due to the generation of fast gamma electrons at the electrode surfaces common to discharges of this type, it was suspected that there was a difference in surface emission of gamma electrons, altering the fast electron to slow electron ratio differently for each sample. The increase in the relative population of the fast electrons would then increase the formation rate of vibrationally excited hydrogen molecules in the bulk causing an increase in the negative ion formation rate through the DA process. As the energy of the secondary gamma electrons

increases beyond $\approx 1-3$ eV the cross section of the DA process for molecules with $V > 3$ begins to reduce dramatically while significantly enhancing the rate of the destruction of pre-existing H^- [188]. An examination into the secondary electron behaviour in these experiments is presented in section 4.5.3.5

Another common process thought to be responsible for negative ions is the backscattering of already neutral atoms [189, 190]. The work function problem still exists however and thermal speeds are not sufficient to overcome the potential barrier to electron capture into H^-. Instead the atoms gain energy by first existing as one of the aforementioned ionic species which can be accelerated by the sheath voltage, acquiring substantial kinetic energy. This ion then undergoes a neutralization event before impacting the surface resulting in a small population of energetic neutrals localized and directed to the surface region. In the experiments on the GEC, because of the significantly dominant proportion of ions which exist as H_3^+, this process may lead to three atoms with enough energy to overcome the surface work function which can bombard the surface and lead to negative ion creation. this is supported by work done by Sharp et.al. [191] which showed the high likelihood of dissociation prior to surface interactions.

4.5.2.3 Surface coatings and their effects on negative ion formation

Something worthy of note is the potential for plasma etching of chamber materials and subsequent re-deposition on the surfaces under study. These deposited coatings can affect the surface physics, masking any differences between the underlying materials. In these experiments, the two primary chamber materials were steel and crystalline silicon dioxide (Quartz glass) in the GEC chamber window hence the likelihood of these materials coating the plates should be discussed.

The etching of SiO_2 quartz glass by hydrogen plasmas has been studied by several authors [192–195]. Of particular interest is the work of Peña et.al. [196] who directed a CW hydrogen plasma directly onto a silicon dioxide sample to observe the etch rates. The plasma density was comparable to that observed in these experiments at around $10^{16}m^{-3}$ and the gas pressure was comparable at 13 Pa. By contrast to the work of this thesis the power deposited into the plasma was relatively low, up to 100 W. The paper reported that the etch rate increased with the temperature of the quartz and rates were generally low (0.5-2.5 nm per minute) with a minimum surface temperature of 400 K.

The conditions in the GEC experiments conducted in this thesis were less ideal for the etching of the quartz glass window. The plasma was not directed onto the window meaning the particle flux to the glass surface was likely to be lower. Because of the 10% duty cycle of the plasma, the surface temperature of the quartz window did not appreciably rise above room temperature. This was measured on and around the window with an infrared thermometer. The window was also further from the plasma, (∼4 cm versus 1 cm) and mounted for viewing the plasma from the side. While the GEC plasma fills the chamber volume to some extent, the plasma density by the outer flanges is significantly lower to that in the center where the experimental work, and the metal plates, were located. Any material etched from the window would be redistributed across the inside of the chamber reducing the deposition rate per unit area on the metal plates. On top of this, the etch rate of SiO_2 at the plate surfaces would have been high compared to the rate of deposition due to the higher particle energies and densities. Due to the consistent differences between the behaviour of the metal plates across multiple trials, it was assumed that the contamination of the plate surfaces due to SiO_2 was negligible. In order to prove this conclusively, a scan of the surface compositions of each plate after the experiments would have been useful, though this was not deemed necessary at the time.

The sputtering yield of ion from the steel chamber walls was also likely to be low and thus the contamination of the surface also minimal. Information on the sputtering yield of 304 stainless steel by a sputtering ion beam was performed by Von Seefeld et. al. [197] showing maximum yields of one iron atom per hundred incident protons with energy of the order 100 eV. This is supported by Kadetov [174] who studied a GEC hydrogen plasma with applied RF powers of 1 kW or lower, similar to the work presented in this thesis. By measuring the anode and cathode potentials, the ion energy distribution function was modelled for H^+, $H_2{}^+$ and $H_3{}^+$. The model predicted ion energies of 20 eV or less and experiments measured energies of 10 eV or less. By similar reasoning to the quartz, the highest energy ions exist between the electrodes as opposed to around the inner periphery of the chamber. This would pair reduced etch rates at these inner surfaces with increased cleaning efficiency on the plates.

The most typical means of improving the efficiency of negative ion sources is by adding a beneficial coating such as a mediator layer of a low work function material to the surface of the bulk metal, reducing the potential barrier to the point where electron tunnelling into adsorbed atoms is much more likely and thus negative ion production at the surface is

enhanced. In fusion negative ion source research [198] and other related fields, [189, 199] this has been achieved by using an alkali metal particularly caesium [198, 200] which has a work function of 2.1 eV. Due to the reactivity of caesium, the additional processes involved in coating surfaces and the ease of etching of the coating, it is not always practical to use a ceasiated coating long term. As a result, experiments like those done in this thesis which attempt to improve understanding of the exact mechanisms for negative ion production may help produce negative ion sources with comparable or even improved output which have better longevity and are simpler to construct.

4.5.2.4 Positive ion species

In plasma surface interaction, ion bombardment of the electrode surfaces is a well-known phenomenon [201–203] used for etching and other kinds of surface processing. This includes surface interactions in the GEC cell and in fact represents one of its primary uses - as a testing device for etching and deposition experiments. While the bombarding ions themselves never reach thermal contact with the surface, the neutrals formed by their Auger neutralization processes can. As such, the behaviour of these species close to the surface is important to the overall plasma-surface system. In simple terms, the Auger neutralization process is the capture of an electron by an incoming ion from the metal surface. The electron is captured from its surface energy state into a lower energy vacant atomic level thus losing energy in the process to the surface. A more detailed overview of the neutralization process and other auger processes may be found in [204].

As discussed in the GEC background, section 3.1.1 onward, there are three major ion species of interest in the hydrogen plasmas used in this study. These species are the proton, hydrogen molecular ion and the tri-hydrogen cation. In each case in the GEC the ion is accelerated towards the sample surface. This is due to the plasma potential being positive with respect to the grounded sample. As such the maximum energy acquired by ions in these experiments depending on their time of flight was around 10-15 eV. As the ion approaches the surface, there exists a potential barrier between the ion and the surface. If the ion has sufficient energy, a surface electron can tunnel through this barrier into the ion, neutralizing it and potentially fragmenting it in the case of larger ions (H_3^+). In the case of a proton, the recombination can result in an neutral atom which has the potential to go on to strike the surface and undergo a backscattering event such as that described in 4.5.2.1 or a recom-

bination event such as those described in 4.5.2.2. Similarly a molecular ion may capture an electron whereby in some cases the recombination provides sufficient energy to dissociate the resulting neutral molecule. One or both atoms may then interact with the surface to form negative ions. The tri-hydrogen cation is similar with the exception that the fragments can be created in two ways, dissociation into an atom and an excited molecule or dissociation into three hydrogen atoms given slightly more incident energy. The molecule may return to the plasma bulk to participate in other reactions while the atom may be converted to H^-. In each case the ions serve to amplify the neutral-surface interaction rates. Any negative ions that form are accelerated away from the surface and into the plasma bulk, typically by the sheath voltage or in this case the 10-15 V from the plasma potential.

4.5.3 Discussion of experiments performed on the GEC in the context of aforementioned processes

The following sections attempt to systematically establish which surface properties and which processes are likely to have contributed to the negative ion results if possible. Some possible causes are explored along with the likelihood of their contribution to the trends observed in the data. These are all qualities of the surface which could affect the Auger electrons released from the surface, the behaviour of hydrogenic species adsorbed to the surface, and/or the properties of the gas molecules in the chamber.

4.5.3.1 Experimental surface properties: Thermal properties

Surface temperature is known to be an important parameter when discussing plasma surface interaction [205]. The thermal properties of molybdenum may have been responsible for this discrepancy due to increased heating of neutral particles which impacted the surface. If there had been a noticeable discrepancy in the thermal conductivity between the target plates, this would have allowed the heat from the plasma to have been more effectively coupled to the water cooled base plate resulting in a more effective loss of heat from the gas in the chamber. The cooling of gas molecules which interacted with the surface could have prevented increases in vibrational excitation thus reducing the negative ion production of that surface by some margin. The thermal conductivities of the metals used were 138 $W(mk)^{-1}$, 173 $W(mk)^{-1}$ and 14-17 $W(mk)^{-1}$ for molybdenum, tungsten and 304 stainless steel respectively. Given the similarities between steel and tungsten, this meant that the

thermal conduction properties of the surface had no significant bearing on the negative ion formation. The trends between metals did not match the differences in conductivity with molybdenum and tungsten being similar by that metric. This makes sense due to their similar atomic mass and crystal structure.

Instead, a parameter worthy of discussion is the uniformity of contact between the different plates and the grounded electrode. What may appear to be a smooth surface is often marked by microscopic divots, peaks and general surface roughness. This surface may also be imperceptibly warped due to machining stresses or handling regardless of surface polishing. The plates used were polished roughly rather than to a mirror shine and the lower GEC electrode is also not mirror-polished and could also be slightly warped. The surface roughness and warp of the plates and electrode were not well known resulting in less than ideal thermal and electrical contact between the two. The quality of this contact could have throttled the heat transfer from the sample to the cooling system resulting in inhomogeneous temperature profiles across each sample and/or general temperature differences between samples during operation. The pulsed plasma and subsequent temperature checks were performed in an effort to limit this effect to a minimum. The temperature of each plate was measured with an infra-red thermometer immediately after returning the chamber to atmospheric pressure and in all cases was found to be within 2 K of the initial temperature. Thermal behaviour within the pulse was not diagnosed and may have contributed to the discrepancies between the results for each plate assuming that the plate had time to equilibrate with the cooling system during the readmission of gas. If the thermo-electric contact could be diagnosed an/or made sufficiently uniform for the different samples, the influence of this transfer to the cooling system would be reduced or eliminated, allowing for better understanding of the effect of the thermal properties of the plate metal.

Owing to the similarities in trends between this and similar studies by others (see comparisons between [165] and [122]) there is some evidence that points towards other surface properties being dominant over temperature in this work. It would still be advisable to quantify the relative contributions in a future version of the experiment in order to determine relative importance.

4.5.3.2 Experimental surface properties: Work function

In the case of metals like caesium, a lower work function leads to a dramatically improved negative ion yield from the atomic adsorption and conversion process. It may have been possible that there was some small but consistent difference in the work functions of the surfaces which may explain the H^- results. The work functions of the metals examined were compared for several crystal planes to estimate the magnitude of their contribution to the results. Values for one common crystal plane are reported here because differing planes within one sample material exhibited similar values and the scaling between these values was similar between materials. The work functions for the (100) planes of tungsten and molybdenum are 4.63 eV and 4.53 eV respectively. To clarify, other crystal planes for these pure metals show similar work functions differing only by around 0.3 eV or less. Being an alloy, steel has a more complex crystal structure and minor shifts in the work function may be achieved using different recipes. Nevertheless, the work function for poly-crystalline stainless steel (304) which is a good proxy for the 304 steel used in this experiment is around 4.3 eV. The work function of stainless steel was the lowest which matched with steel being the best in terms of negative ion production at 25 Pa however the difference between the work functions is small compared to the differences in the negative ion behaviour. The most similar work functions were those of tungsten and molybdenum whereas the negative ion behaviour was most similar between steel and tungsten. Therefore it was unlikely that any differences in the work function were a dominant mechanism in the negative ion production, though this property does relate to many of the processes involving surface interaction and so must be part of the equation somewhere.

4.5.3.3 Experimental surface properties: Surface loss coefficient of hydrogen

A parameter worth noting, relating to the capture and recombination of hydrogen atoms on the surfaces, is the loss coefficient of hydrogen (β_H). If some surfaces readily lose hydrogen atoms more easily than others, the atomic hydrogen density in the plasma would be higher and the surface recombination rate would be lower resulting in fewer molecular species which could be excited to a state suitable for the DA process. Additionally, atomic hydrogen can cause vibrational relaxation of already excited molecules, further reducing the DA reaction rate. Atomic hydrogen can also lead to molecular hydrogen formation in the bulk plasma, however this is via the associative detachment (AD) channel which requires the destruction

of a hydride ion in order to proceed.

In addition, the surface roughness plays a role in the loss processes due to the variable surface area. The samples acquired from Testbourne were machined and polished by the company however their surface roughness was not standardised. The steel sample machined on site underwent some polishing though not to a mirror finish but was not evaluated for surface roughness. This introduces another quantity which would ideally be standardised between samples, however this would be a task for future expansion on this work.

If the adsorption of hydrogen onto the surfaces tested was similar, perhaps the relative ease of escape after capturing an electron was a potential culprit for reduced negative ion density. A reasonable estimate of this factor is β_H. In general, exact values are not commonly available due to a dependence on atomic temperatures however a relative scaling between materials can be evaluated as in [206]. The authors of this paper explain that the surface material has a significant impact on the atomic density. In this paper it was explained that the value of β_H for tungsten was around half the value for stainless steel while a value for molybdenum was not reported. In similar work done by J. Ellis using aluminium and copper surfaces, the beta coefficients did not scale in a way which correlated with the negative ion data for the investigated materials. Similarly the discrepancy in beta between steel and tungsten would seem to imply a significant difference in desorption from the surfaces which was not observed in the negative ion data.

A quantitative measure of the atomic hydrogen densities was also performed by J. Ellis and colleagues [165]. This involved the use of Two-Photon Absorption-Laser induced Fluorescence (TALIF) [207] to measure H density for two samples (copper and steel) as a function of power for three gas pressures. These were initially chosen because like molybdenum the copper surface showed significant differences in the H^- density within the plasma. Both samples showed similar scaling of atomic hydrogen densities with power and pressure as well as agreeing with existing trends and values [205]. Certainly, the trends observed did not correlate obviously to the negative ion trends seen above. A further test at 25 Pa for the three materials presented here as well as copper and aluminium showed aluminium as having the highest atomic hydrogen density while tungsten and molybdenum had the lowest. All were, however comparable in magnitude and none matched the negative ion discrepancies between surfaces.

While the atomic hydrogen density increased with increasing gas pressure, this wasn't

necessarily a forgone conclusion. An increase in pressure for constant volume and gas temperature represents an increase in the number of molecules present by the ideal gas law. A known trend for identical RF power is the increase in electron density with increasing pressure. This leads to more electron-molecule collisions which in turn reduces the electron temperature and the probability of electron driven dissociation. In this case, an increase in pressure would decrease the relative atomic density. Conversely, an increase in gas pressure reduces one of the primary loss mechanisms of atomic hydrogen: losses to the chamber walls [208]. While the increase in the atomic hydrogen density with pressure could explain the decrease in negative ions, more study is required to examine the relative contributions of vibrational de-excitation of H_2(V) and associative detachment.

4.5.3.4 Experimental surface properties: Lattice trapping properties

Another property of crystalline metal surfaces is their ability to trap particles, in this case hydrogen atoms, in the gaps in interstitial sites of the metallic lattice This principle is illustrated thoroughly in [209] which gives a full description of this trapping and related processes with hydrogen. A higher trapping fraction would allow a greater volume of hydrogen to be adsorbed to the surface and thus potentially lead to an increase in negative ion production under similar plasma conditions. The lattice constant of a pure crystalline tungsten bulk is 3.155 angstroms (Å) [210], that of pure molybdenum is 3.147 Å [211], and steel (304) is around 3.593 Å [212] with BCC, BCC, and FCC unit cells respectively.

The atomic radii of tungsten, molybdenum and iron are respectively 2.1 Å, 1.39 Å, and 1.26 Å which are similar. Type 304 stainless steel typically includes 18-20% chromium and 8-12% nickel with up to 2% manganese making the lattice more complex. Surface compositions were likely similar to the bulk because the steel plate was manufactured and mechanically polished on site, where mechanical polishing can be shown (albeit on a nanocrystalline surface) to have little effect on the surface composition [213]. The atomic radii of chromium and nickel are 1.28 Å and 1.24 Å respectively, similar to that of iron. Despite these similarities, steel and pure iron would likely not exhibit the same behaviour if tested for negative ion production. An extension of this study to use an iron plate as well as nickel and chromium would be useful to characterise the contributions of these metals to the behaviour of steel. This may not simply be an additive relationship if there are interactions between the lattice constituents which change the interaction between the surface and the plasma. The relative

contributions to weak binding sites expected to play a part in H_2 (V) formation would also be useful. From a purely volumetric perspective, the interstitial sites are similarly suitable for the presence of atomic hydrogen including steel unit cells with chromium and/or nickel present.

The entropy of solution of hydrogen in tungsten and molybdenum also does not follow the trend of the negative ion data. There is also no major difference in the chemisorption energies for tungsten and molybdenum [214]. The case of stainless steel is more complex again due to the presence of significant concentrations of chromium and nickel. In terms of chemisorption energy, if the only important parameter is the chemisorption energy of the surface atom encountered, the energies are similar for the three main constituents of the 304 SS [214]. Barring significant changes in the interaction between the hydrogen atomic orbital with the valence orbitals of the lattice atoms, there should be no major differences in the relative adsorption of hydrogen to the surfaces of the samples used.

4.5.3.5 Experimental surface properties: Secondary electrons

This section examines the likelihood of an increase in negative ion production due to the release of high energy secondary electrons from the surface due to ion bombardment. It is known that particle bombardment of surfaces causes several effects such as surface restructuring, etching, deposition and importantly, secondary electron emission. In this case, ions are accelerated by the plasma potential into the sample plates over the grounded electrode.

The secondary electron emission coefficients for tungsten, molybdenum and stainless steel are poorly defined at low energy. Some measurements exist in the 50 eV – 1 KeV range but most have been made significantly above this range from several hundred KeV to the MeV scale. This is due to the fact that a popular method for measuring secondary electron yields particularly for clean metal surfaces is by using an ion beam or particle accelerator. The secondary electron emission coefficient (henceforth SEEC) for clean tungsten was estimated by Sternberg (cited in [215]) for low energy proton bombardment as approximately 0.035 electrons per ion impact. The values for $H_2{}^+$ were around 0.02 electrons per ion for ion energies of 50, 100 and 200 eV increasing slightly over the range as measured by Propst and Luscher [216]. The variation at low energy between the two ion-types was negligible. As such, it may be reasonable to assume that the values for the SEEC of the tri-hydrogen cation are likely to be similar in this energy range.

Values of SEEC for clean molybdenum metal were measured by Mahadevan et.al. [217] for low energy proton bombardment as well as for hydrogen 2+ and 3+ molecular ions. The values for proton impact ranged from 0.05 to 0.11, those for H_2^+ were 0.01 to 0.14, and those for H_3^+ were 0.03-0.09. These values are all extremely close to each other, similar to the trend observed in tungsten. This also strengthens the assertion that the H_3^+ SEEC for tungsten is similar to that of 2+ and 1+. For stainless steel (304) in a parallel plate RF discharge configuration at 24 Pa, the SEEC was found by Bohm and Perrin [218] to be in the region of 0.06 and 0.09 depending on the voltage of the applied RF power (200-400 V). The cleanliness of the surface has been found to affect the process but the difference is not significant compared to the incident energy scaling.

The existing work on secondary electron emission coefficients implied that the secondary electron yield from the different surfaces was likely to be extremely similar. This was supported by phase resolved optical emission spectroscopy (PROES) measurements made by J. Ellis [165]. A more detailed explanation of PROES can be found in T. Gans et.al [219] however a brief explanation is given here. PROES works by measuring the electromagnetic emission of a specific atomic transition, resolved in space and time using a fast gated ICCD camera equipped with an interference filter. In these experiments, the specific state within the electronic scheme of hydrogen was the Balmer-alpha transition with emission at 656.45 nm. The camera records the relative intensity of this transition across a viewing chord of the plasma (vertical between the electrodes in this case) as a function of phase within the RF cycle. Using this and knowledge of the effective lifetimes of the upper electronic levels, the excitation rate of the transition may be deduced. The state lifetimes (and atomic hydrogen densities see section 4.5.3.3 for discussion of TALIF and H densities) were also measured by J. Ellis to be 12 ns using a diagnostic known as TALIF.

The PROES measurements shown here initially are those performed by Ellis at 500 W. This was because the difference in the H^- density was larger here than at low power (200 W). As can be seen in figures: 4.17 and 4.18 there were no significant differences in the atomic emission of the plasma throughout the RF cycle corresponding to the changing of the surface material. The samples are located at the bottom of each figure while the powered electrode is located at the top. In each figure the onset of sheath expansion is labelled as (a) ($\approx$ 40 ns) along with the point of full expansion (b) ($\approx$ 70 ns). If the different surfaces were generating significantly different numbers of gamma electrons, there would have been

a noticeable difference in atomic excitation and thus measured emission at point (b) when the sheath was fully expanded. Examples of this kind of peak can be found in [220, 221].

Doyle et.al. [221] performed PROES measurements on a thruster system using a radio frequency plasma in argon which also shows how the PROES results may vary under different conditions for the same plasma source. While that is a thruster and not a GEC cell, the changes in the excitation profile relative to the RF phase were significant. Such changes were not observed in the experiments performed on the GEC cell in hydrogen when only switching the surface material, hence the conclusion that it had little effect on the gamma electron population.

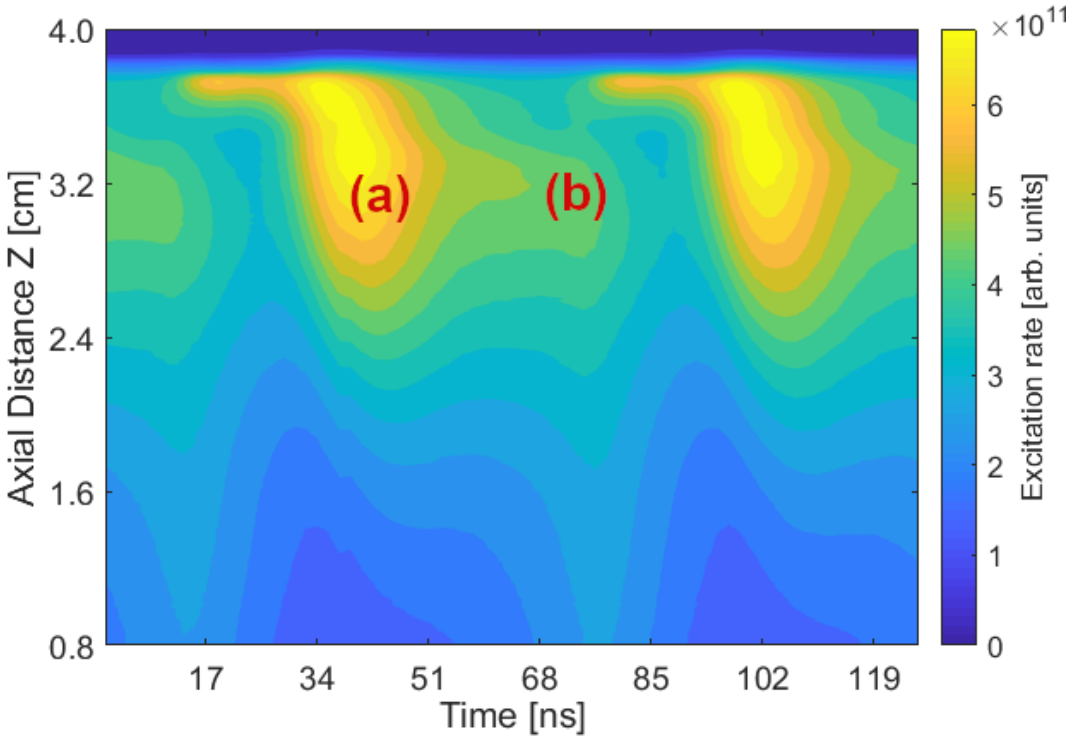

Figure 4.17: PROES image showing the atomic emission profile of hydrogen as a function of time across two RF cycles at 500 W applied with the molybdenum plate installed. Labelled are (a) the initial sheath expansion during the RF cycle and (B) the time of maximum sheath expansion.

By comparison, figure 4.19 shows the effect of changing the applied RF power, reducing it to less than half. The effect of this is evident whereby, while the hot gamma electrons exist spatially in the same region near the upper powered electrode, the signal is weaker and occupies a smaller portion of the vertical space.

These measurements validated the expectation that the gamma electrons released from

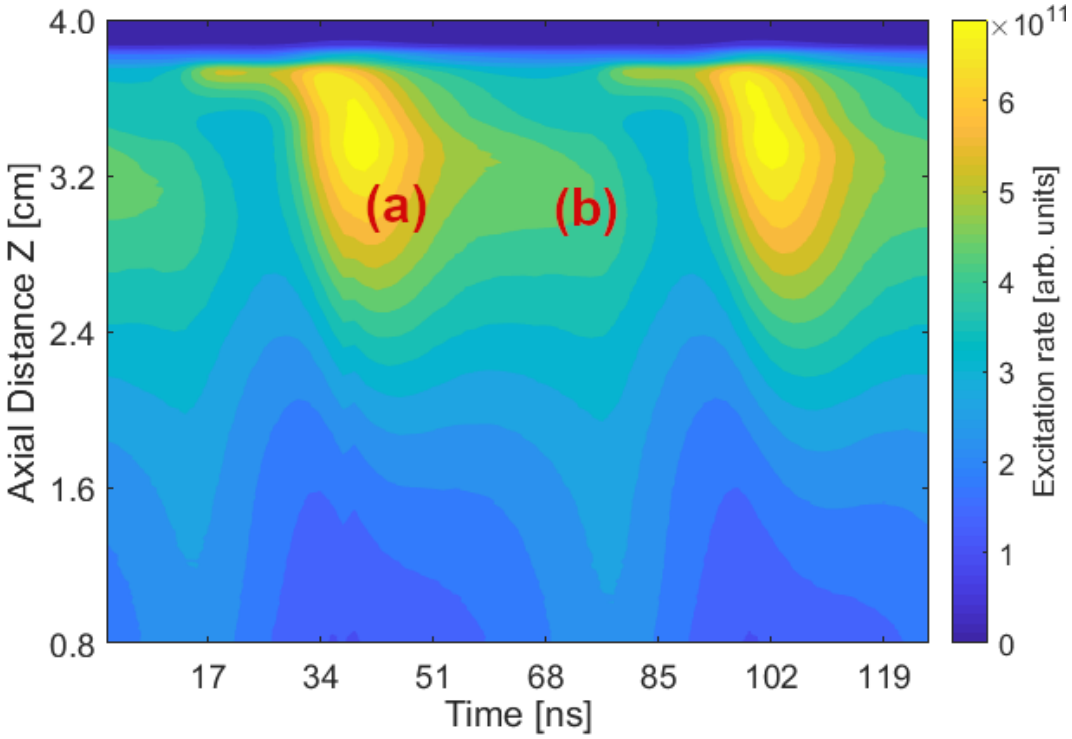

Figure 4.18: PROES image showing the atomic emission profile of hydrogen as a function of time across two RF cycles at 500 W applied with the tungsten plate installed. It can be seen that the areas of high emission are nearly identical in shape and time in the RF cycle between this and the molybdenum. Labelled are (a) the initial sheath expansion during the RF cycle and (B) the time of maximum sheath expansion.

the surface were similar between samples for a given applied power and the ratio of e_{fast} to e_{slow} did not change appreciably due to the surface type.

4.6 Summary

To summarise, while further work is required to completely diagnose the differences in the negative ion dynamics for different surface materials, a number of mechanisms have been identified as having little direct effect. Other mechanisms and properties have been identified as being potential contributors to this behaviour. Owing to the complexity of the system it is not known precisely what caused the discrepancy between the materials studied here. It is also not well understood why steel and tungsten exhibited such a similar trend which itself was significantly different from that of molybdenum. In the additional work by J. Ellis, and J. Branson [165], aluminium and copper appeared to behave similarly to molybdenum suggesting some property or properties which commuted between specific metals e.g. a class

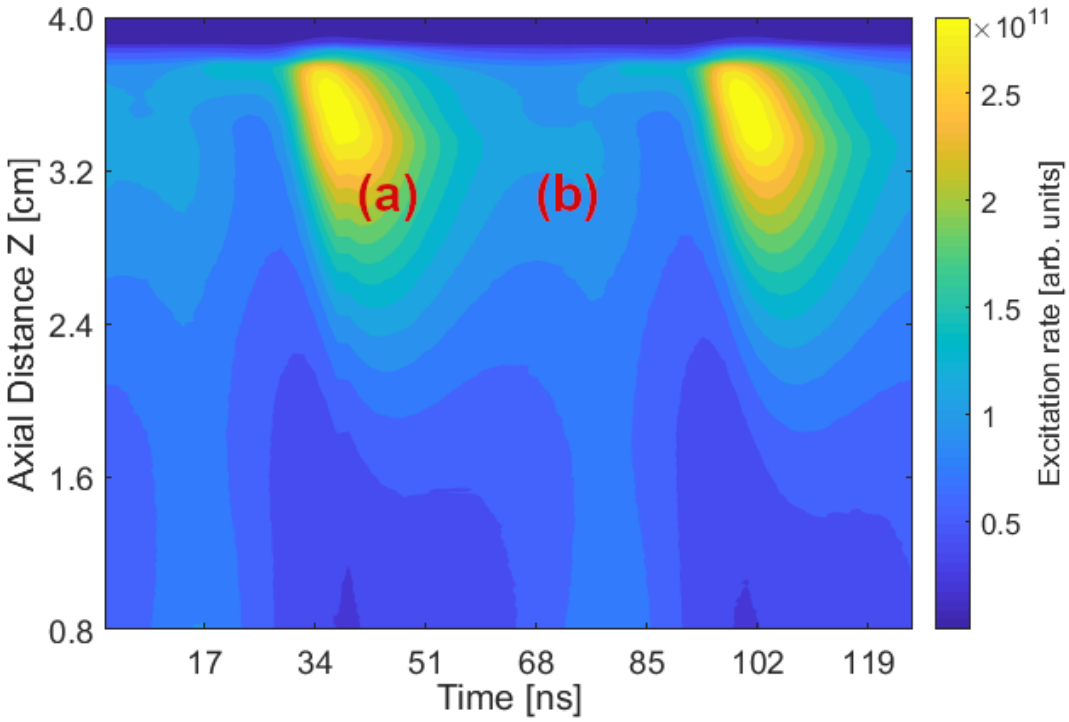

Figure 4.19: PROES image showing the atomic emission profile of hydrogen as a function of time across two RF cycles at 200 W applied with the tungsten plate installed. While this image does not show a peak of gamma electrons at the max sheath expansion, it is clearly different to the 500 W examples. If the material plate had caused differences in the PROES it would have been possible to deduce that the material was having an effect on the electrons released from the surface. Labelled are (a) the initial sheath expansion during the RF cycle and (B) the time of maximum sheath expansion.

of metals with molybdenum-like properties and one for steel-like properties.

One of the potential processes leading to negative ion formation worthy of further study is the acceleration and subsequent neutralization of an abundant H_3^+ ion into energetic atoms. These atoms then possess enough energy to undergo backscattering processes, overcoming the metal work function which can lead to the creation of excited molecular species or atoms which can capture an electron via charge exchange before returning to the bulk as a negative ion. The TALIF measurements indicated that the differences in atomic density were small between materials so the neutralization and dissociation of H_3^+ into atoms is likely not significantly different between metals. This opens up the possibility for there to be differences in the production of $H_2(V)$ and H^- by impingement of the tri-hydrogen cation.

Another potential source of the discrepancy is the hot-atom recombination process for each surface. HA recombination releases vibrationally excited hydrogen molecules suitable for dissociative attachment into the plasma bulk and is likely strongly dependent on weak

binding sites on the material surface. If it could be modeled and confirmed that these sites were present on steel samples and not on those of aluminium and molybdenum it would imply that this effect was significant. The investigation of samples of pure iron, chromium and nickel would also help to diagnose the behaviour or stainless steel by breaking the material down into its fundamental components. A carbon sample would be interesting however there is significant hydrogen trapping to consider which could dominate over the effects under study.

In both processes, the vibrational energy distribution function (VEDF) of the hydrogen molecules is altered. By measuring the VEDF for the materials studied and extending the study to more surface materials, a better picture could be developed of the contributing factors. It would also be useful to examine the contributions of surface geometry to negative ion dynamics, whether there is simply a scaling with presented surface area or if certain structures could be used to enhance or diminish the differences between materials observed. If the experiment were to be repeated as presented in this work, polishing all samples to a mirror finish and assessing their surface roughness would be ideal as well as attempting to homogenize thermal contact to the grounding plate.

It is hypothesized that in this work at higher pressures, increased numbers of H_3^+ ions and more hot atom recombination led to more vibrationally excited molecules. With sufficiently high gas pressure, the collisionality increased to the point whereby the temperature of the available particle species was prohibitively low. That is to say that there was insufficient energy for the significant formation of vibrationally excited hydrogen molecules, either by the hot atom process due to reduced dissociation of molecules by electron collision, or by the tri-hydrogen cation process due to the low impact energy resulting in vibrationally de-excited molecules and more neutral atoms being released from the surface. The additional atoms from the increased gas pressure and low energy H_3^+ impacts would go on to diminish the negative ion population, both by contributing to vibrational de-excitation and by increasing the rate of associative detachment, destroying negative ions.

These volume production observations at low pressure are in line with previous work. At lower pressure, the negative ion production rate decreased with added RF power due to the overabundance of fast electrons among all samples leading to increased rates of dissociation of negative ions coupled with reduced production of excited molecules at the surface leading to lower rates of dissociative attachment.

The primary learning of the experiments performed on the GEC cell relates to the importance of surface physics to the negative ion density in proximity to said surface. Not only does the presence of a surface have a significant effect on the negative ion densities measured approximately 10 mm from the surface but the composition of the surface also plays a significant role. This is relevant for MAR detachment research for fusion devices because the enhancement of detachment phenomena either close to the strike point or further away would improve the cooling efficiency of the detached plasma. While tungsten was a decent material in this small sample size at these conditions, as well as having good thermal properties in general, it may not represent the best choice for some plasma facing divertor components. From these studies alone it is not yet clear what property of the materials investigated was responsible for the differences in negative ion production. Some properties have been discounted as being the single key material property while others have gained credence. Due to the limited number of suitable materials for fusion reactors in general, the optimization of this parameter should not be overwhelmingly complex but is an important avenue to thoroughly investigate.

Chapter 5

Results of experiments performed on the YLPD

5.1 Chapter introduction

This chapter contains results from the York Linear Plasma Device (YLPD). For simplicity and comparison with results from the experiments on the GEC system the pressures in the body of the text are expressed in Pascals. The results are presented in order of relevance from initial testing of the degree of detachment using ion flux measurements, through gas temperature measurements to the negative ion data itself. This helps to build a clearer picture of the processes happening in the YLPD regarding the Molecular Activated Recombination (MAR) detachment state.

5.2 Ion flux measurements

Measurements of the ion flux to the target plate of the YLPD as a function of the target chamber pressure are shown in figure: 5.1. The magnitudes of the measurements were similar across the varied solenoid currents as well as the trend shape with pressure. As the pressure was increased from the base value, the ion flux sharply increased to a maximum around 0.13 Pa before beginning to decrease with additional gas. The downward trend was approximately linear through a range of pressures before changing gradient somewhat abruptly to another linear trend. The peaks in the profiles were observed to correspond closely to the onsets of MAR pinkish glow. The secondary transition was observed to coincide with the shift from

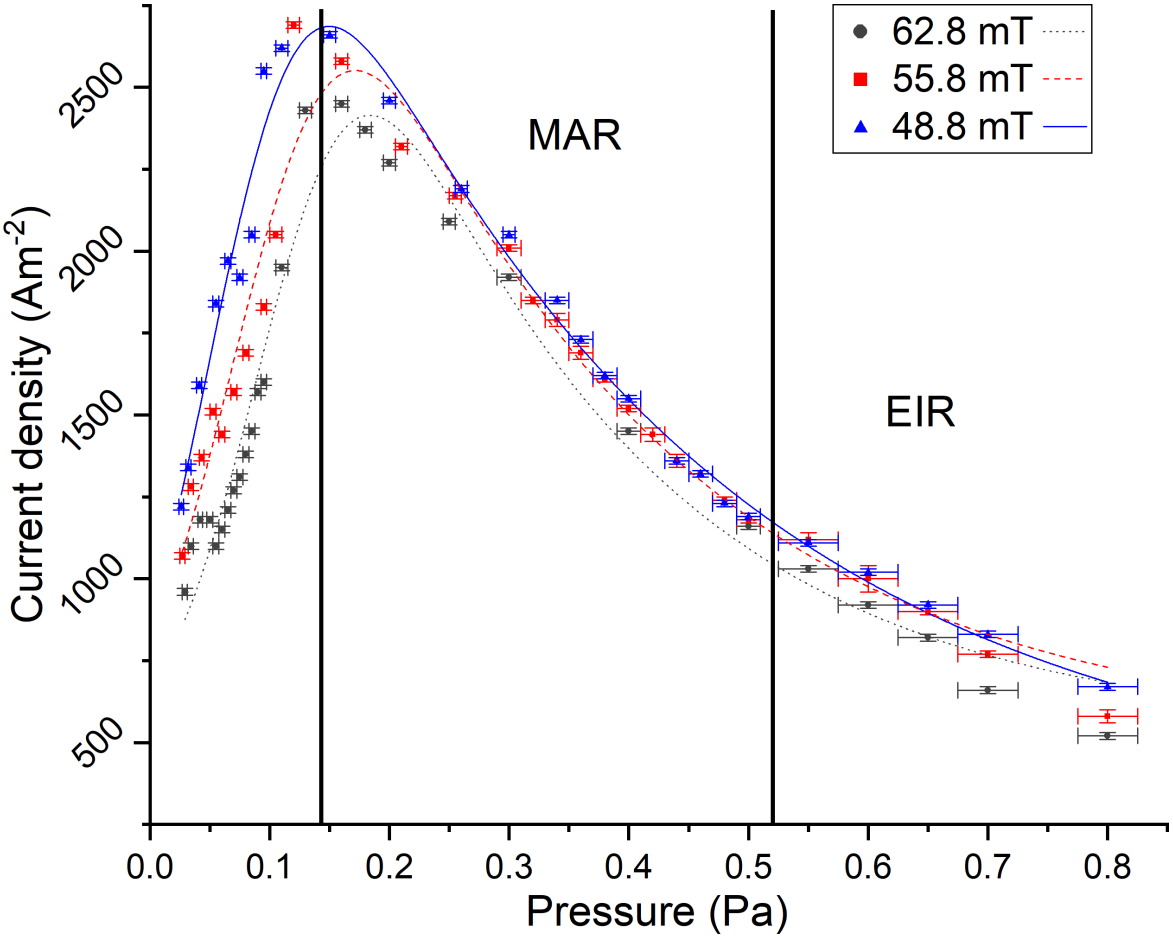

Figure 5.1: Ion current measurements for different axial field strength as functions of gas pressure. The absolute values and trends are similar for all three solenoid fields. The transition to the detached regime can be seen in the sharp rollover at the top near 0.15 Pa. There is also an apparent switch between MAR and EIR corresponding to the kink in the descending part of the curve. The point where this kink occurs corresponded closely to the visual transition between the two types of detachment.

the MAR glow to the blue glow of the EIR / three body recombination dominated regime. It is noteworthy that the ion flux was reduced more per unit change in pressure during the MAR regime when compared to the EIR regime. This implied that the MAR process is more efficient as a recombining mechanism when considering the reduction of ion flux.

In examining the MAR plasma, this plot implied that the prime pressure ranges of interest were between base pressure and 0.15 Pa for the onset of MAR, and 0.1 Pa to 0.5 Pa for the dynamics within and exiting an MAR dominated plasma. No negative ion measurements were made over 0.5 Pa. The similarity in ion flux for the three field values is not unexpected as the source generates similar plasma density regardless of the solenoid conditions.

5.2.1 Central plasma column electron density and temperature profiles

To contextualise the negative ion measurements, profiles were taken for the electron density and temperature as functions of the beam radius. The electron density was assumed to be near-identical to the ion density, particularly in the central region of the beam where the ionization fraction was high. The ion density was measured with the movable probe as described in 3.2.5. These measurements were performed with a solenoid current of 400 A unless otherwise stated.

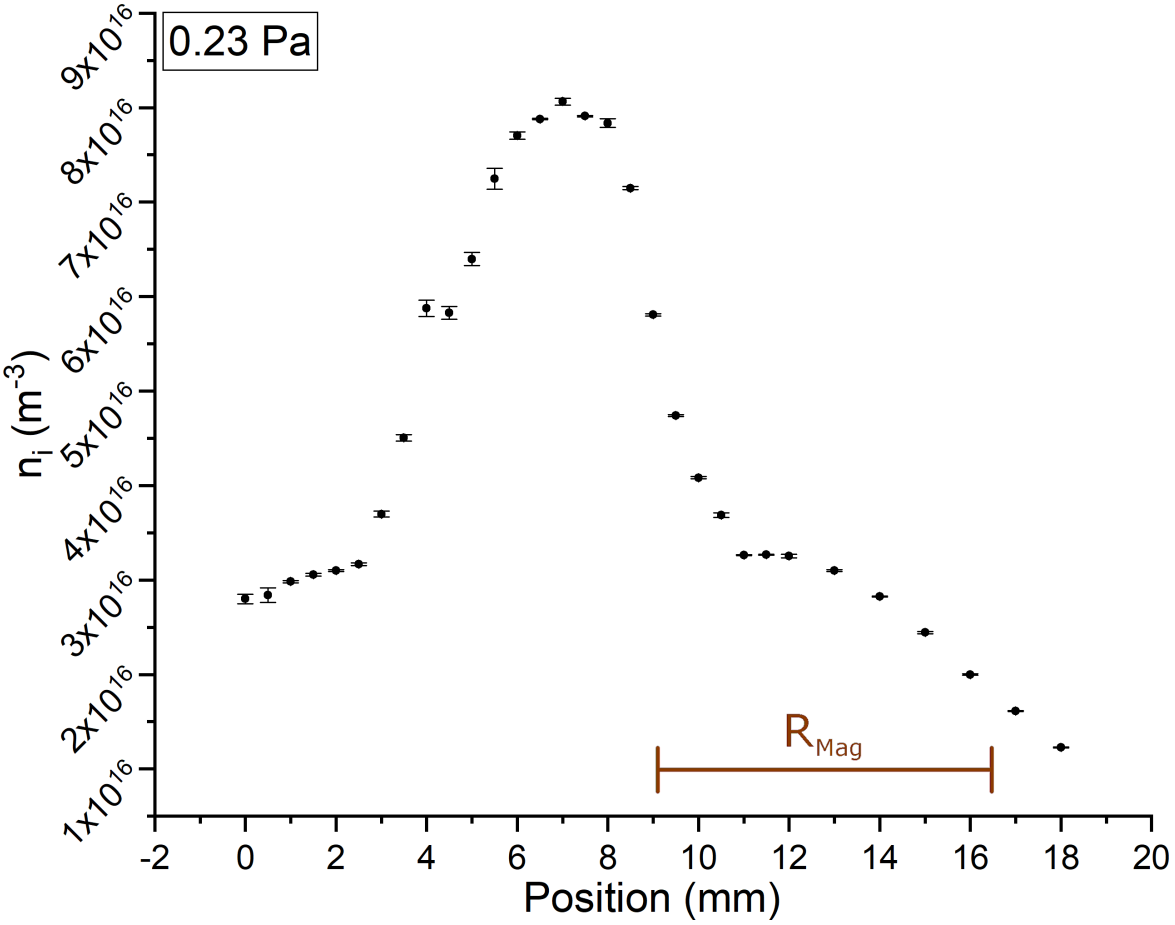

Figure 5.2: Ion density profile as measured by movable probe. The red bar shows the approximate region where the negative ion measurements were made. It is possible to see how dramatic the change is between the central region and the outer halo area. By quasineutrality, the ion density may be used to approximate the electron density

The ion, and by extension the electron density shown in figure 5.2, exhibited a somewhat Gaussian peak centered on a secondary curve outside the central plasma beam. This central peak likely corresponds to a combination of the size of the filament in the source and the diameter of the aperture between the source and the upstream portion of the chamber. The

wider portion of the plasma exhibited a slight curve before decreasing approximately linearly with additional radial distance from the core beam. This illustrated the structure of the beam as a whole including a faint glowing halo region present when gas was puffed into the target chamber for MAR detachment. The core density with puffed gas was approximately six times that without, see figure 5.4.

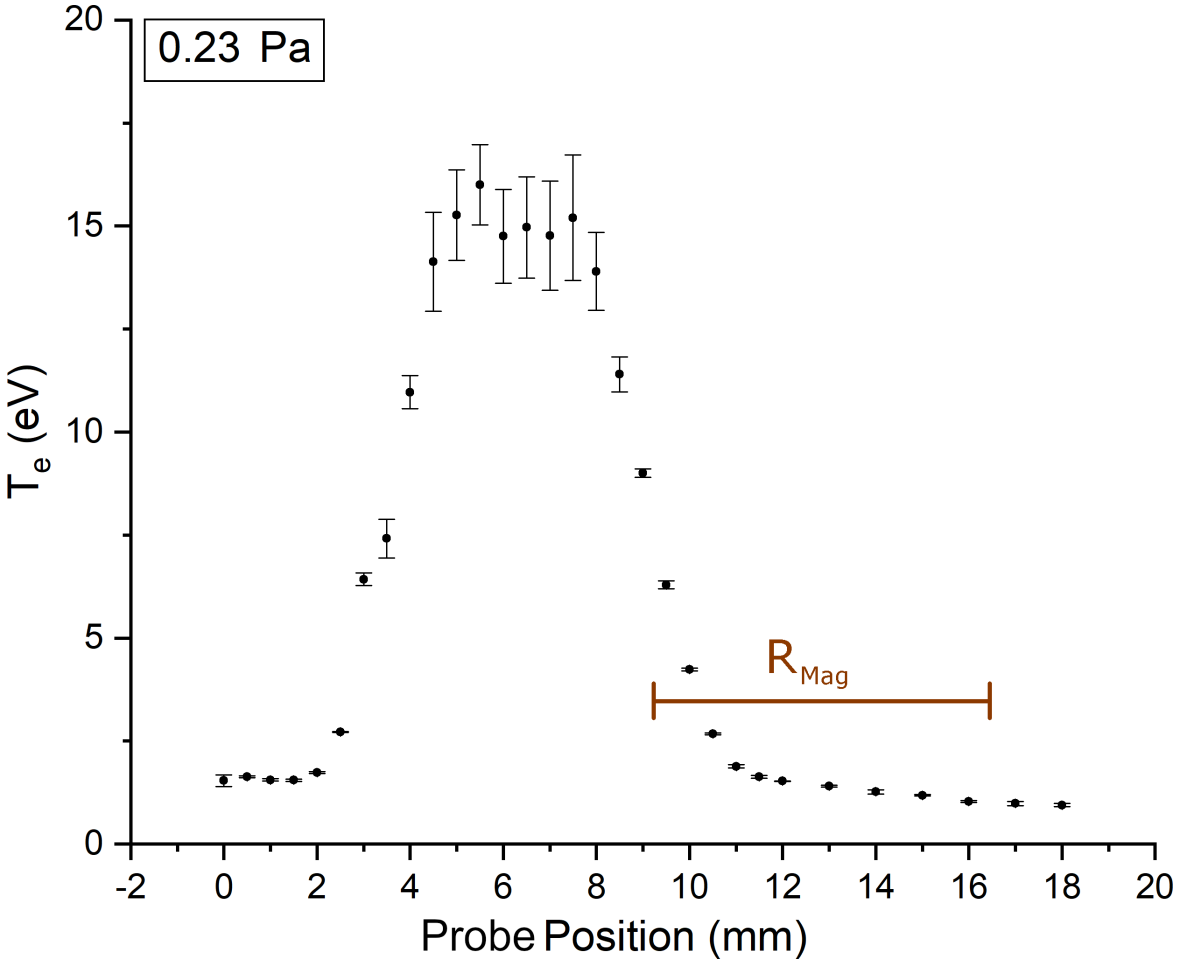

Figure 5.3: Electron temperature profile as measured by movable probe. The red bar shows the approximate region where the negative ion measurements were made. The profile more closely resembles a Gaussian distribution albeit with a slightly flatter top.

The electron temperature of the beam (5.3) under MAR detachment conditions at 0.23 Pa exhibited a similar trend as the ion density (involving a sharp peaked distribution) though with a smoother tail-off far from the beam center. The width of the sharply peaked region was approximately the same according to the density and temperature profiles. The peak temperatures measured in this instance were higher than have typically been measured in previous work. The plasma source had been upgraded and reconfigured before the com-

mencement of this work which would explain this discrepancy. Another potential source of systematic error was the switch between the movable probe which had a short, thick cylindrical tip geometry compared to the thin long photodetachment probe tip (specifically swapping from a 1 mm tall, 1 mm diameter tip to a 10 mm long 0.1 mm diameter tip). It was easier to calculate electron temperature values for measurements made outside the main plasma beam as the I-V characteristics showed a clearer plasma potential and thus the transition region was easier to identify and fit.

5.2.1.1 Scaling of core parameters with pressure

The ion density, and thus by quasineutrality electron density, increased sharply with added gas as the central beam caused significant dissociation of the incoming molecules (figure 5.4). The density peaked before slowly starting to decrease towards the transition from (Molecular Activated Recombination) MAR dominated plasma to (Three Body Recombination) TBR dominated plasma. The pressures in the TBR dominated region were not examined as the TBR regime was not important for Fulcher analysis at this time (lack of sufficient molecular emission). The point at which the increase in density began to stop (around 0.17 Pa) was similar to the maximum in the intensity plots of the Fulcher bands vs pressure figures: 5.6 5.7.

The electron temperature in the core rose sharply with the initial addition of gas and then decreased with additional puffing. There was a clear transition in the core temperature after the initial puffing in the range of 0.1 Pa to 0.2 Pa followed by a gradual decrease across the rest of the range. The brief increase in electron temperature is likely to be a consequence of the first data point being an underestimate. According to previous measurements on the YLPD core electron temperatures at high arc current should be closer to a maximum of 15 eV. When compared to the density graph (fig 5.4) which behaved as expected, the apparent low electron temperature was thought to be a consequence of the low-profile probe missing the higher energy portion of the electron energy distribution function (EEDF). The fastest electrons were moving parallel to the largest portion of the collection area with high velocity with reduced collisionality due to no target gas feed.

The electron velocity parallel to the magnetic axis should be comparable to, or greater than the ion velocity, measured previously by Russbridge et. al. to be around 10^5 m s^{-1} [166]. An estimate of the axial electron drift velocity can be found by assuming the electrons are

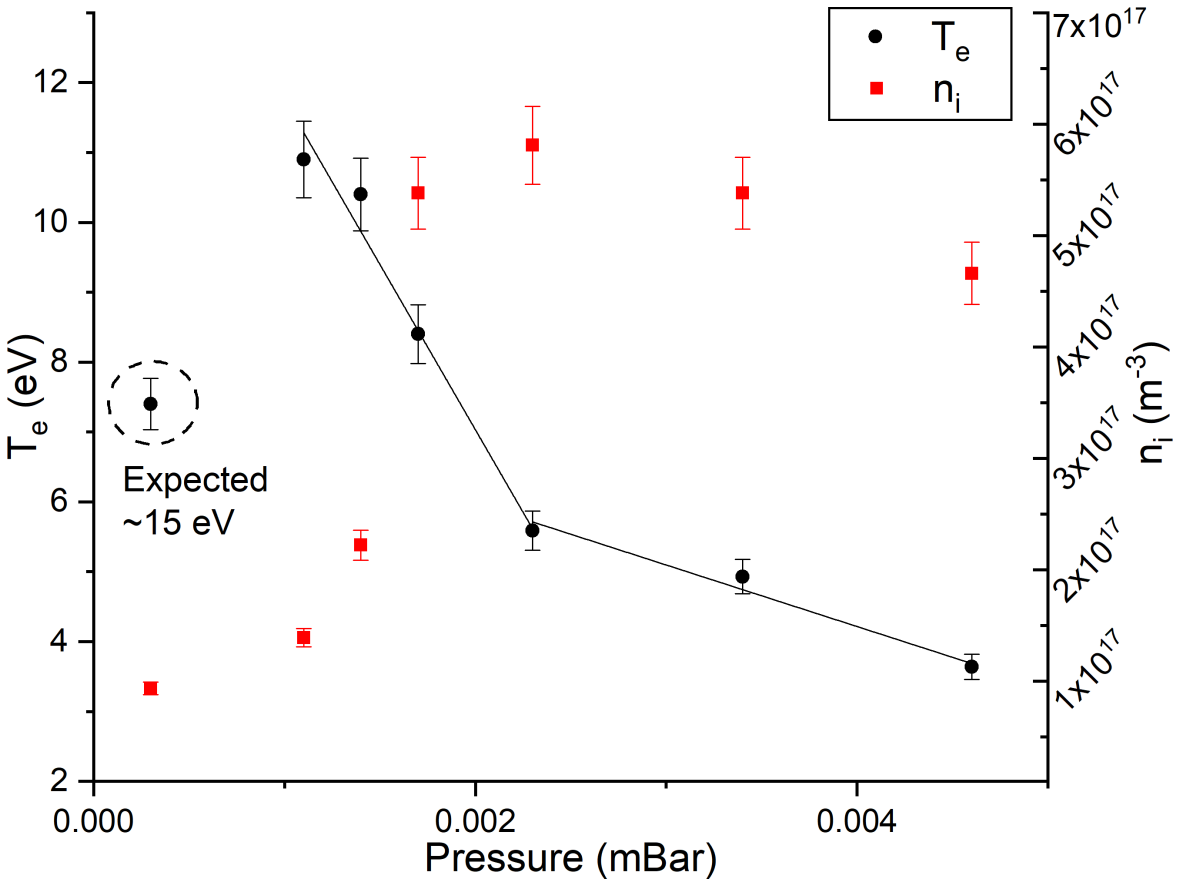

Figure 5.4: Core ion density and electron temperature as functions of pressure using the adjustable probe in a fixed approximately central position. There is a dramatic increase in density as hydrogen molecules are efficiently dissociated into atoms and/or ions. Dissociated atoms can also be impact ionized by the hot central plasma beam before recombination effects begin to take over. There is a sharp drop in electron temperature just before the density spike transitioning into a gentle decline as more gas was added.

accelerated into the chamber from the source by the -65 V intermediate electrode potential (after having sufficient velocity to overcome the repulsive nature of the electrode). In this case, the velocity is approximately 5×10^6 ms^{-1}. The thermal velocity was calculated assuming the 15 eV central temperature measured in previous experiments [3] and expected of this data point. This value was around 1.6×10^6 ms^{-1} meaning the two velocities are comparable. As such, the probe missing a significant portion of the electron population seems unable to explain such a drastic underestimation of the electron temperature.

5.2.2 Fulcher band results from the YLPD

5.2.2.1 Fulcher band intensity vs pressure

A useful estimate for bench-marking the degree of MAR was to plot the relative intensity of the Fulcher bands as a function of pressure. This has been done to some extent in previous work however in this case more data points were included over the pressure range. Figure 5.5 shows an overview of the band intensity as a function of pressure. This gave an estimate as to the pressures whereby the molecular emission was in general at a maximum. The purpose of this in the experiments to follow was to provide some insight into which pressures should be focused on for the negative ion measurements.

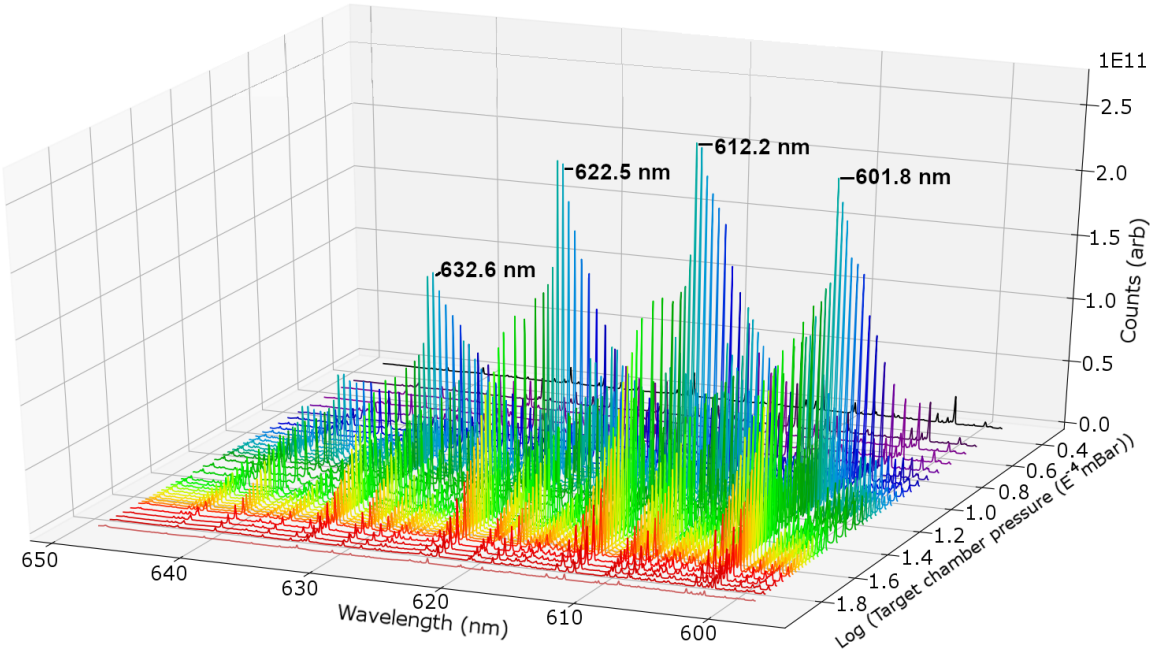

Figure 5.5: Overview of the Fulcher band intensity as a function of target chamber pressure. The colours correspond to the log of the pressure values. There is a maximum around 1.0 on the log scale (bottom right axis) in most/all of the bands. This implied the potential for there to be strong negative ion presence at pressures around this value.

A clearer picture of the general trend of the emission may be found by examining the intensity profile of a single peak. In this case the peak chosen was the first peak arising from the transition associated with the j=1 rotational level of the 0-0 band (j being the rotational quantum number of the molecular excited state). The intensity profile is shown in figure 5.6. The V=1 peaks in the other bands showed similar trends with a sharp peak around 0.15 Pa implying that pressures around this value were of interest. There was a sharp drop-off in

intensity up to 0.2 Pa followed by a smooth roll-off into the TBR dominated pressure range ($>$ 0.5 Pa) before decaying away withing the TBR regime.

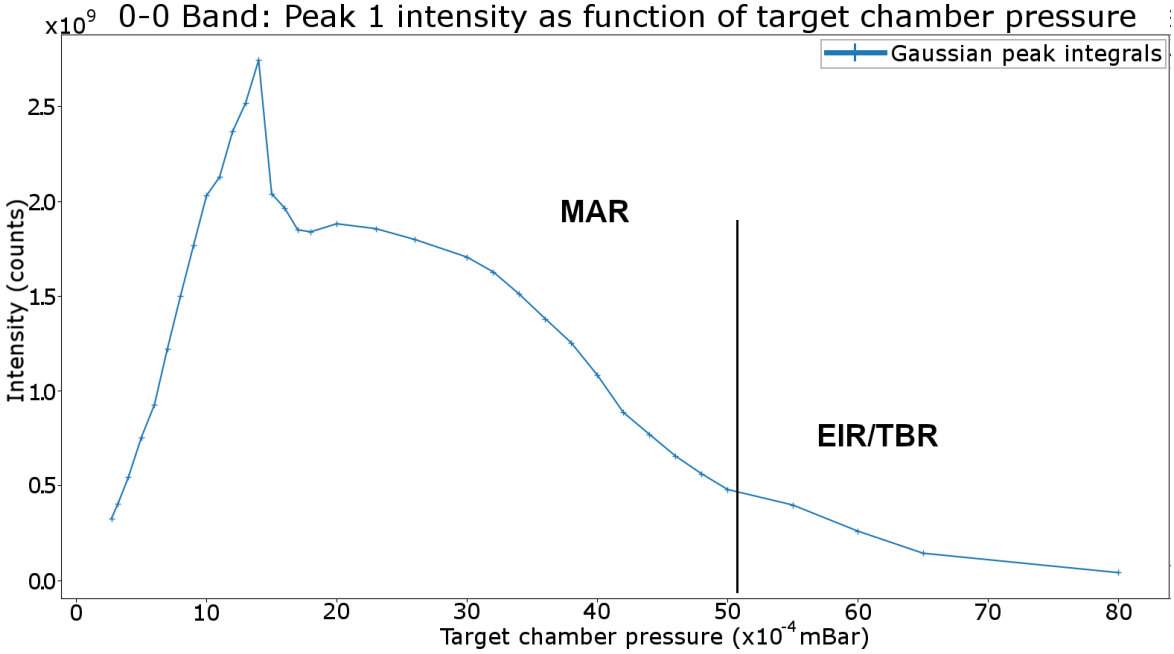

Figure 5.6: Intensity profile of the first peak of the 0-0 band, used to gain an approximate range of study for the negative ion measurements and a general idea of the MAR detached region.

The intensity profile varied slightly between rotational levels within each vibrational band as shown in figure 5.7. The first through third peaks of the 0-0 diagonal band displayed a trend in line with fig 5.6 while both the fourth and fifth peaks were of the form of fig 5.7. In these higher j cases, the sharp peak was not present however the steep rise to maximum around 0.15 Pa was common to both profiles. The transition out of MAR dominated plasma and decay of emission further into the TBR dominant regime was similar in both cases.

These plots implied that the molecular processes were quickly coming to a maximum in terms of excited emitting states for relatively small amounts of gas puffing. There appeared to be a small range of pressures whereby the output of the 0-0 band did not change appreciably before collisional effects likely resulted in a quenching of the excitation processes. This range was around 0.15 Pa to 0.25 Pa or even up to 0.3 Pa. The temperature measurements extracted from these and similar data would shed more light on the transition into the detached states.

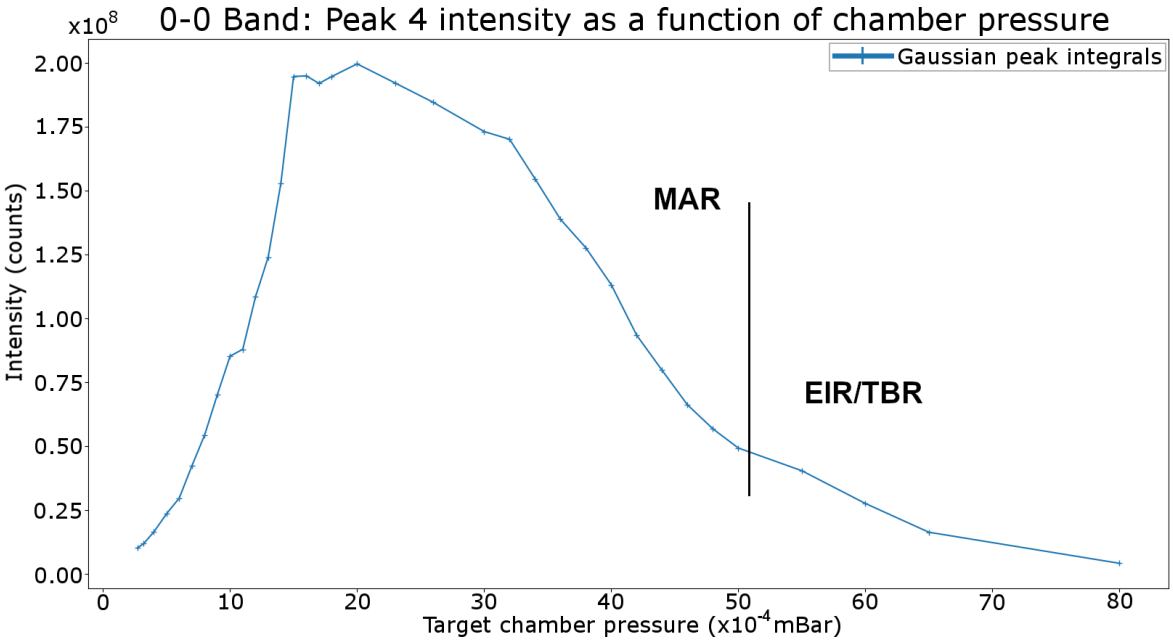

Figure 5.7: Intensity profile of the fourth peak of the 0-0 band. This illustrates the differences in rotational peak intensity within one band.

5.2.2.2 Gas temperatures

Figure 5.8 shows the results of the rotational gas temperature estimates for the 0-0 diagonal band of the Fulcher Alpha lines. The 2-2 band result was similar to this and is not displayed; both showed the sharp increase in rotational temperature within the same pressure window and agreed within error although the 2-2 band result was offset by a small fraction (20 - 30 K) over the entire range. The error bars increased due to the quality of fits to each peak within the 0-0 band and the relative lack of data points for each calculation of T_{rot}. The high resolution 2400 lines grating used for these measurements exhibited some coma (a deviation from a typical Gaussian spectral line-shape) which increased the error in the integrals of each peak. This allowed the fits for each value of rotational temperature to achieve a more consistent trend at the expense of precision. With greater sensitivity, more lines would have been measurable for the fit potentially increasing the accuracy. Nevertheless a clear trend was observed wherein the rotational temperature began to increase steadily with gas pressure until around 0.15 Pa where it sharply transitioned to a stable value. This was true for both bands measured.

As part of the Fulcher band data taken for the estimation of the vibrational temperatures, electron temperatures and ion densities were measured in the center of the plasma beam as

functions of pressure. This data improved the accuracy of the vibrational temperatures to the point where they could have some meaning and provided additional insight into the interaction between the gas and the plasma column in the target chamber. This additional accuracy was due to the electron temperatures providing values of constraint to the analysis provided by Dr. Briefi.

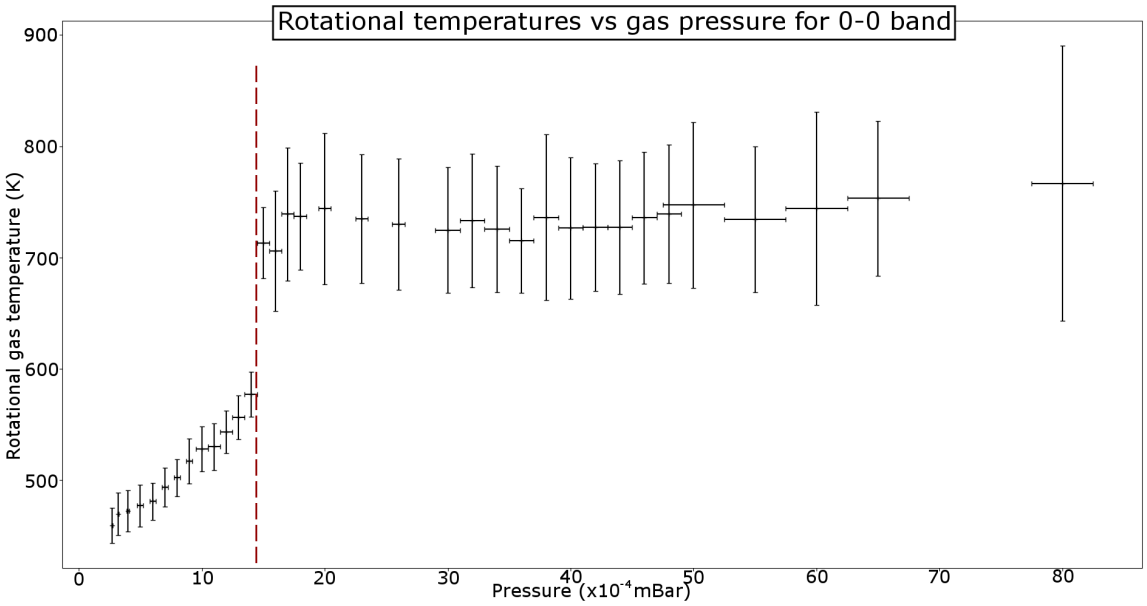

Figure 5.8: Rotational temperatures as function of gas pressure. The flat portion at high pressure was not the initially expected result but was interesting, particularly the lack of change moving into TBR dominated detachment.

By observation, molecular excitation began as pressure increased for 0.1 Pa followed by a dramatic shift in operational conditions at 0.15 Pa. The light emitted by the plasma appeared to shift towards longer wavelengths resulting in a pink glow after 0.15 Pa, consistent with figures 5.6 and 5.7. The source of excitation was likely to be the central hot electron beam from the source causing vibrational excitation of the puffed hydrogen molecules in the target chamber.

A separate set of data as described in 3.2.3 was sent to Dr. Stefan Briefi at the Institute für Physik at Augsberg University for analysis to obtain measurements of the vibrational temperatures. Unfortunately, the available spectrometer exhibited some aberration likely due to slight misalignment, and did not have sufficient spectral resolution to discern the necessary lines to a high degree of accuracy. In order to fit the collisional-radiative model to the relative intensity calibrated spectra, it is necessary to discern spectral peaks as close

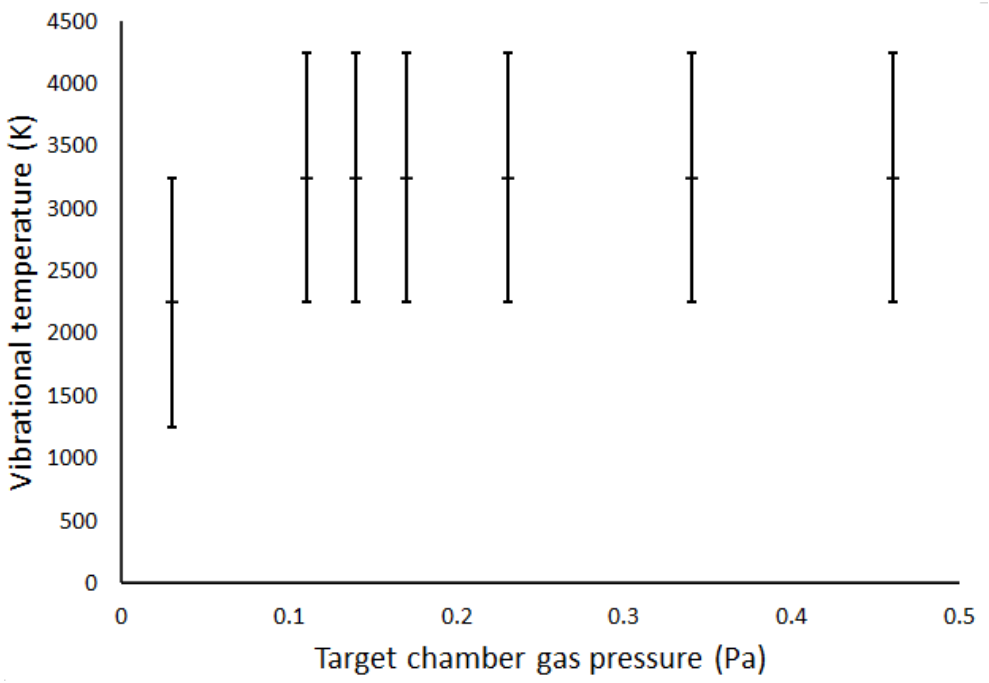

Figure 5.9: Estimates of vibrational temperature calculated through modelling of hydrogen plasma by Dr. Briefi using core electron temperature measurements to reduce uncertainty.

together as 0.7 nm in some cases. Due to the misalignment coma and spectral broadening inherent to the apparatus, the resolving power was insufficient for this task. Higher resolution gratings are not available for the SCT320 so improvements to technique and alignment might provide enough of an improvement to the quality of the spectra to narrow the error bars on these measurements.

By combining the best spectra obtained during this work with probe-measured electron temperatures at the plasma beam center, an estimate was available for the working pressure range. This provided a general trend although without better accuracy it was not worth plotting as a graph. The values reported from the analysis follow. For the low pressure data point at 0.03 Pa, the rotational temperature was found to be 340 $\pm$ 50 K and the vibrational temperature was somewhere 2000-2500 K. For the range of higher pressures, the data points were around 440 $\pm$ 50 K for the rotational temperatures and 3000-3500 K for the vibrational temperatures, shown in figure 5.9.

The rotational temperature trend was similar to that estimated by the author of this thesis however with a less extreme shift at high pressure. The primary point of interest however, was that the vibrational temperature seemed to follow the same trend as the rotational temperature. The degree to which the vibrational temperature changed with added

gas was not known to good accuracy but an increase of 50% or more would be significant for negative ion production. This increase was apparent in the estimates meaning that the high vibrational states were likely to be populated by the hot electrons in the beam as the gas pressure increased. Whether the trend was linear similar to the rotational temperatures is not known at this time with any degree of certainty. Overall, it is important to note that this result is not ideal and the vibrational temperature measurements should be repeated and improved upon in order to make any specific claims about the behaviour with changing pressure.

The rotational temperatures measured in the YLPD were consistent with those measured in similar experiments such as the MAGPIE reactor [68] as well as MAP-II [222] (including vibrational temperatures). The rotational temperatures on magpie fall in the range of a few hundred kelvin while the vibrational temperatures on MAP-II usually fall between 2000-10000 K. The measurements also agree with previous work on the same device found in [3] which were processed at the time by U. Fantz and D. Wünderlich from Augsberg university in Germany.

5.3 Radial profiles of charged species beyond the central core

The radial profiles in the following subsections were obtained by using a fixed magnet to sweep the plasma beam across the dog-legged Langmuir probe. This process is further detailed in section 3.2.6.5. Some uncertainty is attached to later measurements made with this method due to the probe being moved for other measurements between readings taken for different axial field strengths. This is the reason why the measured points in those graphs for weaker solenoid field do not simply cover a slightly wider range and are shifted a little, see sections 5.3.4. The trends measured may still be compared bearing in mind this additional uncertainty. This bending magnet was necessary due to the fact the probe and laser could not be practically moved and realigned for every measurement. A pair of coils would have been more suitable to provide a uniform bending field however the permanent magnet was a simpler solution for these measurements and the size of the plasma beam meant that inhomogeneous bending of the beam was minimal.

5.3.0.1 Electron temperature and density

The electron density and electron temperature profiles are displayed in this subsection, each examined in turn. The electron density profile is shown in figure 5.11. The densities were all measured with the thin dogleg probe for reference in order to render the collection area the same in each case. Due to the diameter of the core region of the plasma beam being of the order of magnitude of the probe tip length, some spatial information was lost. This is because the probe intersects several radial coordinates at once thus providing an integral over this region (see figure 5.10). Because these measurements were made relatively far from the core region, this effect would be reduced due to the chord subtended by the probe tip occupying a narrower range of radial displacements from the plasma beam axis.

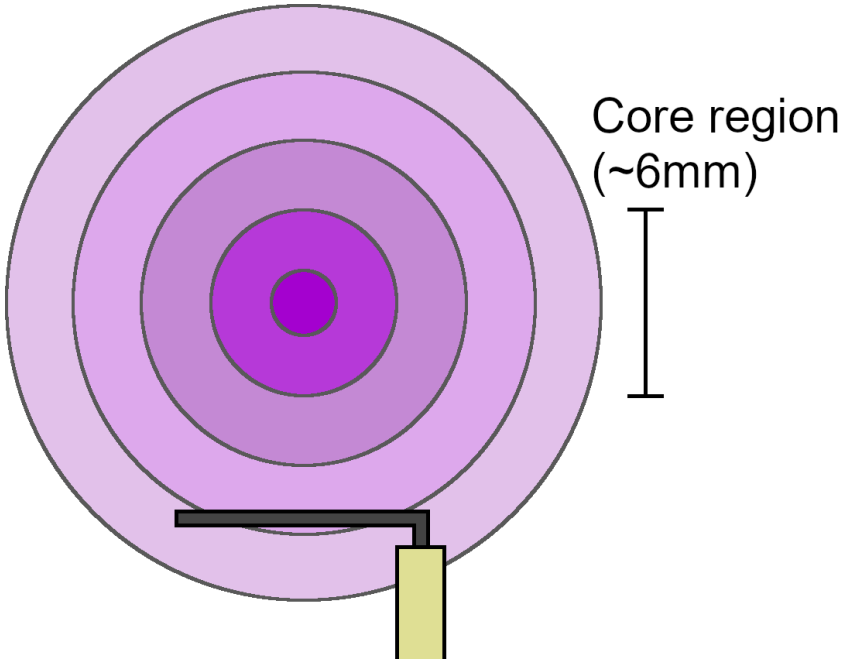

Figure 5.10: Diagrammatic representation of the probe occupying a range of radial coordinates simultaneously (not to scale). Away from the central region of plasma, the range of radii occupied is smaller. The plasma in reality does not have a hard border.

The electron density scaled approximately with increasing pressure with diminishing returns after entering the MAR regime. This would be easier to observe with a density measurement/s between 0.11 Pa and 0.17 Pa however some clues as to whether or not this change was smooth or discontinuous may be inferred from the ion current to the target plate (see section 5.2). It is not unreasonable to expect that the electron density in the outer regions would also vary smoothly. The sharp rise in the electron density between

0.11 Pa and 0.17 Pa closer to the center of the beam could exhibit a discontinuity though it seems unlikely given that other parameters vary smoothly with pressure. Without additional measurements, this cannot be evaluated with certainty. At larger radii, n_e for all pressures, n_e exhibited monotonic decay with increasing distance from the source of ionization.

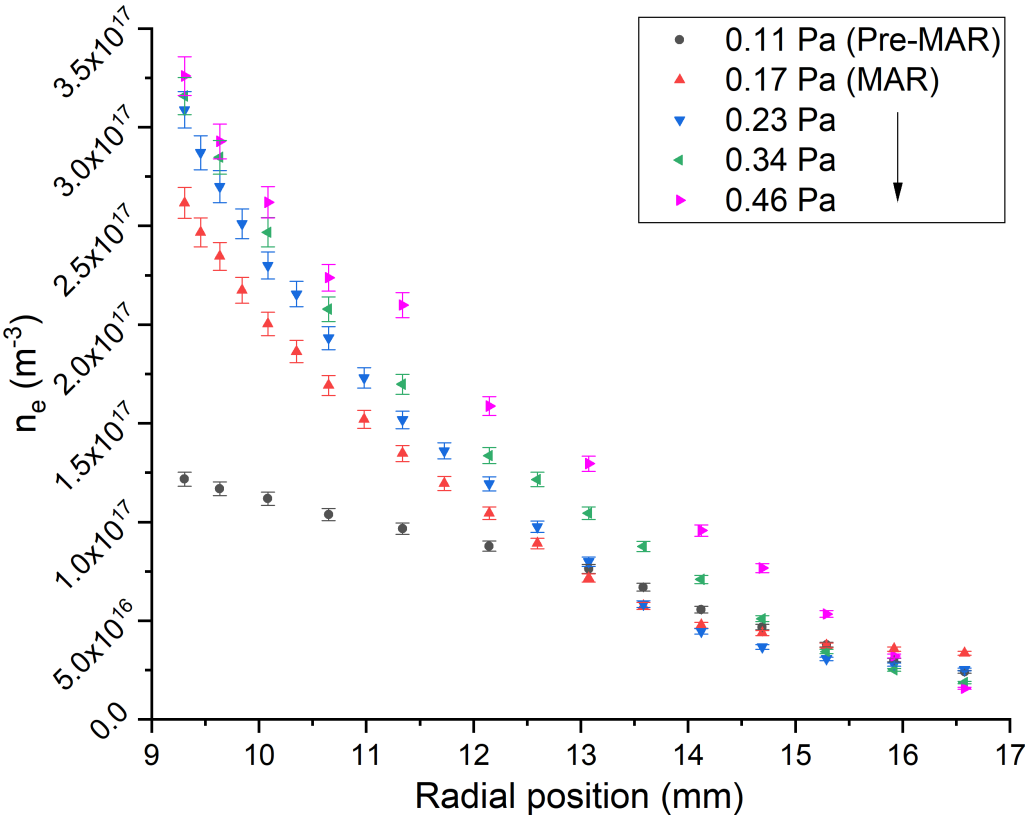

Figure 5.11: Electron densities calculated from ion density measurements used to then measure H^- density. The densities were similar for all pressures above 0.11 Pa. This alone does not explain the profiles observed.

T_e, as expected, decreased in general with increasing gas pressure (figure: 5.12). The temperature gradient over the range also flattened with increasing pressure, indicating either a narrower central maximum in the beam or a flatter temperature profile across the plasma. There was an overall rise in electron temperature for 0.11 Pa. The significant gap in electron temperature echoes the density gap between 0.11 Pa and the rest of the pressures examined close to the central region. Interestingly, the densities become comparable beyond 12 mm when looking at 0.11 Pa and the higher gas pressures while the temperatures remain significantly different.

There were similarities in electron density and temperature in the outermost radial measurements at 0.23 Pa and 0.46 Pa. This would indicate that the negative ion behaviour

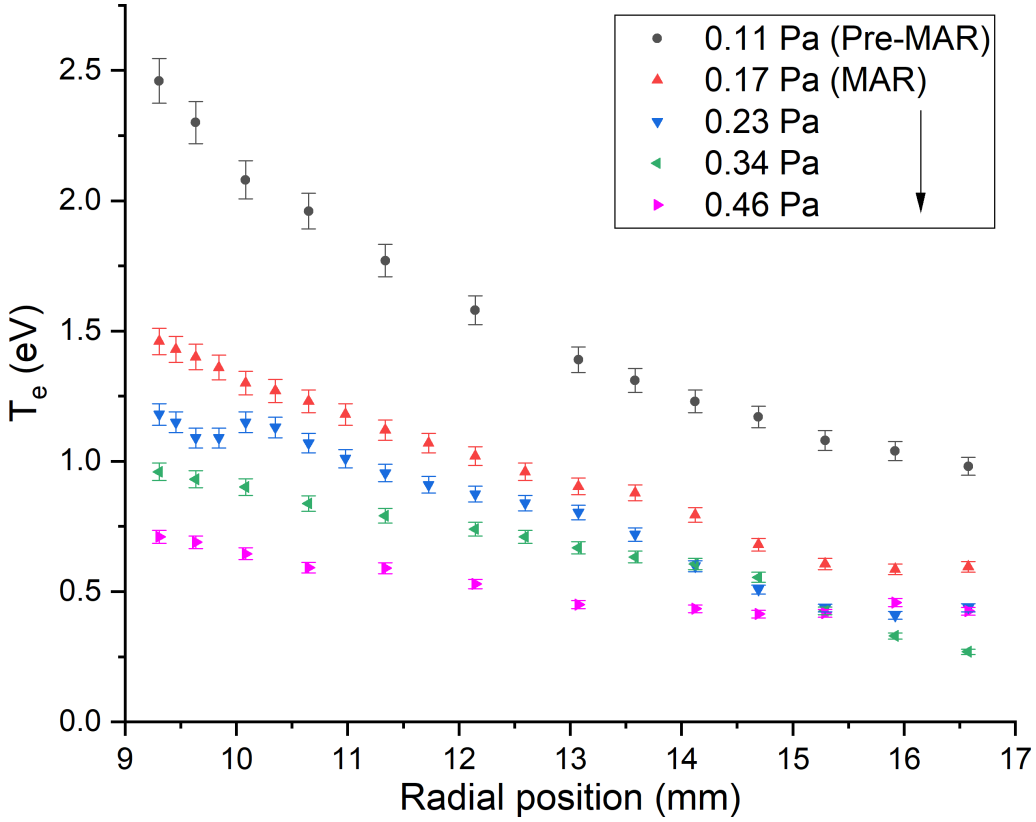

Figure 5.12: Associated T_e measurements for pressure study. T_e is significantly higher at all radii at 0.11 Pa, explaining the reduced production of H^- through dissociative attachment. This trend scales well to follow the other negative ion data vs. pressure.

ought to be the same for these conditions providing that the density and vibrational energy distribution of the molecular hydrogen was also sufficiently similar. The electron temperature also decayed monotonically with increasing radial distance from the plasma beam axis similar to the density measurements. In general, there was also a reduction in the slope of these data with increasing gas pressure.

5.3.0.2 Negative ion fraction vs pressure

The negative ion fraction, being a component of calculating the absolute densities, was also plotted as a function of pressure for insight into the processes taking place: figure 5.13. The negative ion fractions far from the beam were measured to be significantly higher than in (TPD-sheet etc) which may have been due to the nature of the experiment, the plasma geometry, the source conditions or the nature of the gas supply for example. The trends in the negative ion fraction generally mimic the absolute densities with some exception. At

0.23Pa the negative ion fraction continues to increase towards the farthest radial position instead of reaching a turning point and beginning to fall like the absolute density.

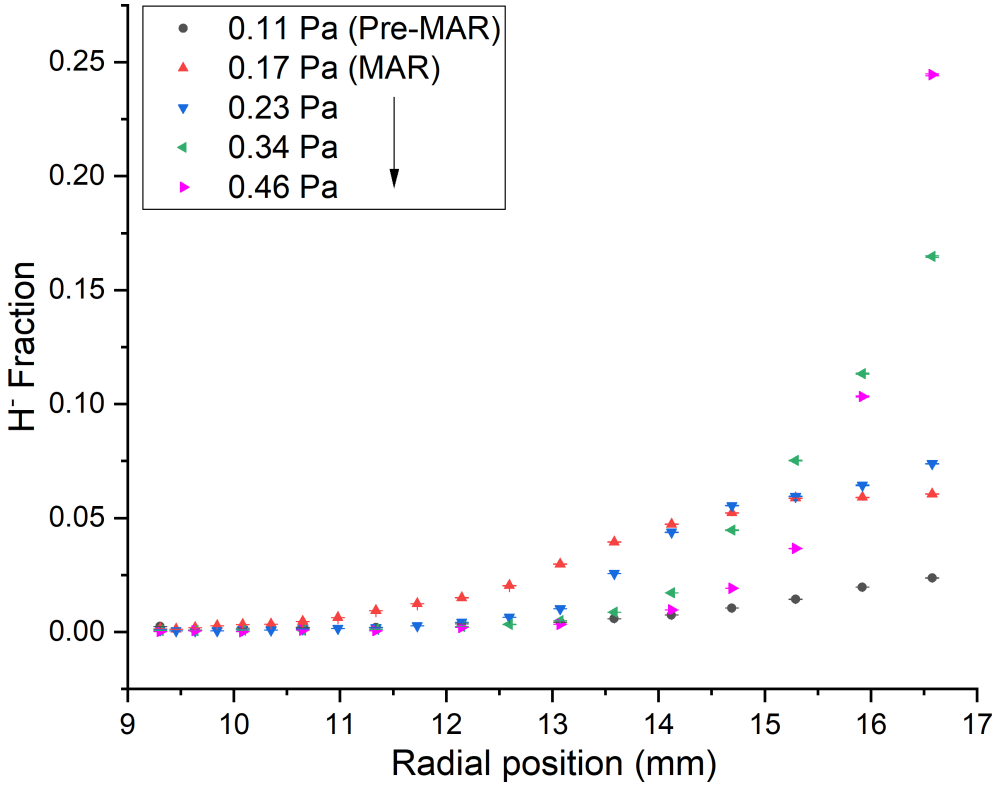

Figure 5.13: The negative ion fraction values also radially resolved as functions of pressure. It is possible to see that there was a turning point in each curve above 0.11 Pa which occurred further from the core plasma bean with increasing pressure.

Similarly, where the negative ion fraction continued to increase at 0.34 Pa, the absolute density had begun to show signs of plateauing. This would indicate that one or more of the reactant species densities were the limiting factor in the generation of H^- in these locations despite the better conditions for production. At 0.17 Pa, as with the absolute density, the negative ion fraction increased more dramatically closer to the plasma center compared to the other pressures before being overtaken at larger radii by the higher values. The negative ion fraction did not however peak and diminish the way the absolute density did, similar to the effects seen at 0.23 Pa and 0.34 Pa. While the conditions for the formation of negative ions may have been more favourable, the density of required species may not have been sufficient to take full advantage of this. This means that it is not necessarily wise to consider only the negative ion fraction when deciding what constitutes "optimal" recombination as this value has different connotations to the density. The system as a whole must be considered

including the other particle species and the total negative ion density.

5.3.1 Negative ion profiles vs pressure

The calculated negative ion densities are shown in figure 5.14 as functions of radius and hydrogen gas pressure. At 0.11 Pa, close to the minimum for onset of the MAR glow, negative ions were detected in relatively small quantities further away from the beam. While the electron density in this region was similar to other pressures investigated, the electron temperature was significantly higher. This could lead to preferential dissociation of vibrationally excited molecules. From the spectroscopic measurements in section 5.2.2, it would appear that there was less emission from vibrationally excited hydrogen molecules at this pressure also. Combining these factors, the relatively low negative ion density across the scanned region and the slow rise towards regions of lower electron temperature further from the core make sense.

At 0.17 Pa the negative ion density rose with radial distance from the beam, exhibiting a peak at 13.5 mm. The negative ion density then decreased for the remainder of the available range of measurements. Compared to 0.11 Pa, there was a dramatic increase in negative ion density across the entire range. This coincided with the sharp increase in the rotational temperature seen in section 5.2.2.2. In addition, while the vibrational temperatures may have been similar, the intensity of the vibrational transition lines was much larger at 0.17 Pa implying a much higher density of vibrationally active molecules. In contrast the vibrational gas temperature was estimated to be similar for both pressures though the uncertainty in the vibrational temperature is relatively large. The peak in the data occurs where the electron temperature and population of vibrationally excited molecules are optimal for dissociative attachment. The decrease in negative ion density with radial position may be explained by the decreasing density of active, vibrationally excited species further from the plasma core and/or a lack of electrons with the appropriate energy to undergo dissociative attachment.

At slightly higher pressure again, at 0.23 Pa, the negative ion density showed a local maximum at $\approx$ 14.7 mm similar to that observed at 0.17 Pa. Beyond this maximum, the negative ion density began to fall, similar to 0.17 Pa however a small deviation at the edge of the measurement range hinted to another maximum. Comparing to the electron temperature and density measurements the temperature was slightly higher for this last position which could explain the small increase in negative ion density. If the local density of vibrationally

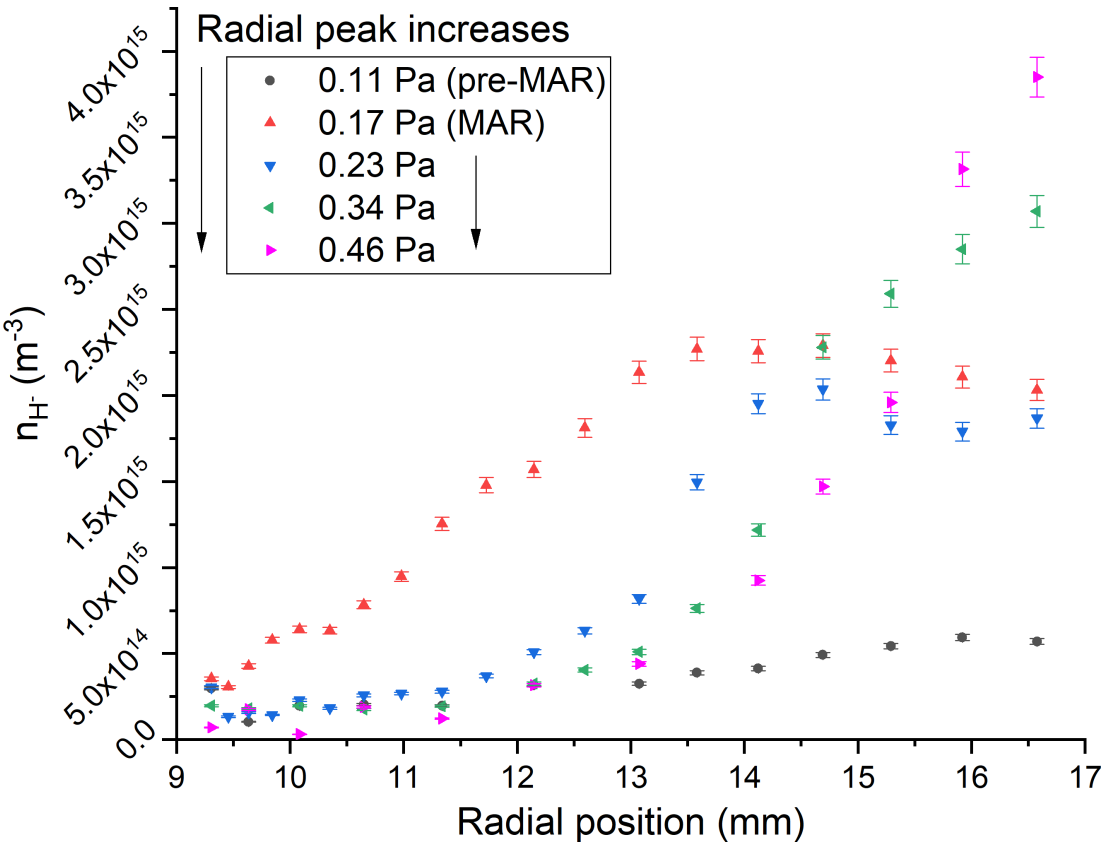

Figure 5.14: Negative ion density measurements radially resolved as functions of gas pressure. It should be assumed that the entire curve may be shifted up or down the radial position axis due to the uncertainty in bending magnet effect at similar pressures.

excited molecules varied minimally in this region, small changes in electron temperature would have noticeable effects on the negative ion density. This would warrant further study to examine the negative ion densities and electron temperatures further away from the plasma in order to verify if this effect was simply a localised error in the measurement. The case of 0.17 Pa may have exhibited a similar behaviour if examined over a wider range but it is not possible to extrapolate such a trend in this case.

At 0.34 Pa the negative ion density rose with increasing distance from the plasma center in an almost exponential fashion before becoming more linear in nature. This transition seems to happen at a similar radial position to the peak or hill in the profile for 0.23 Pa. The densities closer to the beam however are generally lower than those at 0.23 Pa and 0.17 Pa suggesting that the negative ion heavy zone moves radially outwards generally with pressure once the transition to MAR dominated plasma occurs. The peak density measured was higher than that found at lower pressures suggesting some scaling of the maximum with

added gas. It is still unknown whether the shape of the profile would mimic any of those measured at lower pressures, as the peak must exist outside the region examined. It is also unknown whether or not the breadth of the peaked region is consistent between pressures and if they simply exist further away from the center as gas pressure is increased.

At 0.46 Pa the trend was similar to that observed for both 0.23 Pa and 0.34 Pa. The negative ion density increased with distance from the plasma core with what may be the beginning of a turning point toward the end of the curve. A similar decrease in density was observed moving toward the plasma with a trend that looks similar to an exponential relation. In each case, it was notable that the increase appeared to begin later and the gap between each curve with increasing pressure appeared to decrease. The trends observed here indicated that measurements above 0.46 Pa may have been useful in mapping the negative ion population into EIR as it may be non-zero for a significant range of additional pressures.

The relatively similar electron densities 5.11 calculated from ion densities in the outer regions do not explain the differences in negative ion fraction and negative ion density between pressures. For pressures above 0.17 Pa, the electron density and electron temperature were similar beyond $\approx$ 14.7 mm from the core plasma. In particular the electron temperatures were almost identical at 0.23 and 0.46 Pa. Due to this, the atomic and molecular species are likely to be the source of the differences between the curves in this region. In the case of 0.46 Pa, it is likely that the density of vibrationally active species is higher in these regions than for 0.23 Pa. Furthermore it is likely that, because of the geometry (the source of excitation being closer to the plasma beam), it is likely that there is some depletion of vibrationally excited molecules moving away from the core due to collisional de-excitation. This would need to be verified via spatially resolved spectroscopy.

There could be a saturation as the energetic species in the central region deposit energy into vibrational states wherein there are simply more molecules with which to create excited species. There could also be insufficient low energy molecules to effectively absorb and redistribute the energy without completely dissociating. This would result in a relatively minimal population of energetic whole molecules for the dissociative attachment process.

There may also be an increase in dissociation into atomic species at lower pressure where more energy can be deposited into each gas molecule via collisions with electrons. As explained in section 4.5.3.3 concerning the experiments on the GEC, atomic hydrogen can act to destroy negative ions so a in increase in these would cause a corresponding decrease in

negative ion density. There is some evidence to support this in work done by Willett [76] which showed a hollow atomic density profile peaking at 5 mm from the core for an EIR detached plasma. It is not unreasonable to expect that that there would be a similar hollow profile for atoms in the MAR detached plasma considering the high temperatures in the central beam maintaining a high degree of ionization closer to the center.

5.3.2 Variation at single position vs intermediate electrode voltage

The variation in the measured parameters with several values of V_{ie} was examined for a single radial position (∼15.3 mm), pressure and solenoid field. This was done in order to study the effects of changes in the upstream electron temperature in the core plasma on the negative ion profiles in the target chamber. From work done by Mihaljcic [3], it is known that, while the electron density changes minimally with V_{ie}, the electron temperature varies strongly in the region around $V_{ie} = -65V$. A small sample of values was selected around this in to test if a more detailed radial profile would be appropriate.

5.3.2.1 Electron density and temperature

The downstream electron density increased with increasing V_{ie} as shown in figure 5.15. This approximately matches the increase in upstream density recorded by Mihaljcic in this range just before it would typically begin to decrease at around -70 V. This is not to say that the scaling between upstream parameters and downstream conditions is simple given the gas puffing and pressure differential in the target chamber.

Contrary to the central T_e trend observed by Mihaljcic in upstream electron temperature with V_{ie}, the electron temperature further from the plasma decreased with increasing V_ie. This temperature decrease may be explained due to the properties of the source. As the intermediate electrode voltage increased, a larger proportion of electrons were reflected back towards the cathode increasing the cathode temperature and the electron emission rate. The increased electron density caused more ionization and an increase in the overall plasma density emitted from the source aperture. The increase in reflecting potential would also cause electrons to be emitted from the cathode with more energy leading to the upstream electron temperature increase observed in Mihaljcic's work [3]. This effect competed with the increased density of particles leaving the source to produce some effects downstream. The increased electron density and temperature entering the target chamber would result

in more dissociation of hydrogen molecules into atoms making the plasma more collisional. This would explain the slight decrease in electron temperature in the target chamber plasma.

5.3.2.2 Negative ion fraction

The negative ion fraction data is displayed in figure 5.15 There is a slight deviation from a smooth curve in the negative ion fraction which corresponds to the local peak in the absolute density measurements. This may have been an underestimation in error bar, or a result of the variation in an upstream parameter and the point was valid. This was checked using the density and temperature plots. In general, the negative hydrogen fraction decreased with increasing intermediate electrode voltage.

The electron temperature measurements support the negative ion fraction data despite none of the others showing as extreme a trend. For the first three points, the temperature appeared to curve somewhat as if beginning to level out which corresponded to similar behaviour in the negative ion fraction. For the remainder of the plot, the temperature trend was approximately linear and downwards which corresponded to a transition into a relatively flat portion in the negative ion fraction.

5.3.2.3 Negative ion density

The negative ion density trend as a function of V_{ie} is shown in the third plot in figure: 5.15 and varies somewhat inversely to the negative ion fraction. The shape was unexpected as it displayed a small hill before increasing fairly linearly with additional increases in V_{ie}. The variation was less dramatic than that observed during the pressure variations. This makes sense as the target chamber pressure was kept the same in each instance to the limit of the accuracy of the Pirani gauge and the upstream conditions varied less strongly with V_{ie} compared to the target chamber pressure. The changes in V_{ie} were also achieved with relatively minor changes in upstream gas feed rate, meaning the target chamber pressure was generally unaffected by this small upstream change.

The negative ion density varies approximately inversely compared to the negative ion fraction. That is to say that while the conditions for formation were becoming less optimal, likely due to the drop in electron temperature, the absolute number density of negative ions in this location increased. Coupled with the electron density curve and the negative ion fraction curve, the increase in the negative ion density observed at this fixed position was likely due

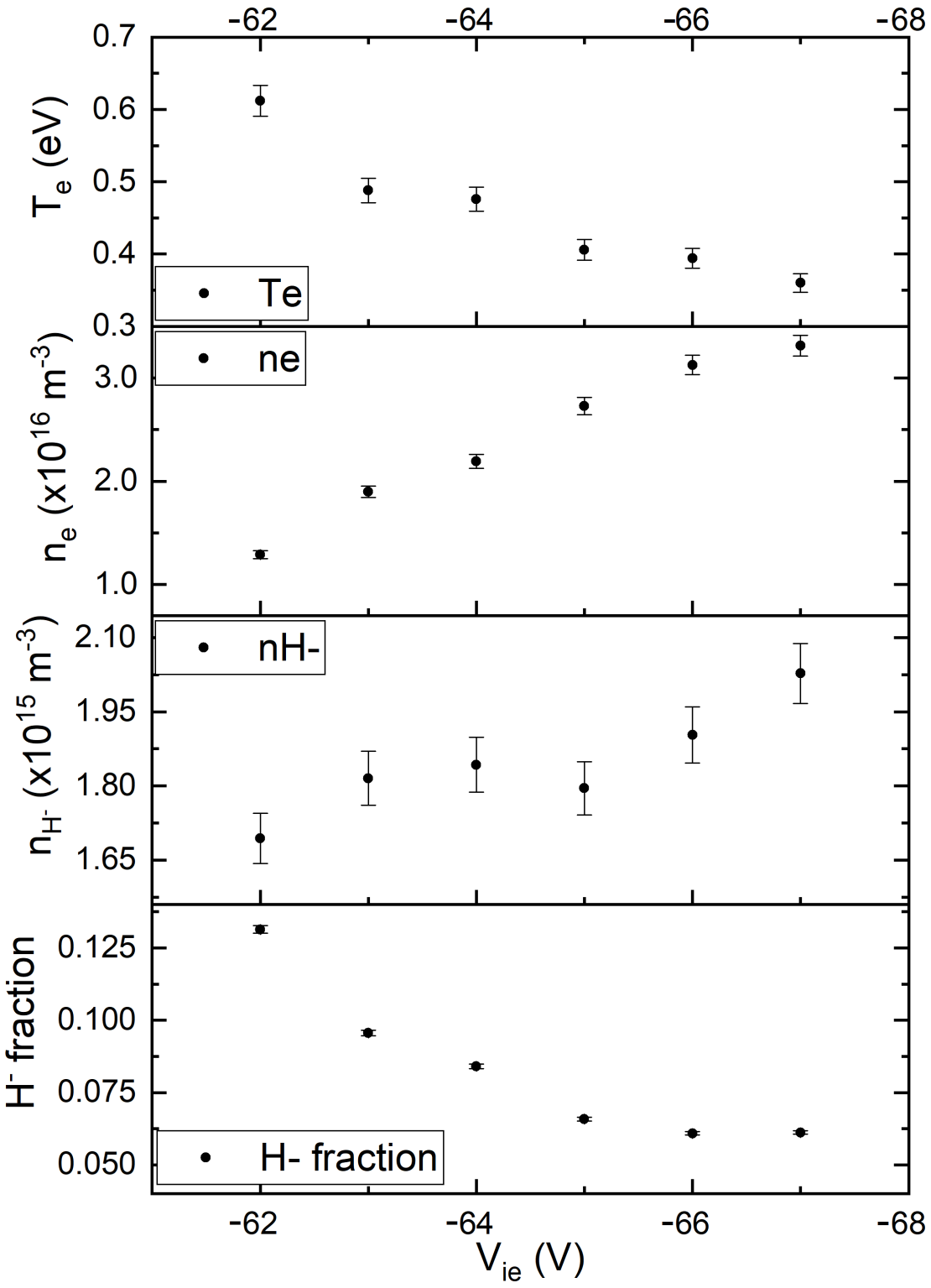

Figure 5.15: Stack of electron temperature and density with negative ion fraction and negative ion density in the target chamber for varying intermediate electrode voltage (upstream electron temperature).

to the number of electrons with suitable energy for dissociative attachment increasing faster than the negative ion fraction could reach a minimum. The temperature measurements also showed a slight bump consistent with the local maximum in the negative ion density. Due to these observations, a radial profile was taken for two values of the intermediate electrode voltage in order to obtain a more detailed picture of the spatial effects of changing the upstream conditions.

5.3.3 Variation with upstream electron temperature - V(ie)

5.3.3.1 Electron temperature and density

The electron density and temperatures were recorded as a function of the intermediate electrode voltage at a fixed location as discussed previously in section 5.3.2. A higher intermediate electrode voltage corresponded to a lower electron temperature at this location. Radial measurement profiles were taken for a given target chamber pressure and solenoid current as a function of the intermediate electrode voltage. This is similar to the measurements in section 5.3 where the pressure was varied except this time the pressure was kept constant and two different values of V_{ie} were used in order to make some inferences on the effects on the processes involving neutral species. The pressure used was 0.23 Pa predominantly due to the local maximum in figure 5.14 followed by the apparent rise in order to confirm if this behaviour was repeatable.

The inferred electron density values and electron temperature measurements are shown in figure 5.16. Overall, the electron density profiles were similar in shape between the two discharges. The reduction in electron temperature matches the increase in density seen in the previous sections whereby the plasma was more collisional reducing the average particle energy. Closer to the central plasma, the density and temperature trends began to diverge slightly, implying stronger variation towards the central region.

Though the temperature range was conducive to negative ion production for both, the -62.5 V case remained at sufficiently high temperatures for optimal dissociative attachment further out than for -64.5 V. These differed more significantly across the range than the electron densities. The electron temperature is a more important parameter in the dissociative attachment process so small changes in the temperature profile may help explain differences in the negative ion measurements. The temperature values, similar to the density values, diverged more at the edges of the region examined. The only remaining parameters to ex-

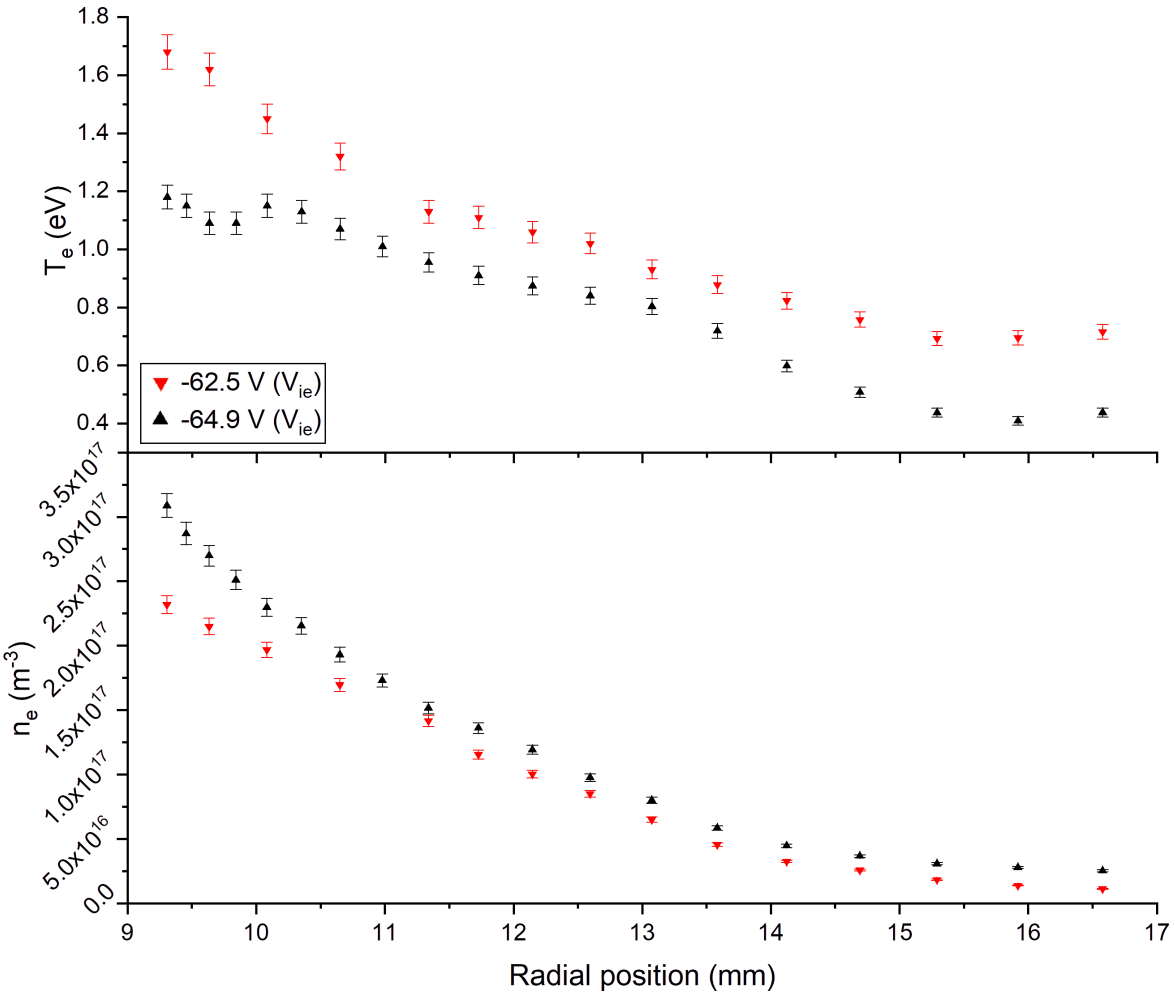

Figure 5.16: Electron temperature measurements and calculated electron densities for varying upstream intermediate electrode voltage. The electron density was calculated via the quasineutrality principle. The electron density scaled in a similar fashion with increasing radius. There were significant differences in the electron temperature between the two cases.

plain the discrepancies would be the radial distribution of relevant neutrals. The leftmost portions of the T_e curves imply a much hotter central region in the -62.5 V case causing significant increases in the rate of formation of relevant $H_2^*(V)$ species which could then be transported radially outwards. This would cause the negative ion formation rate via dissociative attachment to increase accordingly.

5.3.3.2 Negative ion fraction (Vie)

The negative ion fraction values are plotted at the same radial positions shown in figure: 5.17. While the negative ion fraction was close to zero close to the central plasma for both discharges, the negative ion fraction was significantly enhanced at a sufficient distance from the beam center for lower V_{ie}. The difference between the two was larger than initially expected given that the electron densities were extremely similar and the dissociative attachment rate constants from R.K. Janev's research [188] are also extremely similar for electron temperatures between 0.4 eV and 1.0 eV. This meant that the enhancement of the dissociative attachment process was likely not direct, rather enhancement or reduction of related processes was causing the discrepancy.

The negative ion fraction in both cases showed strong agreement until around 14 mm from the plasma axis whereupon the trends began to diverge. Beyond this point the negative ion fraction in the discharge with the higher intermediate voltage did not follow the data from the other discharge, rather undergoing a transition to a shallower slope. This implied that there was some tension occurring between the formation and destruction processes as well as the processes that indirectly affect them which was less apparent at $V_{ie} = -62.5V$.

Looking at the electron temperatures in this region, the discharge at $V_{ie} = -62.5V$ exhibited values between 0.6 eV and 0.9 eV while the discharge at $V_{ie} = -64.9V$ was between 0.4 eV and 0.6 eV. The first type of process worth investigating, affected by this difference is the excitation of hydrogen molecules into vibrational states ideal for dissociative attachment. This would explain the difference in negative ion fraction for a given pressure, similar electron density and discrepancy in electron temperature.

Rate constants for direct excitation of hydrogen molecules by electron impact show increases with temperature of up to two orders of magnitude for $V_{final} = 1$ in the range of electron temperatures between 0.1 eV and 1 eV. For $V_{final} = 2$, in the same temperature range, the rate constant can increase up to one order of magnitude with temperature. Direct

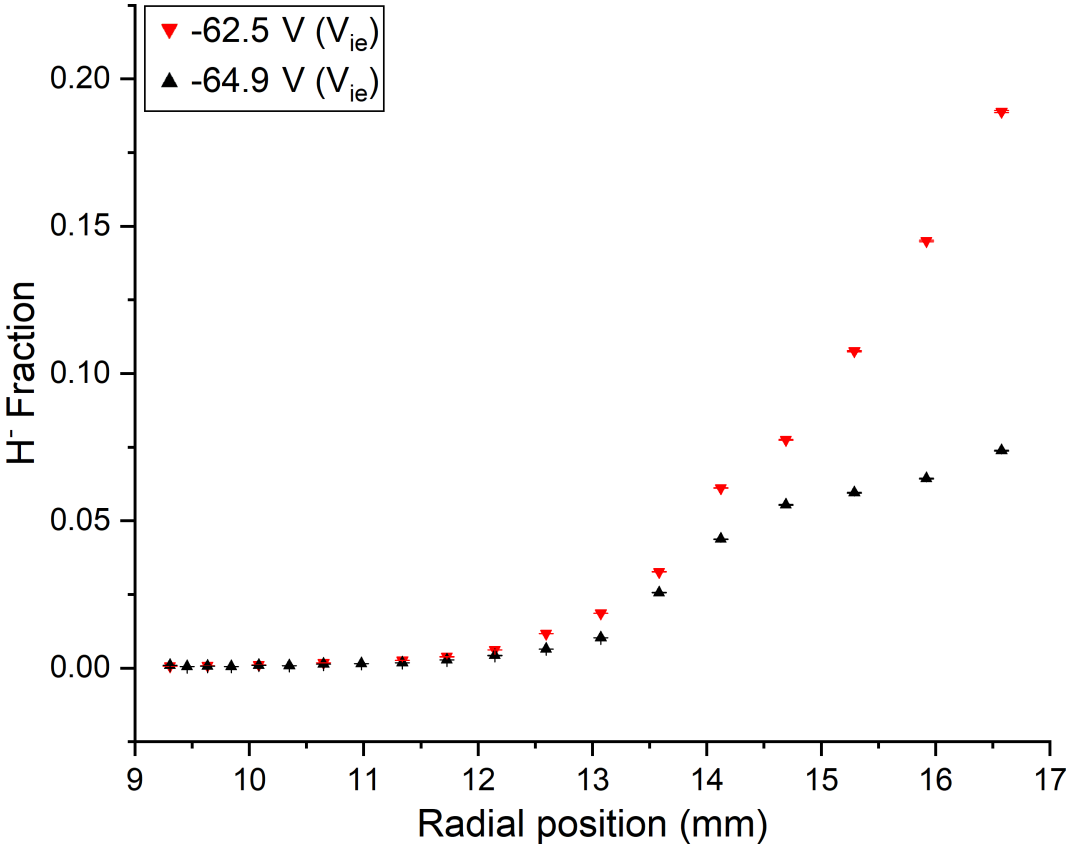

Figure 5.17: Negative ion fraction for two intermediate electrode voltages. The negative ion fraction profiles were significantly different in the latter half of the radial scan. Seemingly lower V_{ie} was beneficial to the production processes with increasing radial distance.

excitation rates into vibrational states greater than $V = 2$ is inefficient, rather it proceeds through a resonant state of H_2^-. In these cases, the rate constants, though relatively small, vary up to four or five orders of magnitude over the same temperature range depending on the final vibrational state of the molecule. This would have drastic effects on the formation rate of molecules available for dissociative attachment while keeping dissociation rates low as the temperature is low (below $\approx 1eV$). Excitation via electron impact excitation and subsequent radiative decay of $H_2^*(N'\Lambda_u)$ states is less efficient than via the resonant molecular ion and so is less likely to contribute meaningfully. A higher core temperature would also enhance these processes. Combined with radial transport, this could also contribute to a relative abundance of $H_2(V)$ in one discharge.

Another species worth considering is atomic hydrogen as discussed previously in the experiments performed on the GEC (see section 4.5). Assuming the collision energy of hydrogen atoms with negative ions was comparable to or less than the electron temperature,

the rate constants for associative detachment (negative ion reacts with atom to produce molecule and electron) exhibit little difference of the order 0.1 eV. by contrast, the non-associative detachment process, whereby two ground state atoms are formed instead of a molecule, varies by one half to one full order of magnitude between these energies and around half an order of magnitude at energies of the order of 1 eV.

There is little difference in the rate of radiative recombination in this temperature range. This is one of the prime pathways for the creation of atomic species in this area and so locally this process should not change the atomic densities significantly. This would mean that radial transport of atoms formed by dissociation closer to the core would have to account for differences in destruction rate of negative ions due to collisions with atoms. The reasoning in these paragraphs was formed using information from [188] and [223].

5.3.3.3 Variation of Negative ion density

The negative ion densities were subsequently calculated and are displayed in figure 5.18. The negative ion density profile is strikingly similar between the intermediate electrode voltage values. This includes the local maximum observed in figure 5.14 (the data set marked by black upright triangles is from that figure). The occurrence of this feature in both plots means that it is likely a feature observed around this gas pressure and not simply some systematic or processing error. The similarity in absolute negative ion density is somewhat unexpected at the larger radial coordinates due to the differences in the negative ion fraction in this region.

There were some minor differences between the two data sets. The rise in the negative ion density showed a slightly more gradual rise to the initial local peak for $V_{ie} = -62.5V$. This was followed by a smaller local minimum and greater secondary increase than for $V_{ie} = -64.9V$. The similarity in the negative ion density despite the differences in negative ion fraction was likely due to to competing effects. While a lower electron temperature meant a reduction in formation of vibrationally excited molecules, it would also cause a reduction in electron impact ionization events across all excited states of atomic and molecular hydrogen. The relative reduction in positive ion species would reduce the rates of processes destructive to negative ions. In addition, a lower electron temperature would also reduce the rate of electron impact dissociation of negative ions by around two orders of magnitude for $T_e = 0.4 - 1eV$. It may be that the remarkable similarity of these data due to competing processes

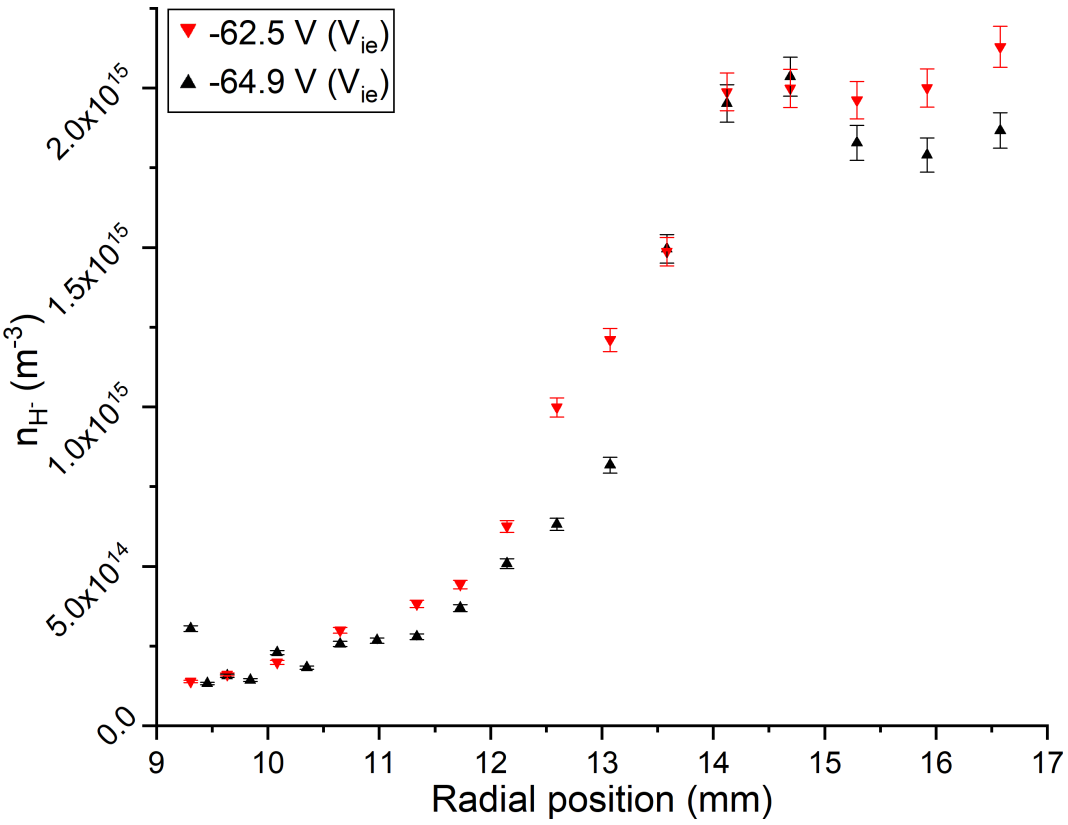

Figure 5.18: Variation in measured negative ion density radially for two values of intermediate voltage. Both exhibited an initial peak structure with a secondary increase afterwards, though to slightly different degrees in the latter case. The profiles look surprisingly similar overall, implying that the intermediate electrode voltage and thus, small changes in the upstream electron temperature, did not have a large effect on the negative ion density profile. This could, however be due to competing factors balancing out. Whether or not this is coincidence is unknown.

is merely a coincidence but this cannot be confirmed without additional data at other values of V_{ie}.

5.3.4 Variation of negative ions with applied field

As a preface to this section, the relative offset of the two data sets is partly due to an adjustment made during the bending magnet calibration phase of the experiment. Between measurements of the position of the plasma relative to the probe, the probe was adjusted. This necessitated the calculation of the relative position of the probe tip in each case based on photographs taken with the magnet removed. In this case, the position of the plasma column ought to be the same for both solenoid fields, assuming sufficient field homogeneity. In the measurements performed here, it was expected that the deflection of the beam would be more

extreme for a 300 A solenoid field however, while this data shows a starting point further from the beam center as expected, the range covered by this is not noticeably extended compared to the 400 A data. This is likely due to a calibration error and more rigorous measurements should be made for improved comparisons regarding the solenoid current. There is still value to the data collected here in the shapes of the trends keeping in mind that they may be slightly stretched in reality. These measurements were made during discharges with 12 A arc current, 0.23 Pa target chamber pressure, -64.9 V intermediate electrode voltage. The data taken at 300 A solenoid current is the same as the $V_{ie} = -64.9V$ data in the previous section and the 0.23 Pa data from section 5.3.

5.3.4.1 Electron density and temperature

The electron density profiles are shown in the latter portion of figure 5.19. The shapes of the two density profiles are similar and appear to take almost identical values at any given distance from the central plasma. Even with some degree of stretching of the data trend in the positive radial direction, it would not be unreasonable to expect the electron densities would not differ significantly in each case. There were signs of some deviation at radial points closest to the central plasma. While subtle, this implies that the electron density curve at 300 A (41.7 mT) has a larger full width half maximum and smaller central maximum than the 400 A case. This matches expectations.

The close similarity further away from the central plasma approximately matches observations made in section 5.3.3.1 where only the intermediate electrode voltage was varied as a control parameter and the electron density did not vary appreciably. This shows that in the cases for these target chamber plasmas with nonzero gas puffing, the neutral pressure was the primary control parameter concerning the density of charged species at larger radii by increasing collisionality in these regions. In these peripheral regions of the plasma, the electrons and ions must have originated from reactions with neutral particles or via cross-field transport from the central plasma because the aperture at the source is of the order of 6-7 mm. In these cases differences in electron density closer to the center of the plasma between solenoid field strengths would be more pronounced as the stronger field limits cross field transport, preserving a greater portion of the electrons originating at the source aperture close to the beam axis.

The electron temperatures (first plot in fig 5.19) showed greater variance than the den-

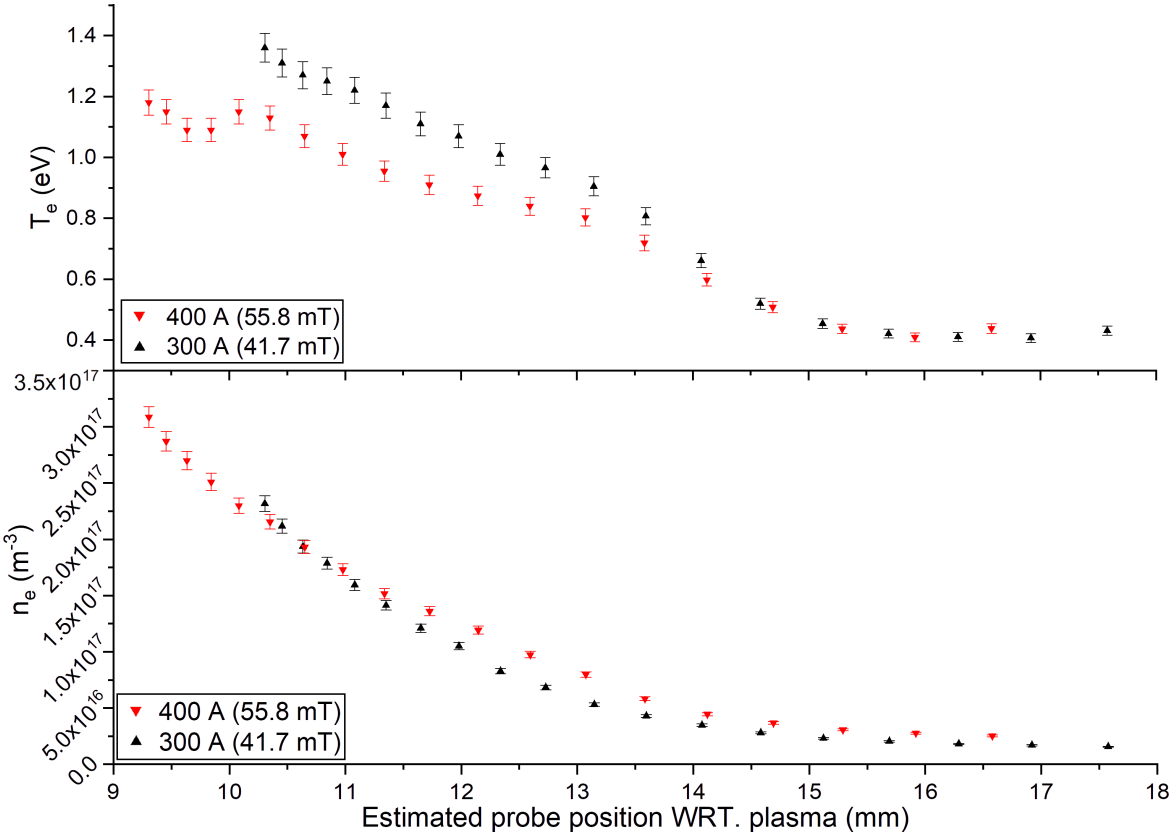

Figure 5.19: Stacked electron temperature and density for two different solenoid fields. In the outer region of the plasma, the electron density does not appear to vary much between field strengths. This is not necessarily true of the inner portion of the curve where the 41.7 mT curve appears to be rising earlier (further away from the core) than the 55.8 mT curve. This may indicate a more constrained central region though the probe could not be moved to this relative position in the 41.7 mT case.

sity profiles. In the furthest region, the electron temperatures were similar and followed a similarly shaped trend moving from a relatively linear region to a slight curve to a minimum value around 0.4 eV. The electron temperatures were higher in the discharge with lower magnetic field strength. This is due to the stronger field being able to effectively trap higher energy electrons preventing them from undergoing cross-field diffusion/transport as often. The maximum electron temperature in the core region of the 400 A discharge would be expected to be higher again due to the restriction of cross-field diffusion of higher energy charged particles.

It is worth noting that the electron temperatures measured in the majority of these experiments are small and thus may be subject to larger error margins than are displayed here due to the nature of the Langmuir probe diagnostic. It is difficult to place a value

on this uncertainty however and the trend-shapes may remain unchanged by adding this systematic error assuming it is a consistent over or underestimation.

5.3.4.2 Negative ion fraction

The negative ion fraction profiles in figure show a significant difference with the negative ion production efficiency being enhanced in this lower field regime (fig 5.20). The data points showed similar initial behaviour with an initial curved increase in negative ion fraction. This was followed by the trends after the 14-15 mm mark showing slightly different behaviour, the lower solenoid field has exhibited a turning point or peak where the higher field discharge did not within the range of study. The low-field discharge negative ion fraction continued to increase to a maximum significantly above that from the high-field case. While it is expected that the high field discharge would exhibit a maximum somewhere just outside the observed range, this would need to be confirmed by broadening the measurement rage using a stronger magnet or a pair of Helmholz coils.

Interestingly, when looking at figure 5.19 and the electron densities and temperatures in the region where the negative ion fraction data diverges, the values are extremely similar. This would likely be the case taking into account some minor stretching of the data points radially for the 300 A case if the position calibration was more accurate. This raises the question of why the negative ion fraction was so different. The author believes that the electron temperature in the 41.7 mT discharge follows a profile with a wider FWHM and lower maximum temperature than the 55.8 mT (400 A) discharge. The wider temperature profile provided a greater volume within which the conditions were suitable for vibrational excitation of hydrogen molecules while also being less suitable for dissociative processes. This allowed more vibrationally excited H_2 to make its way away from the central plasma without being destroyed. This is somewhat speculative and more complete electron density and temperature profiles as well as spatially resolved measurements of the distribution of $H_2(V)$ would be required to solidify this hypothesis.

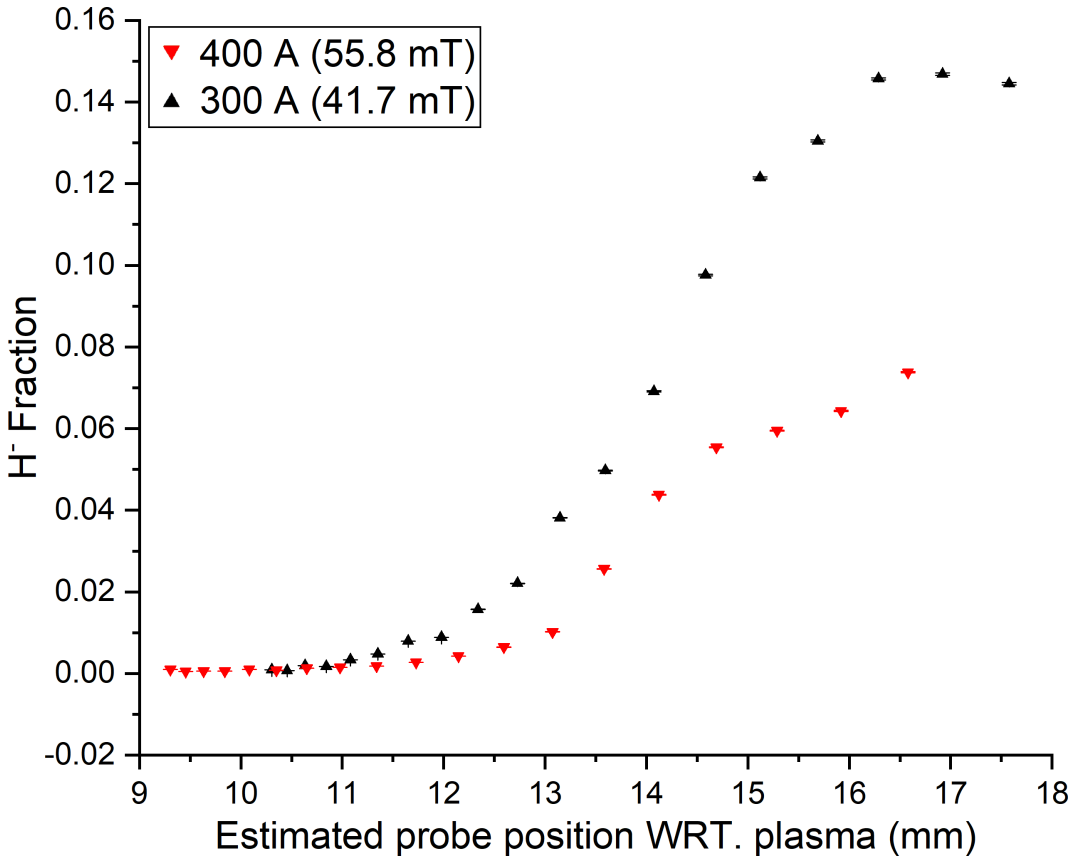

Figure 5.20: Negative ion fraction values for different solenoid field. This showed that negative ions were more efficiently generated for all positions at lower magnetic field. This was likely due to the looser confinement of the electrons to the central regions, allowing them to more easily interact with molecules both for excitation and dissociative attachment processes.

5.3.4.3 Negative ion density

The negative ion densities are shown in figure 5.21. The H^- profile at lower solenoid current resembled that of the 0.17 Pa measurement made earlier (fig 5.14 in section 5.3) with a well defined maximum. There was a turning point at a similar radial position in both instances. The negative ion density also decreased more sharply towards the plasma in the low-field case where the temperature gradient towards the center showed signs of being steeper. The gradient was closer to a linear relation in the 41.7 mT solenoid field discharge. It is likely the negative ion density would curve towards zero closer to the plasma than the available measurement range as opposed to there being an abrupt transition.

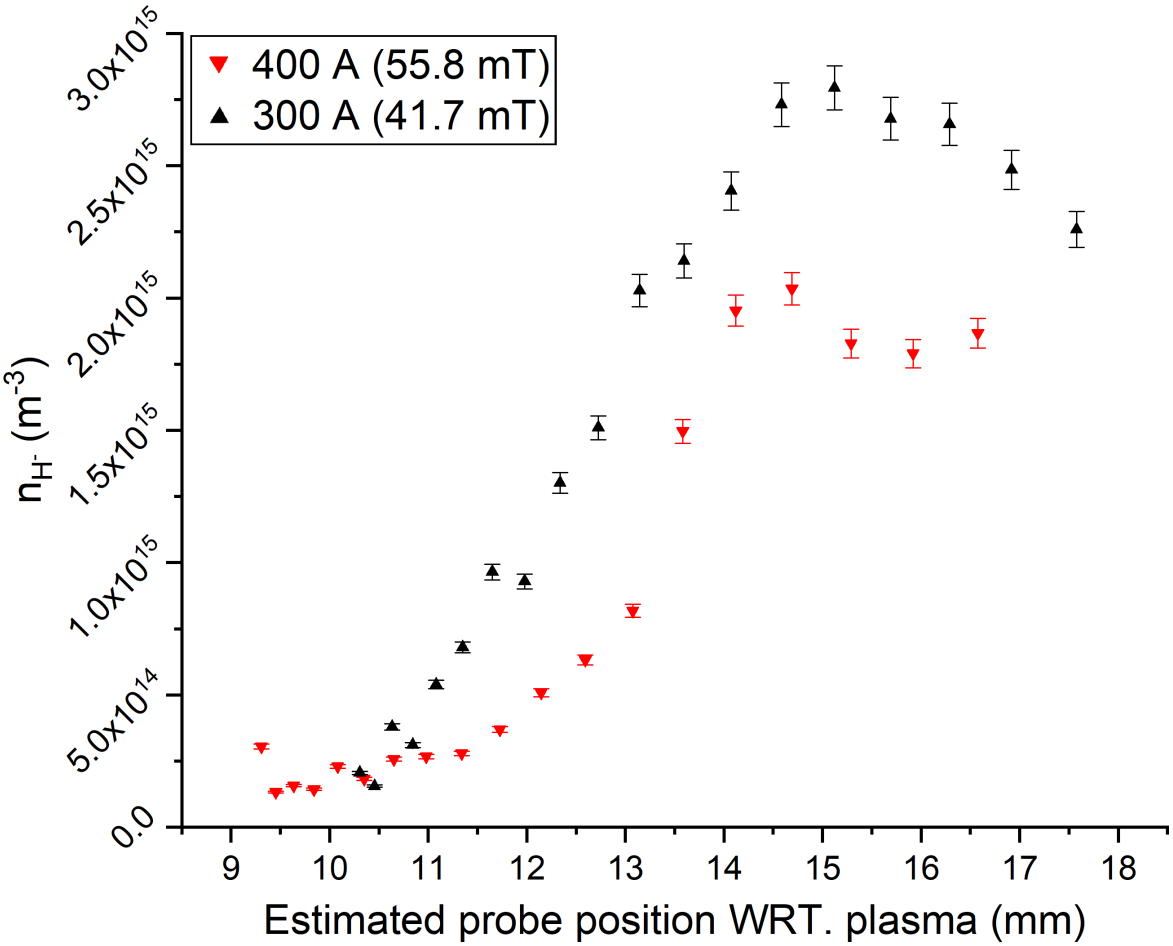

Figure 5.21: Negative ion density profiles for different solenoid fields. The lower field case positions were not performed with the camera and so are more of an estimate than those at higher field. It can be seen that the strength of the field can dramatically affect the negative ion profile. The trend observed at lower solenoid current was similar to that observed at the higher field for lower pressure.

5.3.5 Discussion of results obtained on the Linear Device

A similar experiment was performed on TPDSHEET as mentioned briefly in section 2.5.2.5 [9, 79]. In this experiment they found a hollow profile of negative ions centered on their planar plasma sheet. They found that the negative ion formation was highest at 3.5 mTorr (0.004 mBar or 0.46 Pa) out of the pressures they studied. The peak in their data at this pressure occurred around 11 mm away from the mid-plane of the sheet. The measurements performed on the YLPD showed that the highest negative ion density as a function of pressure was measured at 0.46 Pa at the farthest point measured from the plasma. The negative ion density could be higher at higher pressure in the case of the YLPD but this was not measured here. Future measurements would extend the radial profile measurements beyond 0.46 Pa towards the three body recombination regime. Using the work on TPDSHEET as a guide, it may be expected that the negative ion density would have lowered by 0.8 - 1.0 Pa.

While the radial location of the highest negative ion density peak at 0.46 Pa was larger than both the measurements made on TPDSHEET ($\sim$ 10 mm) and larger than the available range explored here (peak beyond 17 mm), the similarities are encouraging. Both experiments show a hollow negative ion density profile and exhibit absolute densities of the order of 10^{15} m^{-3}. The electron temperatures corresponding to the location of the peak in TPDSHEET were around 2 eV which exceeds the those measured in these experiments in the regions where the negative ion density was large regardless of pressure. The peaking behaviour was mimicked in the measurements made at 0.17 Pa and 0.23 Pa particularly under lower solenoid field conditions.

There was also similarity between measurements made in these experiments and the lowest gas pressure used on TPDSHEET. While small, the negative ion density at 0.11 Pa was nonzero. This is not as dramatic as the double peak observed at 0.8 mTorr ($\sim$ 0.11 Pa) on TPDSHEET but is lower compared to measurements made at higher pressures on the same device. The differences in the behaviour observed between these devices are likely due to a combination of factors such as differences in the source, plasma and chamber geometry, plasma parameters and field geometry. The underlying plasma physics however seems to be highly similar between the two.

The work done on TPDSHEET and also PISCES-A [65–67] supports the notion that creation and transport of vibrationally excited species are of critical importance to the overall rate of the MAR recombination chain. This is supported by this thesis which also cites

the vibrational excitation and subsequent transport of negative ions as one of the most important processes occurring in these divertor relevant DC plasmas. In the results presented here in many cases, the data points towards the creation of vibrationally excited molecules being one of the primary reasons for increased negative ion production. The vibrational temperature estimates as a function of target chamber gas pressure showed a noticeable jump in vibrational temperature (and rotational temperature) somewhere around 0.15 Pa. In several cases, the electron densities were similar and electron temperature differences could be used to explain increases in negative ion density. In other cases, where the electron temperatures were similar, the T_e profiles closer to the core coupled with radial transport of molecules could be used to explain the differences but would require additional measurements to obtain a definitive answer.

The measurements in this chapter show clear negative ion profiles and their variation under different control parameters. These data may be highly useful in the bench-marking of models of linear divertor simulators or a model/modification to an existing code made to be bespoke for the YLPD. The data and the trends observed also support existing similar measurements on a similar device and show negative ion behaviour at relatively high resolution compared to existing literature.

Chapter 6

ITER core TS diagnostic - design considerations from analysing JET data and ITER simulations.

6.1 Outline

A short project was conducted in collaboration with the Culham Centre for Fusion Energy (CCFE). The aim of this project was to analyse the background light gathered by the High Resolution Thomson Scattering (HRTS) diagnostic on the Joint European Torus with the ITER-Like Wall (JET-ILW) and combine this with predicted background light emission on ITER simulations. The aim of this was to provide information to the ITER Core Plasma Thomson Scattering (CPTS) diagnostic design team which would assist in the specification of a final design for the ITER CPTS collection optics, with regards to the filtration of high intensity spectral lines which would not contribute to the electron temperature measurements but could potentially damage the diagnostic.

This work sought to compare a simulation of the background light on ITER to known measurements similarly made on JET-ILW, both to validate the ITER model and to decide on a transfer or filter function for the final ITER diagnostic.

6.2 Thomson scattering on ITER

Thomson scattering is a critical diagnostic on any tokamak device which can support it. The ability to measure electron and ion temperatures with good spatial resolution, at high precision without interfering with the plasma dynamics is invaluable to diagnosing temperature profiles [224] as well as in some cases such as the MAST-U divertor TS diagnostic [225], fast timescale events. ITER will have a systems able to measure both electron [226] and ion [227] temperatures.

The ITER CPTS diagnostic is outlined in a recent updated design paper by Scannell et.al. [15]. As with all Thomson Scattering diagnostics, the signal to noise ratio is extremely sensitive, both in general and to additional sources of light. In tokamak devices which have a divertor, which ITER will have as a necessity, the plasma in the divertor strongly radiates as part of detachment. This radiation represents a potentially serious source of background light for the CPTS diagnostic due to the wide spectral range observed by the diagnostic. The narrow entrance region of the divertor would typically prevent light from reaching the CPTS entrance port by acting as a baffle system however, owing to the reflectivity of the first wall components, there may be sufficient pathways for this light to enter the detection arm.

6.3 Approach to estimating ITER background light

6.3.1 Overview of techniques and posed questions

The estimate of the problem posed by the ITER background light was approached from two directions. The first was using emission data obtained from a SOLPS (Scrape-Off Layer Plasma Simulator code package [228]) run combined with a simulated bremsstrahlung profile. This was then run through a ray-tracing package called CHERAB [229] to calculate the light seen along the CPTS lines of sight originating from the center of the first collection mirror. This code can simulate the effect of the reflectivity of the first wall of ITER by having an internal model and coefficients corresponding to the reflectivity of the various parts. The second approach was to scale up a background light profile obtained from the HRTS diagnostic on JET-ILW. This is the closest device currently in operation in the world so provides the best approximation available at this time.

In each case, it was of interest to try to deduce answers or at least partial answers to

several questions:

1: Whether each was a good representation of the background light profile for the true ITER operating scenario.

2: If there was agreement of some kind between the CHERAB simulations and the JET-ILW shot data (accounting for scaling between devices)

3: If the reflectivity of the first wall caused significant enhancement of background light, both bremsstrahlung and line emission so as to represent a problem compared to a non-reflective wall assumption.

4: If any lines, when enhanced or scaled appropriately would likely cause issues for the ITER CPTS diagnostic

5: If there are any troublesome lines, whether there are already diagnostics with similar sensitivities which view them and if so how they deal with them.

6.3.2 Analysis considerations for JET-ILW and CHERAB data

6.3.2.1 CHERAB data handling

The data used by CHERAB was obtained from a single run (run #2447) [15] of the SOLPS scrape-off-layer (SOL) and divertor model. This run was characterised by 600 MW of fusion power of which 100 MW reached the SOL and 37 MW was radiated throughout these regions. It also modelled emission of species which will be present in these regions including, beryllium, helium and neon. This was combined with a bremsstrahlung radiation profile using a peaked temperature profile at 27 KeV. Figure 6.1 shows the electron temperature profile calculated by SOLPS used to calculate the emission of radiation in the SOL for use in CHERAB.

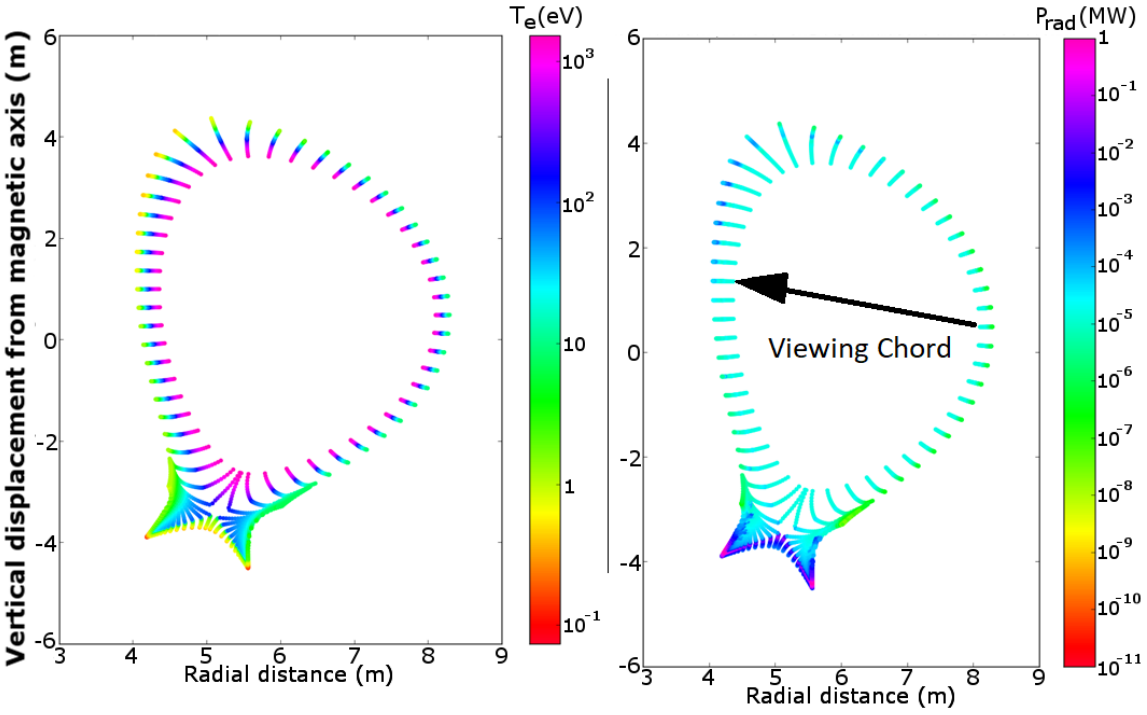

Figure 6.1: Left: Scrape Off layer electron temperature profile from SOLPS fed into CHERAB. Right: Total radiation intensity profile in the range 450-600 nm. There is another profile for a waveband above 600 nm which looks largely the same as the one shown here. The hottest regions near the core emit the least radiation at these wavelengths due to an inability of the plasma to recombine.

Figure 6.2 shows the ray-traced image calculated by CHERAB for both a: non-reflective wall panels and b: reflective walls. These images come as a consequence of processing both the SOLPS data and a 3D model of the ITER wall geometry. Any viewing chord may be selected to give an output of what that chord would "see". The effect of inclusion of the first-wall reflectivity is highly visible between the two images, bearing in mind the apparent brightness is not scaled the same between the two. This being due to the absorbent case exhibiting only radiation from the plasma where the variation in reflectivity on the first wall creates definition in the wall details.

The emission in the wavelength range of 400 nm to 900 nm is one of the outputs of CHERAB and is shown graphically in figure 6.3. The emission lines are mostly present in both although some are seemingly enhanced much more than others. This would make sense because the reflectivity of the first wall allows radiation emitted in out-of-sight regions of the plasma to reach the diagnostic view acceptance cone.

In order to compare the effect of the reflectivity, the data was integrated within 2nm bins

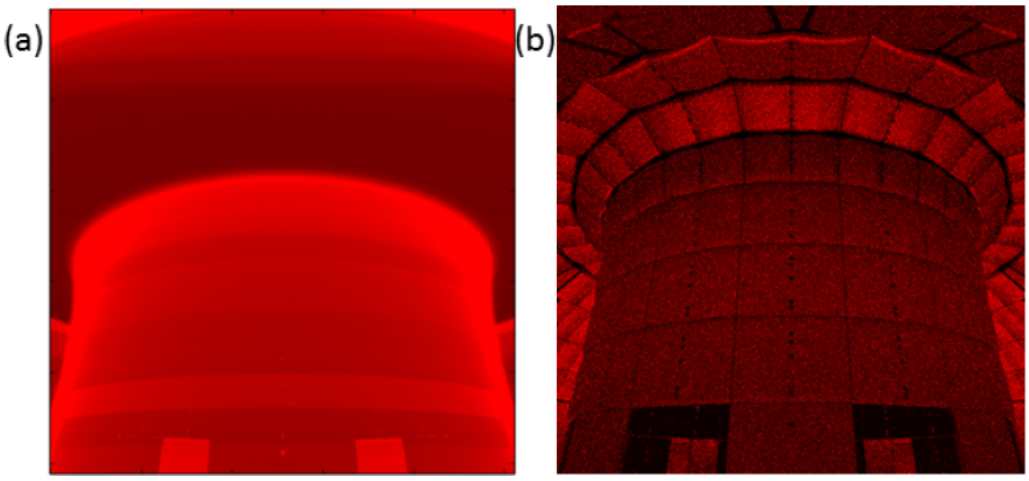

Figure 6.2: Output of the CHERAB code where a) represents the output when the tiles are modeled as absorbent, b) shows the same but with reflectivity taken into account. Image partially taken from [15]

in order to provide sufficient resolution to preserve information about the spectral lines. The output of this was an enhancement factor as a function of wavelength representing the effect of the reflectivity on the model. This could then be compared with literature to evaluate the credibility of the model and the severity of the impact of the reflective wall on background signal.

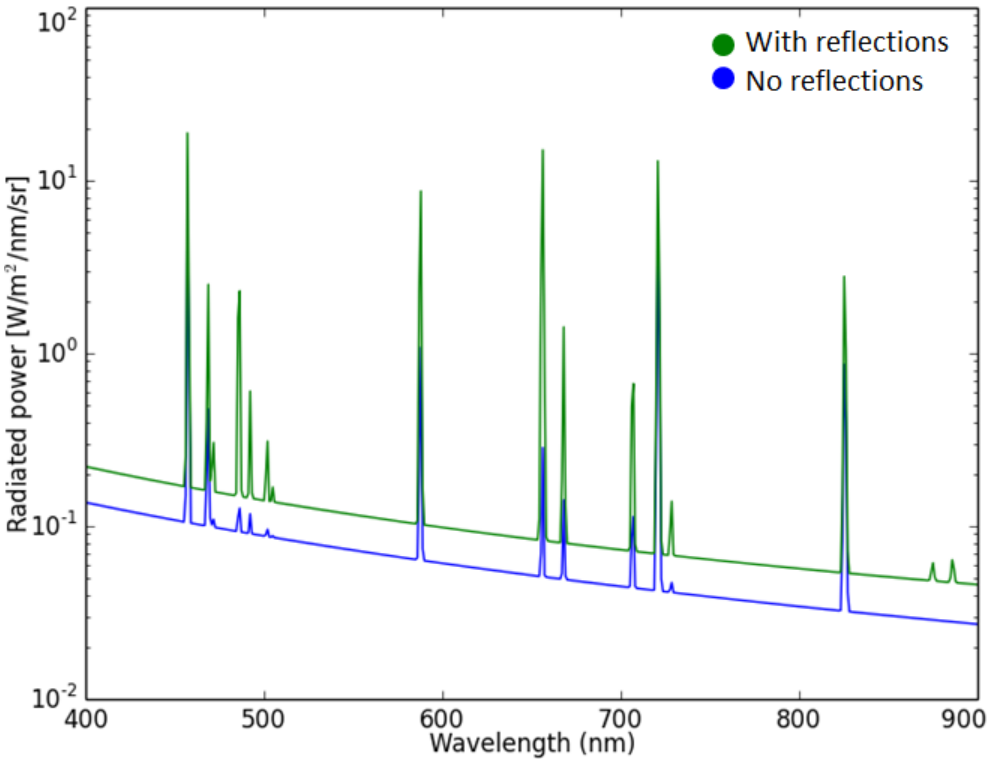

Figure 6.3: Spectral output integrated along the viewing chord with and without reflectivity of the first wall taken into account. The overall effect at a glance appears to be around a factor of two at most which is encouraging.

6.3.2.2 JET-ILW HRTS data handling

The shots used were numbered 92357-92359 and were largely similar in terms of radiated power, NBI power, plasma current and plasma density - see figure 6.4. Data was chosen based on the most stable radiated total power over a given period of one second (50-51 seconds in the figure). These shots were also performed to enhance background radiation to close to worst-case scenario levels. The effective positive charge Z was similar for the three shots, around 2.4, the electron temperatures were 5, 4.1, and 3.7 keV respectively. It is also worthy of note that all of the parameters shown in the figure were relatively stable throughout the time window chosen and similar to each other. This meant that the radiation profiles were not simply similar out of coincidence but because of similar operational conditions in the plasma.

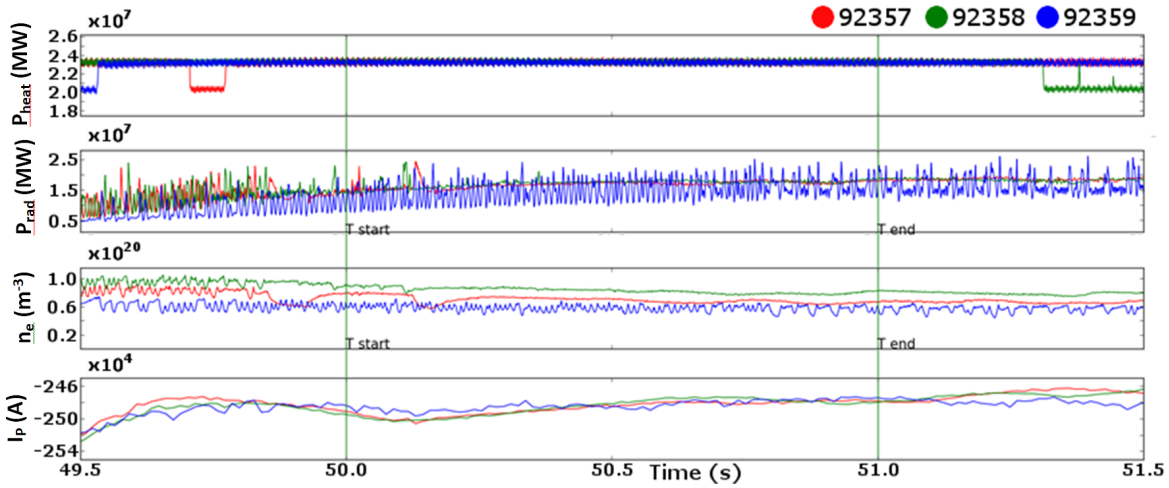

Figure 6.4: Characteristics of the shots examined for the background light study. Jet shots 92357-92359 were used because they exhibited strong similarity and stable periods of operation in terms of many output parameters, particularly radiated power.

The measurements were performed by directing a fibre directly downwards through the HRTS optics without pointing towards the divertor entrance gap as shown in figure 6.5. This was done so as to capture the profile which would be observed by the HRTS diagnostic itself assuming the TS lasers were not discharging.

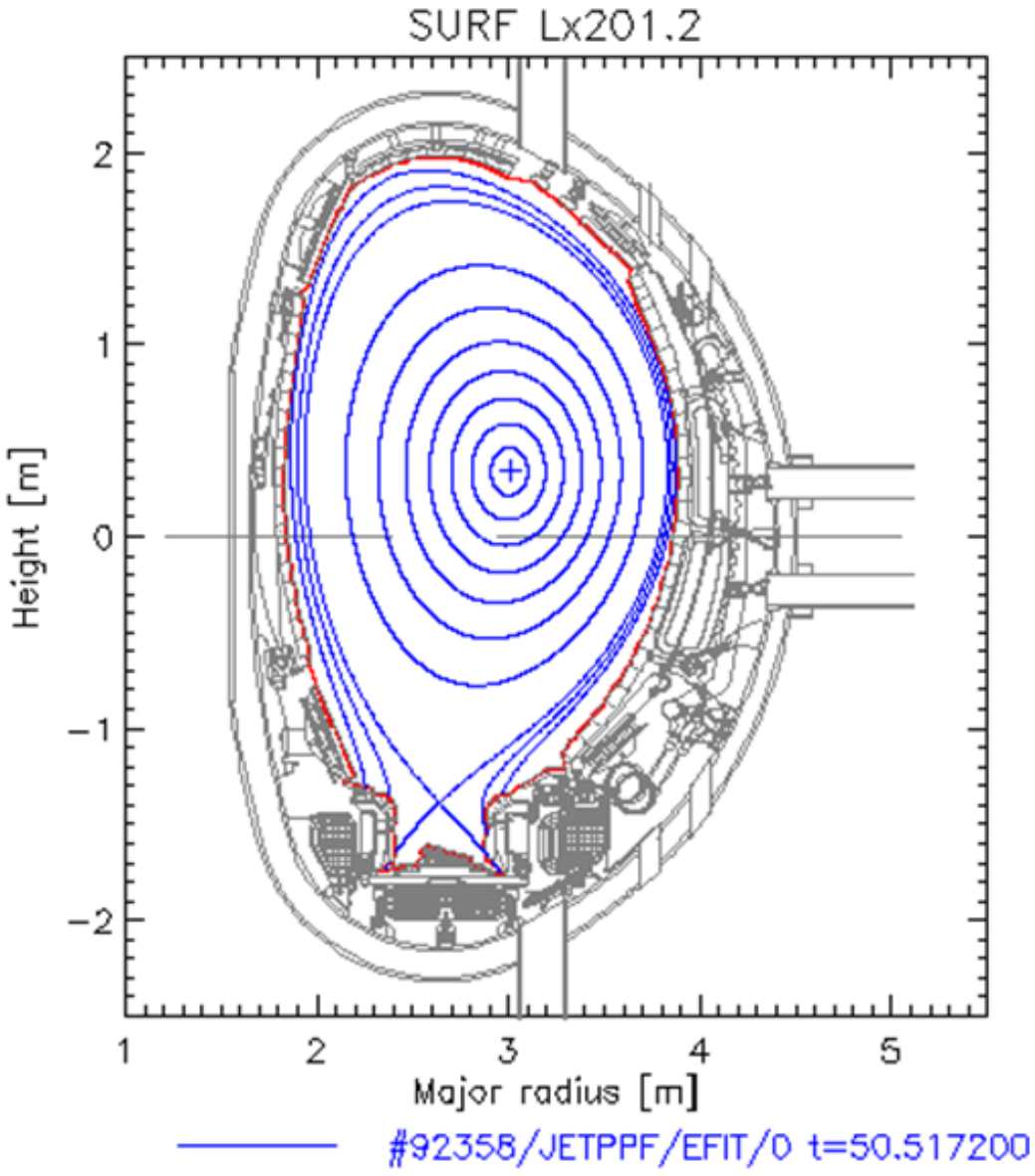

Figure 6.5: Schematic of background light collection viewing chord on JET-ILW in relation to the vessel wall, divertor and first wall. Obtained from R. Scannell and CCFE.

6.3.2.3 Comparisons between CHERAB and JET-ILW data for determining accuracy of CHERAB and choice of spectral binning

In order to compare the CHERAB output with real data, it was scaled so that the bremsstrahlung radiation matched the bremsstrahlung curve found in the JET-ILW shots. This was mainly to evaluate whether or not there were discrepancies in the line radiation and overall trend shape. The spectra could then be analysed with respect to each other both by inspection and through simulated diagnostic acquisition. This simulated diagnostic approach was mainly concerned with the various transfer functions which could be installed on the final collection optics. The reason to use a transfer function of this kind pertains to the extreme high temperature plasmas present in fusion research and how they are diagnosed with Thomson scattering.

Thomson scattering operates through the scattering of laser photons from a population of electrons with some temperature T_e. Through the Doppler effect, the scattered photons are shifted in wavelength and radiated away resulting in a broadened peak centered on the incident laser peak [4]. By performing a fit to this profile, both the electron temperature T_e and density n_e can be measured with high accuracy. For low temperature plasmas this broadening effect is small, to the extent that block filters are not narrow enough to reject small bandwidths corresponding to line emission. Instead a spectrometer is typically used which has the necessary resolution to avoid such ranges. In fusion research, electron temperatures are so high, the peak is extensively broadened. This allows the use of line blocking filters and spectral channels to infer the shape of the emitted curve using analysis and modelling techniques.

These transfer functions would dictate the radiation which made it to the detection system. Based on the line emission present in the JET-ILW data, CHERAB simulation, and the idea to filter nothing, as is the case for the JET-ILW LIDAR diagnostic [230], three notch filter profiles were suggested for analysis which would reject various emission line regions or none at all. The LIDAR style transmission function was included as a way to re-examine if filters were even worth considering in line with question 5 6.3.1.

The notch filters are placed just before a series of photodiodes with integrate the light collected within each channel/bin and those photodiodes are not equally sensitive at all wavelengths. The combination of the sensitivity profile of the photodiodes and the filter/wavelength channel structure designed by the diagnostic team is called the transfer function. The transfer functions speculated upon for this study are shown in figure 6.6.

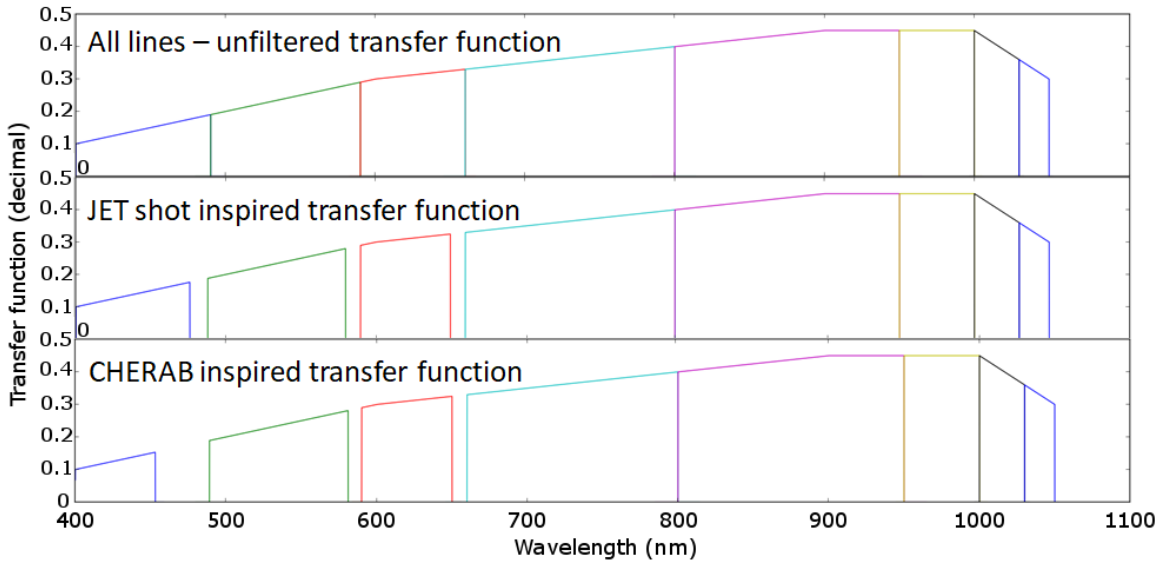

Figure 6.6: Transfer functions based on the emission line profiles of JET-ILW and the CHERAB simulation compared to an unfiltered profile. There were slightly more high intensity lines in the output of the CHERAB code so the filter profile is a little more conservative than the one which would suffice for JET-ILW.

Assuming the true ITER background radiation resembles an up-scaled version of that which is present on JET-ILW already, it would be recommended to filter out Dα at 656.3 nm, Dβ at 486.1 nm, and Helium at 587.5 nm. These represent the strongest atomic emission lines of the most abundant atomic species in the plasma in JET-ILW. The CHERAB transfer function is much the same except for additional filtering around the Beryllium 457.3 nm line.

6.4 Results

6.4.1 Results concerning reflectivity in the CHERAB ray tracing simulation.

The reflectivity was examined by processing the raw data into 2 nm bins. This was done to reduce the number of comparison points without losing detail associated with the spectral lines. More specifically, this allowed the enhancement factors of individual lines to be plotted along with a curve associated with the bremsstrahlung curve. This binning was only used for this analysis and was not repeated for the transfer function analysis performed later on. Figure 6.7 shows the data placed into these 2 nm bins as well as the enhancement factors calculated as a result. It was confirmed that the enhancement factors were independent of the spectral lines in so much as no two lines were enhanced by the same amount by including reflectivity in the simulation. It did, however, appear that the bremsstrahlung was enhanced by a constant factor.

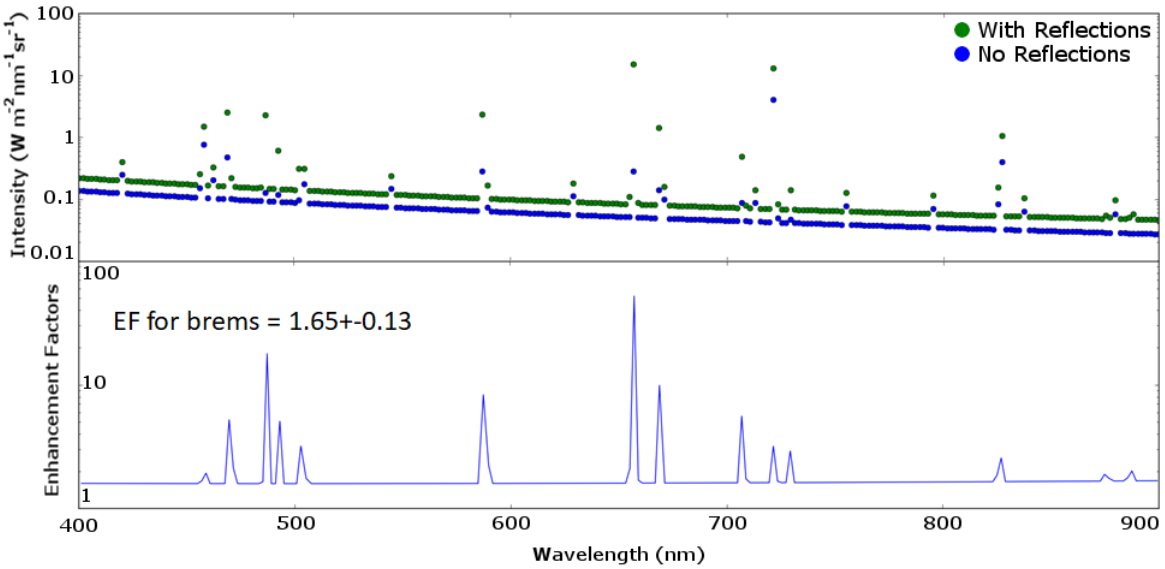

Figure 6.7: Enhancement factors of background light (bremsstrahlung and line radiation) as a function of wavelength from CHERAB code output in 2 nm bins.

To check if the enhancement was in fact constant, the y axis was zoomed to the appropriate scaling, revealing that the enhancement of the bremsstrahlung was not in fact constant but rather a curve. The curve was smooth and seemed somewhat polynomial in nature.

It is known that reflective surfaces do not reflect all wavelengths equally, hence the reflectivity of a surface is wavelength dependent. This is shown for tungsten under different

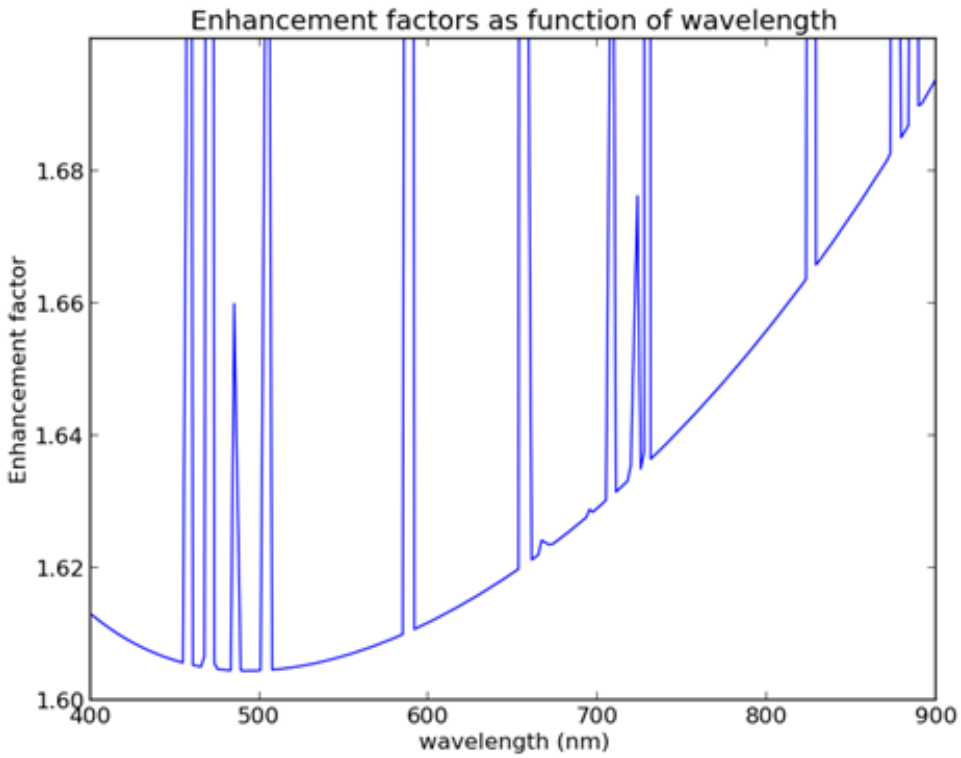

Figure 6.8: Enhancement factors of background light with a focus on the bremsstrahlung radiation which otherwise seemed constant. This revealed the curvature of the enhancement factor as a function of wavelength.

conditions by both Sakaguchi et.al. [16] and Kajita et.al. [231] where the reflectivity varied with wavelength anywhere from 30%-40% in Sakaguchi or 40%-50% in Kajita. An example of this is shown below in figure 6.9. The addition of reflectivity in the model enhanced the continuum radiation by approximately 60% which is order-of-magnitude correct when compared to these previous studies. This is derived from the average enhancement factor for the bremsstrahlung of 1.65 ± 0.13. Differences between the model and measurements could be down to the specifics of the surface crystallography of the tungsten in the experiments compared to a generic value or function used in the CHERAB code.

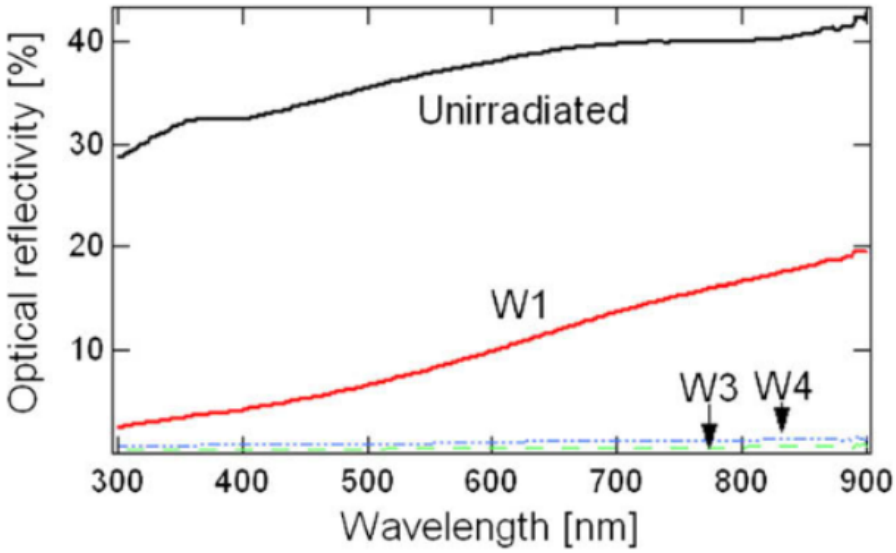

Figure 6.9: Results obtained by Sakaguchi et.al. [16] which show tungsten having a reflectivity of around 40% which would explain the enhancement factors being around 1.6-1.7 (order of magnitude $\approx$ 50% enhancement). The data also shows a general upwards trend for much of the range which is not too dissimilar from the enhancement factor curve.

6.4.2 Analysis of fit between the JET-ILW background and CHERAB

The JET-ILW data and CHERAB data were sampled at 670 nm where there was no significant line emission in order to find a scaling factor between the two. This was then applied in a multiplicative fashion in order to compare the JET-ILW shots and the simulation for agreement. The result of this is shown in figure 6.10.

It can be seen that the major line emission is similar between the two spectra, where some intense lines in JET-ILW have been truncated. The bremsstrahlung curves match well across the entire relevant wavelength range so the two agree with each other well after scaling. The large drop at the low wavelength range and the peak at 1100nm should be ignored as they are systematic aberrations inherent to the JET-ILW optics.

6.4.3 Identification of strong lines for filtering

In order to compare the line and bremsstrahlung emission between the JET-ILW background light and the estimation from CHERAB, a bremsstrahlung curve was calculated using equation 6.2. This was then modified to simulate the diagnostic system to give a detected curve given by 6.1. This allowed the comparison of the relative signal strengths which would be measured when comparing the background light with and without the line emission contri-

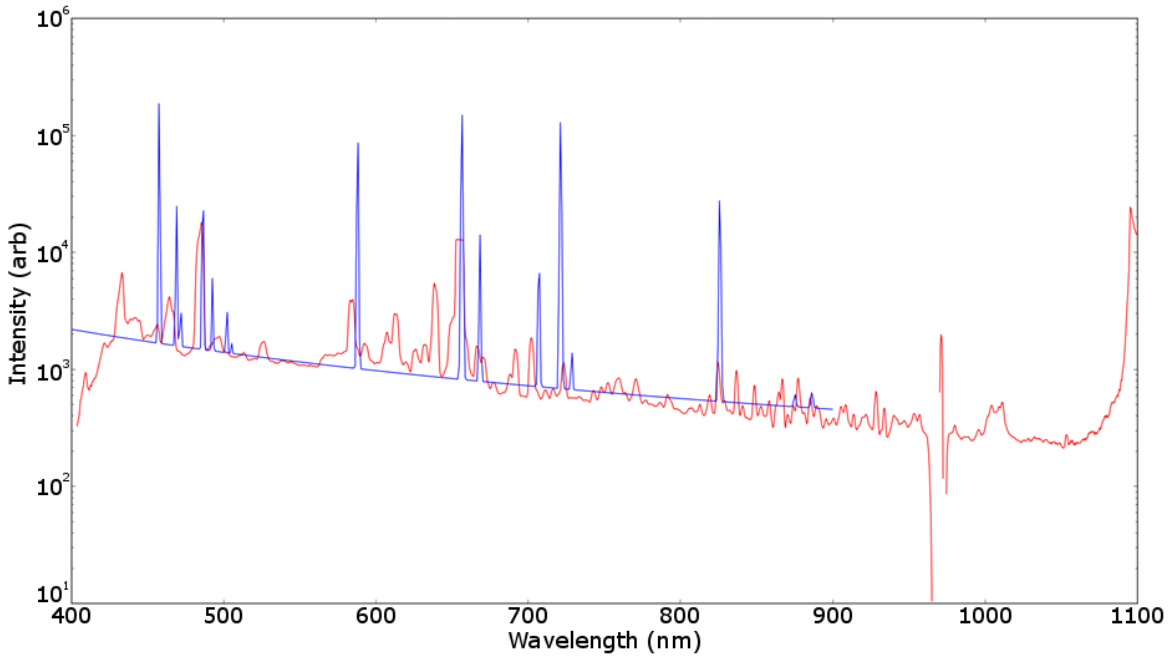

Figure 6.10: A comparison of the JET-ILW emission data and the CHERAB data after scaling to match the bremsstrahlung sampled in each case at 670nm. The two are shown overlaid to provide easy comparison of lines and bremsstrahlung curves. The agreement is good between the two despite the relative size of a few lines and considering the viewing chords are somewhat different.

bution to each channel.

$$PE_{det} = T_p A_{det} \Delta\Omega_{det} T_\lambda \frac{QE}{NF^2} \cdot \int_{-a}^{a} \frac{\epsilon(\lambda, r, T_e, Z_{eff})}{4\pi} dl \tag{6.1}$$

where $\mathrm{PE_{det}}$ is the number of detected photoelectrons in the photodiodes, $\mathrm{T_p}$ is the transmission coefficient of the polarizer in the collection optics, $\mathrm{A_{det}}$ is the detector area and $\Delta\Omega_{det}$ is the detection solid angle. T_λ is the transmission as a function of wavelength, QE/NF^2 is the quantum efficiency and ϵ is the bremsstrahlung emitted by the plasma which is given by equation 6.2.

$$\epsilon(\lambda, r, T_e, Z_{eff}) = \frac{C n_e^2(r) Z_{eff} g_{ff}(T_e)}{\lambda \sqrt{T_e}} \tag{6.2}$$

where $\mathrm{T_e}$ is the electron temperature in eV, $\mathrm{n_e}$ is the electron density per cm^3, λ is the photon wavelength in nm and C is a scaling constant. The gaunt factor $\mathrm{g_{ff}}$ is given by $0.6183 \cdot \ln T_e - 0.0821$. This could then be used to compare the effect of adding the line emission to the detection calculations, allowing decisions to be made as to whether line

radiation within specific channels was significant and warranted filtering.

The result of this is shown in figure 6.11 for the transfer function based on the existing JET-ILW design. It can be seen that the only channel whereby the line emission contributes significantly is the third. Even so the enhancement due to line emission is only a factor 2 which manageable. The difference is due to a larger number of small lines as opposed to one saturated line which should mean that damage is not a problem for the detector.

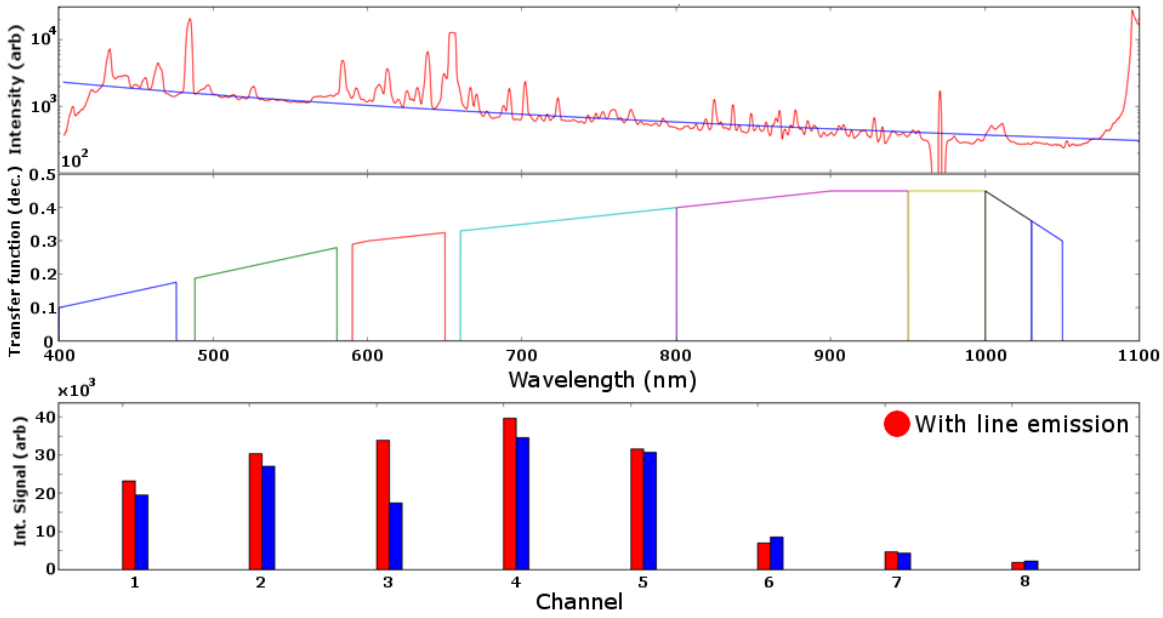

Figure 6.11: Relative contributions to photodiode channel counts with (red) and without line emission (blue) for one of the JET-ILW shots (shot 92358). This represents the analysis subject to the spectral bins based on the strong lines from JET-ILW. The other two shots were practically identical as expected from the similarity on the emission profiles.

The result of performing this process to the reflections-included CHERAB output is shown in figure 6.12, also for the transfer function based on the existing JET-ILW design. It can be seen that the line emission contributed significantly to channels 1 and 4, enhancing the photoelectron signal by approximately 3x in each case.

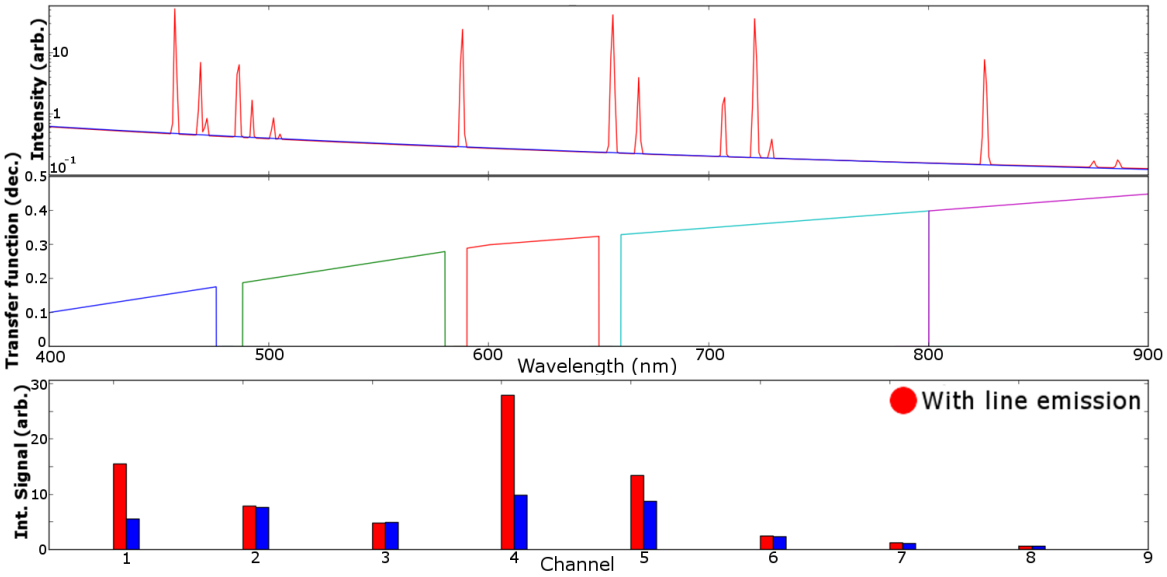

Figure 6.12: Relative contributions to photodiode channel counts with (red) and without line emission (blue) for the CHERAB output (with reflections included). This is also using the signal binning based on JET line emission.

Figure 6.13 displays the comparison between the application of each transfer function from 6.6 applied to one of the three JET-ILW shots examined in the study with and without line emission. The added line emission (displayed as before in red) does not contribute noticeably to the background light except in the channels which either look at strong lines of deuterium and helium or overlap a region occupied by a high density of weaker lines. This is evident in channel 3 which detects the truncated D-α line in the unfiltered function but also detects a series of other, weaker lines which happen to reside close together. If the alpha line was observed without truncation the difference would be much larger. The difference in the line emission does not change much in each case because of this high density of alternate lines. Channel 1 shows the consequence of omitting the D-β line using a filter. The line emission contribution is reduced immediately by around 20% which is significant. This line may even be enhanced under detached ITER divertor conditions so may be worth filtering out. The rest of the channel are relatively unaffected by line emission in the background.

The effects of choosing the transfer function are more obvious when applied to the

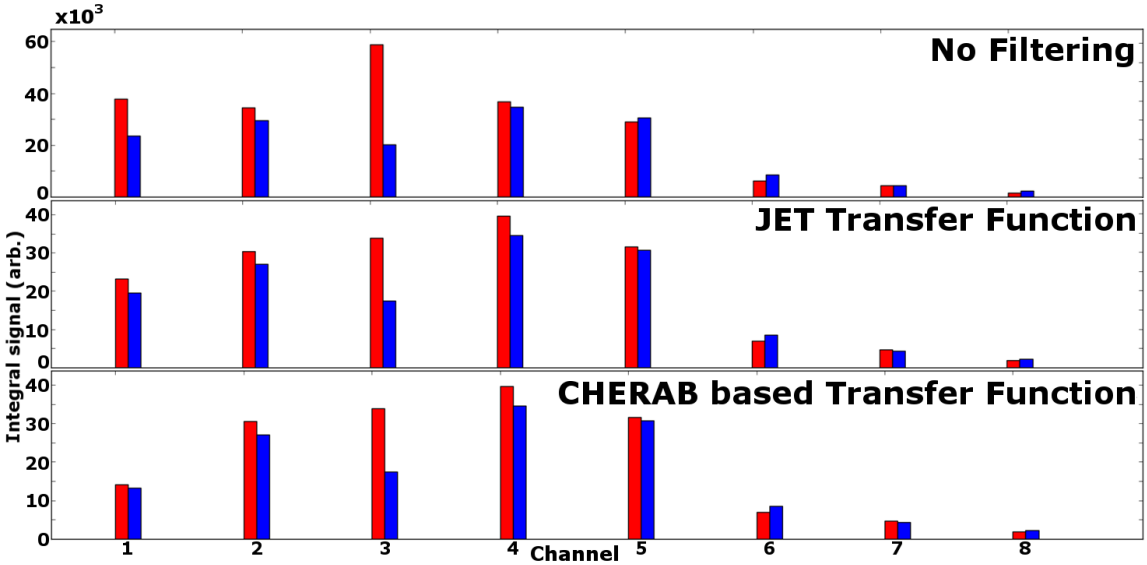

Figure 6.13: Result of comparing the different transfer functions to each other for an example of the JET-ILW background signal. It can be seen that there is not much difference between the JET-ILW-based transfer function and the CHERAB based one. It may be that the lines present in the CHERAB output are an overestimate and not worth being cautious of.

CHERAB data as shown in figure 6.14. Owing to the stronger contributions from lines like beryllium 457.3 nm and the relative intensities of normally weaker lines of deuterium like D-486 nm, the differences in the channel integrals between the unfiltered and transfer function affected integrals are larger. This called into question the trustworthiness of the relative intensities of some of these lines from the CHERAB code. Overall this showed that the JET-ILW-style transfer function was generally good enough for both data sources and that the additional filtering supposedly warranted by the extra lines in CHERAB was potentially not worth the reduction in the Thomson signal.

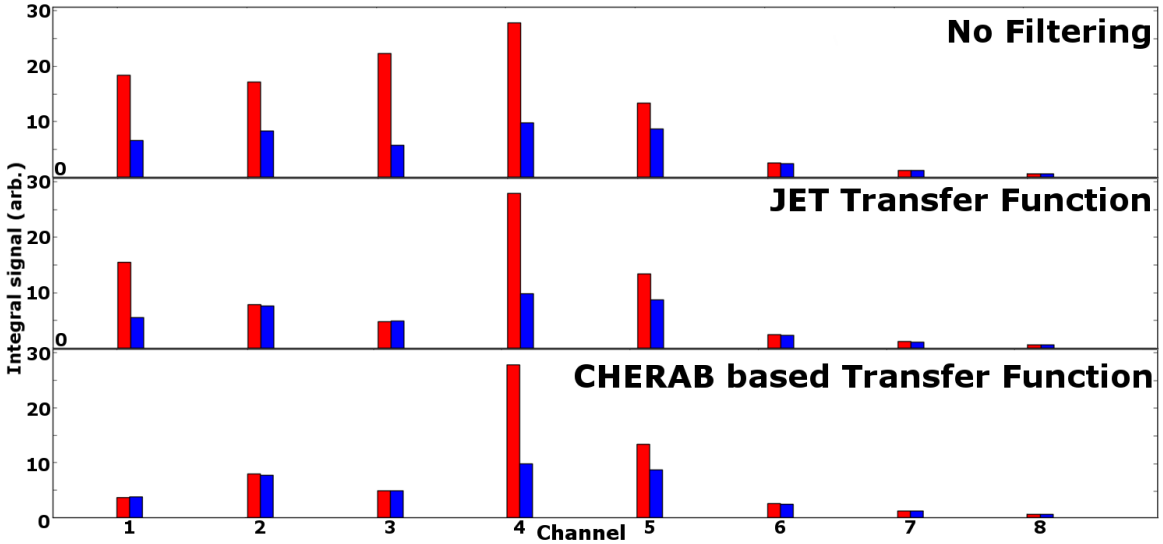

Figure 6.14: Result of comparing the different transfer functions to each other for the reflection-inclusive CHERAB simulated ITER signal. In this case, the difference between the JET-ILW-based transfer function and the CHERAB one is more pronounced. This is to be expected given the extra filtering was only added because of the significant lines in the CHERAB output.

6.5 Conclusions and additional work

To answer the five questions posited earlier in section 6.3.1 the following conclusions were drawn:

1: It was believed by the group that the JET-ILW background signal, if scaled appropriately was a good representation of the likely signal collected by the ITER CPTS diagnostic. This is based on the tangible nature of the data and it being from the closest available device to ITER itself. The CHERAB simulations were thought to be reasonable also, although the intensity of some lines of beryllium and helium which are typically weak in the JET-ILW cases was treated with some skepticism.

2: The agreement between the CHERAB simulations obtained from SOLPS modelling and 3D rendering codes, and the background light profile already observed in JET-ILW, was good for both the bremsstrahlung trend and the major emission lines. The lines present in the CHERAB spectrum originating due to eroded wall materials were also present in the JET-ILW data but in some cases were diminished relative to the stronger lines of H,D or He.

3: Other than the Strong lines of deuterium (D-α, D-β) and the strongest line of helium (He-587.5 nm), no other lines were enhanced noticeably by the reflectivity of the first wall. Those primary problem lines are already intense without reflectivity taken into account meaning the overall effect of the reflectivity was minor, an enhancement of the continuum by around 1.6x and individual, already weak lines by around 5$\times$ at most.

4: Other than the primary lines corresponding to D-α, D-β, and He-587.5nm, no other lines, when scaled between CHERAB and JET-ILW simulations were thought to represent a significant threat to operation for the ITER CPTS diagnostic.

5: Owing to the sensitivity of the Thomson scattering diagnostic compared to the LIDAR, It was decided that the primary lines of deuterium (D-α, D-β) and the strongest line of helium (He-587.5 nm) were worth considering for filtering. This was realised in a recent publication regarding the filter choices for the ITER CPTS diagnostic which also goes into more detail regarding the other considerations regarding the diagnostic [15].

The paper referenced by Scannell et.al. [15] contains a more comprehensive summary of the diagnostic as a whole and contains information which was contributed to, in part by this project.

It would have been desirable to compare the variability on the first wall reflectivity in JET by using data obtained with the Carbon first wall. Unfortunately, the background light

measurements were not conducted back when this wall was installed which would have likely represented a low reflectivity scenario with which to compare with the CHERAB simulations in terms of the continuum and emission line enhancement factors. It would also be ideal to simulate Thomson scattering signals for these transfer functions in order to obtain a value for the ratio between the background an the Thomson signal for each channel. This represents a useful signal:noise ratio benchmark for each channel which could be used to improve the diagnostic by changing the locations of the bins or performing other optimizations regarding filtering or component choice.

Chapter 7

Conclusions and future work

7.1 Summary and conclusions

As ITER nears completion and operational readiness, it is essential that the understanding of divertor detachment be as developed as possible. This is to provide optimal handling of the power and particle flux to the divertor, allowing for long periods of operation. Without a gaseous detached divertor, the plasma facing components will sustain unacceptable levels of damage quickly, requiring regular machine downtime to repair. This would both delay other research on ITER and present an intractable problem for a commercial reactor. Detachment of the plasma from these plasma facing components through the application of gas puffing is currently the best option for handling this problem. By adding a significant number of neutral species, the plasma becomes more collisional and begins to partially neutralise. This removes the influence of the magnetic field from many of the still somewhat energetic species, allowing them to redistribute through collisions, depositing the stored energy over a much larger area. During these processes, the plasma species also radiate more energy through atomic and molecular transitions into 4π steradians, further improving the spread of the stored power onto the walls. In particular, the molecular dominated MAR detached regime reduces hot particle flux more effectively and at higher temperatures compared to the electron ion dominated EIR regime.

Despite how important and potentially valuable MAR detachment is for tokamak divertors, the understanding is still quite limited both to the dominant mechanisms and how to optimise them to enhance divertor longevity. The work in this thesis was done to improve the understanding of MAR by examining the effects of varying surfaces in close proximity

to a divertor relevant hydrogen plasma on the GEC reference cell, and by contributing new measurements of MAR detachment relevant species to the body of work on linear divertor simulators. This was done, in the case of the GEC, by measuring the negative ion densities in close proximity to various grounded electrode materials and studying how the densities evolved for each material as a function of gas pressure and applied RF power. In the case of the linear divertor simulator at the York Plasma Institute (the York Linear Plasma Device), negative ion densities were measured as a function of the radial position from the center of the plasma. The electron temperatures and densities at the respective radial positions were measured in-situ providing direct comparisons between these parameters. These data were combined with estimates for the rotational and vibrational gas temperatures for more insight into the onset of MAR detachment. The pressure, upstream conditions and solenoid field were also varied to observe their effects on the negative ion profiles in order to obtain a picture of the MAR plasma under the various applied conditions.

The GEC standard plasma cell allows the study of fundamental plasma physics with multiple different gasses as well as the interactions between plasmas and surfaces in a relatively well defined and reproducible environment. The lower, grounded electrode is typically made of stainless steel however samples may be placed upon it to investigate the interaction between the plasma and that sample. Samples of Tungsten, Molybdenum and Stainless Steel (304) were used in this work due to their presence in tokamak devices, particularly the divertor. The advantages of the GEC device are the large existing body of work, and the ease of diagnostic access and experiment setup.

The YLPD allows for divertor relevant plasma behaviour to be studied within the confines of a magnetic field at high electron temperatures and densities replicating, to some extent, a filament of plasma one might expect to find in a tokamak scrape-off layer. It also provides access to different detachment regimes through the variation of the various externally controllable parameters, most notably the pressure and composition of neutral gas puffing into the target chamber. The plasma may be studied using optical diagnostics and probe based diagnostics to provide measurements of key parameters.

The experiments on the GEC showed a clear variation in the negative ion population with surface material for a given RF power and gas pressure. The trends observed appeared to be a similar shape for the different materials with the maximum negative ion density at a given pressure manifesting at different applied RF power. Steel and tungsten appeared

to outperform molybdenum over the power and pressure ranges studied. The negative ion fraction varied from non-significant to around 2% at most which is not unusual for plasmas of this type given that most existing work uses the simplified photodetachment technique. The conditions under which the negative ion fraction was maximised differed between surface materials strengthening the position that the surface physics play a vital role in the negative ion dynamics. Absolute negative ion densities around 10^{14} m^{-3} were similar to those found in experiments on other gasses and agree with order of magnitude estimates from various models which tend to predict densities up to around 0.1 n_e.

While some mechanisms are known and have been identified regarding the creation of negative ions, additional physics is required to explain the observed variation with surface material. In the GEC experiments, the most promising processes affect both the number density of vibrationally excited hydrogen molecules and the vibrational energy distribution function. This then enhances the rate of dissociative attachment and thus the formation rate of negative ions. The first of the two processes identified were the hot-atom recombination process which can lead to an increase in the density of hydrogen molecules, particularly in vibrationally excited states. This is due to the surplus energy of the recombination being distributed into molecular energy states. The second process or family of processes is the acceleration and neutralization of the prevalent H_3^+ ion. This recombination can lead to the creation of atoms and molecular hydrogen. The atomic density appeared to scale similarly between materials so the different surfaces may cause different rates of dissociation into molecular species. The implication of the work done on the GEC is that more study is warranted regarding the contribution of surface material choice to MAR detachment and its optimization in the divertor. If the precise surface mechanisms leading to enhanced negative ion production are thoroughly understood, detachment processes can be employed optimally to improve plasma facing component lifetimes in next generation fusion devices.

The experiments on the YLPD provided new high resolution radial profiles of negative ions in an MAR, divertor relevant plasma. These measurements showed a hollow density profile concentric with the plasma axis where n_e and T_e and highest. This is similar to behaviour observed on the linear divertor simulator TPDSHEET, though there are still some differences between them which can be explained by differences in the source, magnetic field profile and overall device design.

The hollow profile, was likely the result of hydrogen molecules from the gas puff entering

the central hot plasma, gaining vibrational energy then travelling radially outwards to regions where the electron temperatures and densities were low enough such that dissociative attachment could take place. This led to the presence of negative ions in a ring or tubular structure around the main plasma beam. The peak in the negative ion density profile could be seen to move away from the central beam with increasing gas pressure. There was some negative ion presence observed at the onset of MAR detachment at 0.11 Pa which showed signs of reaching a maximum at some radial position outside the range available in this work. The change in the profile was dramatic with a relatively small pressure increase to 0.17 Pa where the negative ion population maximum was greater overall and closer to the central portion of the plasma. The radial variation in the negative ion maxima is interesting and warrants further study with similar and complimentary techniques on a wider range of divertor relevant devices.

The negative ion fraction was approximately zero close to the central beam and up to 20% around 16-17 mm from the beam center at high gas pressure. In these regions, the electron density was an order of magnitude lower when compared to the core density. The rise in rotational gas temperature was similar to rotational temperature increases observed in other experiments, showing some level of saturation of the kinetic gas temperature. The vibrational populations ought to change with increasing gas pressure and evidence for this was obtained via the Fulcher band measurements. More study is required in order to obtain data which displays the distribution of vibrational states among molecules in and around the central plasma beam. The increasing pressure could be seen to move the negative ion density maximum outwards further from the plasma. The availability of more data regarding negative ion profiles on linear divertor simulators is invaluable to the testing and development of computational models which may then be applied to larger experiments and varied geometry.

This work supports the general mechanisms thought to constitute the volume processes responsible for the MAR plasma state. This work highlights the critical role of transport to the MAR reaction chains, whereby the vibrational excitation of molecules and dissociative attachment happen in different locations, under different plasma conditions. This means that the optimisation of MAR for divertor survivability is not reducible to a single parameter like the electron temperature. The temperature profiles of the electrons and the gas molecules at least must be optimised together along with the transport of $H_2(V=4+)$ to the regions

where T_e is optimal for dissociative attachment. This requires sophisticated modelling which can handle both particle transport and complex gas-phase chemistry. While high precision transport codes exist and hydrogen plasma chemistry models also exist, codes which perform both adequately to handle this effect are at least not commonplace. Due to the inherent inaccuracies of the simplified photodetachment theory, some normalisation may be necessary. Regardless, the detailed measurements made in this work would provide a useful benchmark for such models, aiming to optimise detachment purely by volume MAR processes.

In addition, while there is some existing work on plasma-surface interaction for tokamak plasmas and divertor relevant plasmas, the surface contribution to detachment, particularly in the context of MAR has not been studied. The work performed on the GEC reference cell shows that the interactions between the plasma and the surface contain an important pathway for the production of negative ions which can enhance detachment physics. It is therefore important that this surface influence on detachment be given more consideration moving forward. For the fusion research community, the variation in surface material of divertor components is extremely limited, at least at the strike points due to the expected heat load and assumption that melting point is the critical parameter (this is not inherently wrong). In the case of divertor models, the inclusion of surface contributions to the overall detachment physics will result in more accurate model output. This is currently largely or completely overlooked.

With additional measurements suggested in the following section, the precision of the gas temperature measurements may be improved as well at the electron temperature and density measurements in the YLPD. Additionally, some similar measurements may be performed on the GEC system to enhance the precision of measurements made of key parameters allowing the mechanisms responsible for the observed surface effects to be deduced. It would also be beneficial to perform additional work investigating the validity and accuracy of the Langmuir probe assisted laser photodetachment technique on the LPD. Similar to the work discussed in section 2.7.2, a model could be constructed to simulate the electron density and temperature gradients present in this work as well as the magnetic field in order to examine the effect these factors have on the photodetachment results.

7.2 Future work - GEC device

The GEC work would ideally be extended to include a much wider array of surface types in order to fully characterise the effect of both additional metal samples as well as insulating materials, semiconductors and complex hybrid surfaces with different surface geometry and/or non uniform surface material. If it is found that multiple processes individually enhance different aspects of MAR relevant reactions near the surface, it may be beneficial to use combinations of materials which form some compromise leading to higher negative ion yields and thus potentially higher recombination rates.

It would also be of interest to use some additional gas pressures within the range studied as well as investigating the H-mode plasma. The H-mode plasma is difficult to reliably operate in pulsed conditions which would result in a smearing of data between the E-mode case and the H-mode case based on the relative probability of each state occurring with each pulse. That is to say if the plasma pulse is in E-mode irregularly around 10% of the time, the error on the H-mode data is significantly enhanced.

7.3 Future work - Linear device

7.3.1 Potential future experiments

Given the diagnostic access and removable target plate of the YLPD, several additional experiments would be desirable to help map the MAR plasma in the target chamber. Some of these would be possible with little to no major alteration of the YLPD proper and would be the studies of immediate interest in the case of additional time to conduct research.

7.3.1.1 Radially resolved OES

It would be beneficial to obtain an estimate for the radial profile of the vibrational temperature of hydrogen molecules in the target chamber. It would be useful to quantify this in order to support the conclusions drawn whereby the molecules are vibrationally excited by the hot central plasma before moving radially outwards to regions of lower electron density and temperature. By changing the gas feed rate into the target chamber, the effect on the radial distribution of vibrational temperature may also be studied in case the optimum vibrational excitation does not exactly correspond to the optimum negative ion production.

7.3.1.2 Atomic hydrogen and H_3^+ measurements

Another two species which has not been extensively studied on the YLPD are atomic hydrogen and the trihydrogen cation. The density of hydrogen atoms could be measured using Laser Induced Fluorescence (LIF) [232] or Two Photon LIF (TALIF) [233] provided enough space to assemble this type of diagnostic. Given that hydrogen atoms can be a destructive species for H^-, understanding its distribution for a few cases would be useful for benchmarking models of the target chamber plasma. Given the nature of the source in the YLPD, it is thought that under normal conditions, the dominant ion is the proton. In the detached cases the density of H_3^+ may rise which can be relevant for surface effects and recombination with volume negative ions. diagnosing these species for a more complete set of measurements on the YLPD would be useful.

7.3.1.3 Thomson and Raman scattering

In order to obtain more accurate electron densities a Thomson scattering diagnostic would be ideal, in conjunction with the bending magnet system, would provide radially resolved electron temperature measurements significantly more reliably and precisely than those obtained with the Langmuir probe. These could also be compared to said probe measurements and also the radially integrated electron temperature measurements made by Willett [76] using the Balmer line ratios. Using relatively little modification, for low temperature plasmas where molecules are present such as those found in MAR divertor plasma, Raman scattering may be performed in conjunction to the Thomson. This was planned however owing to time constraints was not completed. By using a relatively novel filtering technique of using a Bragg grate-notch filter to remove the Rayleigh component [234], the Thomson signal of a low temperature plasma as well as the rovibrational Raman signal may be measured using relatively little space and at a reduced cost compared to a triple grating spectrometer system.

The radially resolved OES, LIF style measurements and Thomson/Raman scattering diagnostics all benefit from the mobility of the plasma column added over the course of this work. Improved characterization and calibration of this or another form of bending would also improve the radial resolution, although because of the dependency of bending on neutral density and solenoid field this may be time consuming. With regards to variables not directly related to the plasma, there are several that would be interesting to examine which are described next.

7.3.1.4 Neutral gas input location

It would be of interest to study the effect of puffing gas at or just after the aperture, potentially at different angles and distances with respect to the plasma, its drift velocity and the magnetic axis. By introducing the gas, relatively pre-diffusion close to the plasma, further upstream it would be possible to examine the effect of this using existing diagnostic techniques. The challenge would be modifying the existing hardware to support this kind of variable gas flow however it could be accomplished using the small crunch seal port on the target chamber end flange, some swagelock or similar tubing and some flexible hose to allow different positions without constant re-configuring.

7.3.1.5 Variation of gas temperature pre-injection

Owing to the need for vibrationally excited molecules for the negative ion production component of MAR, it may be found that pre-heating the gas with some kind of non-ignition based heat exchange system might improve the efficacy of MAR detachment. It may also be the case that loading the gas with energy causes more dissociation effects due to the high energy electron population, reducing the overall rate. Instead the gas could be actively cooled to observe the effect on the rate, allowing the plasma to provide more of the energy required to the vibrational states and potentially reducing the dissociation into atoms.

7.3.1.6 Variable target surface in the YLPD

A custom mount could be made to accommodate sample plates similar to those used in the GEC surface experiments to investigate the effect of surface types at the termination of the plasma. The limitations of this might be that where the diagnostic ports are on the target chamber. These are at least 10cm from the target plate which may mean that surface effects on the plasma at this distance may be minimal. Some studies on linear devices have however reported some reversal of flow in the periphery region of the plasma which could carry surface produced species further back into the target chamber than would otherwise be expected.

7.3.2 Modelling

It would also be prudent to obtain access to a collisional radiative plasma code such as B2-Eirene, CRAMD or similar to model the plasma in the YLPD chamber. Given the

availability of measurements for the device, the code could be bench-marked effectively to the measurements and inform other investigations moving forward. This is particularly pertinent given the relatively low number of radial negative ion profiles for machines with this geometry that exist with good resolution. Furthermore, the ability to model surface effects in a linear device with this geometry would give insight into how significant the surface contributions to the dynamics of the system are at varying distances from said surface.

List of References

[1] Zuvela K, Adlington I, Aljunied SS, and Edwards J. Determining the best approach to commercial fusion power. *PAM Review: Energy Science & Technology*, 1:3–19, June 2014. doi: http://dx.doi.org/10.5130/pamr.v1i0.1383.

[2] JG99.294/1. JET and fusion energy for the next millennia, 2013 (last updated).

[3] Mihaljcic B. *Studies of Detached Recombining Plasmas in the UMIST Linear System - PhD Thesis*. PhD thesis, University of Manchester, 2004.

[4] Wesson J and Campbell DJ. *Tokamaks*. Oxford University Press, October 2011. ISBN 9780199592234.

[5] Hsu WL, Yamada M, and Barrett PJ. Experimental simulation of the gaseous tokamak divertor. *Physical Review Letters*, 49, October 1982.

[6] Imai T, Yoshihiko U, and Takarnura S. Characteristic performance of the ICRF heating in the divertor plasma simulator NAGDIS-II. *Fuel Cells Bulletin*, 2, February 2001.

[7] Schmitz L, Merriman B, Blush L, Lehmer R, Conn RW, Doerner R, Grossman A, and Najmabadi F. Plasma and neutral dynamics in a simulated tokamak gas target divertor. *Physics of Plasmas*, 2, August 1995.

[8] Blackwell BD, Caneses JF, Samuell CM, Wach J, Howard J, and Corr C. Design and characterization of the magnetized plasma interaction experiment (MAGPIE): a new source for plasma–material interaction studies. *Plasma Sources Science and Technology*, 21, October 2012.

[9] Tonegawa A, Ono M, Morihira Y, Ogawa H, Shibuya T, Kawamura K, and Takayama K. Observation of molecular assisted recombination via negative ions formation in a

divertor plasma simulator, TPDSHEET-IV. *Journal of nuclear materials*, 313, March 2003.

[10] Van Eck HJ, Abrams T, Van Den Berg MA, Brons S, Van Eden GG, Jaworski MA, Kaita R, Van Der Meiden HJ, Morgan TW, van de Pol MJ, and Scholten J. Operational characteristics of the high flux plasma generator MAGNUM-PSI. *Fusion Engineering and Design*, 89, October 2014.

[11] Chemistry Department St. Olaf College. Electronic, vibrational, and rotational energy levels in the hydrogen molecule, N/A. URL https://www.stolaf.edu/depts/chemistry/imt/js/h2energy/h2.htm.

[12] Xiao B, Kado S, Kajita S, and Yamasaki D. Rovibrational distribution determination of H_2 in low temperature plasmas by Fulcher-α band spectroscopy. *Plasma Physics and Controlled Fusion*, 46, March 2004.

[13] Lejeune C. Theoretical and experimental study of the duoplasmatron ion source: Part i: Model of the duoplasmatron discharge. *Nuclear Instruments and Methods*, 116(3): 417–428, 1974.

[14] Bradley JW, Forder DA, and Rusbridge MG. The emerging plasma beam from a duoplasmatron source and the potential for material sputtering. *Plasma Sources Science and Technology*, 4:516–526, 1995.

[15] Scannell R, Maslov M, Naylor G, O'Gorman T, Kempenaars M, Carr M, Bilkova P, Bohm P, Giudicotti L, Pasqualotto R, and Bassan M. Design advances of the Core Plasma Thomson Scattering diagnostic for ITER. *Journal of Instrumentation*, 12, November 2017.

[16] Sakaguchi W, Kajita S, and Takagi M Ohno N. In situ reflectivity of tungsten mirrors under helium plasma exposure. *Journal of Nuclear Materials*, 390, June 2009.

[17] Tokimatsu K, Fujino J, Konishi S, Ogawa Y, and Yamaji K. Role of nuclear fusion in future energy systems and the environment under future uncertainties. *Energy Policy*, 31, June 2003.

[18] Ongena J and Van Oost G. Energy for future centuries: Prospects for fusion power as a future energy source. *Fusion Science and Technology*, 61, February 2012.

[19] Salpeter EE. Nuclear reactions in the stars. I. proton-proton chain. *Physical review*, 88(3):547, 1952.

[20] Wong CP, Malang S, Sawan M, Dagher M, Smolentsev S, Merrill B, Youssef M, Reyes S, Sze DK, Morley NB, and Sharafat S. An overview of dual coolant Pb–17Li breeder first wall and blanket concept development for the US ITER-TBM design. *Fusion Engineering and Design*, 81, February 2006.

[21] Chen FF. *Plasma Physics and Controlled Fusion*, volume 1. Plenum Press, 1985. ISBN 9783319223087.

[22] Sarff JS, Almagri AF, Anderson JK, Biewer TM, Blair AP, Cengher M, Chapman BE, Chattopadhyay PK, Craig D, Den Hartog DJ, and Ebrahimi F. Tokamak-like confinement at a high beta and low toroidal field in the MST reversed field pinch. *Nuclear Fusion*, 43(12), December 2003.

[23] Motojima O, Ohyabu N, Komori A, Kaneko O, Yamada H, Kawahata K, Nakamura Y, Ida K, Akiyama T, Ashikawa N, and Cooper WA. Recent advances in the LHD experiment. *Nuclear Fusion*, 43(12), December 2003.

[24] Weisemann K. A short introduction to plasma physics. *CAS-CERN Accelerator School: Ion Sources - Proceedings*, 2014. doi: 10.5170/CERN--2013--007.85.

[25] Smirnov VP. Tokamak foundation in USSR/Russia 1950-1990. *Nuclear Fusion*, 50, December 2009.

[26] Kikuchi M. The large tokamak JT-60: a history of the fight to achieve the Japanese fusion research mission. *The European physical journal H*, 43, December 2018.

[27] Costly AE. On the fusion triple product and fusion power gain of tokamak pilot plants and reactors. *Nuclear Fusion*, 56, April 2016.

[28] Synakowski EJ, Stratton BC, Efthimion PC, Fonck RJ, Hulse RA, Johnson DW, Mansfield DK, Park H, Scott SD, and Taylor G. Measurements of radial profiles of He^{2+} transport coefficients on the TFTR tokamak. *Physical Review Letters*, 65(18), Oct 1990.

[29] Hillis DL, Hogan JT, Finken KH, West WP, Weynants RR, Wade MR, Akaishi K, Baek WY, Boedo J, Burrell KH, and Conn RW. Helium transport in enhanced confinement regimes on the TEXTOR and DIII-D tokamaks. *Journal of Nuclear Materials*, 196, Dec 1992.

[30] Sugie T, Itami K, and Nakamura H. Impurity control and helium exhaust experiment in JT-60. *Proc. 13th Int. Conf. on Plasma Phys. and Controlled Nucl. Fusion Research*, 1991.

[31] Sakasai A, Kubo H, and Hosogane N. Transport and exhaust of helium ash in enhanced confinement regimes on JT-60U. *Proc. 15th Int. Conf. Plasma Physics and Controlled Nuclear Fusion Research*, 1994.

[32] Yoshikawa M, Tazima T, Shimomura Y, Kitsunezaki A, Maeda H, Inoue K, Nagashima T, Tokutake T, Ohtsuka H, Nagami M, and Tanaka M. Research on a tokamak with an axisymmetric divertor and impurity problems in tokamak devices. *Proc. 5th Int. Conf. Plasma Physics and Controlled Nuclear Fusion Research*, 1, November 1974.

[33] Keilhacker M, Lackner K, Behringer K, Murmann H, and Niedermeyer H. Plasma boundary layer in limiter and divertor tokamaks. *Physica Scripta*, 443, 1982.

[34] Widdowson A, Alves E, Baron-Wiechec A, Barradas NP, Catarino N, Coad JP, Corregidor V, Garcia-Carrasco A, Heinola K, Koivuranta S, and Krat S. Overview of the JET ITER-like wall divertor. *Nuclear Materials and Energy*, 12, August 2017.

[35] Herrmann A, Greuner H, Jaksic N, Balden M, Kallenbach A, Krieger K, de Marné P, Rohde V, Scarabosio A, and Schall G. Solid tungsten divertor-III for ASDEX Upgrade and contributions to ITER. *Nuclear Fusion*, May 2015.

[36] Shirai H, Barabaschi P, Kamada Y, and JT-60SA Team. Recent progress of the JT-60SA project. *Nuclear Fusion*, 57(10), jun 2017.

[37] Petrie TW, Fenstermacher ME, Allen SL, Carlstrom TN, Gohil P, Groebner RJ, Greenfield CM, Hyatt AW, Lasnier CJ, La Haye RJ, and Leonard AW. A comparison of plasma performance between single-null and double-null configurations during ELMing h-mode. *Conference preceedings*, Jul 1991.

[38] Krasheninnikov SI, Pigarov AY, Knoll DA, LaBombard B, Lipschultz B, Sigmar DJ, Soboleva TK, Terry JL, and Wising F. Plasma recombination and molecular effects in tokamak divertors and divertor simulators. *Physics of Plasmas*, 4, May 1997.

[39] Janeschitz G, Borrass K, Federici G, Igitkhanov Y, Kukushkin A, Pacher HD, Pacher GW, and Sugihara M. The ITER divertor concept. *Journal of Nuclear Materials*, 220-222, 1995.

[40] Stangeby PC. *The Plasma Boundary of Magnetic Fusion Devices*. Series in Plasma Physics. Institute of Physics Publishing Limited, 2000. ISBN 9780750305594.

[41] ITER Physics Expert Group on Divertors. Chapter 4: Power and particle control. *Nuclear Fusion*, 39(12):2391–2469, 1999. doi: http://iopscience.iop.org/0029-5515/39/12/304.

[42] Matthews GF. Plasma detachment from divertor targets and limiters. *Journal of Nuclear Materials*, 220-222:104–116, April 1995. doi: https://doi.org/10.1016/0022-3115(94)00450-1.

[43] Post DE. A review of recent developments in atomic processes for divertors and edge plasmas. *Journal of nuclear materials*, 1995.

[44] Krasheninnikov SI, Kukushkin AS, and Pshenov AA. Divertor plasma detachment. *Physics of Plasmas*, 23, 2016.

[45] Leonard AW. Plasma detachment in divertor tokamaks. *Plasma Physics and Controlled Fusion*, 60, 2018.

[46] Krasheninnikov SI, Pigarov AY, and Sigmar DJ. Plasma recombination and divertor detachment. *Physics Letters A*, 214, May 1996.

[47] Pigarov AY and Krasheninnikov SI. Application of the collisional-radiative, atomic-molecular model to the recombining divertor plasma. *Physics Letters A*, 222.4, March 1996.

[48] Kallenbach A, Bernert M, Dux R, Casali L, Eich T, Giannone L, Herrmann A, McDermott R, Mlynek A, and Reimold F Müller HW. Impurity seeding for tokamak power exhaust: from present devices via ITER to DEMO. *Plasma Physics and Controlled Fusion*, 55, November 2013.

[49] Pitts RA, Bonnin X, Escourbiac F, Frerichs H, Gunn JP, Hirai T, Kukushkin AS, Kaveeva E, Miller MA, Moulton D, and Rozhansky V. Physics basis for the first iter tungsten divertor. *Nuclear Materials and Energy*, 2019.

[50] Kukushkin AS. Title unavailable. *Proceedings of the 20th IAEA Fusion Energy Conference*, 2004.

[51] Loarte A, Lipschultz B, Kukushkin AS, Matthews GF, Stangeby PC, Asakura N, Counsell GF, Federici G, Kallenbach A, Krieger K, and Mahdavi A. Power and particle control. *Nuclear Fusion*, 47, June 2007.

[52] Fantz U and Heger B. Spectroscopic diagnostics of the vibrational population in the ground state of H_2 and D_2 molecules. *Plasma Physics and Controlled Fusion*, 40, December 1998.

[53] Fantz U, Heger B, and Wünderlich D. Using the radiation of hydrogen molecules for electron temperature diagnostics of divertor plasmas. *Plasma Physics and Controlled Fusion*, 43, May 2001.

[54] Fantz U, Reiter D, Heger B, and Coster D. Hydrogen molecules in the divertor of ASDEX upgrade. *Journal of Nuclear Materials*, 290, March 2001.

[55] Reiter D, May M, Baelmans, and Börner P. Non-linear effects on neutral gas transport in divertors. *Journal of Nuclear Materials*, 241, 1997.

[56] Terry JL, Lipschultz B, Pigarov AY, Krasheninnikov SI, LaBombard B, Lumma D, Ohkawa H, Pappas D, and Umansky M. Volume recombination and opacity in alcator c-mod divertor plasmas. *Physics of Plasmas*, 5, May 1998.

[57] Ohno N. Plasma detachment in linear devices. *Plasma Physics and Controlled Fusion*, 59, February 2017.

[58] Yada K, Matsui N, Ohno N, Kajita S, Takamura S, and Takagi M. Investigation of detached recombining deuterium plasma and carbon chemical erosion in the toroidal divertor simulator NAGDIS-T. *Journal of Nuclear Materials*, 390, June 2009.

[59] Hsu WL, Yamada M, and Tenney FH. Neutral gas blanket effects in a gaseous divertor. *Journal of Nuclear Materials*, 111 & 112, November 1982.

[60] Ohno N, Ezumi N, Takamura S, Krasheninnikov SI, and Pigarov AY. Experimental evidence of molecular activated recombination in detached recombining plasmas. *Physical Review Letters*, 81, July 1998.

[61] Ohno N, Nishijima D, Takamura S, Uesugi Y, Motoyama M, Hattori N, Arakawa H, Ezumi N, Krasheninnikov S, Pigarov AY, and Wenzel U. Static and dynamic behaviour of plasma detachment in the divertor simulator experiment NAGDIS-II. *Nuclear Fusion*, 41, August 2001.

[62] Goebel DM, Campbell G, and Conn RW. Plasma surface interaction experimental facility (PISCES) for materials and edge physics studies. *Journal of Nuclear Materials*, 121, May 1984.

[63] Lee G, Manière C, McKittrick J, Doerner R, Nishijima D, Gattuso A, Abrams T, Thomas D, Back C, and Olevsky EA. Consolidation of molybdenum nanopowders by spark plasma sintering: Densification mechanism and first mirror application. *Journal of Nuclear Materials*, 516, April 2019.

[64] Kreter A, Nishijima D, Doerner RP, Freisinger M, Linsmeier C, Martynova Y, Möller S, Rasinski M, Reinhart M, Terra A, and Torikai Y. Influence of plasma impurities on the fuel retention in tungsten. *Nuclear Fusion*, 59, May 2019.

[65] Cai L, Tynan GR, and Hollmann EM. Evidence for molecular-assisted recombination of He^+ from particle balance measurements in helium-hydrogen mixture plasmas in PISCES-A. *Physics of Plasmas*, 15, October 2008.

[66] Antar GY, Krasheninnikov SI, Devynck P, Doerner RP, Hollmann EM, Boedo JA, Luckhardt SC, and Conn RW. Experimental evidence of intermittent convection in the edge of magnetic confinement devices. *Physical review letters*, 87, July 2001.

[67] Hollmann EM, Pigarov AY, Seraydarian R, Whyte DG, and Krasheninnikov SI. Particle balance measurements during detachment in a gas-target divertor simulator. *Physics of Plasmas*, 9, April 2002.

[68] Samuel CM and Corr CS. Low-pressure hydrogen plasmas explored using a global model. *Plasma Sources Science and Technology*, 25, December 2016.

[69] Zorat R. *Numerical modelling of low temperature radio-frequency hydrogen plasmas.* PhD thesis, Dublin City University, 2003.

[70] Gahan D. *Radio-frequency discharge power measurement with emphasis on collisionless electron heating in capacitive sheaths.* PhD thesis, Dublin City University, 2006.

[71] O'Connell D. *Investigations of high voltage plasma boundary sheaths in radio-frequency discharges operated with multiple frequencies.* PhD thesis, Dublin City University, 2004.

[72] Owen LW, Caneses JF, Canik J, Lore JD, Corr C, Blackwell B, Bonnin X, and Rapp J. B2.5-EIRENE modeling of radial transport in the MAGPIE linear plasma device. *Plasma Sources Science and Technology*, 26, March 2017.

[73] Santoso J, Manoharan R, O'Byrne S, and Corr CS. Negative hydrogen ion production in a helicon plasma source. *Physics of Plasmas*, 22, September 2015.

[74] Chen FF. The low-field density peak in helicon discharges. *Physics of Plasmas*, 10, June 2003.

[75] Lafleur T, Charles C, and Boswell RW. Characterization of a helicon plasma source in low diverging magnetic fields. *Journal of Physics D: Applied Physics*, 44, January 2011.

[76] Willett H. *Applications of linear plasma device studies to the improvement of power injection and handling in tokamaks.* PhD thesis, The University of York, sep 2018.

[77] Takimoto T, Endo R, Tonegawa A, and Sato K. Investigating the effects of a magnetic field divergence on plasma heat load using the linear divertor simulator TPD-SHEET IV. *Nuclear Materials and Energy*, 19, May 2019.

[78] Onda T, Kajita S, Iijima T, Tonegawa A, Ohno N, and Tanaka H. Transverse motion of a plasma column in a sheet plasma. *Contributions to Plasma Physics*, 57, February 2017.

[79] Tonegawa A, Kumita K, Ono M, Shibuya T, and Kawamura K. Characteristics of hydrogen negative ions in sheet plasma. *Japanese Journal of Applied Physics*, 45, October 2006.

[80] De Groot B, Al RS, Engeln R, Goedheer WJ, Kruijt OG, Meiden H, Prins PR, Schram DC, Smeets PH, Veremiyenko VP, and Vijvers WA. Extreme hydrogen plasma fluxes at pilot-PSI enter the ITER divertor regime. *Fusion Engineering and Design*, 87, October 2007.

[81] De Groot B, Van Rooij GJ, Veremiyenko V, von Hellermann MG, van Eck HJ, Barth CJ, Kruijtzer GL, Wolff JC, Goedheer WJ, Cardozo NL, and Kleyn AW. MAGNUM-PSI, a plasma generator for plasma–surface interaction research in ITER-like conditions. *Fusion engineering and design*, 74, November 2005.

[82] Perillo R, Akkermans GR, Barrois R, Classen IG, Vijvers WA, Morgan TW, van Eck HJ, Lu W, de Baar MR, Bret A, and Fajardo M. The influence of N_2 and H_2 seeding on detachment in a divertor-relevant plasma by means of modelling and experiments in MAGNUM-PSI. *44th European Physical Society Conference on Plasma Physics*, January 2017.

[83] Baeva M, Goedheer WJ, and Lopes Cardozo NJ. Kinetics of hydrogen molecules in MAGNUM-PSI. *Plasma Science and Technology*, 10, April 2008.

[84] Baeva M, Goedheer WJ, Lopes Cardozo NJ, and Reiter D. B2-EIRENE simulation of plasma and neutrals in MAGNUM-PSI. *Journal of Nuclear Materials*, 10, April 2007.

[85] Sewell G. *The Interaction of a Plasma Stream with a Neutral Gas Target: Experiments Related to the Gaseous Divertor Concept.* PhD thesis, The University of Manchester Institute for Science and Technology, 1997.

[86] Kay MJ. *A Study of Plasma Attenuation and Recombination in the Gas Target Chamber of a Divertor Simulator.* PhD thesis, The University of Manchester Institute for Science and Technology, 1998.

[87] Gibson KJ, Browning PK, Mihaljcic B, Forder DA, and Hugill J. Studies of detached plasmas on the ULS divertor simulator. *Journal of nuclear materials*, 313, March 2003.

[88] Bacal M and Wada M. Negative hydrogen ion production mechanisms. *Applied physics reviews*, 2, June 2015.

[89] Aanesland A, Rafalskyi D, Bredin J, Grondein P, Oudini N, Chabert P, Levko D,

Garrigues L, and Hagelaar G. The PEGASES gridded ion-ion thruster performance and predictions. *IEEE Transactions on Plasma Science*, 43, December 2014.

[90] Renaud D, Gerst D, Mazouffre S, and Aanesland A. E×B probe measurements in molecular and electronegative plasmas. *Review of Scientific Instruments*, 86, December 2015.

[91] Lettry J, Aguglia D, Andersson P, Bertolo S, Butterworth A, Coutron Y, Dallocchio A, Chaudet E, Gil-Flores J, Guida R, and Hansen J. Status and operation of the Linac4 ion source prototypes. *Review of Scientific Instruments*, 85, February 2014.

[92] Ueno A, Oguri H, Ikegami K, Namekawa Y, and Ohkoshi K. Interesting experimental results in Japan Proton Accelerator Research Complex H^- ion-source development. *Review of Scientific Instruments*, 81, February 2010.

[93] Marinov D, El Otell Z, Bowden MD, and Braithwaite NS. Extraction and neutralization of positive and negative ions from a pulsed electronegative inductively coupled plasma. *Plasma Sources Science and Technology*, 24, October 2015.

[94] Thomas C, Tamura Y, Syazwan ME, Higo A, and Samukawa S. Oxidation states of GaAs surface and their effects on neutral beam etching during nanopillar fabrication. *Journal of Physics D: Applied Physics*, 47, May 2014.

[95] Fantz U, Franzen P, and Wünderlich D. Development of negative hydrogen ion sources for fusion: Experiments and modelling. *Chemical Physics*, 398, April 2012.

[96] Schiesko L, McNeely P, Fantz U, Franzen P, and NNBI Team. Caesium influence on plasma parameters and source performance during conditioning of the prototype ITER neutral beam injector negative ion source. *Plasma Physics and Controlled Fusion*, 53, July 2011.

[97] Zorat R and Vender D. Global model for an RF hydrogen inductive plasma discharge in the deuterium negative ion source experiment including negative ions. *Journal of Physics D: Applied Physics*, 33, July 2000.

[98] Gans T, Osiac M, O'Connell D, Kadetov VA, Czarnetzki U, Schwarz-Selinger T, Halfmann H, and Awakowicz P. Characterization of stationary and pulsed inductively

coupled rf discharges for plasma sterilization. *Plasma physics and controlled fusion*, 47, April 2005.

[99] Dimov GI. Use of hydrogen negative ions in particle accelerators. *Review of scientific instruments*, 67, October 1996.

[100] Ahn TH, Nakamura K, and Sugai H. Negative ion measurements and etching in a pulsed-power inductively coupled plasma in chlorine. *Plasma Sources Science and Technology*, 5, May 1996.

[101] Hemsworth RS. Negative ion based neutral beam injection. *Nuclear Fusion*, 46, June 2006.

[102] Trainham R, Jacquot C, Riz D, Simonin A, Miyamoto K, Fujiwara Y, and Okumura Y. Negative ion sources for neutral beam injection into fusion machines. *Review of scientific instruments*, 69, February 1998.

[103] Kuriyama M, Akino N, Araki M, Ebisawa N, Hanada M, Inoue T, Kawai M, Kazawa M, Koizumi J, Kunieda T, and Matsuoka M. High energy negative-ion based neutral beam injection system for JT-60U. *Fusion Engineering and Design*, 26, January 1995.

[104] Lang ND. Theory of work-function changes induced by alkali adsorption. *Physical Review B*, 4, December 1971.

[105] Langmuir I and Kingdon KH. Thermionic effects caused by vapours of alkali metals. *Proceedings of the Royal Society of London. Series A, Containing Papers of a Mathematical and Physical Character*, 107, January 1925.

[106] Kurutz U and Fantz U. Investigations on caesium-free alternatives for H^- formation at ion source relevant parameters. *AIP Conference Proceedings*, 1655, April 2015.

[107] Goeden C, Dollinger G, and Feulner P. Electron stimulated desorption of negative hydrogen ions from diamond (100). *Diamond and Related Materials*, 9, April 2000.

[108] Wurz P, Schletti R, and Aellig MR. Hydrogen and oxygen negative ion production by surface ionization using diamond surfaces. *Surface Science*, 373, February 1997.

[109] Scheer JA, Wieser M, Wurz P, Bochsler P, Hertzberg E, Fuselier SA, Koeck FA, Nemanich RJ, and Schleberger M. High negative ion yield from light molecule scattering.

Nuclear Instruments and Methods in Physics Research Section B: Beam Interactions with Materials and Atoms, 230, April 2005.

[110] Fukumasa O and Saeki S. Effect of wall material on negative ion production in a hydrogen plasma. *Journal of Physics D: Applied Physics*, 20, February 1987.

[111] Leung KN, Ehlers KW, and Pyle RV. Effect of wall material on H^- production in a multicusp source. *Applied Physics Letters*, 47, August 1985.

[112] Inoue T, Matsuda Y, Ohara Y, Okumura Y, Bacal M, and Berlemont P. Effect of filament material and area on the extracted current from a volume H^- ion source. *Plasma Sources Science and Technology*, 1, May 1992.

[113] Bacal M, Ivanov Jr AA, Glass-Maujean M, Matsumoto Y, Nishiura M, Sasao M, and Wada M. Contribution of wall material to the vibrational excitation and negative ion formation in hydrogen negative ion sources. *Review of scientific instruments*, 75, May 2004.

[114] Ahmad A, Pardanaud C, Carrère M, Layet JM, Gicquel A, Kumar P, Eon D, Jaoul C, Engeln R, and Cartry G. Negative-ion production on carbon materials in hydrogen plasma: influence of the carbon hybridization state and the hydrogen content on H^- yield. *Journal of Physics D: Applied Physics*, 47, February 2014.

[115] Kumar P, Ahmad A, Pardanaud C, Carrère M, Layet JM, Cartry G, Silva F, and Gicquel Aand Engeln R. Enhanced negative ion yields on diamond surfaces at elevated temperatures. *Journal of Physics D: Applied Physics*, 44, August 2011.

[116] Schiesko L, Carrère M, Layet JM, and Cartry G. A comparative study of H^- and D^- production on graphite surfaces in H_2 and D_2 plasmas. *Plasma Sources Science and Technology*, 19, June 2010.

[117] Schiesko L, Carrère M, Layet JM, and Cartry G. Negative ion surface production through sputtering in hydrogen plasma. *Applied Physics Letters*, 95, November 2009.

[118] Fukumasa O and Saeki S. Numerical simulation on volume production of negative ions in hydrogen plasmas (II) - dependence of H^- production on plasma parameters. *Proceedings of the 9th Symposium on ISIAT 85, Tokyo*, 1985.

[119] Graham WG. Wall material and wall temperature effects on negative ion production in a hydrogen plasma. *Journal of Physics D: Applied Physics*, 16, October 1983.

[120] Bacal M. Volume production of H^- ions in plasma. *Physica Scripta*, 2, 1982.

[121] Bacal M, Bruneteau AM, and Nachman M. Negative ion production in hydrogen plasmas confined by a multicusp magnetic field. *Journal of applied physics*, 55, January 1984.

[122] Pealat M, Taran JP, Bacal M, and Hillion F. Rovibrational molecular populations, atoms, and negative ions in H^2 and D^2 magnetic multicusp discharges. *The Journal of chemical physics*, 82, June 1985.

[123] Hall RI, Landau M Čadež I, Pichou F, and Schermann C. Vibrational excitation of hydrogen via recombinative desorption of atomic hydrogen gas on a metal surface. *Physical review letters*, 60, January 1988.

[124] Hebner GA, Blain MG, Hamilton TW, Nichols CA, and Jarecki RL. Surface dependent electron and negative ion density in inductively coupled discharges. *Journal of Vacuum Science & Technology A: Vacuum, Surfaces, and Films*, 17, November 1999.

[125] Greb A, Niemi K, O'Connell D, and Gans T. The influence of surface properties on the plasma dynamics in radio-frequency driven oxygen plasmas: measurements and simulations. *Applied Physics Letters*, 103, December 2013.

[126] Katsch HM, Sturm T, Quandt E, and Döbele HF. Negative ions and the role of metastable molecules in a capacitively coupled radiofrequency excited discharge in oxygen. *Plasma Sources Science and Technology*, 9, August 2000.

[127] Goehlich A, Kawetzki T, and Döbele HF. On absolute calibration with xenon of laser diagnostic methods based on two-photon absorption. *The Journal of chemical physics*, 108, June 1998.

[128] Greb A. *Dynamics of the plasma-surface interface in capacitively coupled radio-frequency oxygen plasmas: Coupling numerical simulations with optical diagnostics.* PhD thesis, The University of York, September 2013.

[129] *Langmuir probe diagnostics*, 2003. URL "https://www.seas.ucla.edu/~ffchen/Publs/Chen210R.pdf".

[130] Chung PM, Talbot L, and Touryan KJ. *Electric probes in stationary and flowing plasmas: theory and application*. Springer Science & Business Media, March 2013. ISBN 3540068007.

[131] Mott-Smith HM and Langmuir I. The theory of collectors in gaseous discharges. *Physical Review*, 28:727–763, October 1926. doi: 10.1103/PhysRev.28.727. URL https://link.aps.org/doi/10.1103/PhysRev.28.727.

[132] Allen JE. Probe theory - the orbital motion approach. *Physica scripta*, 1991.

[133] Bernstein IB and Rabinowitz IN. Theory of electrostatic probes in a low-density plasma. *The Physics of Fluids*, 2(2):112–121, March 1959. doi: 10.1063/1.1705900. URL https://aip.scitation.org/doi/abs/10.1063/1.1705900.

[134] Laframboise JG. Theory of spherical and cylindrical Langmuir probes in a collisionless, Maxwellian plasma at rest. *UTIAS Report*, 100, June 1966. URL https://repository.tudelft.nl/view/aereports/uuid:6093f807-dee0-4807-9fe3-26fbf215d973/.

[135] Panagopoulos T and Economou DJ. Plasma sheath model and ion energy distribution for all radio frequencies. *Journal of applied physics*, 85, April 1999.

[136] Oudini N, Taccogna F, Bendib A, and Aanesland A. Numerical simulations used for a validity check on the laser induced photo-detachment diagnostic method in electronegative plasmas. *Physics of Plasmas*, 21(6), 2014.

[137] Oudini N, Sirse N, Benallal R, Taccogna F, Aanesland A, Bendib A, and Ellingboe AR. Numerical experiment to estimate the validity of negative ion diagnostic using photo-detachment combined with langmuir probing. *Physics of Plasmas*, 22(7), 2015.

[138] Oudini N, Sirse N, Taccogna F, Bendib A, and Ellingboe AR. Photo-detachment signal analysis to accurately determine electronegativity, electron temperature, and charged species density. *Applied Physics Letters*, 109(12), 2016.

[139] Sirse N, Oudini N, Bendib A, and Ellingboe AR. Measurement of electronegativity at different laser wavelengths: accuracy of langmuir probe assisted laser photo-detachment. *Plasma Sources Science and Technology*, 25(4), 2016.

[140] Oudini N, Sirse N, Taccogna F, Bendib A, and Ellingboe AR. Electronegative plasma diagnostic by laser photo-detachment combined with negatively biased langmuir probe. *Physics of Plasmas*, 109(12), 2018.

[141] Fantz U. Basics of plasma spectroscopy. *Plasma sources science and technology*, 15, October 2006.

[142] Ley HH. Analytical methods in plasma diagnostic by optical emission spectroscopy: A tutorial review. *Journal of Science and Technology*, 6, 6 2014.

[143] Sanna G and Tomassetti G. *Introduction to molecular beams gas dynamics*. World Scientific, 2005. ISBN 1783260319, 9781783260317.

[144] Astashkevich SA, Käning M, Käning E, Kokina NV, Lavrov BP, Ohl A, and Röpcke J. Radiative characteristics of 3p σ, π; 3dπ-, δ- states of H_2 and determination of gas temperature of low pressure hydrogen containing plasmas. *Journal of Quantitative Spectroscopy and Radiative Transfer*, 56, November 1996.

[145] Hornkohl JO, Parigger CG, and Nemes L. Diatomic Hönl–London factor computer program. *Applied optics.*, 44, June 2005.

[146] Gans T, Schulz von Der Gathen V, and Döbele HF. Time dependence of rotational state populations of excited hydrogen molecules in an RF excited plasma reactor. *Plasma Sources Science & Technology*, 10, February 2001.

[147] Gavare Z, Revalde G, and Skudra A. Plasma temperature determination of hydrogen containing high-frequency electrodeless lamps by intensity distribution measurements of hydrogen molecular band. *International Journal of Spectroscopy*, 2010, September 2010.

[148] Whiting EE, Schadee A, Tatum JB, Hougen JT, and Nicholls RW. Recommended conventions for defining transition moments and intensity factors in diatomic molecular spectra. *Journal of Molecular Spectroscopy*, 80, April 1980.

[149] Shikama T, Kado S, Zushi H, and Tanaka S. Molecular Zeeman spectroscopy for H_2 Fulcher-α band spectra as a local measurement of rovibrational structures. *Physics of Plasmas*, 14, July 2007.

[150] Land V, Shen E, Smith B, Matthews L, and Hyde T. Experimental and computational characterization of a modified GEC cell for dusty plasma experiments. *New Journal of Physics*, 11, June 2009.

[151] Goeckner MJ, Marquis JM, Markham BJ, Jindal AK, Joseph EA, and Zhou BS. Modified gaseous electronics conference reference cell for the study of plasma-surface-gas interactions. *Review of scientific instruments*, 75, April 2004.

[152] Olthoff JK and Greenberg KE. The gaseous electronics conference RF reference cell — An introduction. *Journal of research of the National Institute of Standards and Technology*, 100, July 1995.

[153] Olthoff JK, Van Brunt RJ, and Radovanov SB. Ion kinetic-energy distributions in argon RF glow discharges. *Journal of applied physics*, 72, November 1992.

[154] Hargis Jr PJ, Greenberg KE, Miller PA, Gerardo JB, Torczynski JR, Riley ME, Hebner GA, Roberts JR, Olthoff JK, Whetstone JR, and Van Brunt RJ. The gaseous electronics conference radio-frequency reference cell: A defined parallel-plate radio-frequency system for experimental and theoretical studies of plasma-processing discharges. *Review of Scientific Instruments*, 65, January 1994.

[155] Tsutsumi T, Greb A, Gibson AR, Hori M, O'Connell D, and Gans T. Investigation of the radially resolved oxygen dissociation degree and local mean electron energy in oxygen plasmas in contact with different surface materials. *Journal of Applied Physics*, 121, April 2017.

[156] Chabert P and Braithwaite N. *Physics of radio-frequency plasmas*. Cambridge University Press, 2011. ISBN 9780521763004.

[157] Vender D and Boswell RW. Numerical modelling of low-pressure RF plasmas. *IEEE Transactions on Plasma Sciences*, 18, August 1990.

[158] Hopkins MB. Langmuir probe measurements in the gaseous electronics conference RF reference cell. *Journal of research of the National Institute of Standards and Technology*, 100, July 1995.

[159] Hopwood J. Review of inductively coupled plasmas for plasma processing. *Plasma Sources Science and Technology*, 1, May 1992.

[160] Sakamoto Y, Maeno S, Tsubouchi N, Kasuya T, and Wada M. Comparison of plasma parameters in CCP and ICP processes appropriate for carbon nanotube growth. *Journal of Plasma Fusion Research*, 8, December 2009.

[161] van de Ven THM. *Ion fluxes towards surfaces exposed to EUV-induced plasmas*. PhD thesis, Eindhoven University of Technology, 2018.

[162] Abdel-Rahman M, Gans T, Schulz-Von Der Gathen V, and Döbele HF. Space and time resolved rotational state populations and gas temperatures in an inductively coupled hydrogen rf discharge. *Plasma Sources Science and Technology*, 14(1), 2005.

[163] Bacal M. Photodetachment diagnostic techniques for measuring negative ion densities and temperatures in plasmas. *Review of Scientific Instruments*, 71, November 2000.

[164] Banna S, Agarwal A, Cunge G, Darnon M, Pargon E, and Joubert O. Pulsed high-density plasmas for advanced dry etching processes. *Journal of Vacuum Science & Technology A: Vacuum, Surfaces, and Films*, 30, July 2012.

[165] Ellis J, Branson J, Niemi K, Wagenaars E, and Gans T. Influence of surface materials on the volume production of negative ions in a radio-frequency driven hydrogen plasma. *Journal of Physics D: Applied Physics*, 2020.

[166] Rusbridge MG, Sewell G, Qaosim H, Forder DA, Kay M, Randewich A, Mirarefin A, Browning PK, Gibson KJ, and Hugill J. Observations of the interaction of a plasma stream with neutral gas: evidence of plasma loss through molecular-activated recombination. *Plasma Physics and Controlled Fusion*, 42(5):579–602, 2000.

[167] Huba JD. *NRL plasma formulary*. Naval research lab Washington DC plasma physics division, January 2006.

[168] Overzet LJ. Microwave diagnostic results from the gaseous electronics conference RF reference cell. *Journal of research of the National Institute of Standards and Technology*, 100, July 1995.

[169] Roberts JR. Comparison of electron density measurements in planar inductively coupled plasmas by means of the plasma oscillation method and Langmuir probes. *Plasma Sources Science and Technology*, 7, May 1998.

[170] Naz MY, Shukrullah S, Ghaffar A, and Rehman NU. Development of simple designs of multitip probe diagnostic systems for RF plasma characterization. *The Scientific World Journal*, 2014, February 2014.

[171] Naveed MA, Rehman NU, Zeb S, Hussain S, and Zakaullah M. Langmuir probe and spectroscopic studies of RF generated helium-nitrogen mixture plasma. *The European Physical Journal D*, 47, May 2008.

[172] Gordillo-Vázquez FJ, Camero M, and Góomez-Aleixandre C. Spectroscopic measurements of the electron temperature in low pressure radio frequency $Ar/H_2/C_2H_2$ and $Ar/H_2/CH_h$ plasmas used for the synthesis of nanocarbon structures. *Plasma Sources Science and Technology*, 15, December 2006.

[173] Ramamurthi B and Economou DJ. Pulsed-power plasma reactors: two-dimensional electropositive discharge simulation in a GEC reference cell. *Plasma Sources Science and Technology*, 11, July 2002.

[174] Kadetov VA. *Diagnostics and modeling of an inductively coupled radio frequency discharge in hydrogen - PhD Thesis.* PhD thesis, Ruhr-Universität Bochum, 2004.

[175] Auger P. The auger effect. *Surface Science*, 48(1), 1975.

[176] Braithwaite NS. Introduction to gas discharges. *Plasma sources science and technology*, 9, November 2000.

[177] Hagstrum HD. Theory of auger ejection of electrons from metals by ions. *Physical Review*, 96, October 1954.

[178] Gans T, Schulz von der Gathen V, Czarnetzki U, and Döbele HF. Observation of fast hydrogen atoms formed by ion bombarding of surfaces. *Contributions to Plasma Physics*, 42, November 2002.

[179] Devynck P, Auvray J, Bacal M, Berlemont P, Bruneteau J, Leroy R, and Stern RA. Photodetachment technique for measuring h- velocities in a hydrogen plasma. *Review of Scientific Instruments*, 60, 1989.

[180] Mosbach T, Katsch H-M, and Döbele HF. Temporal behaviour of the h-minus density in a pulsed multipole discharge investigated by the photodetachment technique. *Plasma Sources Science and Technology*, 7, February 1998.

[181] Christmann K. Interaction of hydrogen with solid surfaces. *Surface Science Reports.*, 9(1-3), 1988.

[182] Rettner CT. Reaction of an h-atom beam with cl/au (111): Dynamics of concurrent eley–rideal and langmuir–hinshelwood mechanisms. *The Journal of chemical physics.*, 101(2), 1994.

[183] Harris J and Kasemo B. On precursor mechanisms for surface reactions. *Surface Science.*, 111(17), 1981.

[184] Kammler T and Küppers J. Interaction of h atoms with cu (111) surfaces: Adsorption, absorption, and abstraction. *The Journal of chemical physics.*, 111(17), 1999.

[185] Kammler T, Kolovos-Vellianitis D, and Küppers J. A hot-atom reaction kinetic model for h abstraction from solid surfaces. *Surface Science.*, 460(1-3), 2000.

[186] Schermann C, Pichou F, Landau M, Čadež I, and Hall RI. Highly excited hydrogen molecules desorbed from a surface: Experimental results. *The Journal of chemical physics*, 101(9), 1994.

[187] Markelj S and Čadež I. Production of vibrationally excited hydrogen molecules by atom recombination on cu and w materials. *The Journal of chemical physics*, 134(12), 2011.

[188] Janev RK, Langer WD, and Douglass Jr E. *Elementary processes in hydrogen-helium plasmas: cross sections and reaction rate coefficients.* Springer Science & Business Media, 1987(2012).

[189] Hiskes J. Formation of hydrogen negative ions by surface and volume processes with application to negative ion sources. *Journal de Phisique Colloques*, 40, July 1979.

[190] Rasser B, Van Wunnik JNM, , and Los J. Theoretical models of the negative ionization of hydrogen on clean tungsten, caesiated tungsten and caesium surfaces at low energy. *Surface Science*, 118, June 1982.

[191] Sharp TE. Potential energy diagram for molecular hydrogen and its ions. *Lockheed Missiles and Space Co., Palo Alto Research Laboratory*, 1969.

[192] Matsumura H, Kamesaki K, Masuda A, and Izumi A. Catalytic chemical sputtering: a novel method for obtaining large-grain polycrystalline silicon. *Japanese Journal of Applied Physics*, March 2001.

[193] Wanka HN and Schubert MB. High silicon etch rates by hot filament generated atomic hydrogen. *Journal of Physics D: Applied Physics*, April 1997.

[194] Chaudhary K, Inomata K, Yoshimoto M, and Koinuma H. Open-air silicon etching by h2–he–ch4 flowing cold plasma. *Materials Letters*, July 2003.

[195] Ohmi H, Kakiuchi H, Nishijima K, Watanabe H, and Yasutake K. Low-temperature crystallization of amorphous silicon by atmospheric-pressure plasma treatment in h2/he or h2/ar mixture. *Japanese journal of applied physics*, October 2006.

[196] Peña O, Muhl S, López W, Rodríguez-Fernández L, and Ruvalcaba-Sil JL. Hydrogen plasma etching of silicon dioxide in a hollow cathode system. *Thin Solid Films*, April 2010.

[197] Von Seefeld H, Schmidl H, Behrisch R, and Scherzer BMU. Sputtering yields of 1 to 20 kev light ions on stainless steel. *Journal of Nuclear Materials*, 1976.

[198] Graham WG. Negative hydrogen ion production by low energy hydrogen atom bombardment. *Physics Letters*, 73A, September 1979.

[199] Melnychuk ST and Siedl M. Reflection of hydrogen atoms from alkali and alkaline earth surfaces. *Journal of vacuum science & technology A*, 9, May 1991.

[200] Lee BS and Siedl M. Surface production of H^- ions by hyperthermal hydrogen atom. *Applied Physics Letters*, 61, December 1998.

[201] Coburn JW and Winters HF. Ion-and electron-assisted gas-surface chemistry—an important effect in plasma etching. *Journal of Applied physics*, 50, May 1979.

[202] Coburn JW, Winters HF, and Chuang T. Ion-surface interactions in plasma etching. *Journal of Applied Physics*, 48, August 1977.

[203] Vossen JL. Glow discharge phenomena in plasma etching and plasma deposition. *Journal of the Electrochemical Society*, 126, February 1979.

[204] Cazalilla M, Lorente N, Diez Muino R, Gauyacq J-P, Teillet-Billy D, and Echenique P. Theory of auger neutralization and de-excitation of slow ions at metal surfaces. *Physical Review B*, 1998.

[205] Abdel-Rahman M, Schulz von der Gathen V, Gans T, Niemi K, and Döbele HF. Determination of the degree of dissociation in an inductively coupled hydrogen plasma using optical emission spectroscopy and laser diagnostics. *Plasma Sources Science and Technology.*, 15(4), 2006.

[206] Sode M, Schwarz-Selinger T, Jacob W, and Kersten H. Surface loss probability of atomic hydrogen for different electrode cover materials investigated in H_2-Ar low-pressure plasmas. *Journal of applied physics*, 116, July 2014.

[207] Stancu GD, Kaddouri F, Lacoste DA, and Laux CO. Atmospheric pressure plasma diagnostics by OES, CRDS and TALIF. *Journal of Physics D: Applied Physics*, 43, March 2010.

[208] Gomez S, Steen PG, and Graham WG. Atomic oxygen surface loss coefficient measurements in a capacitive/inductive radio-frequency plasma. *Applied physics letters*, 81(1), 2002.

[209] Kirchheim R and Pundt A. *Hydrogen in metals.* Elsevier, 5th edition, 2014. ISBN 9780444537706.

[210] Wheeler PD. The lattice parameter and density of pure tungsten. *Physical review*, 26, December 1925.

[211] Wheeler PD. Precision measurements of the lattice constants of twelve common metals. *Physical Review*, 25, June 1925.

[212] Boeuf A, Crico S, Caciuffo R, Rustichelli F, Pomot I, and Uny G. Effects of $m_{23}c_6$ precipitation on the lattice parameter of AISI 304 stainless steel. *Materials Letters*, 3, January 1985.

[213] Wang XY and Li DY. Mechanical and electrochemical behavior of nanocrystalline surface of 304 stainless steel. *Electrochemical Acta*, September 2002.

[214] Nordlander P, Holloway S, and Nørskov JK. Hydrogen adsorption on metal surfaces. *Surface Science*, 136, January 1984.

[215] Czack, Kurtz W, and Stein F. *W Tungsten: Supplement Volume A4 Surface Properties. Electron Emission.* Springer Science & Business Media, 8th edition, 1993 (2013). ISBN 3662101548, 9783662101544.

[216] Propst FM and Luscher E. Auger electron ejection from tungsten surfaces by low-energy ions. *Physical Review*, 132, 1963.

[217] Mahadevan P, Magnuson GD, Layton JK, , and Carlston CE. Secondary-electron emission from molybdenum due to positive and negative ions of atmospheric gasses. *Physical Review*, 40, November 1965.

[218] Böhm C and Perrin J. Retarding field analyser for measurements of ion energy distributions and secondary electron emission coefficients in low-pressure radio frequency discharges. *Review of Scientific Instruments*, 64, 1998.

[219] Gans T, Lin CC, Schulz–Von Der Gathen V, and Döbele HF. Phase-resolved emission spectroscopy of a hydrogen rf discharge for the determination of quenching coefficients. *Physical Review A.*, 67(1), 2003.

[220] Abdel-Rahman M, Schulz von der Gathen V, and Gans T. Transition phenomena in a radio-frequency inductively coupled plasma. *Journal of Physics D: Applied Physics*, 40(6), 2007.

[221] Doyle SJ, Gibson AR, Flatt J, Ho TS, Boswell RW, Charles C, Tian P, Kushner MJ, and Dedrick J. Spatio-temporal plasma heating mechanisms in a radio frequency electrothermal microthruster. *Plasma Sources Science and Technology*, 27, August 2018.

[222] Kado S, Iida Y, Kajita S, Yamasaki D, Okamoto A, Xiao B, Shikama T, Oishi T, and Tanaka S. Diagnostics of recombining plasmas in divertor simulator MAP-II. *Journal of Plasma and Fusion Research*, 81, September 2005.

[223] Janev RK, Reiter D, and Samm U. *Collision processes in low-temperature hydrogen plasmas.* Jülich: Forschungszentrum, Zentralbibliothek, 2003. ISBN 9780521763004.

[224] Frassinetti L, Beurskens MN, Scannell R, Osborne TH, Flanagan J, Kempenaars M, Maslov M, Pasqualotto R, Walsh M, and JET-EFDA Contributors. Spatial resolution

of the JET Thomson scattering system. *Review of Scientific Instruments*, 83, January 2012.

[225] Scannell R, Walsh MJ, Dunstan MR, Figueiredo J, Naylor G, O'Gorman T, Shibaev S, Gibson KJ, and Wilson H. A 130 point Nd: YAG Thomson scattering diagnostic on MAST. *Review of Scientific Instruments*, 81, October 2010.

[226] Bassan M, Andrew P, Kurskiev G, Mukhin E, Hatae T, Vayakis G, Yatsuka E, and Walsh M. Thomson scattering diagnostic systems in ITER. *Journal of Instrumentation*, 11, January 2016.

[227] Salewski M, Nielsen SK, Bindslev H, Furtula V, Gorelenkov NN, Korsholm SB, Leipold F, Meo F, Michelsen PK, Moseev D, and Stejner M. On velocity space interrogation regions of fast-ion collective Thomson scattering at ITER. *Nuclear Fusion*, 51, July 2011.

[228] Coster DP, Bonnin X, and Braams B. Further developments of the edge transport simulation package, SOLPS. *ASDEX Upgrade Team*, 2003.

[229] Carr M, Meakins A, Baciero A, Bernert M, Callarelli A, Field A, Giroud C, Harrison J, Hawkes N, Henderson S, and Lipschultz B. Towards integrated data analysis of divertor diagnostics with ray-tracing. *In 44th EPS Conference on Plasma Physics*, June 2017.

[230] Salzmann H, Bundgaard J, Gadd A, Gowers C, Hansen KB, Hirsch K, Nielsen P, Reed K, Schrödter C, and Weisberg K. The LIDAR Thomson scattering diagnostic on JET. *Review of Scientific Instruments*, 59, August 1988.

[231] Kajita S, Veshchev E, Lisgo S, Barnsley R, Morgan P, Walsh M, Ogawa H, Sugie T, and Itami K. Influence of stray light for divertor spectroscopy in ITER. *Journal of Nuclear Materials*, 463, August 2015.

[232] Shumack AE, Schram DC, Biesheuvel J, Goedheer WJ, and Van Rooij GJ. Diagnosing ions and neutrals via n=2 excited hydrogen atoms in plasmas with high electron density and low electron temperature. *Physical Review E*, 83, March 2011.

[233] Schmidt JB, Roy S, Kulatilaka WD, Shkurenkov I, Adamovich IV, Lempert WR, and Gord JR. Femtosecond, two-photon-absorption, laser-induced-fluorescence (fs-TALIF)

imaging of atomic hydrogen and oxygen in non-equilibrium plasmas. *Journal of Physics D: Applied Physics*, 50, November 2016.

[234] Klarenaar BL, Brehmer F, Welzel S, Van Der Meiden HJ, and Engeln R van de Sanden MC. Note: Rotational Raman scattering on CO_2 plasma using a volume Bragg grating as a notch filter. *Review of Scientific Instruments*, 86, April 2015.